



UNIVERSITÀ DEGLI STUDI DI NAPOLI
FEDERICO II



UNIVERSITÀ DEGLI STUDI DI NAPOLI FEDERICO II

PH.D.THESIS IN

INFORMATION TECHNOLOGY AND ELECTRICAL ENGINEERING

**SENSORY-MOTOR ENHANCEMENT IN
MINIMALLY INVASIVE ROBOTIC SURGERY**

GIUSEPPE ANDREA FONTANELLI

TUTOR: PROF. BRUNO SICILIANO

XXXI CICLO

**SCUOLA POLITECNICA E DELLE SCIENZE DI BASE
DIPARTIMENTO DI INGEGNERIA ELETTRICA E TECNOLOGIE DELL'INFORMAZIONE**

To my grandmother, Ida

Contents

Summary	9
List of Acronyms	11
Robotic Dictionary	13
List of Tables	15
List of Figures	17
1 Introduction	1
1.1 Minimally Invasive Laparoscopic Surgery	1
1.2 Minimally Invasive Robotic Surgery	1
1.3 Minimally Invasive Robotic Surgery Platforms	4
1.3.1 The da Vinci Robotic Platform	4
1.3.2 Senhance™ Surgical System	5
1.3.3 MiroSurge	6
1.3.4 Others Surgical Platforms	7
1.3.5 Shortcomings of existing surgical systems	8
1.4 Sensory-Motor enhancement in MIRS	9
1.4.1 Ergonomics in MIRS	9
2 da Vinci Research kit: Modelling and Simulated Environment	13

2.1	Preliminaries: Robot Dynamic Modelling	14
2.2	dVRK Kinematic and Dynamic Modelling	18
2.2.1	Setup Joints Arm Kinematics	18
2.2.2	PSM Arm Kinematics and Dynamics	19
2.2.3	MTM Arm Kinematics and Dynamics	26
2.2.4	ECM arm kinematics	29
2.3	Identification of the Dynamic Parameters	31
2.3.1	LMI-Based Identification	32
2.3.2	Regressor Normalisation	35
2.3.3	Optimal Trajectory Generation	35
2.3.4	Identification Results	37
2.4	dVRK V-REP Simulator	40
2.4.1	Simulator Description	41
2.4.2	Simulator Architecture	42
3	Sensory Enhancement Through Force Feedback	45
3.1	Sensorless Force Estimation: a Model Based Approach . . .	48
3.1.1	Residual-Based External Force Reconstruction . . .	48
3.2	Sensorized Force Estimation: The Trocar Force Sensor . . .	51
3.2.1	Sensor Operating Principle	52
3.2.2	Sensor Modelling and Calibration	61
3.2.3	Experimental Validation of the Sensing System . . .	72
3.3	Sensorized Force Estimation: FBG for finger tip sensor design	76
3.3.1	Sensorized Fingertip Mechanical Design	78
3.3.2	Sensor Calibration and Validation	79
3.4	Vision-based Force Estimation	83
3.4.1	Deformation and Interaction Models	84
3.4.2	Deformation Estimation Using RGB-D Data	87
3.4.3	Estimation of Elasticity Parameters	89
3.4.4	Pointwise Contact Force Estimation	91
3.4.5	Experimental Validation	93

3.5	Vision-based Force Feedback	98
3.5.1	An Intuitive Vision-Based Force Feedback Method for the Trocar Sensor	99
3.6	Conclusions	103
4	Motor Enhancement Through Advanced Instruments	107
4.1	A New Laparoscopic Tool with In-Hand Rolling Capabilities for Needle Reorientation	109
4.1.1	Clinical Motivations	111
4.1.2	Preliminaries: Dexterity Evaluation with Joint Limits	112
4.1.3	Tool Working principle	114
4.1.4	Evaluation Trough 3D Printed Prototype	119
4.1.5	Evaluation Trough Simulated Case Studies	120
4.2	The MUSHA Underactuated Hand for MIRS	129
4.2.1	The MUSHA Prototype	130
4.2.2	Analysis of Different Kinematic Solutions	135
4.2.3	Comparison with a standard laparoscopic instrument in a simulated environment	142
4.3	Conclusions	145
5	Physical-Mental Workload Reduction Through Shared Control Strategies	147
5.1	Preliminaries: Master Robot Compliance	151
5.1.1	Master Impedance Control	151
5.1.2	Master Robot Passivity	152
5.2	Robot Contextual Knowledge of the Environment	156
5.2.1	Force-based task classification	156
5.2.2	Needle Tracking	160
5.2.3	Wound Tracking	164
5.3	A Shared Control Method for Suturing	168
5.3.1	Assisted Suturing Framework	168

5.3.2	Performance Evaluation	176
5.4	A Shared Control Method for Dissection	184
5.4.1	Virtual Fixture Generation and Adaptation	189
5.4.2	Performance Evaluation	192
5.5	Conclusions	199
6	Conclusions	201
	Bibliography	203

Summary

Robot-assisted surgery has revolutionized many surgical subspecialties, mainly where procedures have to be performed in confined, difficult to visualize spaces. The introduction of a robot interposed between patients and surgeons has paved the way for the development of advanced tools, sensing systems and control strategies aimed at improving surgeons capabilities. We imagine a surgeon of tomorrow work in symbiotic interaction with the robotic systems sharing cognitive and manipulation skills to define new levels of precision, performance and effectiveness in common surgical procedures. In this thesis, these issues are faced by presenting new sensing strategies and devices, new surgical instruments with high dexterity capabilities and new human-in-the-loop control strategies to improve surgeons abilities. In details, chapter 1 introduce thesis showing the background of surgical robotics and introducing the approach; in Chapter 2 we will describe our experimental setup composed by the da Vinci Research Kit (dVRK) focusing on kinematics and dynamics modelling and on the simulated environment; in Chapter 3 new strategies for force estimation and feedback in the surgical scenario will be analysed; in Chapter 5 we present two novel and innovative surgical instruments for MIRS promising to improve surgeon's dexterity, comfort and capabilities; in Chapter 5

we present new control strategies to help the surgeon during tedious and repetitive tasks; finally, Chapter 6 conclude the presented work.

List of Acronyms

The following acronyms are used throughout this text.

HRI	Human-Robot Interaction
LS	Laparoscopic Surgery
OR	Operative Room
MIS	Minimally Invasive Surgery
MIRS	Minimally Invasive Robotic Surgery
HALS	Hand Assisted Laparoscopic Surgery
dVRK	da Vinci Research Kit
PSM	Patient Side Manipulator
MTM	Master Tool Manipulator
ECM	Endoscopic Camera Manipulator
FBG	Fiber Bragg Grating
VF	Virtual Fixture

FDA	Food and Drug Administration
DH	Denavit-Hartenberg
SUJ	Setup Joints
V-REP	Virtual Experimentation Platform

Robotic and Medical Dictionary

Manipulability index Measure for identifying manipulation in a workspace.

Dexterity Skill in performing tasks.

Ergonomics Derived from the two Greek words ergon (labor) and nomia (arrangement). Designing the working environment to fit the worker, instead of forcing the worker to fit the working environment.

Trocar Medical or veterinary device that is made up of an obturator (which may be a metal or plastic sharpened or non-bladed tip), a cannula (basically a hollow tube), and a seal.

Laparoscopy A surgical procedure in which a fibre-optic instrument is inserted through the abdominal wall to view the organs in the abdomen or permit small-scale surgery.

Suture Medical device used to hold body tissues together after an injury or surgery. A suture is composed of multiple stitches.

Stitch Single knot of a suture.

Phantom Device used to train surgeons.

Contextual knowledge Knowledge in context, information, and/or skills that have particular meaning because of the conditions that form part of their description.

Surgical Dissection Surgical procedure consisting in making incisions on organ or tissues.

Compliance To define what compliance is, the definition of non-compliance is useful. A non-compliant (stiff) robot end effector is a device which is designed to have predetermined positions or trajectories.

Telemanipulation control System telecontrolled by the user at the low level.

Supervised control System with high automation capabilities where the user is demanding the task to supervise the system actions using high level inputs.

Shared control System that uses both user control and an automation component. Human users interact with automated entities such as robots and artificial intelligence to work together to achieve a common goal.

List of Tables

2.1	General DH table. R: rotoidal, P: prismatic.	14
2.2	DH parameters of the SUJ	19
2.3	DH parameters of the PSM	21
2.4	DH parameters of the MTM	28
2.5	DH parameters of the ECM	30
2.6	Trajectory joint space constraints (PSM)	37
2.7	Trajectory joints space constraints (MTM)	38
2.8	Trajectory Cartesian space constraints (MTM)	38
2.9	PSM identification results [RMS error]	40
2.10	MTM identification results [RMS error]	40
3.1	CAD dynamic parameters of the instruments' shaft	71
3.2	Identified dynamic parameters of the PSM	73
3.3	RMS errors using methods (A) and (B)	75
4.1	Maximum rolling angles for different needles	119
4.2	DH parameters of the modified tool (MT)	121
4.3	Robot joint limits (in meters or radians)	122
4.4	Suture procedures	128
4.5	Overall performance of the MT	128

List of Figures

1.1	The evolution of surgery over years.	2
1.2	Robotic surgery advantages for the patient.	3
1.3	The da Vinci TM Xi robotic platform.	4
1.4	The Senhance TM Surgical System.	5
1.5	The MIRO surge robot.	6
1.6	Surgical platforms currently under development.	7
1.7	Ergonomics in Minimally Invasive Robotic Surgery. We highlights in green all the aspects that are already available in the commercial surgical robot such as the da Vinci platform and in yellow the aspects that are included but that can be improved substantially.	10
1.8	Summary of the ergonomic advantages of robotic surgery compared with traditional surgical instrumentation and operating techniques.	11
1.9	The proposed framework.	12
2.1	The da Vinci Research Kit (dVRK) in the ICAROS center University of Naples Federico II.	14
2.2	Hyperbolic tangent friction model $\tau_{fi}(\dot{q}_i) = F_v \dot{q}_i + F_s \tanh(s \dot{q}_i)$. In the figure $F_v = 0.2$, $F_s = 0.1$, $s = 50$	17

2.3	SUJ kinematic description.	18
2.4	Patient Side Manipulator (PSM) kinematics	20
2.5	Master tool Manipulator (MTM) kinematics with Denavit-Hartenberg frames	27
2.6	ECM kinematic description.	30
2.7	The optimal identification trajectory for the PSM (left) and MTM (right): arm top, instrument bottom.	36
2.8	Comparison between measured and identified torques: Left: PSM arm, Right: MTM arm.	39
2.9	The da Vinci Research Kit V-REP simulator.	41
2.10	Software architecture.	42
3.1	Sketch describing the framework of the proposed force sensing system.	46
3.2	Experimental setup, the instrument is linked to the ATI force sensor with a Spring.	49
3.3	External force reconstruction with the residual-based algorithm (red) and with the static mapping (dashed black); ground truth (blue).	50
3.4	Trocar sensor versions.	53
3.5	Exploded view of the force sensor CAD model.	54
3.6	FEM analysis results. Top: schematic of the instrument with the relevant reference frames and zoomed section of the trocar sensor. Bottom: von Mises stress and displacements along x_S and y_S axes in the case of a 10 N force applied to the tip along the x_E axis.	57
3.7	Polarization circuit (a) and characteristic curve (b) of the GP2S60 optical sensor.	59
3.8	The da Vinci PSM robotic arm with the force sensor placed at the end of the trocar: kinematic frames description.	61

3.9	Single axis sensor operating principle. The points G , S , O , R are respectively the center of mass of the instrument shaft, the contact point between the instrument shaft and the sensor (bronze ring), the attaching point between the instrument shaft and the instrument box, the RCM.	63
3.10	Experimental setup. The ATI Mini 45 force sensor mounted at the end tip of the surgical instrument (a); interaction of the spherical probe attached at the bottom of the ATI sensor with a soft tissue phantom (b).	73
3.11	Static characterization. Force along the axis x_E (top), force along the axis y_E (middle), prismatic joint trajectory (bottom).	74
3.12	Time histories of the estimated force. Method (A) is used in the first three plots from the top and method (B) in the last three plots.	76
3.13	Sensor structure integrated into the distal phalanges. The section view shows the four columns and the holes built to glue three Bragg fibers.	77
3.14	Finite element analysis of the proposed finger sensor design. (a) structure stress, (b,c,d) simulated deformation of the three Bragg fibers when the phalanx is subject to a normal, tangential and vertical force.	78
3.15	Left: measurement system. Right: a detailed view of the prototype finger and the reference sensor.	79
3.16	Coefficients associated with the sensor characteristic.	81
3.17	Force measure evaluation along z axis. F_a :ati force, F_s :sensor force.	82
3.18	External forces based on Nearest neighbors searches.	88

3.19	Surface triangular (in red) and volumetric tetrahedral mesh (elements in blue colors) of the tuff toy (left). On the right, the experimental set-up, with the tool mounted on the robotic arm equipped with a force sensor, compressing the object.	94
3.20	Fitting error with respect to the elasticity parameters. In 3.20b a closer view around the global minimum is shown.	96
3.21	Results of the Nelder-Mead process for the first initial configuration.	97
3.22	Results of the Nelder-Mead process for the second initial configuration.	98
3.23	Registration process, with in Fig. 3.23a the fitting result between the mesh and the segmented point cloud.	99
3.24	Results of the Nelder-Mead process for force estimation, for the first initial configuration.	100
3.25	Results of the Nelder-Mead process for force estimation, for the first initial configuration.	101
3.26	Vision-based force feedback. The tissue reaction force is shown in augmented reality. Top: Tissue pushing, Middle: Needle insertion, Bottom: Knot tying.	103
4.1	Object rolling capability of the novel suturing tool inspired by that of the human hand.	109
4.2	Suturing sequence flow charts. Left: standard tool (ST); right: modified tool (MT). The steps involving needle reorientation are highlighted in gray.	110
4.3	Percentage of stitches requiring needle reorientation and average/variance of the time lost for reorienting the needle. Data provided by the JIGSAWS dataset (-Dat) and real procedures (-InVivo) performed by novice (Nov-), intermediate (Int-) and expert (Exp-) surgeons.	111

4.4	Tool versions.	115
4.5	The new suturing tool: exploded view and cross section (in the frame).	116
4.6	New suturing tool working principle. A rotation of the internal pulley of an angle $\Delta\vartheta$ causes the opposite translation of the two fingers (Δx) and hence the rotation of the grasped object of an angle $\Delta\alpha$	117
4.7	Rolling model representation.	118
4.8	3D printed prototype of the new tool (scale 2:1): evaluation of the working principle with a circular shape needle.	119
4.9	Snapshots sequence of a single stitch trajectory. Top: standard tool (ST); Bottom: modified tool (MT).	122
4.10	Needle tip paths. p_e_s is the path performed using the ST, p_d is the desired circular path and p_e_m is the path simulated using the MT. The point sp is the trajectory starting point.	123
4.11	Numerical results for the single stitch trajectory. Top: time history of the joint variables for ST; Middle: time history of the joint variables for MT. Bottom: time history of the dexterity index with ST (d_s) and MT (d_m).	125
4.12	Collected data in 13 sutures (SU1, . . . , SU13) of 5 stitches. Top: Number of stitches requiring needle reorientation for each suture (gray bar), number of reorientations for which the MT would have been helpful (red bar), number of reorientations for which the MT would have been successful (blue bar). Bottom: Total time lost for reorienting the needle with the ST (red line) and with the MT (green line).	126
4.13	The hand configurations.	132
4.14	MUSHA versions.	133
4.15	The hand prototype and the tendon configuration.	134
4.16	The hand with the motors box	134

4.17	Principal direction of motion are represented on the left images along the two grasp paths, on the top the path along z and on the bottom the path in the $y - z$ plain. SGV cost variations along the paths are represented.	138
4.18	Object errors in the Cartesian space for S_1 and S_2 and S_3 in a vertical motion (along z) is represented. The top pictures are taken from real experiments performed on the prototype implementing S_1 coupling matrix.	139
4.19	Object errors in the Cartesian space for S_1 and S_2 and S_3 in a horizontal motion (along y) is represented. The top pictures are taken from real experiments performed on the prototype implementing S_1 coupling matrix.	140
4.20	Object errors in the Cartesian space for S_1 and S_2 and S_3 in a rotational motion (in the $y - z$ plane) is represented. The top pictures are taken from real experiments performed on the prototype implementing S_1 coupling matrix.	140
4.21	Simulation environment of the MH mounted on the daVinci robot.	142
4.22	Retractor simulation. Top: real surgical procedure, Bottom: simulated environment.	143
4.23	Grasp simulation. Top: real surgical procedure, Bottom: simulated environment.	144
4.24	Caliper simulation. The hand direct kinematics can be used to estimate organs or tissues critical dimensions.	145
5.1	Six levels of autonomy in surgical robotics. Curtsey of [162].	148
5.2	Example of task classification during a robotic surgical reconstructive procedure. The graph on the left depicts the Patient Side Manipulator tool tip Cartesian trajectory segmented using our approach. The pictures on the right represent some relevant suturing states.	158

5.3	Force norm variation during a reconstructive procedure used as test set. Different states are classified and shown using different colors.	160
5.4	(5.4a): Frames of interest in our discussion. (5.4b)-(5.4c)-(5.4d): Prediction failure scenario compared with the vision-based corrected estimation. (5.4e): Detection failure scenario compared with the estimation. The white circle represents the image area in which the needle is assumed to be found, based on its radius and the depth of the gripper with respect to the camera.	161
5.5	Stitch plan. β_i/β_e : insertion/extraction angles	165
5.6	Snapshots: (a) initial image, (b) segmentation trimap mask, (c) segmented image, (d) wound skeleton, (e) wound model and stitching points overlapping, (f) registration onto the 3D point cloud. In (e,f) the central spline is indicated in blue, the lateral splines are indicated in green while the stitch points are indicated in red.	167
5.7	Left: robustness w.r.t. wound motion or deformation. Right: robustness w.r.t. partial occlusion occurrence.	167
5.8	Proposed master-slave control structure. MTM: Master Tool Manipulator, PSM: Patient Side Manipulator.	168
5.9	Slave side frames disposition. With $\Sigma_s, \Sigma_t, \Sigma_{e1}, \Sigma_{p1}$ we indicate respectively the stitch frame, needle-tip frame, end-effector frame of the PSM1 and base frame. With x_e and x_i we indicate the insertion and extraction poses. $\beta_b, \beta_i, \beta_e$ represent respectively the base, insertion and extraction angles described in Sub. Section 5.3.1.	169
5.10	A visualization of the mapping between the master DoFs and the slave DoFs in the two implemented shared controllers.	171

5.11	Description of the experimental setup. Left: Augmented Reality (AR) feedback. Right: setup used in the proposed experiments.	177
5.12	Description of the password-based state machine.	178
5.13	Experiment timeline. (t, s, v, m): telemanipulation, supervised, virtual fixtures, mapping controllers; (i, e): insertion, extraction phase. (a,b) needle tip position and orientation displacement, (c,d) MTMR position and orientation, (e,f) MTML position and orientation, (g) PSM1 out-of-tangent needle tip force, (h) master stiffness. We indicate with α , β and γ the orientation expressed in Euler angles.	179
5.14	Out of tangent needle tissue interaction force in the four control cases. σ represents the curvilinear abscissa.	179
5.15	Needle tip trajectory during the needle insertion (top) and the needle extraction (bottom). The insertion is from the right to the left, the extraction is from the left to the right.	181
5.16	Performance evaluation of the four proposed controllers considering time spent for each stitch and out-of-tangent force exerted on the tissue.	182
5.17	Nasa TLX workload survey using the four control strategies. Values near the center indicate better results.	183
5.18	Example of Guidance Virtual Fixture (GVF) spline geometry and minimum distance from the robot tool central point \mathbf{x} . $\hat{\mathbf{t}}$ and $\hat{\mathbf{n}}$ denote the tangent and the normal directions, respectively, with origin in \mathbf{x}_d , i.e., the \mathbf{x} nearest point on the curve. $\mathcal{F}_i : \{\mathbf{O}_i; \mathbf{x}_i, \mathbf{y}_i, \mathbf{z}_i\}$ = inertial frame, $\mathcal{F}_{vf} : \{\mathbf{O}_{vf}; \mathbf{x}_{vf}, \mathbf{y}_{vf}, \mathbf{z}_{vf}\}$ = virtual fixture frame.	188
5.19	VF impedance shaping function $\beta(\tilde{x})$ used to limit the VF spatial influence. \tilde{x} denotes the difference between the desired and current value or the master task space variable.	193

5.20	VF pose adaptation experiment. Time histories of: (a) VF and tool central point pose along the x direction; (b) stiffness; (c) energy tank level; (d) slave interaction force; (e) human operator force on the master side.	195
5.21	Geometry adaptation experiment. (a) First VF geometry generated by the recorded interaction points. (b) Second VF geometry. (c-e) Time histories of: (c) stiffness; (d) tank energy level; (e) human operator estimated force on the master side.	197

Introduction

1.1 Minimally Invasive Laparoscopic Surgery

The applications for minimally invasive surgery have increased over the past several decades. Minimally invasive surgery includes laparoscopy and robot-assisted surgery and is common in general in urology, gynecology in particular for oncology [30, 90, 131, 105]. Since 90's, Laparoscopic Surgery (LS) has gained wide acceptance among the surgeons for the treatment of gastrointestinal diseases as well as colon cancer, gallbladder disease, gastroesophageal functional disorders and cancer [16, 15]. However, LS has many constraints such as straight instruments, unsatisfactory 3D vision sometimes associated with motion sickness, instruments clashing and a limited haptic feedback. These limitations determine trouble during the learning curve of LS, reducing the spread of this approach.

1.2 Minimally Invasive Robotic Surgery

At the beginning of 2000s, Robotic Surgery (RS) has been introduced as a new approach in MIS with the aim of overcoming the limits of LS.

In many fields, it quickly replaced the LS such as urologic procedures, pancreatic and liver surgery and rectal surgery [8].

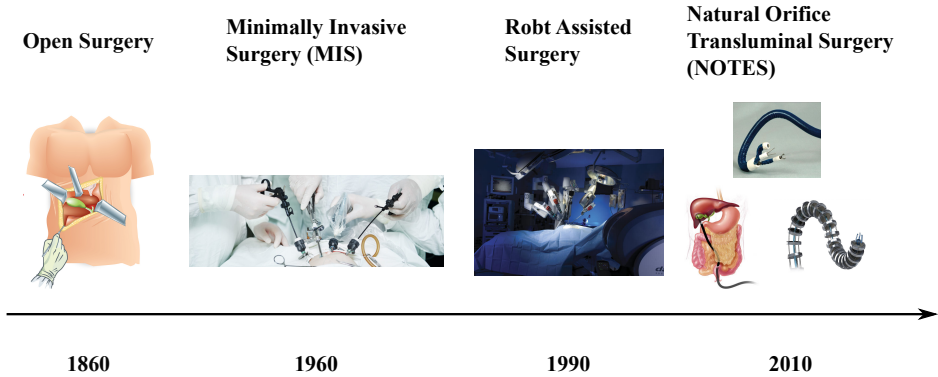


Figure 1.1. The evolution of surgery over years.

Minimally Invasive Surgery represents nowadays the gold standard approach in many surgical procedures useful for the treatment of abdominal benign and malignant diseases. A complete list of surgery field in which a robotic surgical system can be adopted is listed below:

- Radical prostatectomy, pyeloplasty, cystectomy, nephrectomy and ureteral reimplantation,
- Hysterectomy, myomectomy and sacrocolpopexy; Hiatal hernia repair,
- Spleen-sparing distal pancreatectomy, cholecystectomy, Nissen fundoplication, Heller myotomy, gastric bypass, donor nephrectomy, adrenalectomy, splenectomy and bowel resection,
- Internal mammary artery mobilization and cardiac tissue ablation,
- Mitral valve repair and endoscopic atrial septal defect closure,

- Mammary to left anterior descending coronary artery anastomosis for cardiac revascularization with adjunctive mediastinotomy,
- Transoral resection of tumors of the upper aerodigestive tract (tonsil, tongue base, larynx) and transaxillary thyroidectomy,
- Resection of spindle cell tumors originating in the lung.

The most important advantages of MIRS instead of MIS are articulated instruments, a better 3D vision, an enhanced dexterity with a consequent better precision and a substantial improved comfort for the surgeon. This translates in (see Fig. 1.2): *(i)* smaller scars, *(ii)* shorter hospitalization time, *(iii)* lower risk for adverse side effects, *(iv)* faster overall recovery time, *(v)* less pain, *(vi)* no blood donation prior to surgery, *(vii)* less blood loss, *(viii)* quicker return to normal activity[100].



Figure 1.2. Robotic surgery advantages for the patient.

1.3 Minimally Invasive Robotic Surgery Platforms

In this section the most advanced robotic surgical platforms currently on the market or under development are briefly shown.

1.3.1 The da Vinci Robotic Platform

"The da Vinci surgical system is a robotic surgical platform made by the American company Intuitive Surgical. Intuitive surgical is leader in the surgical robotics market. The da Vinci systems have been designed to decrease variability in surgery by offering consistency in functionality and user experience with dependability for surgeons seeking better outcomes."¹ With the da Vinci Surgical System, surgeons operate through



Figure 1.3. The da VinciTM Xi robotic platform.

just a few small incisions. The da Vinci System features a magnified 3D high-definition vision system and tiny wristed instruments that bend and

¹<https://www.intuitive.com/en/products-and-services/da-vinci>

rotate far greater than the human hand. As a result, da Vinci enables your surgeon to operate with enhanced vision, precision and control. Three different platforms are currently on the market: (i) the da Vinci X that is an upgradable solution, (ii) the da Vinci Xi that is the most advanced multi-port solution (see Fig. 1.3); (iii) the da Vinci SP representing the single port proposal of the American company. Moreover, an interesting selection of different surgical instruments is provided by the company to extend the applicability of the da Vinci platform to many surgical procedures and different surgeon's techniques. Some disadvantages of the da Vinci solution are: (i) the robot is fully telemanipulated and no any advanced control strategy is included, (ii) absence of haptic feedback, (iii) high cost of the robot and in particular for all the consumables.

1.3.2 Senhance™ Surgical System

Another surgical robotic platform for laparoscopy that is emerging on the market in the last few years is the Senhance™ surgical system. The

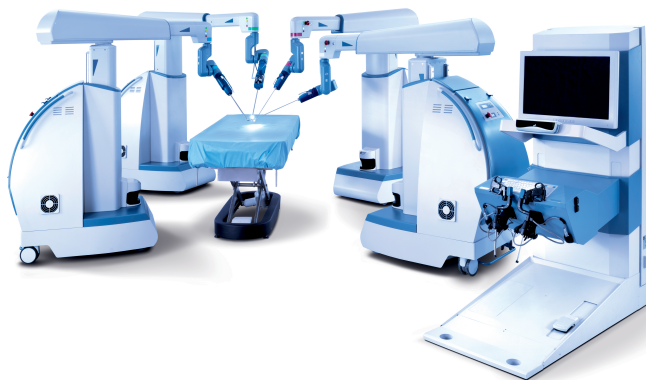


Figure 1.4. The Senhance™ Surgical System.

proposed robotic platform named ALF-X (see Fig. 1.4) was invented by the Italian SOFAR surgical robotics company and after was acquired by the American company TransEnterix. The robotic platform inherits from the da Vinci the same philosophy for a multi-port robot with customisable arms and different interchangeable instruments but adding a better sensing capability introducing haptic force feedback.

1.3.3 MiroSurge

The MiroSurge (see Fig. 1.5) is a new platform currently under development and not yet approved by the FDA by the German Aerospace Center (DLR). The DLR telesurgery MiroSurge includes a master con-



Figure 1.5. The MIRO surge robot.

sole with a 3D-display and two haptic devices as well as a teleoperator consisting of three MIRO robot arms. Usually two MIROs carry surgical instruments (DLR MICA), the third MIRO (automatically) guides a stereo video laparoscope. The stereo video stream as well as information about the system state e.g. the currently used instruments or workspace limits is displayed to the surgeon at the master console. As the Senhance

also in the MIRO the surgeon is not limited to seeing but can, via force feedback, feel workspace limits or collisions of the instruments in the hand controllers.

1.3.4 Others Surgical Platforms

In the previous paragraphs we show the surgical platform already available or close to the market, however, there are a lot of novel and advanced solutions that are currently under development. Some of the most promising solutions are listed below. In [115] a recent review of the last results in



Figure 1.6. Surgical platforms currently under development.

the surgical robotics field is reported presenting up to 19 surgical systems (see Fig. 1.6) that are under development or ready for the market. Some interesting examples approved by the FDA are: (i) Sensei X robotic catheter system; (ii) FreeHand robotic camera controller; (iii) Invendoscopy E200 handheld system; (iv) Flex single port robotic system; (v) Auris robotic endoscopy system (ARES); (vi) NeoGuide colonoscope. Moreover, some other under development/certification are: (i) MMI micro surgery system, (ii) ViaCath system; (iii) SPORTTM surgical system; (iv) SurgiBotTM; (v)

Versus Robotic System.

1.3.5 Shortcomings of existing surgical systems

Despite the improvements of the current robotic solutions available on the market for minimally invasive surgery, some limitations have not yet been overcome. Following some of that are summarized:

- Some surgical platforms such as the da Vinci robot are not equipped with any system to give the surgeon the sense of touch or any force feedback. In some other, this is present but with some limitations regarding the types of instruments equipped with this functionality.
- All the surgical systems are extremely expensive in particular for equipment and consumables.
- The surgical platforms are not equipped with any control strategy to reduce the surgeon physical-mental workload.
- Only some surgical procedure can be performed using the available robotic systems mainly for the lack of specific instruments.

In the next sections, some of these aspects are evaluated finding some solutions to improve the surgical robotic systems and most importantly to enhance the surgeon capabilities and comfort.

1.4 Sensory-Motor enhancement in MIRS

In traditional open surgery, tissue manipulation is characterized by the direct interaction of the surgeon with the anatomic structures, which is mediated by his hands and standardized instrument designs. In microsurgical and video-endoscopic procedures, tissue manipulation is achieved exclusively through the control of handheld surgical instruments. The direct hand-tissue interaction is replaced by the less intuitive, more complex and ergonomically challenging hand-tool and tool-tissue interactions. The advent of robotic telesurgery has further widened the gap between the site of surgery and the surgeon, who in this case controls the surgical instruments remotely, sitting in front of a workstation. Hence, the introduction of a robot between patients and surgeons opened the way to the development of advanced tools, sensing systems, control strategies that were impossible in MIS.

1.4.1 Ergonomics in MIRS

A major consequence of the advent of robotic surgery is an emerging active partnership between surgeons and machines. The analysis of this partnership and the study of the interaction between surgeons and the machines included in the OR is therefore of paramount importance. Such an analysis is the subject of *ergonomics*, the scientific discipline concerned with the understanding of interactions among humans and other elements of a system, and the profession that applies theory, principles, data, and methods to design to optimize human well-being and overall system performance[143]. In [32] a survey on the evolution of ergonomics in MIRS is proposed showing different applications. In [45] the ergonomics in robotic surgery has been evaluated through an ergonomic training program. Moreover, in [11] a classification of the major aspects influencing ergonomics in surgery has been done showing the most important issues

in OR that can influence surgeons comfort.

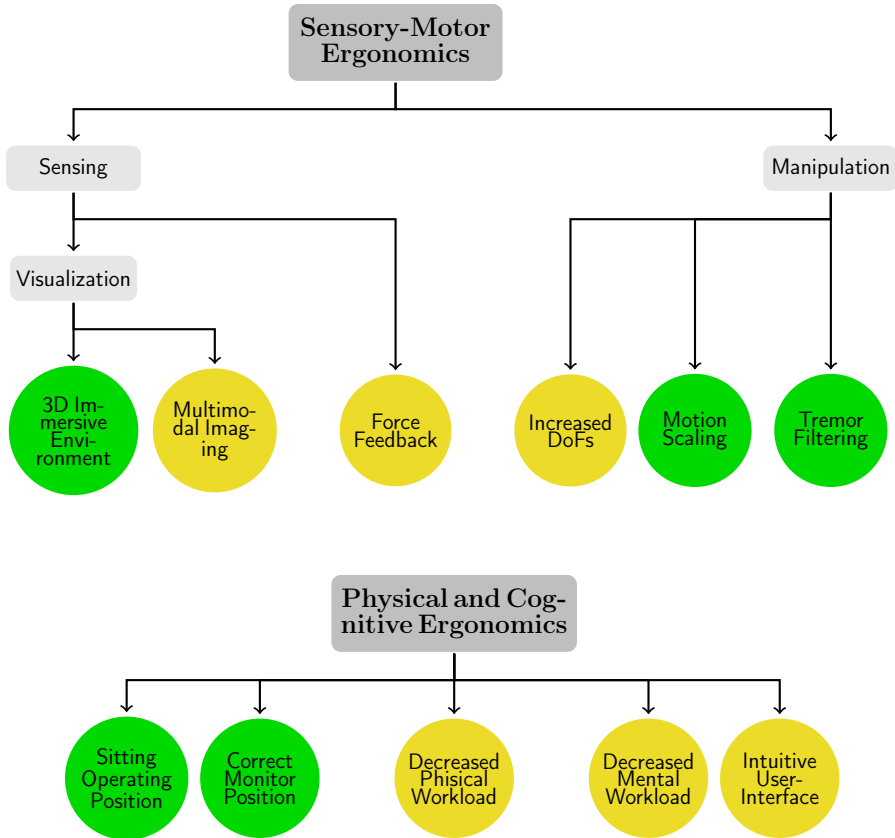


Figure 1.7. Ergonomics in Minimally Invasive Robotic Surgery. We highlights in **green** all the aspects that are already available in the commercial surgical robot such as the da Vinci platform and in **yellow** the aspects that are included but that can be improved substantially.

In Fig. 1.7 we summarise these aspects focusing, in particular, on that have been improved thanks to the introduction of a robot in the minimally invasive surgical site. With this aim we consider two definition for ergonomics: (i) *Sensory-Motor ergonomics* which studies the sensory-motor interaction between the surgeon and the environment through the robotic

system; (ii) *Physical-Cognitive ergonomics* which studies surgeon's comfort in using the robotic system. In greater details, we evaluate with *Sensory-Motor ergonomics* (Fig. 1.7 Top) all the improvements that a robot has been introduced in the surgical site, focusing on perception e.g. visual perception, force perception. and manipulation e.g. increased DoFs, motion scaling, tremor filtering. On the other hand, with *Physical-Cognitive ergonomics* (Fig. 1.7 Bottom) we consider the improvements relative specifically to the surgeon comfort e.g. improved sitting and visualization of the surgical site, decreased physical and mental workload and the intuitiveness of the user interface. The improved comfort, perception and manipulation capabilities translate in an increased safety, less stress for the surgeon, better outcomes for the patient[143] enabling new procedures not possible in MIS (see Fig. 1.8).

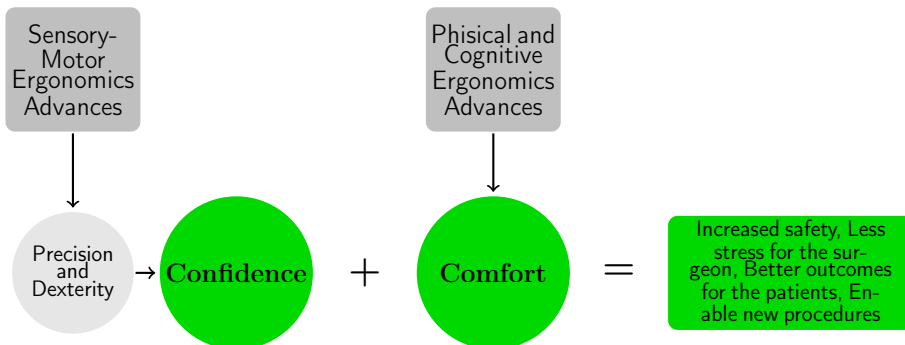


Figure 1.8. Summary of the ergonomic advantages of robotic surgery compared with traditional surgical instrumentation and operating techniques.

In Fig. 1.7 we highlight in green the already existing improvements in the commercial surgical robot such as the da Vinci platform and in yellow the some of the aspects that are not included or that can be substantially improved.

In this thesis, we aim to discuss new design solutions and strategies to improve some of the aspects defined previously. In Fig. 1.9 the proposed

framework is reported graphically showing the three principal aspects we have addressed in this dissertation: (i) improving surgeon's sensing capabilities, (ii) improving surgeon's manipulation capabilities, (iii) assist the surgeon through advanced control strategies. In details, in Chapter 2 we will describe our experimental set-up composed by the da Vinci Research Kit (dVRK) focusing on kinematics dynamics and simulation; in Chapter 3 new strategies for force estimation and feedback in the surgical scenario will be analysed; in Chapter 4 we present two novel and innovative surgical instruments for MIRS promising to improve +substantially dexterity, comfort and capability of the next surgeon generation; finally in Chapter 5 we present new control strategies to help the surgeon during tedious and repetitive tasks.

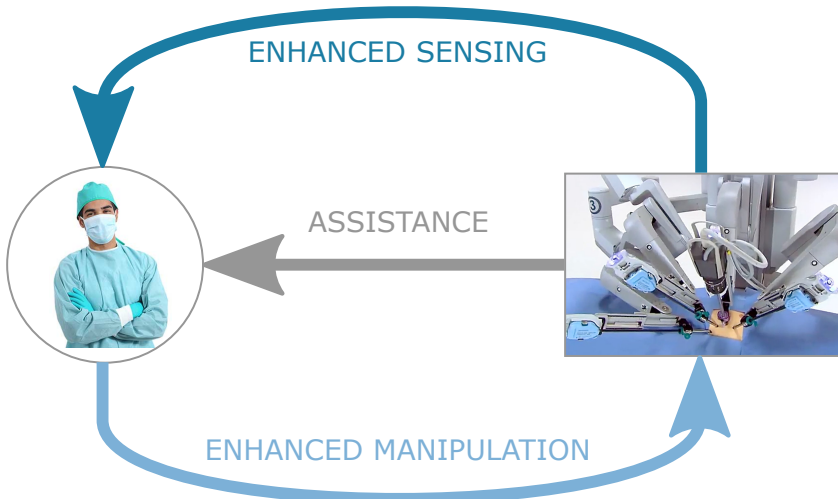


Figure 1.9. The proposed framework.

Chapter 2

da Vinci Research kit: Modelling and Simulated Environment

In this Chapter, the da Vinci Research Kit (dVRK) platform is described focusing on kinematic and dynamic models and on the developed V-REP simulated environment. In details, we discuss the kinematic modelling of the complete dVRK system and the identification of the dynamic parameters of its PSMs and MTMs arms. Using an LMI-based approach and a constrained optimization method we allow including the physical consistency constraints of the dynamic parameters in the identification procedure. Furthermore, all the problems related to trajectory generation, signal filtering, the presence of counterweights and elasticity due to the presence of springs or the power cables are evaluated and treated. Moreover, a V-REP simulator has been developed to create an easy and powerful simulated environment to test our control strategies. Some of the results reported in this section have been published in [41] and [42].

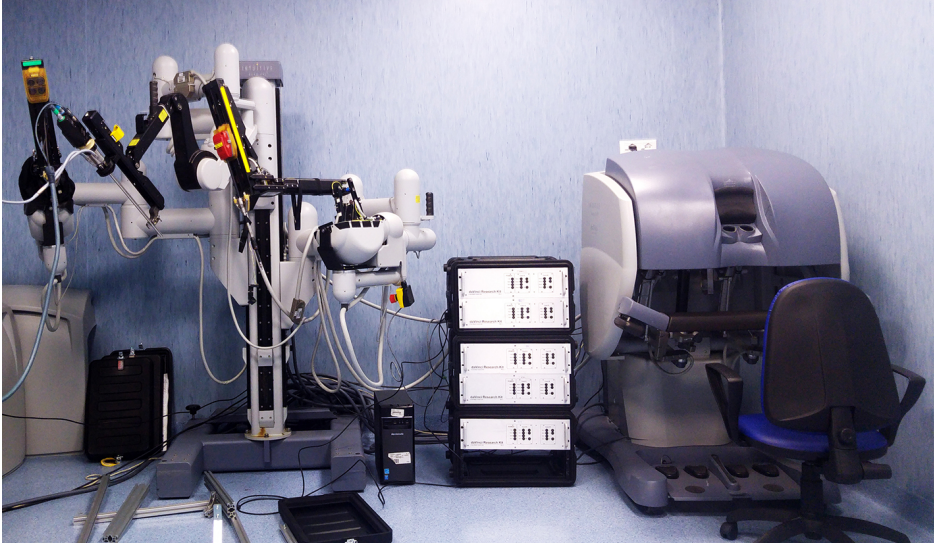


Figure 2.1. The da Vinci Research Kit (dVRK) in the ICAROS center University of Naples Federico II.

2.1 Preliminaries: Robot Dynamic Modelling

The dynamic model of a generic n-DoFs robot can be obtained by considering the recursive Newton-Euler algorithm. This approach allows an easy computation of the model in symbolic form. In details, considering a robot kinematics chain modelled using the Denavit and Hartenberg (DH) convention, the robot structure can be uniquely modelled filling with the DH parameters and the chain indexes a Table 2.1. For each link of Table 2.1,

Table 2.1. General DH table. R: rotoidal, P: prismatic.

link	joint type (R/P)	previous link	successive link	a_i	α_i	d_i	θ_i
1	—	—	—	—	—	—	—
—	—	—	—	—	—	—	—
n	—	—	—	—	—	—	—

the rotation matrix \mathbf{R}_i^{i-1} of the frame attached to link i with respect to

frame attached to link $i - 1$ can be computed as:

$$\mathbf{R}_i^{i-1}(q_i) = \begin{bmatrix} c_{\vartheta_i} & -s_{\vartheta_i}c_{\alpha_i} & s_{\vartheta_i}s_{\alpha_i} \\ s_{\vartheta_i} & c_{\vartheta_i}c_{\alpha_i} & -c_{\vartheta_i}s_{\alpha_i} \\ 0 & s_{\alpha_i} & c_{\alpha_i} \end{bmatrix}, \quad (2.1)$$

where c_{ϑ_i} and s_{ϑ_i} are the standard abbreviations of $\cos(\vartheta_i)$ and $\sin(\vartheta_i)$ respectively. The angular velocity $\boldsymbol{\omega}_i^i$, the angular acceleration $\dot{\boldsymbol{\omega}}_i^i$, and the linear acceleration $\ddot{\mathbf{p}}_i^i$ of link i are computed through forward recursion as:

- for a revolute joint:

$$\boldsymbol{\omega}_i^i = \mathbf{R}_i^{i-1\text{T}}(\boldsymbol{\omega}_{i-1}^{i-1} + \dot{\vartheta}_i \mathbf{z}_0)$$

$$\dot{\boldsymbol{\omega}}_i^i = \mathbf{R}_i^{i-1\text{T}}(\dot{\boldsymbol{\omega}}_{i-1}^{i-1} + \ddot{\vartheta}_i \mathbf{z}_0 + \dot{\vartheta}_i \boldsymbol{\omega}_{i-1}^{i-1} \times \mathbf{z}_0)$$

$$\ddot{\mathbf{p}}_i^i = \mathbf{R}_i^{i-1\text{T}}\ddot{\mathbf{p}}_{i-1}^{i-1} + \dot{\boldsymbol{\omega}}_i^i \times \mathbf{r}_{i-1,i}^i + \boldsymbol{\omega}_i^i \times (\boldsymbol{\omega}_i^i \times \mathbf{r}_{i-1,i}^i)$$

- for a prismatic joint:

$$\boldsymbol{\omega}_i^i = \mathbf{R}_i^{i-1\text{T}}\boldsymbol{\omega}_{i-1}^{i-1}$$

$$\dot{\boldsymbol{\omega}}_i^i = \mathbf{R}_i^{i-1\text{T}}\dot{\boldsymbol{\omega}}_{i-1}^{i-1}$$

$$\ddot{\mathbf{p}}_i^i = \mathbf{R}_i^{i-1\text{T}}(\ddot{\mathbf{p}}_{i-1}^{i-1} + \ddot{d}_i \mathbf{z}_0) + 2\dot{d}_i \boldsymbol{\omega}_i^i \times \mathbf{R}_i^{i-1\text{T}}\mathbf{z}_0.$$

Moreover, the force \mathbf{f}_i^i and the moment $\boldsymbol{\mu}_i^i$ exerted by link i on link $i - 1$, and the torques τ_i on joint i are computed through backward recursion as:

- for a revolute joint

$$\begin{aligned}
 \mathbf{f}_i^i &= \mathbf{R}_{i+1}^i \mathbf{f}_{i+1}^{i+1} + m_i \mathbf{R}_i^{i-1T} \ddot{\mathbf{p}}_{i-1}^{i-1} + \dot{\boldsymbol{\omega}}_i^i \times \mathbf{m}_{r_i}^i \\
 &\quad + \boldsymbol{\omega}_i^i \times (\boldsymbol{\omega}_i^i \times \mathbf{m}_{r_i}^i) \\
 \boldsymbol{\mu}_i^i &= \mathbf{R}_{i+1}^i \boldsymbol{\mu}_{i+1}^{i+1} - \mathbf{R}_{i+1}^i \mathbf{f}_{i+1}^{i+1} \times \mathbf{r}_{i-1,i}^i \\
 &\quad - \mathbf{R}_i^{i-1T} \ddot{\mathbf{p}}_{i-1}^{i-1} \times \mathbf{m}_{r_i}^i + \mathbf{I}_{r_i}^i \dot{\boldsymbol{\omega}}_i^i + \boldsymbol{\omega}_i^i \times (\mathbf{I}_{r_i}^i \boldsymbol{\omega}_i^i) \\
 \boldsymbol{\tau}_i &= \boldsymbol{\mu}_i^{iT} \mathbf{R}_i^{i-1T} \mathbf{z}_0
 \end{aligned}$$

- for a prismatic joint

$$\begin{aligned}
 \mathbf{f}_i^i &= \mathbf{R}_{i+1}^i \mathbf{f}_{i+1}^{i+1} + m_i \ddot{\mathbf{p}}_i^i + \dot{\boldsymbol{\omega}}_i^i \times \mathbf{m}_{p_i}^i \\
 &\quad + \boldsymbol{\omega}_i^i \times (\boldsymbol{\omega}_i^i \times \mathbf{m}_{p_i}^i) \\
 \boldsymbol{\mu}_i^i &= \mathbf{R}_{i+1}^i \boldsymbol{\mu}_{i+1}^{i+1} - \mathbf{f}_i^i \times \mathbf{r}_{i-1,i}^i - \ddot{\mathbf{p}}_i^i \times \mathbf{m}_{p_i}^i \\
 &\quad + \mathbf{I}_{p_i}^i \dot{\boldsymbol{\omega}}_i^i + \boldsymbol{\omega}_i^i \times (\mathbf{I}_{p_i}^i \boldsymbol{\omega}_i^i) \\
 \boldsymbol{\tau}_i &= \mathbf{f}_i^{iT} \mathbf{R}_i^{i-1T} \mathbf{z}_0,
 \end{aligned}$$

where m_i is the mass of link i , $\mathbf{I}_{r_i}^i$ ($\mathbf{m}_{r_i}^i$) is the constant inertia tensor (first moment) of link i relative to the origin of frame $i - 1$ expressed in the frame i , and $\mathbf{I}_{p_i}^i$ ($\mathbf{m}_{p_i}^i$) is the constant inertia tensor (first moment) of link i relative to the origin of frame i expressed in the frame i .

The dynamical model calculated with the Newton Euler recursive algorithm can be obtained in symbolic Lagrangian form extracting the inertia, Coriolis, gravity, friction and elasticity matrix from the symbolic $\boldsymbol{\tau}_{PSM}$ vector.

$$\mathbf{B}(\mathbf{q})\ddot{\mathbf{q}} + \mathbf{N}(\mathbf{q}, \dot{\mathbf{q}}) + \boldsymbol{\tau}_{offset} = \boldsymbol{\tau} - \mathbf{J}^T(\mathbf{q})\mathbf{h}_e \quad (2.2)$$

where

$$\mathbf{N}(\mathbf{q}, \dot{\mathbf{q}}) = \mathbf{C}(\mathbf{q}, \dot{\mathbf{q}})\dot{\mathbf{q}} + \mathbf{g}(\mathbf{q}) + \mathbf{F}(\dot{\mathbf{q}}) + \mathbf{K}_e \mathbf{q} \quad (2.3)$$

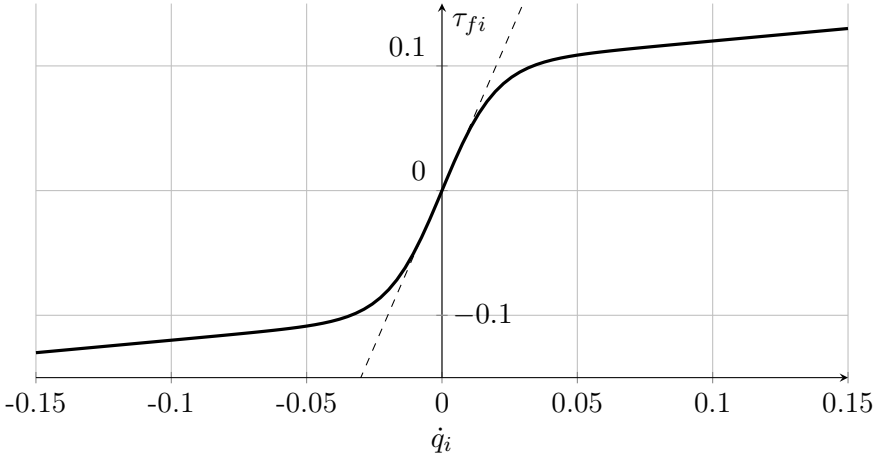


Figure 2.2. Hyperbolic tangent friction model $\tau_{fi}(\dot{q}_i) = F_v \dot{q}_i + F_s \tanh(s\dot{q}_i)$. In the figure $F_v = 0.2$, $F_s = 0.1$, $s = 50$.

\mathbf{q} , $\dot{\mathbf{q}}$ $\ddot{\mathbf{q}}$ are respectively the n – dimensional vectors of generalized joint positions, velocities and accelerations. $\mathbf{B}(\mathbf{q})$ is the $(n \times n)$ inertia matrix, $\mathbf{C}(\mathbf{q}, \dot{\mathbf{q}})$ is the $(n \times n)$ coriolis and centrifugal matrix, $\mathbf{g}(\mathbf{q})$ is the gravity vector. The friction contribution $\mathbf{F}(\dot{\mathbf{q}})$ can be computed as the sum of viscous and static friction at the actuator side. In order to guarantee a continuous friction function keeping a linear model an the following hyperbolic tangent model has been used.

$$\mathbf{F}(\dot{\mathbf{q}}) = (\mathbf{J}_j^a)^T [\mathbf{F}_v \mathbf{J}_j^a \dot{\mathbf{q}} + \mathbf{F}_s \tanh(\mathbf{S} \mathbf{J}_j^a \dot{\mathbf{q}})] \quad (2.4)$$

with $\mathbf{F}_s = \text{diag}\{F_{s1}, \dots, F_{sn}\}$, $\mathbf{F}_v = \text{diag}\{F_{v1}, \dots, F_{vn}\}$ and $\mathbf{S} = \text{diag}\{s, \dots, s\}$. The term $s F_v$ represent the slope of the static friction contribution, see Fig. 2.2 and can be set as constant value. Moreover, the term $\dot{\mathbf{q}}_a = \mathbf{J}_j^a \dot{\mathbf{q}}$ represent the actuator side velocities vector mapped into obtained from the joint velocities $\dot{\mathbf{q}}$ through the Jacobian matrix \mathbf{J}_j^a .

2.2 dVRK Kinematic and Dynamic Modelling

The full dVRK is a first-generation da Vinci Surgical System consisting of two/three PSMs, one ECM, and two Master Side Manipulators (MTMs). The slave side manipulators are mounted on a SUJ that allows the manual spatial positioning of the arm bases. The kit available at ICAROS center of the University of Naples Federico II is shown in Fig. 2.1.

2.2.1 Setup Joints Arm Kinematics

The two PSMs and the ECM are mounted on the SUJ, an articulated robotic structure composed by three or, in the newest versions, four arms. The two PSMs are located at the end of two 6-degree-of-

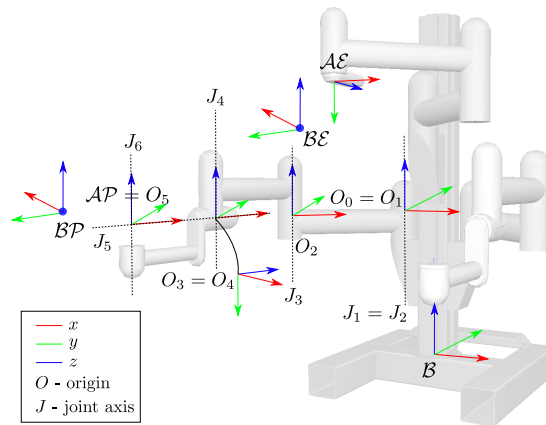


Figure 2.3. SUJ kinematic description.

freedom (DoFs) arms (that we indicate hereafter as SUJ-PSMs) while the ECM is located at the end of a 4-DoFs arm (SUJ-ECM). All the robotic arms in the SUJ are not actuated by motors but it is possible to control breaks in each joint and read the angular position using potentiometers [1]. Denoting with $\mathbf{q}_{sp} = [q_{sp,1}, \dots, q_{sp,6}]$ the vector of the SUJ-PSMs arms generalized coordinates, the homogeneous transforma-

tion matrix¹ $\mathbf{T}_{\mathcal{AP}}^{\mathcal{B}}(\mathbf{q}_{sp}) \in SE(3)$, representing the pose of the SUJ-PSMs end-effector frame $\mathcal{AP} : \{\mathbf{O}_{ap}; \mathbf{x}_{ap}, \mathbf{y}_{ap}, \mathbf{z}_{ap}\}$ with respect to the base frame $\mathcal{B} : \{\mathbf{O}_b; \mathbf{x}_b, \mathbf{y}_b, \mathbf{z}_b\}$, can be easily computed applying the standard DH convention to the kinematic chain $\{J_1, \dots, J_6\}$ of Fig. 2.3 (see Table 2.2 where $a_2 = 0.58\text{m}$, $a_3 = 0.56\text{m}$ and $d_4 = 0.425\text{m}$). Moreover, denoting with $\mathbf{q}_{se} = [q_{se,1}, \dots, q_{se,4}]$ the vector of the SUJ-ECM arm generalized coordinates, the pose of the SUJ-ECM end-effector frame $\mathcal{AE} : \{\mathbf{O}_{ae}; \mathbf{x}_{ae}, \mathbf{y}_{ae}, \mathbf{z}_{ae}\}$ with respect to the base frame $\mathcal{B} : \{\mathbf{O}_b; \mathbf{x}_b, \mathbf{y}_b, \mathbf{z}_b\}$, defined by the homogeneous transformation matrix $\mathbf{T}_{\mathcal{AE}}^{\mathcal{B}}(\mathbf{q}_{se}) \in SE(3)$, can be computed considering only the first four rows of Table 2.2. Notice that, two constant homogeneous transformation matrices $\mathbf{T}_{\mathcal{BP}}^{\mathcal{AP}} \in SE(3)$ and $\mathbf{T}_{\mathcal{BE}}^{\mathcal{AE}} \in SE(3)$ must be considered to complete the kinematics description, providing the transformation between \mathcal{AP} and \mathcal{AE} (respectively the last SUJ-PSM and SUJ-ECM frames) and the base frames \mathcal{BP} and \mathcal{BE} of the PSMs and of the ECM described in Sec. 2.2.2 and 2.2.4 (see Fig. 2.3).

Table 2.2. DH parameters of the SUJ

link	joint	prev	succ	a_i	α_i	d_i	θ_i
1	P	-	2	0	0	$q_{se,1}$	-
2	R	1	3	a_2	0	-	$q_{se,2}$
3	R	2	4	a_3	0	-	$q_{se,3}$
4	R	3	5	0	$-\pi/2$	-	$q_{se,4}$
5	R	4	6	0	$\pi/2$	$-d_4$	$q_{se,5}$
6	R	5	-	0	0	-	$q_{se,6}$

2.2.2 PSM Arm Kinematics and Dynamics

Each PSM is a 7-DOF actuated arm, which moves a surgical instrument about a Remote Center of Motion (RCM), i.e., a fixed fulcrum point that is invariant to the configuration of the PSM joints [55]. In detail, with reference to Fig. 2.4: (i) the overall structure may rotate about axis J_1

¹Hereafter, we use the matrix notation \mathbf{T}_b^a , where the superscript a denotes the frame in which vector components are expressed, the subscript b the current frame. *E.g.*, $\mathbf{T}_{\mathcal{AP}}^{\mathcal{B}}$ denotes the pose of the SUJ-PSM attach point expressed in the base frame.

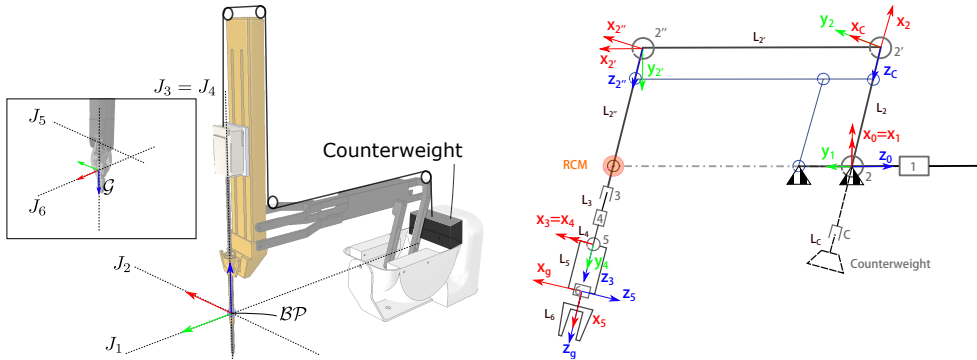


Figure 2.4. Patient Side Manipulator (PSM) kinematics

of an angle θ_1 ; (ii) a double parallelogram mechanism allows the rotation of the surgical instrument about axis J_2 of an angle θ_2 ; (iii) the surgical instrument may translate along axis J_3 of a length d_3 and rotate about axis $J_4 \equiv J_3$ of an angle θ_4 ; (iv) the axes J_1 , J_2 , J_3 and J_4 intersect in the RCM, whose position does not depend on the joint variables; (v) the revolute joints J_5 (angle θ_5) and J_6 (angle θ_6) are orthogonal and, together with J_4 , form a non-spherical wrist.

The first 6 degrees of freedom correspond to Revolute (R) or Prismatic (P) joints, combined in a RRP RRR sequence. The last degree of freedom, corresponding to the opening and closing motion of the gripper, is not considered here since we are interested in computing the position and orientation of a frame attached to the center of the gripper (frame g) with respect to a base frame (frame b) as a function of the the joint vector:

$$\mathbf{q} = [\theta_1 \quad \theta_2 \quad d_3 \quad \theta_4 \quad \theta_5 \quad \theta_6 \quad \theta_7]^T.$$

The homogeneous transformation matrix $T_G^{\mathcal{B}\mathcal{P}}(\mathbf{q}_p) \in SE(3)$, representing the pose of the gripper frame $\mathcal{G} : \{\mathbf{O}_g; \mathbf{x}_g, \mathbf{y}_g, \mathbf{z}_g\}$ with respect to the base frame $\mathcal{B}\mathcal{P} : \{\mathbf{O}_{bp}; \mathbf{x}_{bp}, \mathbf{y}_{bp}, \mathbf{z}_{bp}\}$, can be easily computed by

choosing the origin of frame \mathcal{BP} in the RCM point and applying the standard Denavit-Hartenberg (DH) convention [141] to the kinematic chain $\{J_1, \dots, J_6\}$ of Fig. 2.4 with $a_2 = 0.2$, $a'_2 = 0.5$ and $a_5 = 0.0091$. Notice that, to respect the consistency with the kinematics implemented in the DVRK open controller [2], two suitable transformation ($T_0^b(\mathbf{q})$ and $T_g^5(\mathbf{q})$) must be considered to map the first DH frame $\{\mathcal{O}_0; \mathbf{x}_0, \mathbf{y}_0, \mathbf{z}_0\}$ into the base frame \mathcal{BP} and the last DH frame $\{\mathcal{O}_5; \mathbf{x}_5, \mathbf{y}_5, \mathbf{z}_5\}$ into the gripper frame \mathcal{G} . Noticeably, for the computation of $T_{\mathcal{G}}^{\mathcal{BP}}(\mathbf{q})$, the kinematics of the double parallelogram can be ignored. Moreover, the PSM arm is mounted on a passive base (the so-called setup joint) which allows translating and rotating the arm with respect to the patient, i.e., to modify the position and orientation of the frame \mathcal{BP} attached to the RCM. Hence, a suitable constant homogeneous transformation matrix $T_{\mathcal{BP}}^{\mathcal{W}}$ must be introduced to define the position and orientation of the base frame \mathcal{BP} with respect to a world frame \mathcal{W} . In computing the dynamic model of the PSM, the constant rotation $R_{\mathcal{BP}}^{\mathcal{W}}$ of the base frame \mathcal{BP} with respect to the world frame \mathcal{W} must be taken explicitly into account because it affects the gravity torque reflected at the joints.

Table 2.3. DH parameters of the PSM

link	joint	prev	succ	a_i	α_i	d_i	θ_i
1	R	–	2	0	$-\pi/2$	–	θ_1
2	R	1	$2', \chi$	a_2	0	–	θ_2
$2'$	R	2	$2''$	a'_2	0	–	$\theta_{2'}$
$2''$	R	$2'$	3	0	$-\pi/2$	–	$\theta_{2''}$
3	P	$2''$	4	0	0	d_3	–
4	R	3	5	0	$\pi/2$	–	θ_4
5	R	4	6	a_5	$-\pi/2$	–	θ_5
6	R	5	–	0	$-\pi/2$	–	θ_6
χ	P	2	c	0	$-\pi/2$	–	–
c	P	χ	–	0	0	d_c	–

The computation of the dynamic model of the PSM arm can be performed using, e.g., the recursive Newton-Euler approach [141]. The clas-

sical version of the algorithm for open kinematic chains must be suitably modified to include the dynamic effects of:

- the counterweight used to balance the motion of the instrument along the prismatic joint (see Fig. 2.4);
- the links of the double parallelogram mechanism.
- the coupled friction in the instrument

With reference to Fig. 2.4, representing the complete kinematic structure of the PSM, the forward and backward recursions can be applied to the open kinematic chain composed by joints $\{1, 2, 2', 2'', 3, 4, 5, 6\}$. An additional branch of the chain must be considered to take into account the counterweight. The effects of the double parallelogram can be accounted by imposing constraints to the kinematic variables and to the joint torques.

Table 2.3 reports the Denavit-Hartenberg parameters corresponding to the reference frames set as in Fig. 2.4, using the same notation of [141]. In particular, the joint variable q_i is denoted as θ_i in case of revolute joint and as d_i in case of prismatic joint. The last two rows of the table allows to take into account the counterweight, modelled as a link which slides along a prismatic joint attached to link L_2 and linked by a tendon driven mechanism to the actuator of the prismatic joint 3. In detail, row c specifies a frame attached to the counterweight, while row χ corresponds to a frame attached to a fictitious link L_χ , which coincides with link L_2 and must be introduced to comply with the Denavit-Hartenberg convention. Considering the Newton Euler approach described in subsection 2.1 the forward recursion equations allow to compute $\boldsymbol{\omega}_i^i, \dot{\boldsymbol{\omega}}_i^i, \ddot{\boldsymbol{p}}_i^i$ as a function of $\boldsymbol{q}, \dot{\boldsymbol{q}}, \ddot{\boldsymbol{q}}$, for all the links of the kinematic chain composed by joints $\{1, 2, 2', 2'', 3, 4, 5, 6\}$ starting from the initial conditions $\boldsymbol{\omega}_0^0, \dot{\boldsymbol{\omega}}_0^0, \ddot{\boldsymbol{p}}_0^0 - \boldsymbol{g}_0^0$, being \boldsymbol{g}_0^0 the vector of the gravity acceleration, $\boldsymbol{r}_{i-1,i}^i$ the vector from the origin of frame $i-1$ to the origin of frame i , and $\boldsymbol{z}_0 = \begin{bmatrix} 0 & 0 & 1 \end{bmatrix}^T$. For the

other branch of the chain composed by links L_χ and L_c , the velocities and accelerations of the fictitious link L_χ can be computed from those of link L_2 , using the forward recursion equations for the case of prismatic joint with $\dot{d}_\chi = \ddot{d}_\chi = 0$, and so on. Moreover, the backward recursion equations allow to compute \mathbf{f}_i^i , $\boldsymbol{\mu}_i^i$ and τ_i for all the links of the robot through a backward recursion, taking into account that the kinematic chain contains two branches originating from link L_2 . For the first branch, starting from link L_6 with the terminal conditions $\mathbf{f}_7^7 = \boldsymbol{\mu}_7^7 = \mathbf{0}$, the above equations can be used to compute the forces and moments exerted on links L_5 , L_4 , L_3 , $L_{2''}$, $L_{2'}$, till $\mathbf{f}_{2'}^{2'}$ and $\boldsymbol{\mu}_{2'}^{2'}$. These vectors are respectively the force and the moment exerted by link L_2 on the first branch. Analogously, starting from link L_c with the terminal conditions $\mathbf{f}_{c+1}^{c+1} = \boldsymbol{\mu}_{c+1}^{c+1} = \mathbf{0}$, the force \mathbf{f}_c^c and the moment $\boldsymbol{\mu}_c^c$ exerted by the fictitious link L_χ on link L_c can be computed. At this point, the backward recursion can be applied to the fictitious link L_χ , considering null the mass, first moment and inertia, to compute \mathbf{f}_χ^χ and $\boldsymbol{\mu}_\chi^\chi$. Finally, for link L_2 , the interaction with both the branches must be considered, i.e.:

$$\begin{aligned} \mathbf{f}_2^2 &= \mathbf{R}_{2'}^2 \mathbf{f}_{2'}^{2'} + \mathbf{R}_\chi^2 \mathbf{f}_\chi^\chi + m_2 \mathbf{R}_2^{1T} \ddot{\mathbf{p}}_1^1 + \dot{\boldsymbol{\omega}}_2^2 \times \mathbf{m}_{r_2}^2 \\ &\quad + \boldsymbol{\omega}_2^2 \times (\boldsymbol{\omega}_2^2 \times \mathbf{m}_{r_2}^2) \end{aligned}$$

$$\begin{aligned} \boldsymbol{\mu}_2^2 &= \mathbf{R}_{2'}^2 \boldsymbol{\mu}_{2'}^{2'} - \mathbf{R}_{2'}^2 \mathbf{f}_{2'}^{2'} \times \mathbf{r}_{1,2}^2 \\ &\quad + \mathbf{R}_\chi^2 \boldsymbol{\mu}_\chi^\chi - \mathbf{R}_\chi^2 \mathbf{f}_\chi^\chi \times \mathbf{r}_{1,2}^2 \\ &\quad - \mathbf{R}_2^{1T} \ddot{\mathbf{p}}_1^1 \times \mathbf{m}_{r_2}^2 + \mathbf{I}_{r_2}^2 \dot{\boldsymbol{\omega}}_2^2 + \boldsymbol{\omega}_2^2 \times (\mathbf{I}_{r_2}^2 \boldsymbol{\omega}_2^2), \end{aligned}$$

and may be resumed in the standard form with link L_1 .

To take into account that the counterweight is linked to the actuator of the prismatic joint 3, the following constraints must be imposed to the

corresponding joint variables:

$$q_c = -q_3, \quad \dot{q}_c = -\dot{q}_3, \quad \ddot{q}_c = -\ddot{q}_3.$$

Moreover, the torque on joint 3 can be computed as:

$$\tau_3 = \mathbf{f}_3^{3T} \mathbf{R}_3^{2''T} \mathbf{z}_0 - \mathbf{f}_c^{cT} \mathbf{R}_c^{2T} \mathbf{z}_0$$

The presence of the parallelogram is taken into account by imposing the closed-chain constraints to the joint positions, velocities and acceleration, for the joints 2, 2' and 2''. Notice that joint 2 is actuated or active, while joints 2' and 2'' are unactuated or passive. In detail, the following equalities hold for the joint variables:

$$q_2 = q_a, \quad q_{2'} = -q_a, \quad q_{2''} = q_a$$

where q_a denotes the active joint variable. The corresponding constraints for the joint velocities can be written in compact form as

$$\dot{\mathbf{q}}_p = \mathbf{Y} \dot{q}_a, \quad \mathbf{Y} = \begin{bmatrix} 1 & -1 & 1 \end{bmatrix}^T, \quad (2.5)$$

where $\dot{\mathbf{q}}_p = \begin{bmatrix} \dot{q}_2 & \dot{q}_{2'} & \dot{q}_{2''} \end{bmatrix}^T$. Similarly, the equation $\ddot{\mathbf{q}}_p = \mathbf{Y} \ddot{q}_a$ holds for the accelerations.

By denoting as τ_a the torque performing work on the active joint q_a , in view of (2.5) and of the principle of the virtual works, the following equality holds:

$$\tau_a = \mathbf{Y}^T \boldsymbol{\tau}_p, \quad (2.6)$$

where $\boldsymbol{\tau}_p = \begin{bmatrix} \tau_2 & \tau_{2'} & \tau_{2''} \end{bmatrix}^T$ is the vector of the torques of joints 2, 2' and 2'' resulting from the backward recursion of the Newton-Euler algorithm applied to the open kinematic chain.

In conclusion, the above procedure allows computing the (7×1) vector

of the joint torques

$$\boldsymbol{\tau} = \left[\tau_1 \quad \tau_a \quad \tau_3 \quad \tau_4 \quad \tau_5 \quad \tau_6 \quad \tau_7 \right]^T$$

taking into account the inertia, Coriolis, centrifugal and gravity generalized forces. Notice that τ_7 correspond to the torque due to the instrument gripper opening and closing movement. We consider its dynamics depending only by friction contribution and than we set $\tau_7 = 0$. The contributions due to joint friction and to elastic forces acting on some of the joints can be added separately, i.e.:

$$\boldsymbol{\tau}_{PSM} = \boldsymbol{\tau} + \boldsymbol{\tau}_f + \boldsymbol{\tau}_e.$$

The friction contribution $\boldsymbol{\tau}_f$ has been obtained as described in Section 2.1 from equation 2.4 where $s = 50$ and

$$\mathbf{J}_j^a = \begin{bmatrix} 1 & 0 & 0 & 0 & 0 & 0 & 0 \\ 0 & 1 & 0 & 0 & 0 & 0 & 0 \\ 0 & 0 & 1 & 0 & 0 & 0 & 0 \\ 0 & 0 & 0 & -0.639 & 0 & 0 & 0 \\ 0 & 0 & 0 & 0 & 0.982 & 0 & 0 \\ 0 & 0 & 0 & 0 & 0.669 & 0.821 & -0.410 \\ 0 & 0 & 0 & 0 & 0.669 & 0.821 & 0.410 \end{bmatrix} \quad (2.7)$$

In this way the diagonal friction matrix in the actuator side is mapped in the joint side to take into account the coupling of the last three joints due to the tendon driving mechanism. Notice that in order to consider the complete friction model due to the coupling between the last three joints we need to consider also the seventh joint that corresponding to the opening and closing motion of the gripper. It is necessary because the 6 and 7 DOF of the PSM arm are coupled because the motion is obtained by the independent motion of the two fingers of the gripper that could be controlled to rotate the wrist about the axis z_5 in Fig. 2.4 (sixth DOF) and

to open and close the gripper (seventh DOF). Then we need to consider the 7x1 velocities vector $\dot{\mathbf{q}}$.

The elastic contribution $\boldsymbol{\tau}_e$ models the elastic forces acting on some joints. In particular, for joint 1 and 2 the elasticity is created by the power cables, while an elastic torque produced by an torsional spring is present on joint 4. These torques tend to bring back the joints to their zero angular positions and can be modeled as:

$$\boldsymbol{\tau}_e = \mathbf{K}_e \mathbf{q}, \quad (2.8)$$

with $\mathbf{F}_s = \text{diag}\{k_{e1}, k_{e2}, 0, k_{e4}, 0, 0\}$.

Finally, for the last four links, the mass and inertia properties have been neglected and the corresponding parameters have been set to zero.

2.2.3 MTM Arm Kinematics and Dynamics

The two MTMs, used to remotely teleoperate the two PSMs and the endoscopic manipulator, are identical except for their wrists, that are mirrored. Each MTM is an 8-DOF manipulator. The last degree of freedom is not actuated and is used to command the opening and closing of the gripper of the instrument. Only the first 7 degrees of freedom are considered in the kinematic and dynamic model described here.

In detail, with reference to Fig. 2.5:

(i) the overall structure may rotate about the vertical axis J_1 of an angle θ_1 ; (ii) the revolute joints with axes J_2 , J'_2 , J''_2 and J_3 form a 2-DOF parallelogram mechanism; the two actuated joints of the parallelogram are those about axes J_2 (angle θ_2) and J_3 (angle θ_3); (iii) the axes J_4 , J_5 , J_6 and J_7 intersect in the same point and correspond to revolute joints with angles θ_4 , θ_5 , θ_6 and θ_7 .

All the joints are actuated with the exception of the two revolute joints of the parallelogram about axes $J_{2'}$ and $J_{2''}$.

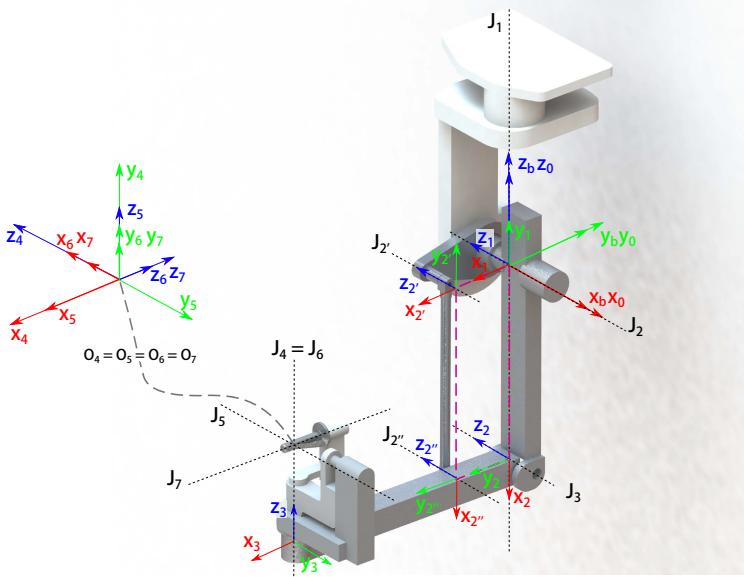


Figure 2.5. Master tool Manipulator (MTM) kinematics with Denavit-Hartenberg frames

The kinematic model of the MTM arm can be computed as a function of the vector of the actuated joints: $\mathbf{q} = [\theta_1 \dots \theta_7]^T$ by using the DH convention extended to closed kinematic chains [141]. The reference frames corresponding to the DH table reported in Table 2.4 are shown in Fig. 2.5. Notice that the base frame $\mathcal{B}_M : \{\mathbf{O}_{bm}; \mathbf{x}_{bm}, \mathbf{y}_{bm}, \mathbf{z}_{bm}\}$ coincides with frame $\{\mathbf{O}_0; \mathbf{x}_0, \mathbf{y}_0, \mathbf{z}_0\}$.

The homogenous transformation matrix $\mathbf{T}_7^{\mathcal{B}_M}(\mathbf{q})$ can be computed, e.g., by considering the kinematic chain $\{1, 2, 3, 4, 5, 6, 7\}$ and taking into account that the parallelogram mechanism imposes the following constraints to the joint variables:

$$q_{2'} = q_2 + q_3, \quad q_{2''} = -q_3. \quad (2.9)$$

Table 2.4. DH parameters of the MTM

link	joint	prev	succ	a_i	α_i	d_i	θ_i
1	R	—	2, 2'	0	$\pi/2$	0	θ_1
2	R	1	3	0.279	0	0	θ_2
2'	R	1	2''	0.1	0	0	$\theta_{2'}$
2''	R	2'	—	0.279	0	0	$\theta_{2''}$
3	R	2	4	0.365	$-\pi/2$	0	θ_3
4	R	3	5	0	$\pi/2$	0.151	θ_4
5	R	4	6	0	$-\pi/2$	0	θ_5
6	R	5	7	0	$\pi/2$	0	θ_6
7	R	6	—	0	0	0	θ_7

The computation of the dynamic model of the MSM arm, as for the PSM arm, can be performed using the recursive Newton-Euler approach. The version of the algorithm for closed kinematic chains must be adopted, to take into account for the parallelogram mechanism.

In detail, the joint 3 can be virtually cut and the recursive Newton-Euler algorithm described in the previous section can be employed for the two open kinematic chains, the first composed by the joints $\{1, 2, 3, 4, 5, 6, 7\}$ and the second composed by the joints $\{1, 2', 2''\}$. Then, the effects of the parallelogram can be accounted by imposing constraints to the kinematic variables and to the joint torques.

By denoting as $\mathbf{q}_p = [q_2 \ q_3 \ q_{2'} \ q_{2''}]^T$ the vector of all the joints of the parallelogram, and as $\mathbf{q}_a = [q_{a2} \ q_{a3}]^T$ the vector of the active joints of the parallelogram, in view of the constraint equations (2.9) on the joint positions, the following equation can be derived for the velocities:

$$\dot{\mathbf{q}}_p = \Upsilon \dot{\mathbf{q}}_a, \quad \Upsilon = \begin{bmatrix} 1 & 0 \\ 0 & 1 \\ 1 & 1 \\ 0 & -1 \end{bmatrix}, \quad (2.10)$$

and the equation $\ddot{\mathbf{q}}_p = \Upsilon \ddot{\mathbf{q}}_a$ follows for the accelerations.

If $\boldsymbol{\tau}_a = [\tau_{a2} \ \tau_{a3}]^T$ denotes the vector of the torques performing work on the active joints \mathbf{q}_a , in view of (2.10) and of the principle of the virtual works, the equality $\boldsymbol{\tau}_a = \boldsymbol{\Upsilon}^T \boldsymbol{\tau}_p$ holds, where $\boldsymbol{\tau}_p = [\tau_2 \ \tau_3 \ \tau_{2'} \ \tau_{2''}]^T$ is the vector of the torques of joints 2, 3, 2' and 2'' resulting from the backward recursion of the Newton-Euler algorithm applied to the open kinematic chain.

In conclusion, the above procedure allows computing the (7×1) vector of the joint torques

$$\boldsymbol{\tau} = \begin{bmatrix} \tau_1 & \tau_{a2} & \tau_{a3} & \tau_4 & \tau_5 & \tau_6 & \tau_7 \end{bmatrix}^T$$

taking into account the inertia, Coriolis, centrifugal and gravity torques.

As for the PSM dynamic model, the contributions due to joint friction and to elastic torques acting on some of the joints are added separately, i.e.:

$$\boldsymbol{\tau}_{MTM} = \boldsymbol{\tau} + \boldsymbol{\tau}_f + \boldsymbol{\tau}_e.$$

The friction contribution $\boldsymbol{\tau}_f$ has been set as the sum of viscous and static friction as in (2.4) with \mathbf{F}_s and \mathbf{F}_v set as diagonal matrices and \mathbf{J}_j^a set as identity matrix. The torque $\boldsymbol{\tau}_e$, set as in (2.8) with diagonal \mathbf{K}_e , models the elastic torques acting on joint 1, due to the power cables, and on joints 4, 5 and 6, caused by torsional springs.

2.2.4 ECM arm kinematics

The ECM is a 4-DoF actuated arm, which moves the endoscopic camera about the RCM through revolute and prismatic joints, combined in a RRPR sequence. The homogeneous transformation matrix $\mathbf{T}_C^{\mathcal{B}\mathcal{E}}(\mathbf{q}_e) \in SE(3)$ (where $\mathbf{q}_e = [q_{e,1}, \dots, q_{e,4}]$), representing the pose of the camera frame $\mathcal{C} = \{\mathbf{O}_c; \mathbf{x}_c, \mathbf{y}_c, \mathbf{z}_c\}$ with respect to the base frame $\mathcal{B}\mathcal{E} = \{\mathbf{O}_{be}; \mathbf{x}_{be}, \mathbf{y}_{be}, \mathbf{z}_{be}\}$, can be easily computed by choosing the origin of frame $\mathcal{B}\mathcal{C}$ in the RCM point and applying the standard DH convention to the

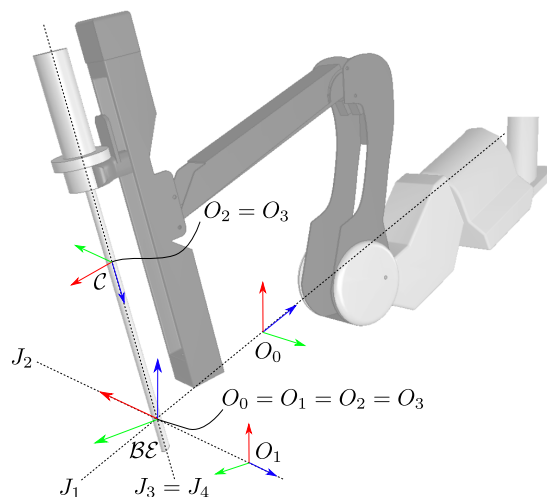


Figure 2.6. ECM kinematic description.

kinematic chain $\{J_1, \dots, J_4\}$ of Fig. 2.6 (parameters are given in Table 2.5, where $d_4 = 0.007\text{m}$).

Table 2.5. DH parameters of the ECM

link	joint	prev	succ	a_i	α_i	d_i	θ_i
1	R	-	2	0	$-\pi/2$	-	$q_{e,1}$
2	R	1	3	0	$-\pi/2$	-	$q_{e,2}$
3	P	2	4	0	0	$q_{e,3}$	-
4	R	3	-	0	0	d_4	$q_{e,4}$

2.3 Identification of the Dynamic Parameters

The methods of identification of the dynamic model of a rigid robot are based on the property of linearity of the equations with respect to a suitable set of dynamic parameters. In general, for a n -DOF manipulator, the dynamic model can be written in the form:

$$\boldsymbol{\tau} = \mathbf{Y}(\mathbf{q}, \dot{\mathbf{q}}, \ddot{\mathbf{q}})\boldsymbol{\delta} \quad (2.11)$$

where $\boldsymbol{\delta}$ is a suitable ($p \times 1$) vector of dynamic parameters and \mathbf{Y} is a ($n \times p$) matrix known as regressor; standard notation has been used for the other quantities. In principle, vector $\boldsymbol{\delta}$ can be obtained by stacking the vectors $\boldsymbol{\delta}_i$ of the dynamic parameters of link L_i , that, in the general case, includes:

- the mass m_i
- the three components of the first moment \mathbf{m}_i (\mathbf{m}_{r_i} for revolute joints and \mathbf{m}_{p_i} for prismatic joints);
- the six independent elements of the inertia tensor \mathbf{I}_i (\mathbf{I}_{r_i} for revolute joints or \mathbf{I}_{p_i} for prismatic joints);
- the static (F_{si}) and viscous (F_{vi}) friction coefficients.

Moreover, in the robots considered here, the link parameters include also:

- the elasticity coefficients K_{ei} for some of the links;
- a constant additive torque $\tau_{o,i}$ modelling the static friction offset, which may also take into account the motor current offset and the residual elastic force of the cables.

It is known that not all the dynamic parameters of the links appear explicitly in the dynamic model (3.14) and can be identified. There are

some parameters that are unidentifiable due to the mechanical structure of the manipulator and some others that are identifiable only in linear combination [48].

A reduced vector $\boldsymbol{\beta}$ of $r < p$ parameters can be found using, e.g, a numerical algorithm based on the Singular Value Decomposition (SVD) of the regressor \mathbf{Y} [48], so that:

$$\boldsymbol{\tau} = \mathbf{Y}_r(\mathbf{q}, \dot{\mathbf{q}}, \ddot{\mathbf{q}})\boldsymbol{\beta}, \quad (2.12)$$

being \mathbf{Y}_r the $(n \times r)$ reduced regressor. Vector $\boldsymbol{\beta}$ can be computed as $\boldsymbol{\beta} = \mathbf{K}_I \boldsymbol{\delta}$, where \mathbf{K}_I is a constant $(r \times p)$ matrix of coefficients.

2.3.1 LMI-Based Identification

The standard method proposed in the literature to identify the robot dynamic parameters is based on a simple least-squares optimal solution. Namely, if the robot joint torques, as well as the joint positions, velocities and accelerations are measured at given time instants t_1, \dots, t_M along a given trajectory, one may write:

$$\boldsymbol{\tau}_M = \begin{bmatrix} \boldsymbol{\tau}(t_1) \\ \vdots \\ \boldsymbol{\tau}(t_M) \end{bmatrix} = \begin{bmatrix} \mathbf{Y}_r(t_1) \\ \vdots \\ \mathbf{Y}_r(t_M) \end{bmatrix} \boldsymbol{\beta} = \mathbf{Y}_M \boldsymbol{\beta}. \quad (2.13)$$

The least-squares optimal solution to (2.13) is obtained through the left pseudo-inverse matrix of \mathbf{Y}_M as:

$$\hat{\boldsymbol{\beta}} = (\mathbf{Y}_M^T \mathbf{Y}_M)^{-1} \mathbf{Y}_M \boldsymbol{\tau}_M. \quad (2.14)$$

More advanced approaches allow to preserve the physical consistency of the parameters [50, 9]. The method proposed by Sousa e Cortesão [142] is adopted, which is based on a semidefinite programming reformulation

of the least squares method.

In detail, the identification problem is formulated in terms of a constrained optimisation problem:

$$\begin{aligned} & \underset{(\boldsymbol{\beta}, \boldsymbol{\delta})}{\text{minimize}} && \|\boldsymbol{\tau}_M - \mathbf{Y}_M \boldsymbol{\beta}\|^2 \\ & \text{subject to} && \boldsymbol{\beta} = \mathbf{K}_I \boldsymbol{\delta} \\ & && \boldsymbol{\delta} \in \mathcal{D} \end{aligned} \tag{2.15}$$

where both the existence domain \mathcal{D} of vector $\boldsymbol{\delta}$ and the objective function are expressed in a Linear Matrix Inequality (LMI) form, suitable for semidefinite programming techniques.

For the generic link L_i , the conditions that guarantee the physical feasibility of the inertial parameters are [164]:

$$m_i > 0, \quad \bar{\mathbf{I}}_i \succ 0,$$

where the symbol \succ means positive definite and $\bar{\mathbf{I}}_i$ denotes the inertia tensor of link L_i with respect to its center of mass. The above inequalities can be rewritten in terms of the components of vector $\boldsymbol{\delta}_i$ in the LMI form $\mathbf{D}_i(\boldsymbol{\delta}_i) \succ 0$ as reported in [142], where:

$$\mathbf{D}_i(\boldsymbol{\delta}_i) = \begin{bmatrix} \mathbf{I}_i & -\mathbf{S}(\mathbf{m}_i) \\ \mathbf{S}(\mathbf{m}_i) & m_i \mathbf{I} \end{bmatrix}, \tag{2.16}$$

being $\mathbf{S}(\cdot)$ the (3×3) skew-symmetric matrix operator and \mathbf{I} the (3×3) identity matrix.

The physical feasibility conditions for the other parameters of link L_i are that the friction coefficients F_{vi} and F_{si} , and the elastic coefficient K_{ei} are positive.

By defining the matrix

$$\mathbf{E}(\boldsymbol{\delta}) = \text{diag}\{\mathbf{D}_1(\boldsymbol{\delta}_1), \dots, \mathbf{D}_n(\boldsymbol{\delta}_n), \\ F_{v1}, F_{s1}, K_{e1}, \dots, F_{vn}, F_{sn}, K_{en}\},$$

the set of all physically feasible parameters of the optimisation problem (2.15) can be defined as:

$$\mathcal{D} = \{\boldsymbol{\delta} \in \mathbb{R}^p : \bar{\mathbf{E}}(\boldsymbol{\delta}) \succeq 0\}, \quad (2.17)$$

where $\bar{\mathbf{E}}(\boldsymbol{\delta}) = \mathbf{E}(\boldsymbol{\delta}) - \varepsilon \mathbf{I}$, with ε an infinitesimally small positive scalar and \mathbf{I} identity matrix of proper dimension. The non-strict inequality is required for semidefinite programming.

In the case of PSM arm, the inertial properties of the last two links have been neglected. Therefore, the corresponding constraints on matrices \mathbf{D}_i have been omitted in the formulation (2.17). Moreover, the constraint imposed to the viscous friction coefficients of the last two joints, in view of (2.4), is that the corresponding (2×2) matrix is positive definite.

By following the approach proposed in [142], by defining the scalar

$$u \geq \|\boldsymbol{\tau}_M - \mathbf{Y}_M \boldsymbol{\beta}\|^2, \quad (2.18)$$

representing an upper bound of the squared error, it can be shown that the problem (2.15) is equivalent to the semi-definite programming problem

$$\begin{aligned} & \underset{(u, \boldsymbol{\delta})}{\text{minimize}} \quad u \\ & \text{subject to} \quad \mathbf{F}(u, \boldsymbol{\delta}) \succeq 0 \end{aligned} \quad (2.19)$$

where

$$\mathbf{F}(u, \boldsymbol{\delta}) = \begin{bmatrix} \bar{\mathbf{E}}(\boldsymbol{\delta}) & 0 \\ 0 & \mathbf{U}(u, \boldsymbol{\delta}) \end{bmatrix}, \quad (2.20)$$

and matrix $\mathbf{U}(u, \boldsymbol{\delta})$ is defined in [142]. The solutions to this problem can be found numerically using software tools for solving SDP problems like CVX [52]. Although there are multiple optimal solutions $\boldsymbol{\delta}^*$, all the solutions map to a unique optimal vector $\boldsymbol{\beta}^* = \mathbf{K}_I \boldsymbol{\delta}^*$.

2.3.2 Regressor Normalisation

Since the joint torques of both the PSM and MTM arm may have very different values, numerical errors may occur. These errors can be reduced by multiplying both sides of Eq. (2.12) by a suitable diagonal weighting matrix \mathbf{W} whose elements are inversely proportional to the maximum torque measured on the respective joint along a given trajectory, namely:

$$\mathbf{W} = \text{diag}\{w_1, \dots, w_n\}$$

with $w_i = 1/\tau_{i,max}$.

Another weighting matrix \mathbf{P} can be introduced to normalise the regressor \mathbf{Y}_M with respect to the difference in magnitude of the parameters, defined as:

$$\mathbf{P} = \text{diag}\left(\frac{1}{\|\mathbf{Y}_{M,1}\|}, \dots, \frac{1}{\|\mathbf{Y}_{M,r}\|}\right), \quad (2.21)$$

where $\|\mathbf{Y}_{M,i}\|$ is norm of the i -th column of the regressor \mathbf{Y}_M . The optimal solution computed using the weighted regressor must be premultiplied by \mathbf{P}^{-1} to obtain $\boldsymbol{\beta}^*$.

2.3.3 Optimal Trajectory Generation

The trajectory used for the identification must be sufficiently *rich* to allow an accurate estimation of the dynamic parameters. On the other hand, the trajectory must not excite the unmodeled dynamics, like link or joint elasticity. The condition number of the regression matrix \mathbf{Y}_M is a measure of the sensitivity of the solution $\hat{\boldsymbol{\beta}}$ respect to the errors on \mathbf{Y}_M or $\boldsymbol{\tau}_M$

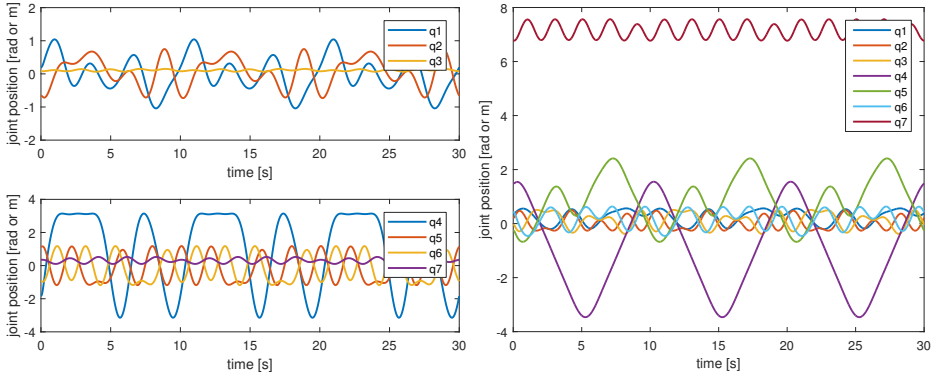


Figure 2.7. The optimal identification trajectory for the PSM (left) and MTM (right): arm top, instrument bottom.

[78, 49]. Therefore the problem of the optimal trajectory generation can be formulated as that of minimising the condition number of the matrix $\mathbf{Y}_M \mathbf{P}$ being \mathbf{P} the weighting matrix defined in (2.21).

The method proposed in [146, 147] is adopted, based on the composition of sinusoidal trajectories for joint i of the form:

$$q_i(t) = \sum_{l=1}^L \frac{a_l^i}{\omega_f l} \sin(\omega_f l t) - \frac{b_l^i}{\omega_f l} \cos(\omega_f l t) + q_{i_0} \quad (2.22)$$

where ω_f is the fundamental frequency and L is the number of the Fourier series harmonics. For both the PSM arm and the MTM arm these parameters have been set to $\omega_f = 0.1$ and $L = 5$. The quantities a_l^i , b_l^i and q_{i_0} for $l = 1, \dots, L$ are the degrees of freedom used to minimize the condition number, by solving a nonlinear optimisation problem with $2L + 1$ free variables per joint. It is possible to consider also the constraints deriving

from joint positions and velocity limits:

$$\begin{aligned} \mathbf{q}_{\min} &\leq \mathbf{q}(pT_s) \leq \mathbf{q}_{\max} \\ \dot{\mathbf{q}}_{\max} &\leq \dot{\mathbf{q}}(pT_s) \leq \dot{\mathbf{q}}_{\max} \\ \{\mathbf{k}(\mathbf{q}(pT_s))\} &\subset \mathcal{S} \end{aligned}$$

where $p = 0, 1, 2, \dots, T_f/T_s$, T_f is the final time, T_s is the sampling time, \mathcal{S} is the robot workspace and $\mathbf{k}(\mathbf{q})$ is the robot direct kinematic function. The constrained nonlinear optimization method active-set included in the *fmincon* MATLAB[®] function has been used.

2.3.4 Identification Results

The dynamics of the the PSM arm, corresponding to the first three joints, and that of the instruments, corresponding to the last four joints, are decoupled because we consider for the instrument only the friction contribution. Therefore, a separate identification must be considered. In detail, Fig. 2.7 left shows the trajectory used for the identification of the PSM arm (first three joints), while Fig. 2.7 right shows the trajectory used for the instrument. The trajectories are calculated using the optimization procedure, described previously. The constraints applied for the optimization are reported in the Table:

Table 2.6. Trajectory joint space constraints (PSM)

	J1	J2	J3	J4	J5	J6	J7
$q_{\min}[deg - m]$	-60	-45	0.05	-135	-60	-60	12
$q_{\max}[deg - m]$	60	45	0.18	135	60	60	45
$\dot{q}_{\min}[rad/s - m/s]$	-2	-2	-0.4	-6	-5	-5	-5
$\dot{q}_{\max}[rad/s - m/s]$	2	2	0.4	6	5	5	5

We filter all the signal using a moving average filtering technique. Furthermore after filtering the output signal x^F result scaled respect to the input signal x^i due to the filter attenuation. Therefore a rescaling proce-

h

Table 2.7. Trajectory joints space constraints (MTM)

	J1	J2	J3	J4	J5	J6	J7
$q_{min}[deg]$	-40	-15	-50	-200	-90	-45	-480
$q_{max}[deg]$	65	50	35	90	180	45	450
$\dot{q}_{min}[rad/s]$	-1.1	-1.1	-1.1	-2	-2	-2	-2
$\dot{q}_{max}[rad/s]$	1.1	1.1	1.1	2	2	2	2

Table 2.8. Trajectory Cartesian space constraints (MTM)

	x	y	z
$p_{min}[mm]$	-60	-60	-80
$p_{max}[mm]$	250	100	100

cedure was performed. Then the rescaled signal x^{FS} is calculated using the relations in the equations 2.23.

$$x_i^{FS} = k_i x_i^F \quad k_i = (x_i)^{-1} x_i^F \quad (2.23)$$

In Fig. 2.8 left are shown the identification results when the robot is moving with a different trajectory respect to the one used for the identification. In table 2.9 there are the RMS absolute errors and the RMS percent errors of the identification. The resultant errors are not negligible in particular for the joints 5, 6 and 7 in which only the friction components are modeled but this is a good result considering the sensors noise and the unmodelled dynamics. The identification of the MTM arm was performed using the same procedure. In Figure 2.7 right is shown the trajectory calculated using the optimization procedure, described previously. In the Table 2.7 and in Table 2.8 are the constraints applied for the optimization. For the MTM also a constrain in the Cartesian space is needed to avoid the collision between the MTM arm and the console frame structure. We apply the constraints shown in Table 2.8 considering the direct kinematics between the base frame and the frame of the link 3 (T_0^3) and we constrain the relative motion of this frame in a cube delimited by the value p_{min} and p_{max} . In Fig. 2.8 left there are the results of the identification and in

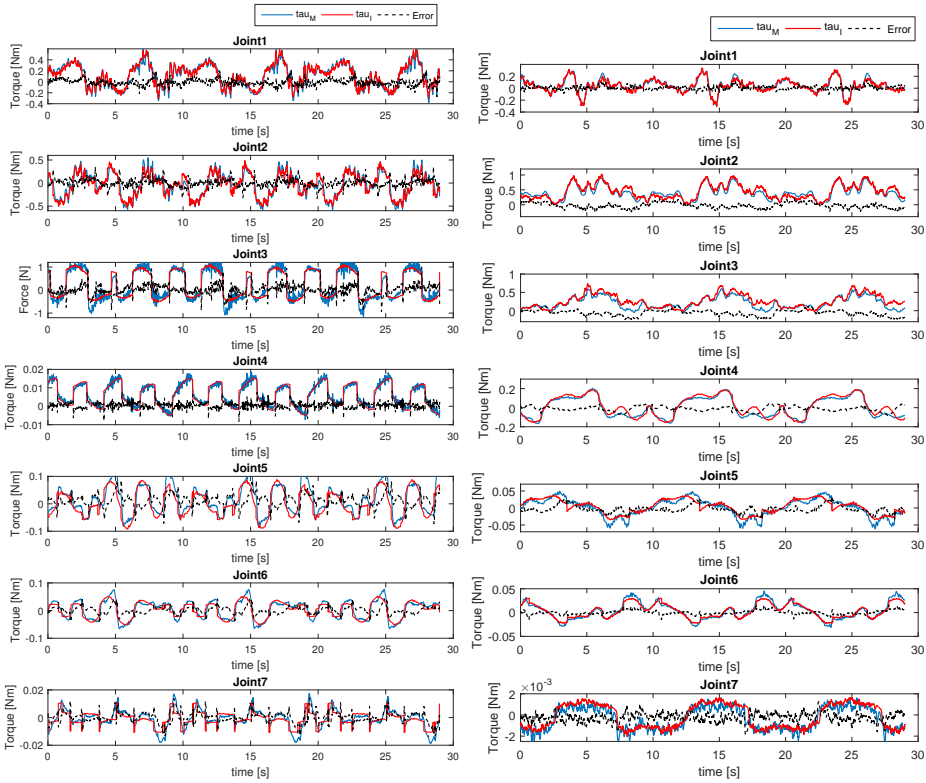


Figure 2.8. Comparison between measured and identified torques: Left: PSM arm, Right: MTM arm.

the table 2.10 there are the RMS absolute errors and the RMS relative % errors of the identification. Also for the MTM the errors are not negligible in particular for the joints 5 and 7. In both the robotics arms the results show an identification with errors below 30% that is a good result due to the noise of the velocity and the acceleration measure, the absence of torque sensors and the unmodelled dynamics like friction of the tendons or elasticity.

Table 2.9. PSM identification results [RMS error]

	J_1	J_2	J_3	J_4	J_5	J_6	J_7 (grip)
Abs err	0.05	0.08	0.194	0.0029	0.025	0.013	0.004
Rel err %	23.84	31.33	29.56	16.79	48.14	40.19	60.2

Table 2.10. MTM identification results [RMS error]

	J_1	J_2	J_3	J_4	J_5	J_6	J_7
Abs err	0.031	0.097	0.102	0.029	0.011	0.004	0.0005
Rel err %	27.06	21.04	39.07	28.36	43.54	25.42	42.83

2.4 dVRK V-REP Simulator

In this section, we present a V-REP simulator developed for the da Vinci Research Kit (dVRK) we extensively used to test our algorithms. The simulator contains a full robot kinematic model and integrated sensors. A robot operating system (ROS) interface has been created for easy use and development of common software components.

We choose V-REP² as simulator engine because of its versatility and simplicity for multi-robot applications. V-REP is based on a distributed control architecture. Each object/model can be individually controlled via an embedded script, a plugin, a ROS or BlueZero node, a remote API client, or a custom solution. Controllers can be written in C/C++, Python, Java, Lua, Matlab or Octave. Therefore, the simulator can be easily interfaced with the real surgeon master console, and new objects and robots can be imported in the scene by using a graphical interface. The complete simulator, together with the four developed application scenes, is available at <https://github.com/unina-icaros/dvrk-vrep.git>.

²<http://www.coppeliarobotics.com>

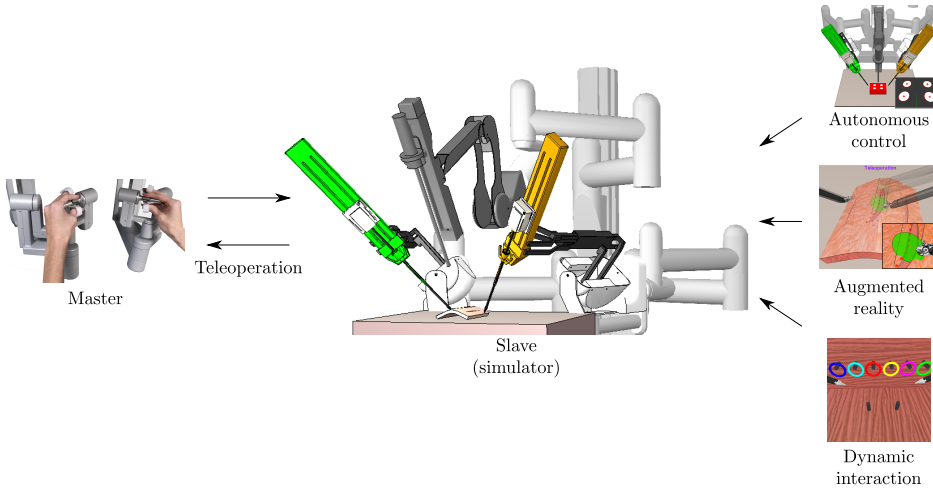


Figure 2.9. The da Vinci Research Kit V-REP simulator.

2.4.1 Simulator Description

In this section, the simulator is described focusing on the robot structure and on the general performances. With reference to Fig. 2.9, our V-REP simulator is composed of a SUJ, two PSMs and one ECM. The robotic arms have been modeled starting from the CAD models included in the John Hopkins dVRK git webpage³, except for the SUJ. Each link was made using two types of mesh: (i) one visual mesh with structure and texture similar to the real robot link, (ii) one simplified convex dynamic and responsible mesh used to simulate dynamics and contacts⁴. With reference to Sect. 2 we realized the kinematic chain of each robotic arm by linking mesh and joints in a *joint-responsible-visual* sequence. For each responsible link of the two PSMs we included the dynamic parameters obtained by identification, as described in Sec. 2.

At the end of the endoscope link, two cameras have been included to

³<https://github.com/jhu-dvrk>

⁴Dynamic responsible shapes influence each other during dynamic collisions and are subject to gravity and inertial forces.

simulate the binocular vision system of the real dVRK endoscope. We set a resolution for the cameras at 320×288 pixels, *i.e.*, half the resolution of the real endoscope, that results a trade-off option to have a good resolution and a good simulated sampling time.

The resulting complete robot is composed of 10178 triangles. Hence, considering a computer powered by a Intel I7-7770HQ processor, 16GB of ram and Nvidia GeForce 960M the scene is rendered at 45 fps and the dynamics is simulated at 200 Hz.

2.4.2 Simulator Architecture

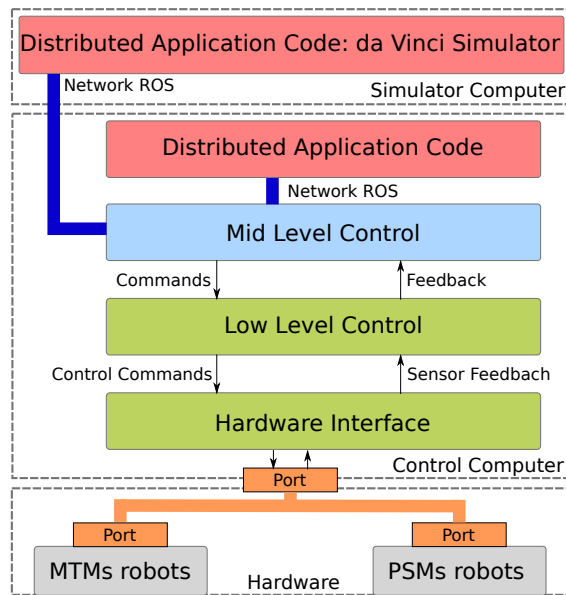


Figure 2.10. Software architecture.

We designed the proposed V-REP simulator to be fully integrated into the dVRK control infrastructure. Hence, the high-level ROS framework has been used to link our simulator to the low-level control [71]. This allows the user to use the simulator in different modalities: (i) telemanipulated

using the dVRK MTMs; *(ii)* in combination with the real robotic PSMs and ECM, to implement augmented reality algorithms; *(iii)* as standalone, by controlling the simulated robot using the ROS framework (*e.g.*, through C++, MATLAB and Python ROS nodes), or directly in V-REP using the embedded scripts.

With reference to Fig. 2.10, the control architectures of the dVRK, described in detail in [22], is composed of: *(i)* a hardware interface to communicate with the embedded actuator controllers through the fire-wire bus, implementing the safety checks; *(ii)* a low level layer implementing all the algorithms for the inverse kinematics and impedance master control; *(iii)* a mid-level layer implementing the ROS communication and the high level controllers. The communication between the da Vinci simulator, running in a dedicate computer, and the dVRK console is implemented through ROS topics. In detail, we use the *v_repExtRosInterface* to publish the state of the robot joints (PSMs, SUJ, ECM) and the gripper state for the PSMs. Moreover, the simulator subscribes to two topics *sensor_msgs::joint_state* to control the robots joints motion from ROS.

The computer configuration described in the previous section is able to stream cameras topics at 60 Hz⁵. The joints and objects topics are streamed at 220Hz.

This architecture allows to easily interface the simulator with the mid level control of the dVRK (for commanding the simulated robot through MTMs) or to other ROS-integrated input device (*e.g.*, haptic devices).

⁵The simulation requires to be run in *threaded-rendering* mode, in order to decouple the rendering and the control scripts and speed up the execution.

Chapter 3

Sensory Enhancement Through Force Feedback

As depicted in Sec. 1.2 robotic surgery increases dexterity, precision and steadiness by filtering tremors and allowing motion scaling [110] however, considering the most adopted systems available on the market e.g. da Vinci Platform, the use of a robot can limit the surgeon's sensory perception and situational awareness. In details, during open surgeries, surgeons rely mostly on vision and haptic/force feedback to have the contextual knowledge of the environment. However, in MIRS, no (or limited) force information is available, since the surgeon does not handle the tools directly [108] and current systems do not provide force feedback, limiting the ability to carry out surgeries as easily as in open surgery, increasing also intra-operative injuries [161]. For instance, in a task like suturing arterial anastomosis the surgeon relies on the sense of touch to accomplish it; when using the da Vinci, sutures are often broken and tissue is torn, due to the exertion of excessive forces [110]. Other studies conducted on laparoscopic grasping showed that often procedural errors occur due to the lack of force perception [59]. For systems like the da Vinci, where

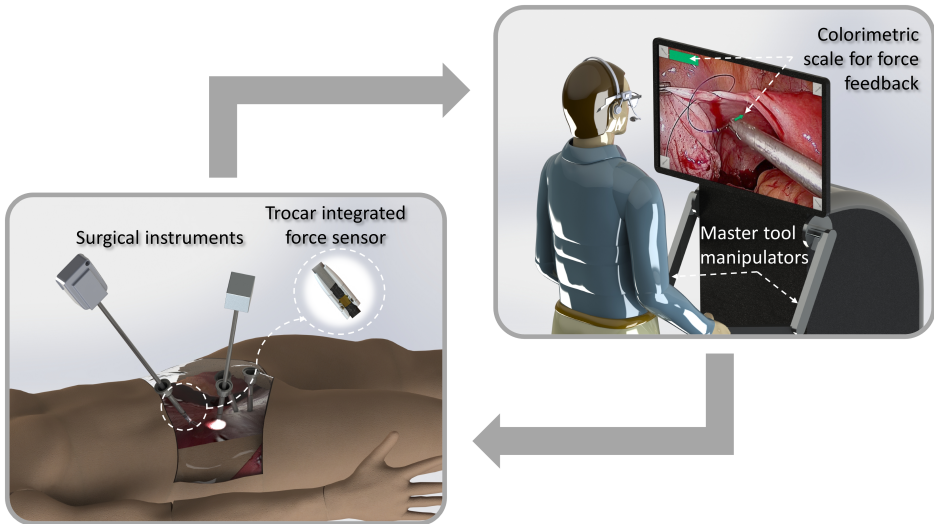


Figure 3.1. Sketch describing the framework of the proposed force sensing system.

the surgeon mostly relies on vision, force perception becomes very important also because there is no proportional relationship between the angular displacement at the master hand controller and the angular output at the slave grasper [66]. Therefore, the surgeon's force judgment is affected when handling tissues and may lead to an increase of the applied force by the grasper in the attempt to reach the desired angle. In needle insertion [109] knowledge of the applied force is also needed because the path of the needle is not always observable and the clinician relies mostly on the senses interaction between the tissue and the needle [5]. Furthermore, without force information it is impossible to identify undesired interactions between the tools and the environment (*organs*) when they are out of the visual area. Consequently, experience and ability of the surgeon make the difference. Another interesting field of application of force feedback is palpitation and tissue stiffness estimation. Here force feedback is required to estimate the

stiffness of a tissue which allows evaluating tumours in cases where it is covered by healthy tissue layers. Moreover, through palpation, it is possible to create stiffness models of the targeted tissue [86, 84, 73]. As mentioned above, force information is of uttermost importance in robotic surgery and it is what is manly hindering it from spreading [96]. It is also well known in robotics that knowledge of the interaction forces can be exploited to design controllers more suitable than pure motion controllers. As a matter of fact, motion controllers allow successful executions of interaction tasks only if the environment and the robot are precisely modelled, otherwise errors in the models may lead to the rise of unwanted and unexpected reaction forces, in turn leading to instability and damages[141] [140]. These drawbacks can be overcome by ensuring a compliant behaviour between the robot and the environment, either passively (e.g. through structural compliance of links, joints) or actively through impedance/admittance control, stiffness/compliance control, hybrid force/position control and parallel force/position control. In many surgical applications, for example, the surgeon applies some kind of hybrid force/position control, being capable of accurately positioning a knife and of modulating the applied force to avoid damages [17]. Possibly, surgical robots will achieve the same capabilities of industrial robotic manipulators or humans when it comes to interacting with the environment.

In this Chapter, we aim to discuss new developed methods and devices that can be used in MIRS to provide force feedback information to the surgeon improving his/her perception. All the methods and devices have been designed to work with the dVRK robot hence we will refer to this platform in the next sections. However, the proposed approaches could be easily extended to other surgical robotic systems. We will discuss in detail a model based approach based on the robot dynamic model knowledge in Sec. 2, a new sensing solution in Sec. 3.2, a vision-based method in Sec. 3.4 and finally a simple vision-based force feedback method in Sec. 3.5.

3.1 Sensorless Force Estimation: a Model Based Approach

In this section, we discuss the possibility to estimate the external force through the joint current measure and the knowledge of the dynamic model of the surgical robotic platform. This allows the force estimation without recurring to fragile and costly force sensing solutions. Some of the results reported in this section have been published in [41].

3.1.1 Residual-Based External Force Reconstruction

The knowledge of the robot dynamic model allows the estimation of the external forces acting on the robot structure. On this purpose in literature, different approaches have been proposed. In this section, we discuss the approach proposed by De Luca et al in [91].

The residual vector \mathbf{r} for a robot with dynamics 2.2 is defined as:

$$\mathbf{r}(t) = \mathbf{K}_I \left(\mathbf{B}(\mathbf{q})\dot{\mathbf{q}} - \int_0^t \left(\mathbf{r}(\sigma) + \boldsymbol{\tau} + \tilde{\mathbf{N}}(\mathbf{q}, \dot{\mathbf{q}} - \boldsymbol{\tau}_{\text{offset}}) \right) d\sigma \right) \quad (3.1)$$

$$\tilde{\mathbf{N}}(\mathbf{q}, \dot{\mathbf{q}}) = \mathbf{C}^T(\mathbf{q}, \dot{\mathbf{q}})\dot{\mathbf{q}} - \mathbf{g}(\mathbf{q}) - \mathbf{F}(\dot{\mathbf{q}}) - \mathbf{K}_e \mathbf{q} \quad (3.2)$$

where $\mathbf{B}(\mathbf{q})\dot{\mathbf{q}}$ is the robot generalized momentum and $\mathbf{K}_I > \mathbf{0}$ is a diagonal gain matrix. The evolution of the residual vector \mathbf{r} is a stable first-order filter

$$\dot{\mathbf{r}} = \mathbf{K}_I(\boldsymbol{\tau}_E - \mathbf{r}). \quad (3.3)$$

Hence, for large gains \mathbf{K}_I , we can assume that

$$\mathbf{r} \simeq \boldsymbol{\tau}_E = \mathbf{J}^T(\mathbf{q})\mathbf{f}_E$$

Therefore, reversing the previous equation it is possible to obtain the end-effector external forces \mathbf{f}_E

$$\hat{\mathbf{f}}_E = (\mathbf{J}^T(\mathbf{q}))^\dagger \mathbf{r} \quad (3.4)$$

We validate the method considering only the first three joints because we are interested only in the force estimation and not in the torque estimation. The residual based force estimation was compared with an ATI Mini 45 torque-force sensor. The experimental setup has been defined as in Figure 3.2: a suturing thread traction force was estimated. In detail, a spring was used to transmit the force exerted by the instrument to the ATI sensor through the suturing thread. In this way, at the steady state, the force measured at the end effector is equal to the force applied at the ATI force sensor. A rotation matrix was obtained in order to project the ATI force sensor measurements in the end-effector base Frame. The com-



Figure 3.2. Experimental setup, the instrument is linked to the ATI force sensor with a Spring.

parison between the force reconstruction along the axis x , y and z of the PSM base frame and the Ati measure in the same frame has been performed. In Figure 3.3 are shown the estimated forces using the residual based approach described previously and the forces reconstructed using the Jacobian transpose projection of the joint effort without the use of the PSM dynamical model. The robot was controlled in telemanipulation

mode. It's possible to see that the error between the ATI force measure and the force reconstructed using the residual is noticeably lower when the dynamic model and the residual-based approach is used. Moreover, in Sec. 3.2 we will discuss the performance of the method also in comparison with our new trocar force sensor.

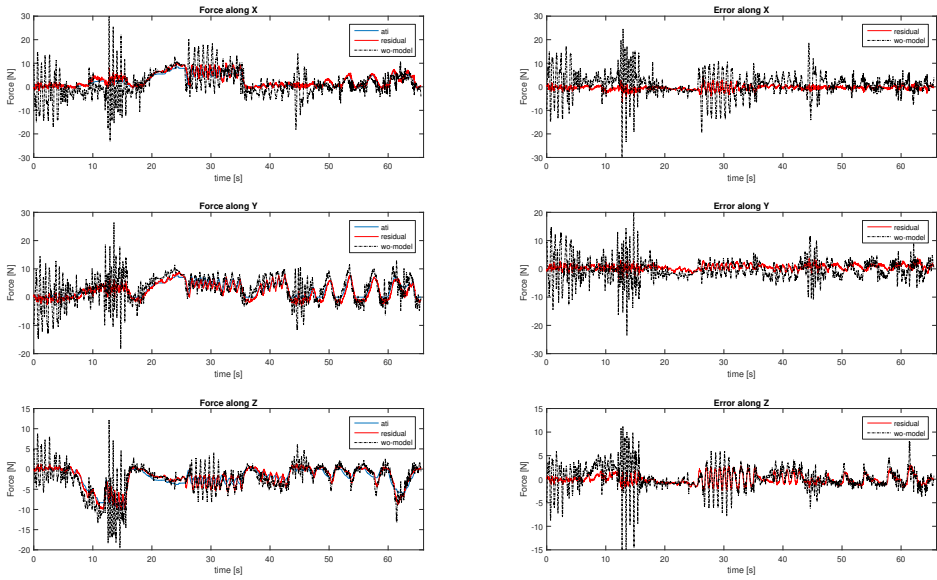


Figure 3.3. External force reconstruction with the residual-based algorithm (red) and with the static mapping (dashed black); ground truth (blue).

3.2 Sensorized Force Estimation: The Trocar Force Sensor

In this section, a new non-invasive force feedback system is proposed and evaluated. A solution based on a novel force sensor placed in the terminal part of the trocar is shown in detail. With respect to the state of the art, our system allows measuring the interaction forces between the surgical instrument and the environment inside the patient's body without any changes to the instrument structure and with full adaptability to different robotic platforms and surgical tools.

Several works on the development of force sensing to measure the interaction between surgical instruments and the patient body are available in the literature. Some of them investigate the possibility to provide force measurement without making changes to the robot, e.g. in [116] using only visual information or, as in [37] and [38], using the control torques and the dynamic model of the robot.

Many prototypes of sensorised surgical instruments have been developed by integrating force sensors in the instrument shaft or wrist, or even in the gripper fingers and clamp faces. In [58] a 6-axis force sensor using Bragg reticula is presented, while in [163, 125, 121] the fiber-optic technology is used to build miniaturized and robust force sensors for different surgical applications. As reported in these works, the fiber-optic technology has many advantages, including the high miniaturization capability and the immunity to the EMI noise. Optical or thin-film organic solutions like that presented respectively in [24, 156] to develop a sensitive skin could be adapted for sensing the forces directly on the surgical gripper or on the instrument shaft. Moreover, promising research for miniaturized force sensors are based on MEMS technology [85] as well as on piezoelectric [26] and capacitive effects [113, 80]; the sensing devices are placed inside the instrument gripper or in the wrist. The common feature of the above works

is that they require the modification of the instrument structure to host the force sensor. This entails higher costs, problems related to sterilization, increased likelihood of instrument breakage, the need of miniaturizing complex structures able to withstand high stresses, problems related to the tendon driven mechanisms of the instruments. Moreover, the instruments may be used for a limited number of interventions and thus the cost of the sensor represents an additional cost for each surgical procedure. On the other hand, the proposed sensing device allows is capable of measuring the forces in the orthogonal plane to the shaft of the surgical instrument without modifying the surgical instrument structure. The idea is to place the sensor in the trocar allowing reducing costs and saving time. Moreover, this solution can be fully adapted to different robotic platforms and surgical tools. The price to pay is that the axial force component, i.e, the force acting along the axis of the instrument's shaft, cannot be directly measured. This problem is overcome here by adopting the residual-based estimation method of [28] which, used to estimate only the axial force component, requires the knowledge of a reduced set of dynamic parameters of the robot and of the instrument.

The accuracy of the proposed trocar sensor is evaluated experimentally with the dVRK and a first prototype of the sensor developed using a polyjet 3D printing technology. Moreover using a commercial force-torque sensor as ground truth, the static and dynamic characterization of the sensor is provided together with an extensive experimental validation. Some of the results reported in this section have been published in [40] and have been submitted to TRMECH 2018.

3.2.1 Sensor Operating Principle

The innovation of the solution proposed in this paper concerns the sensing element that is allocated at the end-tip of the trocar. Fig. 3.1 shows a sketch of the proposed idea with a zoomed view of the trocar where the

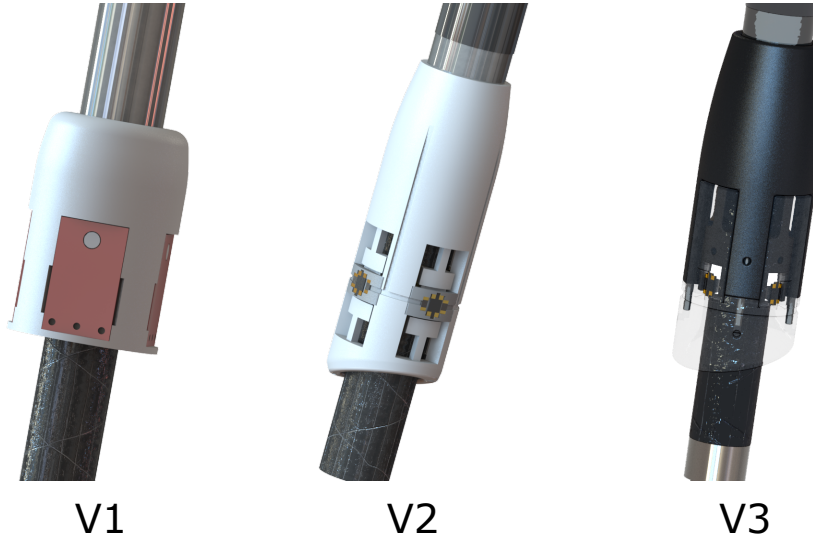


Figure 3.4. Trocar sensor versions.

sensor is placed.

The sensor is composed by a bronze ring that has an internal diameter lower than the internal diameter of the trocar; the bronze ring is glued to a deformable structure (see Fig. 3.5). The interaction force between the instrument end effector and the patient body produces a displacement of the bronze ring, pushed by the instrument shaft, with respect to the trocar axis, which causes the deformation of the elastic frames that compose the sensor. This deformation, which depends on the elasticity of the deformable elements and is measured using four proximity optical sensors mounted in an appropriate way, is proportional to the force applied by the shaft to the ring.

More specifically, consider a sensor reference frame $O_S-x_Sy_Sz_S$ attached to the sensor, with the axes x_S and y_S lying on a plane orthogonal to the trocar axis. The deformation of the elastic frames is proportional to the forces applied along the axis x_S and y_S to the ring.

This solution has a number of advantages with respect to the state of

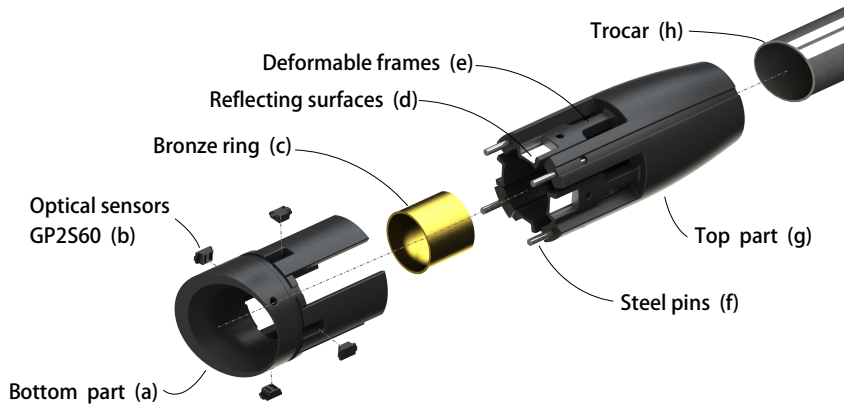


Figure 3.5. Exploded view of the force sensor CAD model.

the art:

- the trocar sensor is cheap and can be used with different surgical instruments, which can be replaced easily during the surgical procedure and no modification of the robot structure is required;
- the forces measured by the trocar sensor are not influenced by the tendon forces, as it happens for the sensors located in the instrument shaft;
- compared to the solutions with sensors located at the end-tip of the instrument, the connection cables and the data acquisition system of the trocar sensor are fixed and far away from the surgical site.

In the next subsections, the mechanical design, the optical sensor and the electronics required for signals acquisition and processing are described in detail.

Mechanical Design

The exploded view of the CAD model of the trocar sensor is shown in Fig. 3.5. The sensor is composed of three main parts. The top part (g) is attached at the trocar end-tip and is composed by four deformable frames designed with four digs holding flat reflective surfaces; the surgical instrument slides inside a bronze ring (c) that is glued on the four deformable frames. The bronze ring ensures a homogeneous deformation of the four deformable frames, when a force is applied by the instrument shaft; moreover, it allows to reduce the sliding friction and to reinforce the overall structure. In order to measure the deformation, four optical sensors are fixed to the bottom part of the sensor (a), in correspondence of the reflective surfaces.

In this first prototype the parts have been produced in plastic using a 3D printed technology based on the polyjet process. This technology was chosen due to the high precision and quick fabrication time, without requiring cleaning or post-print treatments. However, it is not suitable for a real working version of the sensor, because the mechanical properties of the printed material are not stable and change with time.

The mechanical design was supported by the use of a Finite Element Model (FEM) optimization procedure to compute the optimal dimensions of the deformable frames according to the following specifications:

- the force along x_S and y_S axes set in the range $[-20, 20]$ N
- the maximum von Mises stress (safety factor) settled as two times the value of the material yield stress, which is in the range $[50, 65]$ MPa
- minimum size of the overall structure, especially the diameter, compatible with the constraints of the printer.

The prototype was verified using FEM analysis to validate the expectations of the project pre-requirements. The behaviour of the trocar sensor

was simulated when a force of 10 N was applied to the instrument end effector frame O_E - $x_E y_E z_E$ along the x_E axis, as shown in Fig. 3.6 (top). The point O on the top of the tool was considered as stuck. In the same way, the end-tip of the trocar can be considered as a fixed point since it constitutes a constraint for the motion of the tool shaft except for the sliding motion. In the configuration considered in the FEM analysis, the tool is placed with respect to the trocar in such a way that the distance of the end effector frame from point O is two times the distance of the sensor frame from the same point. Hence, due to the lever effect, in static conditions, a 20 N force is applied to the sensor frame along the x_S axis. The Von Mises stress and the displacements of the four reflective surfaces are shown in Fig. 3.6 (bottom).

It can be seen that the von Mises stress on the deformable structure is about half of the yield stress value, that for the used material is around $6.5e^7$ N/m². Moreover, a force applied along the x_S -axis causes a displacement of the reflecting surfaces perpendicular to the x_S -axis (in orange) while the other two surfaces (in blue) do not move. Therefore, the deformations of the structure caused by the forces along the x_S and y_S are decoupled as desired.

The zoomed section of the sensor represented in Fig. 3.6 (top) shows the eccentricity between the instrument shaft and the fixed trocar caused by the force applied to the instrument's tip. In detail, it is possible to observe how the interaction force between the instrument and the environment causes a displacement of the instrument shaft that collides with the bronze ring of the trocar sensor glued to the four deformable frames. The displacement of the frames orthogonal to the direction of the force is quoted in the zoomed section for an applied force of 20 N in the sensor frame.

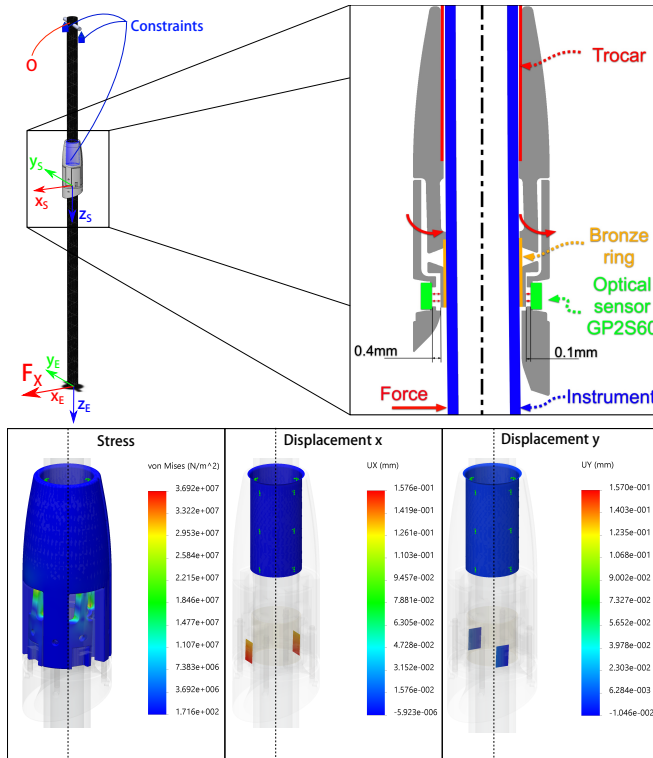


Figure 3.6. FEM analysis results. Top: schematic of the instrument with the relevant reference frames and zoomed section of the trocar sensor. Bottom: von Mises stress and displacements along x_S and y_S axes in the case of a 10 N force applied to the tip along the x_E axis.

Optical Sensors and Electronics

In the tested prototype, the measurement of the deformation of the frames is obtained using four *GP2S60* proximity optical sensors. The sensors are positioned in suitably designed trays. To improve the sensitivity of the device, the four proximity sensors are located at 90 deg one from the other, and thus they are in couple one in front of the other. Therefore, for a given displacement of the sensitive structure, one sensor detects a posi-

tive displacement while the opposite one detects a negative displacement. These differential readings allow to double the gain of the device.

Each optical sensor is equipped with an IR source and a photo-diode detector capable of measuring the amount of reflected light, which is related to the distance of the sensor from the reflective surface placed in front of it. This kind of sensing system is affected by light interference and cross-talk disturbance. In our prototype the four trays are designed opportunely to reduce these effects and all the external parts of the trocar sensor are painted in black, except for the reflective surfaces that are painted in white. Moreover, the overall structure of the sensitive device was designed to reduce the external light disturbances.

The use of proximity optical sensors instead of other sensing solutions has the advantage that the electronics needed to acquire the signals is very simple. Namely, only a polarization circuit and an analog to digital converter (ADC) are required.

In the presented prototype the ADS1015 analog to digital converter (ADC) was selected, since it is equipped with a four channel converter which offers the possibility to read in differential mode and to amplify the input signal with an internal amplifier. The internal amplification factor G was set to the maximum value to maximize the resolution in the measurement range. The maximum frame rate of the ADC is 1.5 KHz for the differential acquisition mode, with a 12-bit resolution, which is good enough for our application. Finally, the ADC is provided with a serial bus I2C which allows to use only four connection wires to communicate with the micro-controller.

The micro-controller LPC1768, which is a mbed platform¹, was used for signal processing. This device performs a numerical pre-filtering at frequency of 1Khz.

Moreover, Fig. 3.7 (a) reports the relating polarization circuit, where:

¹<https://developer.mbed.org/platforms>

$R_1 = 330\Omega$, $R_2 = 15K\Omega$, $v_{cc} = 5V$. Moreover, Fig. 3.7 (b) shows the characteristic curve representing the relative collector current with respect to the distance between the sensor and the reflecting surface. This current value is reported as a percentage since it is a function of the device polarization condition. Therefore it depends on the maximum current i_{Cmax} and on the collector dark current i_{CEO} that flows in the device in the absence of light:

$$i_{C\%} = \frac{i_C - i_{CEO}}{i_{Cmax}}. \quad (3.5)$$

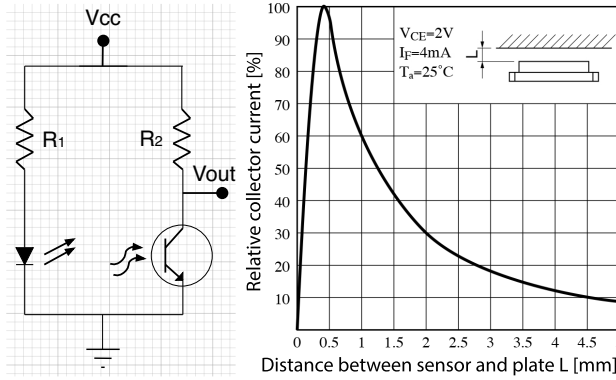


Figure 3.7. Polarization circuit (a) and characteristic curve (b) of the GP2S60 optical sensor.

The sensor is used in the first part of the characteristic curve, i.e., in the region where the distance belongs to the interval $[0, 0.4]$ mm, with almost linear characteristic and high gain. Let G_I the gain in this linear region between the displacement of the sensor δ_x and the current $i_{C\%}$. By taking into account (3.5), the following relationship between the k -th output sensor voltage $v_{out,k}$ and the k -th displacement $\delta_{x,k}$ can be found

$$\begin{aligned} v_{out,k} &= v_{cc} - R_2 i_{C,k} = v_{cc} - R_2 i_{C\%,k} i_{Cmax} + R_2 i_{CEO} = \\ &= v_{cc} - R_2 G_I i_{Cmax} \delta_{x,k} + R_2 i_{CEO}. \end{aligned} \quad (3.6)$$

In our design, the output voltage from the ADC, with gain G , is the difference between the output voltage of two opposite sensors. Assuming the same parameters $V_{cc}, R_2, I_{Cmax}, G_I, I_{CEO}$ for each sensor, the output voltage for each couple is:

$$v_s = G(v_{out,1} - v_{out,2}) = GG_I R_2 i_{Cmax} (\delta_{x,1} - \delta_{x,2}). \quad (3.7)$$

Moreover, assuming $\delta_{x,1} = -\delta_{x,2} = \delta_x$, it is:

$$\delta_x = \frac{1}{2GG_I R_2 i_{Cmax}} v_s = Q v_s. \quad (3.8)$$

Finally, if K is the stiffness coefficient modeling the elastic behavior of the deformable structure of the sensor, the external force can be computed as:

$$f_s = K \delta_x = K Q v_s. \quad (3.9)$$

Therefore, the sensor calibration matrix \mathbf{W} describing the relationship between the output voltages vector $\mathbf{v}_s \in \mathbb{R}^2$ and the vector $\mathbf{f}_s \in \mathbb{R}^2$ of the forces applied to the sensor can be defined as:

$$\mathbf{W} = \begin{bmatrix} K_{11}Q & K_{12}Q \\ K_{21}Q & K_{22}Q \end{bmatrix}. \quad (3.10)$$

Notice that two off-diagonal terms $K_{12}Q$ and $K_{21}Q$ have been introduced in the calibration matrix (3.10) to capture the non perfect symmetry of the sensor and the residual crosstalk effects.

A software calibration procedure was implemented to compensate the residual bias due to the non negligible differences between the parameters of each sensor and their asymmetry.

3.2.2 Sensor Modelling and Calibration

The force \mathbf{f}_S measured by the trocar sensor is influenced by the external force acting on the instrument shaft, but also by gravity and inertial forces due to the instrument motion.

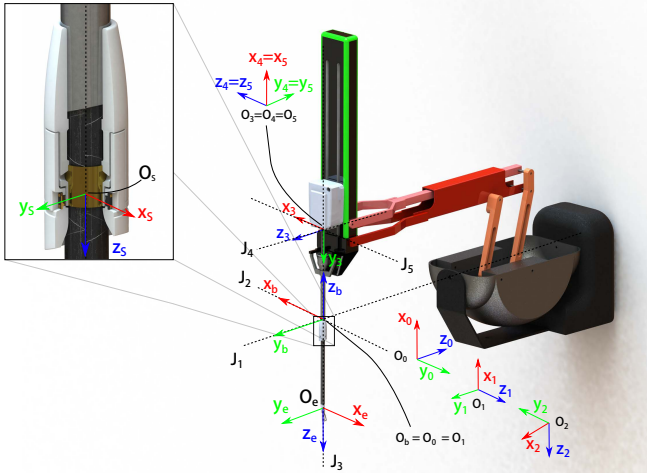


Figure 3.8. The da Vinci PSM robotic arm with the force sensor placed at the end of the trocar: kinematic frames description.

Fig. 3.8 shows the sensing system mounted on the Patient Side Manipulator (PSM) of a dVRK whose detailed description is in Sec. 2.

The sensor is mounted on the terminal part of the trocar, in proximity of the RCM of the robot, which is located at the intersection of axes J_1 and J_2 . Fig. 3.9 represents a planar view of the system, where the RCM is at point R , in the center of the two yellow semicircles. In this figure the shaft of the instrument (blue segment) is linked to point O , which corresponds to the intersection of axes J_4 and J_5 of Fig. 3.8, and can translate with respect to the RCM along axis J_3 . The rotational motion of the shaft about the axis J_1 and J_2 is described by joint variables q_1 and q_2 , while the translational motion along axis J_3 is described by q_3 . The joints J_1 ,

J_2 and J_3 are actuated by the motors of the PSM, and the corresponding joint variables are collected in the vector $\mathbf{q} = [q_1, q_2, q_3]^T$.

It is assumed that the external force $\mathbf{f}_E \in \mathbb{R}^3$ is applied to the end point of the shaft. The sensing element is placed on point S of Fig. 3.9, at a distance L_S from the remote center of motion R . The sensor measures the displacement of the shaft with respect to its rest position under the action of the external force, gravity and inertial forces, and $\mathbf{f}_S \in \mathbb{R}^2$ is the reaction force of the deformable part of the sensing element. To model this displacement, we assume that the shaft (a carbon fiber tube) is rigid and can rotate with respect the pivot point O about the orthogonal axes J_4 and J_5 of Fig. 3.8, modeled as passive revolute joints. The corresponding joint variables are collected in the vector $\mathbf{q}_S = [q_4, q_5]^T$.

In static conditions and in absence of gravity, the relationship between the force \mathbf{f}_S applied to the sensor and the external force \mathbf{f}_E depends only on the distance of the end point from point S as explained in Subsection 3.2.2. This relationship is used in Subsection 3.2.2 for sensor calibration and in Subsection 3.2.2 for sensor characterization. In dynamic conditions, the weight and inertia of the instrument shaft must be suitably taken into account to estimate the external forces from sensor readings, as illustrated in Subsection 3.2.2.

Static Modelling

In static conditions and absence of gravity, assuming that the shaft (a carbon fiber tube) is rigid and can only rotate about the axes J_4 and J_5 , the relationship between \mathbf{f}_S and \mathbf{f}_E can be simply obtained from the static equilibrium of the corresponding torques about O as follows:

$$\mathbf{J}_E^T \mathbf{f}_E = \mathbf{J}_S^T(\mathbf{q}) \mathbf{f}_S \rightarrow \mathbf{f}_E = (\mathbf{J}_E^T)^\dagger \mathbf{J}_S^T(\mathbf{q}) \mathbf{f}_S, \quad (3.11)$$

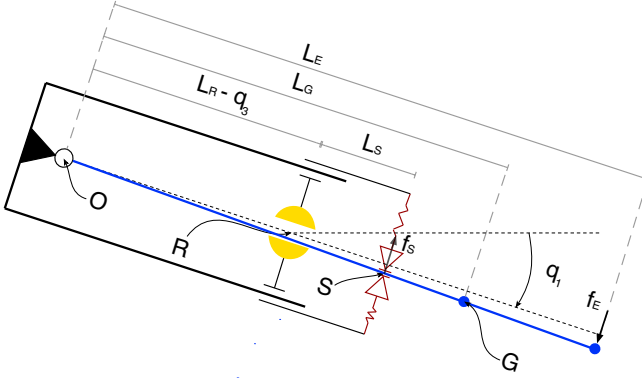


Figure 3.9. Single axis sensor operating principle. The points G , S , O , R are respectively the center of mass of the instrument shaft, the contact point between the instrument shaft and the sensor (bronze ring), the attaching point between the instrument shaft and the instrument box, the RCM.

where the Jacobian matrices $\mathbf{J}_E \in \mathbb{R}^{3 \times 2}$ and $\mathbf{J}_S \in \mathbb{R}^{2 \times 2}$ are defined as:

$$\mathbf{J}_S(\mathbf{q}) = \begin{bmatrix} L_{OS3} & 0 \\ 0 & L_{OS3} \end{bmatrix}, \quad \mathbf{J}_E = \begin{bmatrix} L_E & 0 \\ 0 & L_E \\ 0 & 0 \end{bmatrix}, \quad (3.12)$$

being $L_{OS3} = L_S + L_R - q_3$ the distance from point S to point O , L_R the distance from point R to point O when $q_3 = 0$ and L_E the shaft length. Notice that, here and in the sequel, both \mathbf{f}_E and \mathbf{f}_S are defined in the end effector frame. Moreover, the third element of vector \mathbf{f}_E computed in (3.11) is always null, because the trocar sensor allows to measure only the components of the interaction force lying in the plane orthogonal to the instrument's shaft, corresponding to the first two elements of \mathbf{f}_E .

Sensor Calibration

The calibration of the trocar sensor is aimed at computing the calibration matrix $\mathbf{W} \in \mathbb{R}^{2 \times 2}$ in (3.10) which maps the vector of the sensed voltages \mathbf{v}_S to the vector of the measured forces \mathbf{f}_S , i.e,

$$\mathbf{f}_S = \mathbf{W} \mathbf{v}_S.$$

We have chosen to compute directly the mapping between the external forces and the output voltages, and not that between the displacements δ_x and the forces, due to the simplicity to measure forces with respect to displacements. However, if matrix Q in (3.9) is known, also the relationship between δ_x and voltages could be obtained.

A commercial force-torque sensor ATI Mini 45 was attached to the instrument's tip using a 3D structure printed on purpose, with the axes of the ATI reference frame $O_A-x_Ay_Az_A$ of the ATI sensor aligned to the axes of the end effector frame.

The calibration is performed by applying a force on the ATI sensor and reading the signals of the two sensors simultaneously. The ATI sensed forces are mapped to the trocar sensor frame using the equation

$$\mathbf{f}_A^S = \mathbf{J}_S^{-T}(\mathbf{q}) \mathbf{J}_E^T \mathbf{f}_A \quad (3.13)$$

obtained by inverting the mapping (3.11). The numerical value of the calibration matrix was then derived as

$$\mathbf{W} = \mathbf{F}_A^S \mathbf{V}_S^\dagger,$$

being $\mathbf{F}_A^S \in \mathbb{R}^{2 \times n}$ and $\mathbf{V}_S \in \mathbb{R}^{2 \times n}$ the matrices obtained by stacking n samples of the measurements of \mathbf{f}_A^S and \mathbf{v}_S respectively.

We found experimentally that the trocar sensor exhibits different behaviors for positive and negative voltages. This is due to the non perfect

symmetry of the optical sensors that have been glued to the plastic frame. Hence, two different calibration matrices were identified:

$$\mathbf{W}_P = \begin{bmatrix} 34.86 & -1.47 \\ -1.25 & 37.71 \end{bmatrix}, \quad \mathbf{W}_N = \begin{bmatrix} 30.99 & -1.46 \\ -1.11 & 47.19 \end{bmatrix},$$

for positive and negative voltages respectively. The following numerical values have been used: $L_S = 0.0254$ m, $L_R = 0.4046$ m, $L_E = 0.389$ m for a standard needle driver surgical instrument.

Sensor Characterization

The resolution of the trocar sensor depends on different factors. First of all, the output of the couple of optical sensors is an analog signal in the range ± 0.512 V that is converted to a digital signal by a 12 bit ADC in differential configuration. Therefore, it is possible to define a voltage quantum $p = 0.512/2^{11}$ V, which is the minimal voltage value that can be discriminated.

Moreover, the resolution depends on the distance between the point where the external force is applied (the instruments' tip) and the point where the sensitive element is placed. Such a distance is a function of the prismatic joint variable q_3 . The effect on the force can be evaluated from the mapping (3.11) which allows to define the force resolution vector

$$\boldsymbol{\sigma} = (\mathbf{J}_E^T)^\dagger \mathbf{J}_S^T(\mathbf{q}) \mathbf{W} \mathbf{p}$$

with $\mathbf{p} = [p, p]^T$. Hence, the resolution is not constant but depends on the prismatic joint position. In the following evaluation, without loss of generality, only the positive values matrix $\mathbf{W} = \mathbf{W}_P$ has been considered.

Therefore, the theoretical resolution of the sensing system in the range of motion $q_3 \in [70, 250]$ mm is $\boldsymbol{\sigma} = [0.0082, 0.0089]^T$ N in the worst case and $\boldsymbol{\sigma} = [0.0042, 0.0046]^T$ N in the best case. Without loss of general-

ity, these quantities have been computed considering only the calibration matrix \mathbf{W}_P .

Notice that also the measurement range of the sensor is influenced by the value of the prismatic joint variable q_3 . Considering that the sensor is designed to measure a force \mathbf{f}_S in the range ± 20 N and assuming that q_3 is in the range $[70, 250]$ mm, from Eq. (3.11ssan ca) it follows that the allowed range of \mathbf{f}_E is between ± 10 N for $q_3 = 250$ mm and ± 19 N for $q_3 = 70$ mm.

Dynamic Modelling and Force Estimation

The forces measured by the sensor are influenced by gravity and inertial forces acting on the shaft. This means, for example, that the sensor measurements are different from zero also in the absence of interaction. Moreover, the sensor allows to measure only the components of the external force belonging to the plane orthogonal to the axis of the shaft.

On the other hand, using a sensorless approach like the residual-based technique [28], an estimation of the external force could be obtained from the currents and the dynamic model of the PSM moving the instrument. In this case the estimation error will mainly depend on the accuracy of the dynamic model that should be carefully identified. An identification procedure for the dynamic parameters of the PSM arm of the dVRK robot is proposed in [41], where it is shown that an accurate identification is hard to obtain due to the relatively high measurement noise of the joint position sensors and to presence of non negligible dynamics effects like friction, elasticity, backlash, that are difficult to model. The experimental results presented in the next Section show that the resolution that can be achieved using the residual-based approach alone is of about 1 N, making this method unsuitable to measure small interaction forces.

The idea here is to improve the estimation of the external forces by combining the measurements obtained by the trocar sensor with the residual-

based approach, which takes into account the dynamic interaction between the PSM arm and the sensor.

To this purpose, the dynamic model of the PSM arm and of the instrument can be computed by considering the kinematic chain composed by the actuated joint J_1 , J_2 and J_3 of the PSM and the two passive joints J_4 and J_5 (see Fig. 3.8). The dynamic model can be computed using a Lagrangian approach, by taking into account that:

- the instrument can rotate with respect to the remote center of motion RCM about the axes J_1 and J_2 , with joint variables q_1 and q_2 respectively
- the instrument can translate along the axis J_3 , with joint variables q_3
- the instrument is modeled as a rigid cylinder which can rotate about the two passive revolute joints J_4 and J_5 .

The equations of motion can be computed in terms of the vector of the generalized coordinates $\boldsymbol{\eta} = [\mathbf{q}^T, \mathbf{q}_S^T]^T$ as:

$$\mathbf{B}(\boldsymbol{\eta})\ddot{\boldsymbol{\eta}} + \mathbf{C}(\boldsymbol{\eta}, \dot{\boldsymbol{\eta}})\dot{\boldsymbol{\eta}} + \mathbf{g}(\boldsymbol{\eta}) + \mathbf{d}(\boldsymbol{\eta}, \dot{\boldsymbol{\eta}}) = \boldsymbol{\tau}_M + \mathbf{J}^T(\boldsymbol{\eta})\mathbf{f}_E, \quad (3.14)$$

where $\mathbf{B}(\boldsymbol{\eta}) \in \mathbb{R}^{5 \times 5}$ is the inertia matrix, $\mathbf{C}(\boldsymbol{\eta}, \dot{\boldsymbol{\eta}}) \in \mathbb{R}^{5 \times 5}$, set so that $\dot{\mathbf{B}} = \mathbf{C} + \mathbf{C}^T$ is the Coriolis and centrifugal matrix, $\mathbf{g}(\boldsymbol{\eta}) \in \mathbb{R}^5$ is the gravity generalized torque, $\mathbf{d}(\boldsymbol{\eta}, \dot{\boldsymbol{\eta}}) \in \mathbb{R}^5$ is the torque vector modeling viscous and Coulomb friction, the elasticity of the PSM cables and other disturbances (see [41] for details). Moreover, $\mathbf{J}(\boldsymbol{\eta}) \in \mathbb{R}^{3 \times 5}$ is the Jacobian matrix, mapping the joint velocities to the translational velocity of the instrument's tip referred to the end effector frame and:

$$\boldsymbol{\tau}_M = \begin{bmatrix} \boldsymbol{\tau}_R \\ \boldsymbol{\tau}_S \end{bmatrix}, \quad (3.15)$$

where $\boldsymbol{\tau}_R \in \mathbb{R}^3$ is the vector of the motor torques acting on the first three joints of the PSM and $\boldsymbol{\tau}_S = \mathbf{J}_S^T(\mathbf{q})\mathbf{f}_S \in \mathbb{R}^2$ is the vector of the torques produced on the passive joints 4 and 5 by the force \mathbf{f}_S sensed by the trocar sensor, being $\mathbf{J}_S(\mathbf{q})$ the Jacobian defined in (3.12).

The residual based approach [28] allows to compute an estimate of the external force, assuming that the torque $\boldsymbol{\tau}_M$ and the dynamic model (3.14) of the system are known. The advantage of this approach is that the acceleration measure, that is very noisy in most of the cases, is not needed.

In detail, the residual vector is defined as:

$$\mathbf{r} = \mathbf{K}_I \left(\mathbf{B}(\boldsymbol{\eta})\dot{\boldsymbol{\eta}} - \int_0^t (\mathbf{r}(\sigma) + \boldsymbol{\tau}_M + \mathbf{n}(\boldsymbol{\eta}, \dot{\boldsymbol{\eta}})) d\sigma \right) \quad (3.16)$$

where

$$\mathbf{n}(\boldsymbol{\eta}, \dot{\boldsymbol{\eta}}) = \mathbf{C}^T(\boldsymbol{\eta}, \dot{\boldsymbol{\eta}})\dot{\boldsymbol{\eta}} - \mathbf{g}(\boldsymbol{\eta}) - \mathbf{d}(\boldsymbol{\eta}, \dot{\boldsymbol{\eta}}) \quad (3.17)$$

and $\mathbf{K}_I \in \mathbb{R}^{5 \times 5}$ is a positive definite diagonal gain matrix.

The residual vector \mathbf{r} satisfies the first-order equation

$$\dot{\mathbf{r}} = \mathbf{K}_I(\boldsymbol{\tau}_E - \mathbf{r}), \quad (3.18)$$

hence, we can assume that

$$\mathbf{r} \simeq \boldsymbol{\tau}_E = \mathbf{J}^T(\boldsymbol{\eta})\mathbf{f}_E, \quad (3.19)$$

although the convergence is asymptotic, depending on the choice of \mathbf{K}_I . Eq. (3.19) corresponds to an overdetermined linear transformation that can be inverted to compute vector \mathbf{f}_E from \mathbf{r} using the weighted left inverse as:

$$\mathbf{f}_E = (\mathbf{J}^T(\boldsymbol{\eta}))^\dagger \mathbf{r}. \quad (3.20)$$

This is a least squares solution, whose value depends on the choice of the weights of the left inverse matrix. Notice that the computation of

the components of the residual (3.16) requires the measurement of the vector of the generalized coordinates $\boldsymbol{\eta}$ (i.e. \mathbf{q} and \mathbf{q}_S) and of its first time derivative $\dot{\boldsymbol{\eta}}$. While the measurements of the joint variables \mathbf{q} of the PSM are available, and their time derivatives can be approximated via finite difference, the passive variables \mathbf{q}_S and $\dot{\mathbf{q}}_S$ could be computed from the deflections of the trocar sensor. However these deflections are very small and can be neglected in a first approximation. This produces a substantial simplification of the residual vector (3.16) and of the Jacobian $\mathbf{J}(\boldsymbol{\eta})$, that can be computed by setting $\mathbf{q}_S = \dot{\mathbf{q}}_S = \mathbf{0}$, and thus $\boldsymbol{\eta} = [\mathbf{q}^T, \mathbf{0}^T]^T$ and $\dot{\boldsymbol{\eta}} = [\dot{\mathbf{q}}^T, \mathbf{0}^T]^T$. In particular, the Jacobian matrix can be computed as:

$$\mathbf{J}^T(\mathbf{q}) = \begin{bmatrix} L_{OE3}c_2 & 0 & 0 \\ 0 & L_{OE3} & 0 \\ 0 & 0 & 1 \\ L_E & 0 & 0 \\ 0 & L_E & 0 \end{bmatrix}, \quad (3.21)$$

with $c_i = \cos(q_i)$ and $s_i = \sin(q_i)$ and $L_{OE3} = L_R - L_E - q_3$. By inspecting the Jacobian matrix in (3.21) and in view of (3.19), it is possible to see that the external force along the x_E and y_E axes of the end effector frame can be estimated by considering either the first two residual values (\mathbf{r}_{12}) or the last two (\mathbf{r}_{45}). Therefore, the vector \mathbf{f}_E of the external forces can be computed in three different ways:

- (A) from the first three components of the residual vector \mathbf{r} in (3.16) which, in view of (3.15) depend only on the motor torques $\boldsymbol{\tau}_R$, without making use of the measured force \mathbf{f}_S ;
- (B) from the last three components of the residual vector \mathbf{r} in (3.16); namely, r_3 , which depends on the motor torque of the prismatic joint J_3 , allows to estimate f_{zE} , while \mathbf{r}_{45} , which depends on the measured force \mathbf{f}_S , allows to estimate f_{xE} and f_{yE} ;

- (C) from Eq. (3.20), with suitable weights in the left inverse; the criterion to adopt for the weights selection should be that of using the force sensor information when the force is in the trocar sensor measurement range, and the motor currents outside this range.

In this paper, to gain a better insight into the accuracy of the different available input data (motor currents and force sensor readings) the case (A) and (B) are considered. In particular, in case (A) the first three components of the residual vector (3.16) depend on the base parameters of PSM arm and instrument, by considering only the first three joints and assuming that the instrument is rigidly connected to the arm. The symbolic expressions of these parameters and their identified numerical values can be found in [41]. In the (B), the last three components of the residual vector (3.16) can be computed in terms of a reduced subset of dynamic parameters of the PSM and of the instruments' shaft. In detail, in view of (3.19) and (3.21), vector \mathbf{f}_E can be computed as

$$\mathbf{f}_E = \begin{bmatrix} r_4/L_E \\ r_5/L_E \\ r_3 \end{bmatrix}. \quad (3.22)$$

The vector \mathbf{r}_{45} collecting the last two components of the residual vector (3.16) can be expressed as:

$$\mathbf{r}_{45} = \mathbf{K}_{45I} \left(\mathbf{B}_{xy}(\mathbf{q})\dot{\mathbf{q}} - \int_0^t (\mathbf{r}_{45}(\sigma) + \boldsymbol{\tau}_S + \mathbf{n}_{xy}(\mathbf{q}, \dot{\mathbf{q}})), d\sigma \right)$$

with:

$$\mathbf{B}_{xy}(\mathbf{q}) = \begin{bmatrix} b_{x1} & 0 \\ 0 & b_{y2} \end{bmatrix}$$

$$\mathbf{n}_{xy}(\mathbf{q}, \dot{\mathbf{q}}) = \begin{bmatrix} c_{x1}\dot{q}_1 + c_{x2}\dot{q}_2 + c_{x3}\dot{q}_3 - g_x \\ c_{y1}\dot{q}_1 + c_{y3}\dot{q}_3 - g_y \end{bmatrix},$$

and:

$$\begin{aligned}
b_{x1} &= (mp_{xS}(q_3 - L_R) - I_{yyS}) c_2 \\
b_{y2} &= mp_{xS}(q_3 - L_R) - I_{zzS} \\
c_{x1} &= (I_{xxS} + I_{yyS} - I_{zzS}) s_2 \dot{q}_2 \\
c_{x2} &= -(I_{yyS} - I_{xxS} + I_{zzS} + mp_{xS}(L_R - 2q_3)) s_2 \dot{q}_1 \\
c_{x3} &= -2mp_{xS} c_2 \dot{q}_1 \\
c_{y1} &= -2(I_{xxS} - I_{yyS} + (2q_3 - L_R) mp_{xS}) s_2 c_2 \dot{q}_1 \\
c_{y3} &= -2mp_{xS} \dot{q}_2 \\
g_x &= 9.81 mp_{xS} c_1 s_2 \\
g_y &= 9.81 mp_{xS} s_1.
\end{aligned}$$

In the above equations mp_{xS} is a first moment of the instruments' shaft, and I_{xxS} , I_{yyS} , I_{zzS} are the elements of its inertia matrix. The numerical values of these parameters, for a standard da Vinci needle driver instrument, were derived using CAD and are reported in Table 3.1. The quantities are referred to frame $O_5-x_5y_5z_5$ of Fig. 3.8 and expressed in SI basic standard measurement units, that are omitted here for brevity.

Table 3.1. CAD dynamic parameters of the instruments' shaft

parameter	value	parameter	value
mp_{xS}	$-5.1e^{-3}$	I_{yyS}	$8e^{-4}$
I_{xxS}	$2.8e^{-7}$	I_{zzS}	$8e^{-4}$

The third component of the residual vector (3.16) can be expressed in the form:

$$r_3 = k_{3I} \left(\mathbf{b}_z^T(\mathbf{q}) \dot{\mathbf{q}} - \int_0^t (r_3(\sigma) + \tau_{3R} + n_z(\mathbf{q}, \dot{\mathbf{q}})) d\sigma \right),$$

with:

$$\mathbf{b}_z^T(\mathbf{q}) = [b_{z1} \quad b_{z2} \quad b_{z3}]$$

$$n_z(\mathbf{q}, \dot{\mathbf{q}}) = c_{z1}\dot{q}_1 + c_{z2}\dot{q}_2 - g_z - f_z,$$

and:

$$b_{z1} = mp_{yI}c_2$$

$$b_{z2} = mp_{xI}$$

$$b_{z3} = m_I + m_C$$

$$c_{z1} = 2mp_{yI}s_2\dot{q}_2 - 0.0312m_Ic_2^2\dot{q}_1 + 0.4m_Cc_2^2\dot{q}_1 +$$

$$+ 2mp_{zI}c_2^2\dot{q}_1 + 2(m_I + m_C)q_3c_2^2\dot{q}_1 + 2mp_{xI}c_2s_2\dot{q}_1$$

$$c_{z2} = 0.4m_C\dot{q}_2 - 0.0312m_I\dot{q}_2 - 2mp_{zI}\dot{q}_2 +$$

$$+ 2(m_I + m_C)q_3\dot{q}_2$$

$$g_z = -9.81(m_I - m_C)c_1c_2$$

$$f_z = F_{vI}\dot{q}_3 + F_{sI}\tanh(50\dot{q}_3).$$

In the above equations m_I is mass of the translating link of the PSM, mp_{xI} , mp_{yI} , mp_{zI} are the corresponding first moments, m_C is the mass of the counterweight, and F_{vI} , F_{sI} are friction coefficients. The numerical values of the above parameters have been estimated through the identification procedure presented in 2 and are reported in Table 3.2. The quantities are referred to frame $O_E-x_Ey_Ez_E$ and are expressed in SI basic standard measurement units, that are omitted here for brevity.

3.2.3 Experimental Validation of the Sensing System

This section is devoted to the experimental validation of the sensor in static and dynamic conditions, by using an ATI Mini 45 force sensor, mounted at the end tip of the surgical instrument, as ground truth.

Table 3.2. Identified dynamic parameters of the PSM

parameter	value	parameter	value
m_I	0.146	m_C	0.179
mp_{xI}	0.001	F_{vI}	2.695
mp_{yI}	0.033	F_{sI}	0.496
mp_{zI}	-0.039		

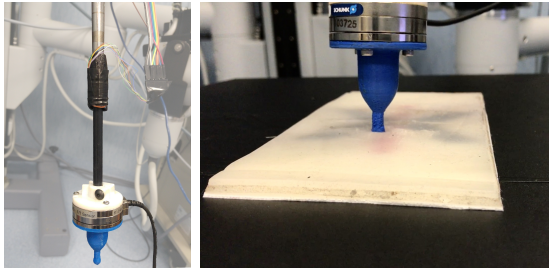


Figure 3.10. Experimental setup. The ATI Mini 45 force sensor mounted at the end tip of the surgical instrument (a); interaction of the spherical probe attached at the bottom of the ATI sensor with a soft tissue phantom (b).

Static Validation

To cancel the effects of gravity a force is applied to the ATI sensor while keeping the shaft of the surgical instrument aligned to the vertical direction, as shown in Fig. 3.10 (a). A motion of the instrument along the vertical direction is commanded, by considering a constant velocity displacement of 0.1 m of the prismatic joint q_3 , in order to test the trocar sensor for different distances of the instrument's tip from the position of the sensitive elements. Fig. 3.11 reports the time histories of the components along the axes x_E and y_E of the force measured by the ATI sensor and of the force estimated by using the trocar sensor and Eq. (3.11). The time history of the prismatic joint q_3 is reported in the bottom of the figure.

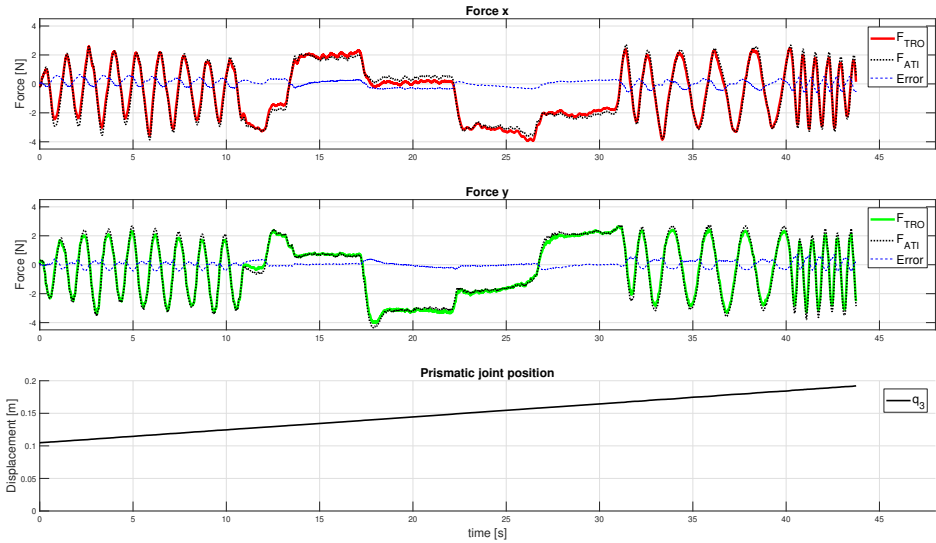


Figure 3.11. Static characterization. Force along the axis x_E (top), force along the axis y_E (middle), prismatic joint trajectory (bottom).

The results show that the trocar sensor has a good response, close to that of the commercial sensor ATI mini 45. The relative error between the force components measured by the ATI sensor and the trocar sensor is less than 12% along both the axes. The error is higher in the central region of the graph, when a constant force is applied. This is due to undesired hysteresis effects of the material used for the prototype.

Dynamic Validation

The validation of the complete dynamic model has been performed on a simulated diagnostic procedure involving the interaction between the instrument and a soft tissue phantom.

A spherical probe was attached at the bottom of the ATI sensor mounted at the end tip of the instrument shaft (see Fig. 3.10 (b)). By using the PSM arm in telemanipulation mode, the probe was pushed against the soft

tissue phantom. The dynamic parameters reported in Table 3.1 and Table 3.2 have been properly updated to take into account the mass and inertia of the ATI sensor.

The estimation of the external force was performed considering both methods (A) and (B) described in Sec. 3.2.2. The time histories of the estimated force components together with the corresponding quantities measured using the ATI force sensor are shown in Fig. 3.12. In the first three plots, the force components along the axes x_E , y_E and z_E computed with method (A) are reported. The last two plots show the components along the axes x_E and y_E computed with method (B), using the trocar sensor measurements. The visual inspection of the plots shows that the trocar sensor allows a more accurate estimation of the force components along the directions x_E and y_E , compared to those computed with method (A).

A quantitative analysis, in terms of the RMS errors reported in Table 3.3, shows that with method (B) the errors are one tenth lower than with method (A).

Table 3.3. RMS errors using methods (A) and (B)

method	$RMS e_x$ [N]	$RMS e_y$ [N]	$RMS e_z$ [N]
(A)	0.618	0.9027	0.949
(B)	0.094	0.112	0.949

From the experimental data we can say that, for the considered set up, the resolution of the force estimation using method (A) is of about 1, which decrease to 0.1 N for the components in the plane orthogonal to the instruments' shaft axis estimated with method (B), using the trocar sensor. It is worth pointing out that this value is larger than the theoretical resolution that could be obtained with the trocar sensor in ideal conditions and absence of motion.

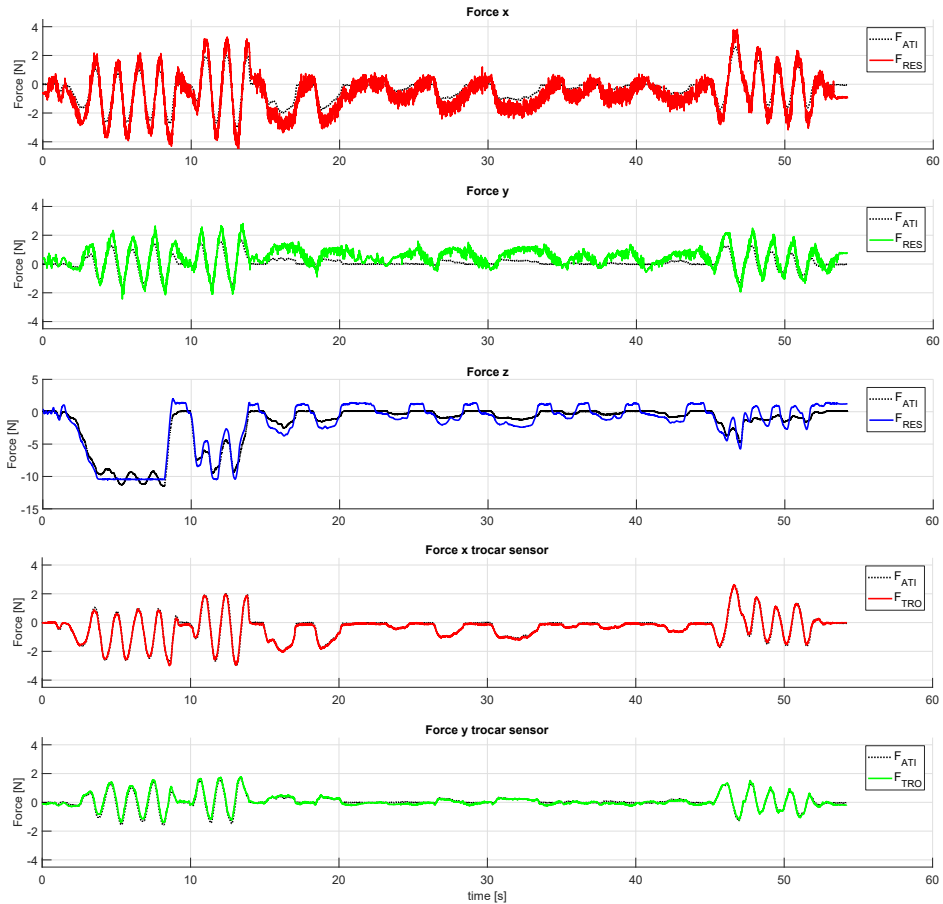


Figure 3.12. Time histories of the estimated force. Method (A) is used in the first three plots from the top and method (B) in the last three plots.

3.3 Sensorized Force Estimation: FBG for finger tip sensor design

The development of new surgical instruments, e.g. our MUSH A hand (see Sec. 4.2), open the possibility to evaluate in a different way also the force sensing problem. In this section, we propose a solution for a

miniaturized force sensor integrated into the fingertip of a hand suitable for surgical applications. The proposed tree fingered, reconfigurable and underactuated hand is presented in detail in Sec. 4.2. Here, we focus on the design, calibration and evaluation of a sensorized fingertip based on the Fiber optic Bragg technology.

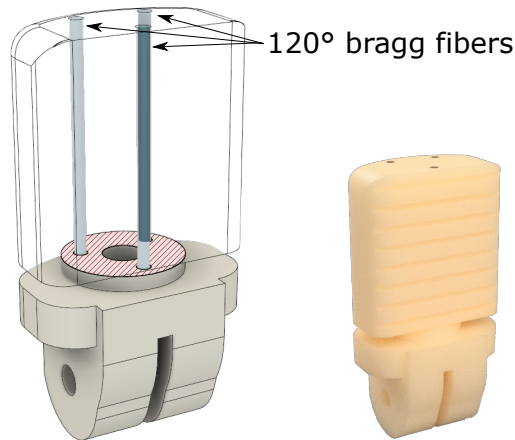


Figure 3.13. Sensor structure integrated into the distal phalanges. The section view shows the four columns and the holes built to glue three Bragg fibers.

On the basis of these requirements, the Bragg technology has been chosen as the suitable one for the sensor realization. The Bragg technology has many advantages, including miniaturization, possibility to include different sensors on the same optical fiber, high resolution, immunity to the Electromagnetic interference noise and the high integration capability. In the surgical scenario, optical fibers are used in [58] to realize a 6 DOF Bragg-based force sensor for a robotic laparoscopic instrument. While in [87] a sub-miniaturized force sensor composed of three optical fibers and based on the Fabry-Pérot interferometry method for vitreoretinal microsurgery is presented.

3.3.1 Sensorized Fingertip Mechanical Design

Our force sensor is composed by three Bragg Gratings for each finger. The distal finger has been designed with a bottom part (highlighted in white in Fig. 3.13) linked to the joint axis and controlled by the tendon-driven mechanism. A central column with three holes is located in the finger structure: in our design, each hole is disposed at 120 degrees one from another in which optical fiber has been glued inside. The design choice has been evaluated using the Finite Element Analysis (FEA) to evaluate the deformation of the regions in which is glued the Bragg gratings and thus the ability of the sensor to decouple the three force components. In particular, considering the plastic material adopted for the prototype a non-linear analysis have been chosen. In Fig. 3.14 the results are shown. More in detail, in Fig. 3.14(a) the stress of the structure subjected to three component of force (one normal and two tangential to the finger surface) of amplitude about 7N is reported. The result shows a maximum stress about 4 time lower than the material yield stress ($4.0e^7 N/m^2$). Moreover, in Fig. 3.14(b,c,d) the deformation of the three Bragg fibers under a normal and two tangential components along two orthogonal directions are

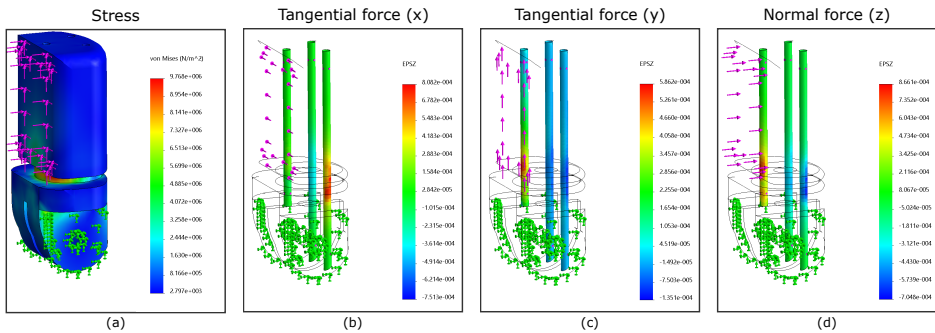


Figure 3.14. Finite element analysis of the proposed finger sensor design. (a) structure stress, (b,c,d) simulated deformation of the three Bragg fibers when the phalanx is subject to a normal, tangential and vertical force.

represented. It is possible to see that the three component of force causes different deformations of the structure. However, such deformations are coupled. This means that it could be possible to find a calibration matrix that maps the three forces to the deformations of the three fibers as reported following.

3.3.2 Sensor Calibration and Validation

In order to obtain a mathematical model that relates fiber Bragg sensor's deformations with the three forces, a measurement system has been set up as shown in Fig. 3.15. The system is composed by two ver-

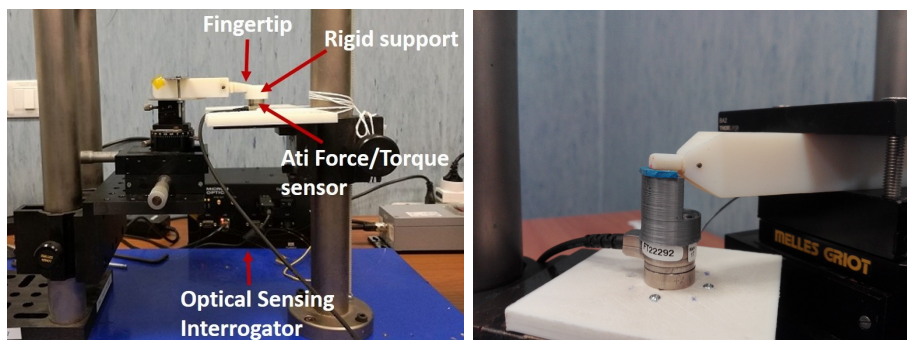


Figure 3.15. Left: measurement system. Right: a detailed view of the prototype finger and the reference sensor.

tical holders, the one mounting the finger prototype allows three linear independent motions, the one mounting the ATI Force/Torque reference sensor can translate along the vertical direction. In order to acquire the Bragg wavelength sensors's variation, an Optical Sensing Interrogator (Micron Optics sm130) provides the simultaneous interrogation of the sensors.

The aim is to acquire a sufficient number of measurements of Bragg wavelength variations related to forces applied along X, Y and Z axis in

order to obtain the 3×3 coefficient matrix in Eq. (3.23)

$$\begin{bmatrix} F_x \\ F_y \\ F_z \end{bmatrix} = \begin{bmatrix} A_1 & B_1 & C_1 \\ A_2 & B_2 & C_2 \\ A_3 & B_3 & C_3 \end{bmatrix} \begin{bmatrix} \Delta\lambda_1 \\ \Delta\lambda_2 \\ \Delta\lambda_3 \end{bmatrix} \quad (3.23)$$

The vertical holder allows controlling motions along the three axes with very high precision to stimulate a pressure on the reference sensor from the prototype finger that perfectly fit a rigid support designed on purpose and attached to the reference sensor (Figure 3.15Right). Thus, the system allows applying forces along single directions with increasing intensity in order to obtain a sufficient number of measurements contained in a range suitably chosen.

A Fiber Bragg sensor consists of a periodic modulation of the refractive index in the core of a single-mode optical fiber. When the light from a broadband source is launched from one side of the fiber, only a particular wavelength which satisfies Bragg condition will be reflected while the remainder is transmitted without any loss [68]. It can be also demonstrated that the reflectivity is a function of the grating length, thus fiber gratings are excellent elements in sensing applications [3]. The operating principle is to monitor the shift in Bragg wavelength related to the changes in the measure. The Bragg wavelength is a function of the grating period Λ and the effective refractive index n_{eff} of the fiber core:

$$\lambda_B = 2n_{eff}\Lambda \quad (3.24)$$

Any change in the refractive index or the grating period due to external measure will change the Bragg wavelength and can be detected [70]. In this experiment, a strain variation is the parameter that directly tunes the center wavelength of the Bragg grating. Due to the wavelength-based

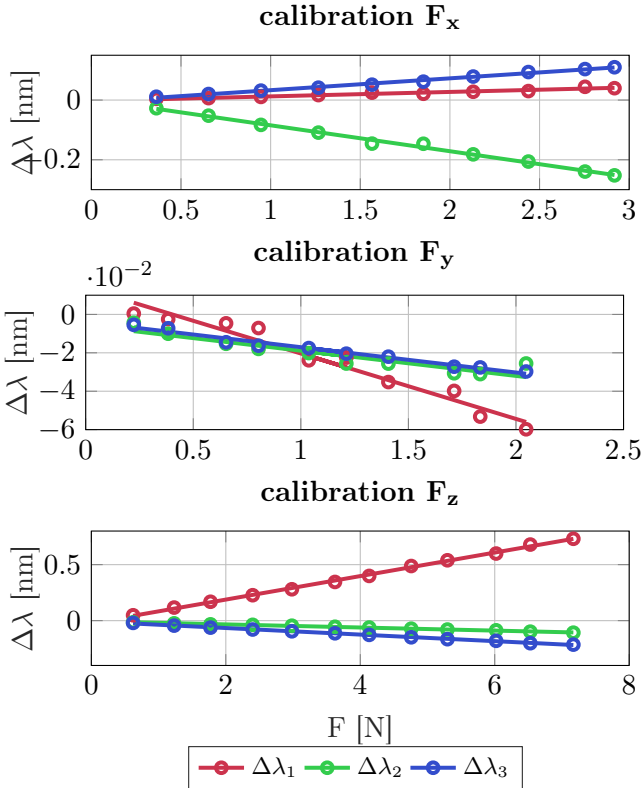


Figure 3.16. Coefficients associated with the sensor characteristic.

working principle of Bragg sensing technology, the measurement is not affected by the amplitude variation of the light emission caused by fiber bending outside the Bragg zone [128]. This makes FBG technology suitable for force measurements even when the fiber is bending inside the MH joints. In a first experience, the Bragg wavelength and the relative mechanical variation along z-axis have been simultaneously acquired obtaining a sample of ten measurements for different values of the force. Afterwards, data have been manipulated via MATLAB to calculate the best linear fit and to extract the coefficients related to the sensor characteristic (Figure

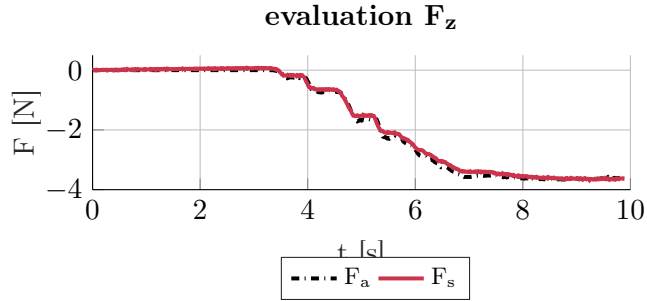


Figure 3.17. Force measure evaluation along z axis. F_a :ati force, F_s :sensor force.

3.16). To prove the effectiveness of the FBG sensor, we have compared ten measurements of the force component along z-axis measured by the ATI sensor and the FBG sensor (see Fig. 3.17). The percentage error associated with the average carried out on the measurements is of 5%.

3.4 Vision-based Force Estimation

The purpose of this section is to propose a method enabling the measurements of contact forces between the operator and a deformable object through an RGB-D camera. The task is very challenging, since a given deformation can be gendered by a multiplicity of interactions.

Capturing interactions in manipulation based on computer vision has aroused much interest recently and may represent a convenient, minimally invasive and cheap sensing set-up. Some efforts have been focused on sensing interactions between rigid objects, but the field remains open when considering deformations. For instance, the changes in the appearance of the fingertip are measured through photodetectors or an external camera, and are processed to estimate contact forces using statistical models, as in [60, 95, 145, 154, 54, 144]. These technologies are limited to measure the normal force and cannot simultaneously consider shear or slip. A promising approach [165], also based on visual observations, relies on the GelSight sensor [130]. In this case the deformations, measured by marker-based visual tracking techniques on an embedded elastomer medium, are interpreted as known responses to the external load exerted on the sensor.

All the above force sensing methods require precise calibration, and instrumenting the interacting tool/hand and/or the manipulated object with cumbersome and expensive equipment which can also limit the range of motion. Often they are tailored to particular objects and hard to generalise, whereas we wish to design a generic data-driven system. Moreover, several works have suggested the use of an external vision system to capture the interactions and to sense contact forces in the case of object manipulation by a human or any manipulation tool. In the motion capture field, this approach has been demonstrated by some works using marker-based or markerless vision tracking to capture and synthesise hand/object interaction [75, 10, 107], by providing a kinematic analysis of the interactions through discriminative or generative processes and by introducing some

physics-based constraints to deal with occlusions or collision detection. Some other approaches [159, 169] propose to bridge the gap between the kinematics provided by the motion capture systems and the contact forces by linking physical constraints to visual observations.

Here we demonstrate that, by confronting a physical deformation model based on continuum mechanics and on known material properties of the object, with deformations measured through vision, it is possible to retrieve a single point-wise contact force exerted by an operator (a human hand, a robot end-effector) on the considered object. Relying on a physical model implies knowing the mechanical properties of the object. Here we employ the Finite Element Method to model the object and its elasticity, which is described by two parameters, the Young Modulus and the Poisson ratio.

Material properties, represented by elasticity parameters, are estimated in a preliminary step by using a force sensor and an optimisation technique. Then, assuming that the object lies on a flat surface and that the tool/object interaction consists in a known single contact point, a similar optimisation technique is used to infer the value of the 3D force exerted on that point by fitting the simulated deformations with those estimated by the vision system. This approach is based on the techniques suggested in [120], [117] moreover the results reported in this section have been published in [116].

3.4.1 Deformation and Interaction Models

The basic concept of this work, for both objectives, is to rely on a realistic physical deformation model of the considered elastic and isotropic object.

The Finite Element Method (FEM) provides accurate physical realism, by relying on continuum mechanics, instead of finite differences for mass-spring systems for instance. For an exhaustive description, the reader can refer to [25]. It consists in tessellating the deformable object into

a mesh made of elements connecting a set $X = \{\mathbf{x}_j\}_{j=1}^{n_x}$ of 3D vertices. The deformation fields over the elements are approximated as continuous interpolations of the displacements of the vertices. We rely here on a volumetric linear FEM approach with tetrahedral elements.

Modelling Elastic Deformations

In order to model elasticity for a continuous isotropic material, we follow the method proposed in [119], by resorting to the linear elasticity, with Hooke's law, and to the infinitesimal strain theories [25], modified by adopting a corotational approach [33, 99, 103], so as to accommodate to rotation transformations. The infinitesimal strain tensor ϵ_e (6×1) and stress tensor σ_e (6×1) within a tetrahedron e can be written as:

$$\begin{aligned}\epsilon_e &= \mathbf{L}_e \hat{\mathbf{u}}_e^r = \mathbf{L}_e \mathbf{R}_e^{-1} \mathbf{x}_e - \mathbf{x}_{e,0} \\ \sigma_e &= \mathbf{C}_e(E, \nu) \epsilon_e.\end{aligned}\tag{3.25}$$

where \mathbf{L}_e is the constant 6×12 matrix related to the interpolation function, \mathbf{C}_e is a 6×6 symmetric matrix depending on two elastic parameters of the material, the Young modulus E and the Poisson ratio ν , and \mathbf{R}_e is a rotation matrix corresponding the rotational component of the deformations of the element. Moreover, being $\hat{\mathbf{u}}_e^r = \mathbf{R}_e^{-1} \mathbf{x}_e - \mathbf{x}_{e,0}$, with $\mathbf{R}_e^{-1} \mathbf{x}_e$ the back rotated deformed coordinates of the vertices of e . The internal elastic forces \mathbf{f}_e exerted on the four vertices of e can then be related to their displacements $\hat{\mathbf{u}}_e$ as:

$$\mathbf{f}_e = \mathbf{R}_e \mathbf{K}_e \hat{\mathbf{u}}_e^r\tag{3.26}$$

being $\mathbf{K}_e = V_e \mathbf{L}_e^T \mathbf{C}_e \mathbf{L}_e$ the stiffness matrix of the element of volume V_e . The forces $\mathbf{K}_e \hat{\mathbf{u}}_e^r$ are re-rotated to the current deformed element through multiplication by \mathbf{R}_e .

Interaction Model

Besides the object and its own deformation model, we describe here the model of its interaction its contact environment to infer contact forces.

Here we consider the case of a manipulated object lying on a known flat rigid surface. The object is then deformed through a single contact force which acts vertically, so that the contact between the object and the plane remains constant. In the carried out experiments (see section 3.4.5), this force is applied by a tool mounted on a robotic arm. We assume a pointwise contact on a point of known position lying on the surface of the object. Considering for the simulation model the mesh $X = \{\mathbf{x}_j\}_{j=1}^{n_X}$, and using the corotated deformation model described in section 3.4.1, the Lagrangian dynamics is described by the equations:

$$\begin{aligned} \mathbf{M}\ddot{\mathbf{x}} + \mathbf{C}\dot{\mathbf{x}} + \mathbf{f} &= \mathbf{f}_{ext}^{sim} & (3.27) \\ \text{with } \mathbf{f}_{ext}^{sim} &= \mathbf{g} + \mathbf{f}^{ground} + \mathbf{f}^{op} \end{aligned}$$

where \mathbf{g} is the gravity and \mathbf{f}^{ground} is the contact forces of the flat rigid surface or ground, exerted on the vertices in contact with it. These forces act on vertices of the mesh for which the signed distance is negative (below the plane), attracting them thus towards the plane. We simply model them as damped linear springs according to the signed distance between the vertices of mesh and the known plane representing the surface. We assume an inelastic surface, meaning that the stiffness of the springs is set high. For simplicity and since we deal with a vertical compressing effort on the object, we neglect adhesive sticky effects, as well as tangential friction.

Finally \mathbf{f}^{op} is the pointwise external force exerted by the operator deforming the considered object. Our objective in this paper is to estimate this force, based on observations provided by a vision system.

3.4.2 Deformation Estimation Using RGB-D Data

In this section is described the way we use external vision data to estimate, in a physically realistic manner, the deformations undergone by the object which will then drive the estimation of the force exerted by an operator (see section 3.4.3).

The registration problem we tackle consists in fitting the point cloud data, provided by an RGB-D sensor, with the tetrahedral mesh, in terms of both rigid and non-rigid transformations, and directly employing the approach proposed in [119], for which the main steps are recalled hereafter.

Preliminary Visual Segmentation

The visual segmentation step presented in [119] is carried out in order to restrict the acquired point cloud to the considered object, so as to avoid ambiguities in the matching process with the background or with occluding shapes. This phase provides us with the set Y of the 3D points of the target point cloud. For computational concerns, we limit the size of Y by sampling \mathbf{D}^k on a regular grid in the image plane.

Rigid Iterative Closest Point

A second step in our method is to register the observed segmented point cloud Y in terms of rigid translation and rotation transformations, initially considering the mesh of the object as rigid. We employ a classical rigid Iterative Closest Point (ICP) algorithm [21] between Y and the vertices of the visible surface X_V of the mesh, transformed with respect to the previous RGB-D data. Through this procedure a fair initialization for the non-rigid process can be obtained.

Deformable Registration Process

Following the approaches in [119, 120], the basic idea is to derive external forces exerted by the point cloud on the mesh, and to balance them with the internal forces based on the deformation model presented in Sect. 3.4.1, with respect to the displacements of the vertices of the mesh. We use external forces f_{ext}^g related to geometrical information as introduced in [119]. The method consists first in determining nearest neighbors correspondences, both from the segmented point cloud to the mesh and from the mesh to the segmented point cloud, as shown in Fig.3.18.

Based on the two sets of mesh-to-point cloud and point cloud-to-mesh correspondences, an external elastic force \mathbf{f}_{ext}^g exerted on each \mathbf{x}_j in X_V , can be computed as follows:

$$\mathbf{f}_{ext}^g(\mathbf{x}_j) = k_{ext}^g(\mathbf{x}_j - \mathbf{y}_j^f) \quad (3.28)$$

where, as described in [119], \mathbf{y}_j^f is a linear combination of points in the point clouds which are matched to \mathbf{x}_j , either from mesh-to-point cloud and from point cloud-to-mesh correspondence sets. k_{ext}^g is the stiffness of these external elastic forces.

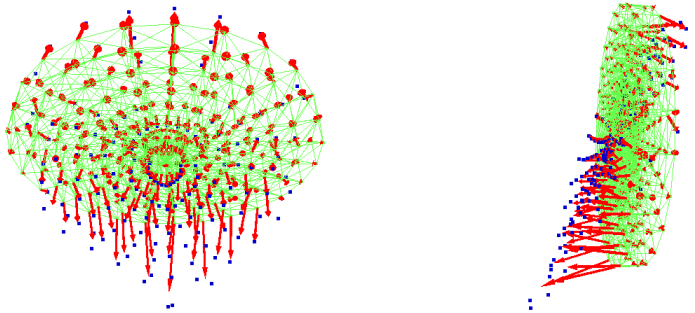


Figure 3.18. External forces based on Nearest neighbors searches.

Resolution

Estimating the deformations of the mesh consists in solving a dynamic system of linear ordinary differential equations involving the internal and external forces, based on the Lagrangian dynamics:

$$\begin{aligned} \mathbf{M}\ddot{\mathbf{x}} + \mathbf{C}\dot{\mathbf{x}} + \mathbf{f} &= \mathbf{f}_{ext}^g & (3.29) \\ \text{with } \mathbf{f} &= \mathbf{K}\mathbf{x} + \mathbf{f}_0 \end{aligned}$$

where \mathbf{x} is a n_X vector containing the positions to estimate of the vertices in X , \mathbf{M} and \mathbf{C} are the $n_X \times n_X$ mass and damping matrices, \mathbf{K} the $n_X \times n_X$ global stiffness matrix which sums the $n_X \times n_X$ element-wise *rotated* stiffness matrices $\mathbf{K}_e = \mathbf{R}_e \mathbf{K}_e \mathbf{R}_e^{-1}$, written with respect to whole set of vertices, and \mathbf{f}_0 the corresponding global offset summing the element-wise ones $\mathbf{R}_e \mathbf{K}_e \mathbf{x}_{e,0}$.

k_{ext}^g is the stiffness of these external spring elastic forces. They can be seen as gains in the estimation process and weights between the different forces. An Euler implicit integration scheme is used to solve the system with respect to \mathbf{x} , along with a conjugate gradient method. Since we consider the static case, with the static equilibrium of the deformations assumed to be reached, the transient and the dynamic terms of equation (3.29) can be neglected.

3.4.3 Estimation of Elasticity Parameters

Our system consists in estimating the elasticity parameters of the object using the point cloud data observing the deformations, provided by an RGB-D sensor, and a force sensor. For the estimation of these parameters, we follow the data-driven approaches described in [46, 157], by minimizing a fitting error between the deformations simulated based on the designed deformation and interaction models presented above, with the input operator force provided by the sensor, and the deformation captured by the

RGB-D sensor. These two methods also employ finite elements for the deformation model. The work [157] goes further by proposing a framework that sequentially tracks the shape and estimates both material and dynamic parameters (damping), through the dynamic deformation model and solely based on a complete vision capture set-up with various RGB-D sensors around the scene. Here we reason statically for modeling and we limit this preliminary process as an estimation process of the Young modulus and the Poisson ratio of the material, employing a single RGB-D sensor and the force sensor on an robotic operator, with a set-up similar to the one proposed in [46]. The deformations are indeed generated by applying an effort, in our case compression, on the deformable object and we observe the deformations with the vision sensor once static equilibrium is reached. These deformations can be simulated, starting from the same initial rest shape, provided the deformation and interaction model presented above, the elasticity parameters, and the input measured contact force. As a data-driven approach, our problem is thus addressed by minimizing the deviation between these simulated deformation, and the observed ones, with respect to the elasticity parameters. This deviation is defined by a fitting function accounting for the sum of squared distances between the measured real displacements, observed on the acquired object point cloud and the simulated deformations. It is written as:

$$e(E, \nu) = \text{dist}(\text{sim}(E, \nu, \mathbf{f}^{op}, \mathbf{x}_{i_c}), Y) \quad (3.30)$$

where E and ν are respectively the Young modulus and the Poisson ratio, \mathbf{f}^{op} is the measured force exerted by the operator on the object, \mathbf{x}_{i_c} is the contact point, Y is the acquired point cloud. We use the point cloud segmented on the considered object by running the segmentation phase described in section 3.4.2.

For a relevant significant error function, we design it by employing the matching technique presented in section 3.4.2 between the segmented point

cloud and the visible part of mesh of the virtual object and conversely. Based on the two sets of mesh-to-point cloud and point cloud-to-mesh correspondences, the error function is calculated as:

$$e(E, \nu) = \frac{1}{n_{X_V}} \sum_{i=0}^{n_{X_V}} (\mathbf{x}_i - \mathbf{NN}_Y(\mathbf{x}_i))^2 + \quad (3.31)$$

$$\frac{1}{n_Y} \sum_{j=0}^{n_Y} (\mathbf{y}_j - \mathbf{NN}_{X_V}(\mathbf{y}_j))^2 \quad (3.32)$$

where $X_V = \{\mathbf{x}_i\}_{i=0}^{n_{X_V}}$ are the vertices of the visible part of the mesh and $Y = \{\mathbf{y}_j\}_{j=0}^{n_Y}$ are those of the segmented point cloud ones. $\mathbf{NN}_Y(\mathbf{x}_i)$ and $\mathbf{NN}_{X_V}(\mathbf{y}_j)$ define the correspondence of \mathbf{x}_i and \mathbf{y}_j , through nearest neighbour based matching process, respectively within the sets Y and X_V .

This optimization problem with respect to (E, ν) is non-linear and the evaluation of the objective function is expensive and its gradients are non-trivial to compute making gradient-based optimization methods prohibitive. We thus employ the gradient-free Nelder-Mead, which is an extension of the downhill simplex method to the nonlinear case.

We point out that, during the Nelder-Mead processs, for each evaluation of the objective function in the Nelder-Mead process, the mesh is initially reset to its rest shape before applying the virtual contact force \mathbf{f}^op on the known vertex of the mesh, given the elasticity parameters (E, ν) determined throughout the Nelder-Mead algorithm.

For each evaluated value of (E, ν) , a simulation is then started until a static equilibrium is reached. From this static equilibrium, the matching process to derive equation (3.32) is handled.

3.4.4 Pointwise Contact Force Estimation

By inverting the method for parameter estimation, the problem of recovering the contact force exerted on the manipulated object relies on

the interaction model between the object, the deforming operator and the ground, presented in section 3.4.1. Similarly, we then employ a fitting process, with respect to the force this time, between simulated deformations given the interaction model and the deformations observed using the vision. Since the material parameters are now determined, we can use the deformation model and the registration technique described in section 3.4.2 as the vision observation, providing a regularized and complete observation of the deformations.

We consider here the static case to estimate the interaction force, for which the static equilibrium state of the deformed material due to the exerted contact force is reached.

Our system consists in determining the force for which the resulting simulated deformations best fit the mesh deformed by the vision data. More formally, we minimize, with respect to \mathbf{f}^{op} the least square error e between the deformations sensed through vision $X = \{\mathbf{x}_j\}_{j=1}^{n_x}$ and the deformations simulated based on the interaction model involving \mathbf{f}^{op} .

$$e(\mathbf{f}^{op}) = \sum_i (\mathbf{x}_i^{vision} - \mathbf{x}_i^{sim}(\mathbf{f}^{op}))^2 \quad (3.33)$$

The derivation of e , given the full interaction model presented above is a non-trivial task which requires the inversion of the model, making iterative method like Newton methods tricky to handle. Instead, as for the estimation of the material parameters, since we aim at performing a quite global process without any strong guess on this force, we suggest a Nelder-Mead optimization framework to minimize e with respect to $\mathbf{f}^{op} = [f_x^{op} \ f_y^{op} \ f_z^{op}]^T$.

In practice, to compute e for a given force \mathbf{f}^{op} in the Nelder-Mead process, we start from the state of the mesh deformed through the vision registration. We then substitute all the external forces due to the point

cloud data by \mathbf{f}^{op} on the known vertex in contact with the operator. A simulation is evolved based on this force and the interaction model presented in Section 3.4.1. After a few iterations in the simulation process, e can be computed and thus measures the ability of \mathbf{f}^{op} to reproduce the actions of the forces provided by vision on the object.

3.4.5 Experimental Validation

The results presented here involve a deformable object, a stuff toy undergoing a compression deformation effort applied by a tool fixed on the end-effector of a Kuka LWR arm, which is equipped with a FT force sensor fixed on its last wrist joint (see Fig. 3.19). The point clouds of the investigated scenes are acquired using a calibrated RGB-D camera Asus Xtion, 320×240 RGB and depth images being processed. For both the estimation of the elasticity parameters and the applied contact compression force, we process the data of single RGB-D camera, taken at static equilibrium (see Fig. 3.19).

To build the deformation model of the stuff toy, a surface mesh of the undeformed object was reconstructed offline using an RGB-D based dense 3D reconstruction technique [104], by flying around the object with the Xtion sensor, and then manually segmenting the part of scene featuring the object. Finally, some remeshing and smoothing procedures are performed with a modelling engine in order to obtain a fair, closed and clean surface mesh of the object.

The volumetric tetrahedral mesh was then generated by carrying out a 3D Delaunay triangulation on the surface mesh, with the CGAL library. As a compromise between modeling accuracy and real-time constraints, we have generated a volumetric mesh with 951 vertices and 5015 tetrahedral elements, as seen in Fig. 3.19. As an approximation, we assume the isotropicity of the material of the stuff toy to apply the deformation model described in 3.4.1.

For modeling, we have employed the Simulation Open Framework Architecture (SOFA) simulator [34], which enables to deal with various physical models and to evolve simulations in real-time. In terms of hardware, a standard laptop with an NVIDIA GeForce 720M graphic card has been used, along with a 2.4GHz Intel Core i7 CPU.



Figure 3.19. Surface triangular (in red) and volumetric tetrahedral mesh (elements in blue colors) of the tuff toy (left). On the right, the experimental set-up, with the tool mounted on the robotic arm equipped with a force sensor, compressing the object.

Estimation of the Elasticity Parameters

In order to carry out tests for the estimation of the elasticity parameters, we first measure the contact force exerted by the tool mounted on the robotic arm to compress the object, giving a value of $\mathbf{f}_{mech}^{op} = [0.17, 1.125, 4.006]^T$.

Due to the particular shape of the considered object, the application of the pointwise virtual contact force may result in the loss of the static equilibrium. In order to yield more reliable results, we constrain the system by fixing some boundary conditions which consist in fixing the position of certain vertices. For the considered object, we fix some vertices on the lower part of the shape, close to the contact area with the flat surface, so that the object may not get bent excessively or turned over and its base

remains quite rigidly attached to the flat contact surface.

Following the Nelder-Mead algorithm basic implementation and the parameter space for (E, ν) being of dimension 2, 3 samples will be sorted after each iteration of the optimization, while performing the reflection, expansion, contraction and shrinking steps, providing a best, a good and a worst candidate. We also integrate the specific boundaries for both E and ν in the process, in the sense that inequalities $E > 0$ and $0 < \nu < 0.5$ should be preserved during the different steps. If an inequality is violated, E or ν is reset slightly below or above.

We have tested our parameters estimation technique with two different initialization configurations. In Figs. 3.21b and 3.22b we can observe for these two configurations the trajectories of the 3 sorted candidates, along E and ν throughout the iterations of the Nelder-Mead process. Figs. 3.21c and 3.22c show the fitting error for the 3 candidates after each iteration. In the first case the initial values are quite far from the actual estimated one, stressing out the robustness of the estimation with respect to coarse initial guesses, while in the second configuration, the process starts from closer.

For both configurations convergence is achieved respectively towards $(E, \nu) = (4268.65 \text{ Pa}, 0.412031)$ and $(E, \nu) = (4328.12 \text{ Pa}, 0.415625)$. The fitting error being prone to local minima, convergence may be reached after a certain number of iterations, around 8 in the first case and around 11, despite its closer initial values. As it can be noticed on the plot of the fitting error in Fig. 3.23, the non-convexity can be especially observable for the ν parameter, along which the error is quite flat, resulting in some local minimas.

Estimation of the Operator Contact Force

With the aim of testing the operator contact force estimation based on the vision tracking system, we first proceed by setting the material

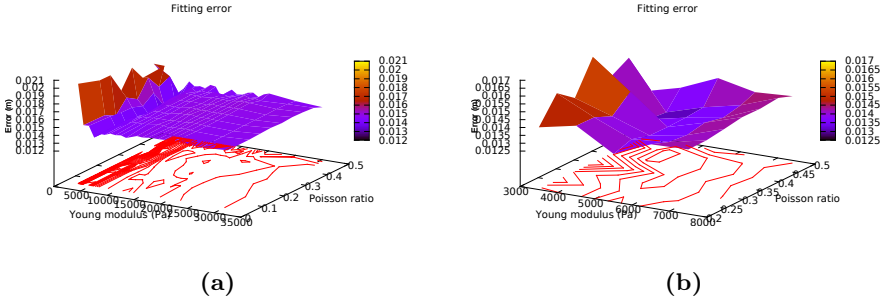


Figure 3.20. Fitting error with respect to the elasticity parameters. In 3.20b a closer view around the global minimum is shown.

parameters of the deformation models used in the vision system (here we use $(E, \nu) = (4268.65 \text{ Pa} \quad 0.412031)$).

Let us remind that for each evaluation of the error function in the Nelder Mead process, the registered mesh is relaxed from the forces exerted by vision while applying the point wise contact force to evaluate on the known vertex. Some fixed points are not necessary as boundary conditions to constraint the simulation since we measure here the ability of this force to keep the static equilibrium already reached by the action of the vision forces. The parameter space being of dimension 3, there will be 4 samples to sort after each iteration, the best, the worst and two intermediate ones. Two different initial configurations are also tested here, starting respectively quite far, without any particular guess on the intensity and direction of the force, and close to the actual value of the force given by the sensor $\mathbf{f}_{mech}^{op} = [0.17, 1.125, 4.006]^T$. Figs. 3.24a and 3.25a show in both cases the trajectories of the four candidates for the estimate of the contact force \mathbf{f}^{op} , along X, Y and Z, while Figs. 3.24d and 3.25d feature the corresponding fitting errors. In both cases, the algorithm converges respectively towards a force $\mathbf{f}^{op} = [0.618, 0.0687929, 3.54801]^T$ and $\mathbf{f}^{op} = [-0.462414, 0.247626, 3.71292]^T$, which are relatively close to the

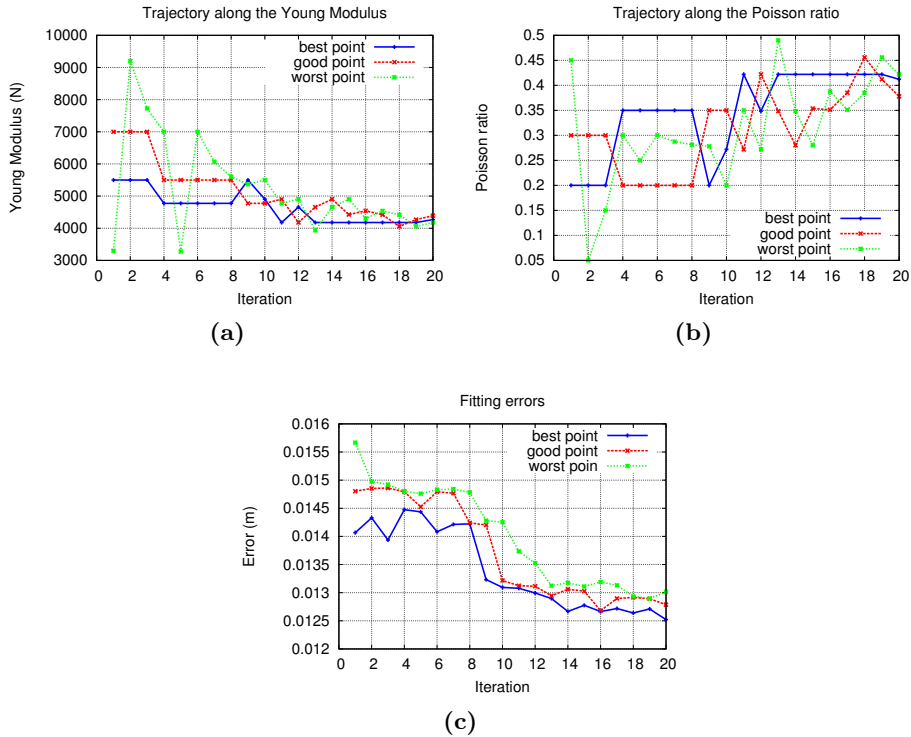


Figure 3.21. Results of the Nelder-Mead process for the first initial configuration.

value sensed by the force sensor mounted on the robot, thus validating our whole model. Convergence is of course reached much faster in the second case.

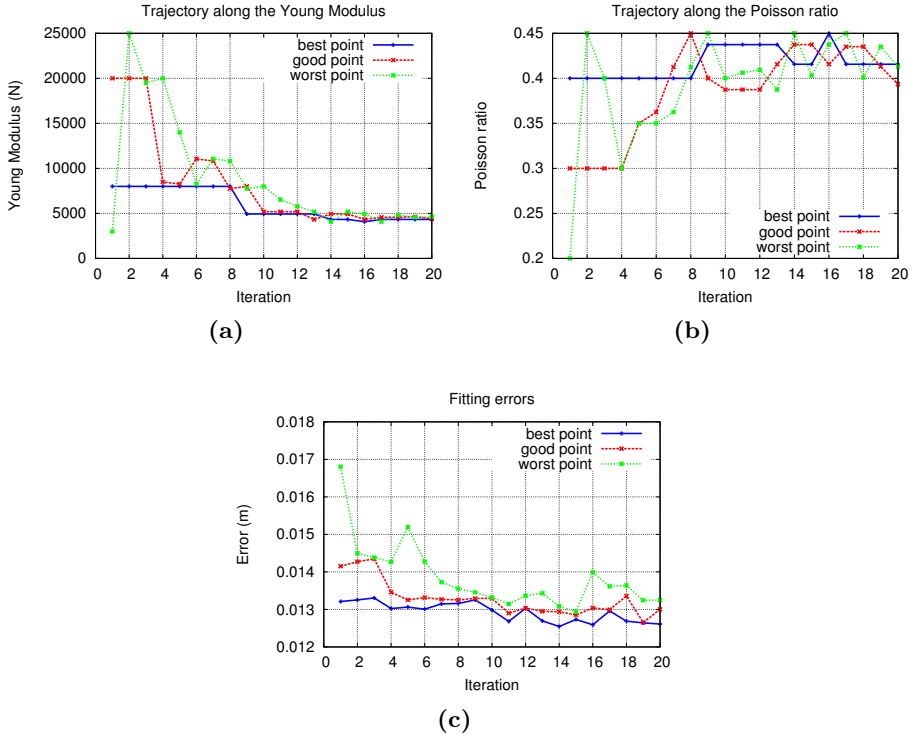


Figure 3.22. Results of the Nelder-Mead process for the second initial configuration.

3.5 Vision-based Force Feedback

In this Section, we aim to show a simple and effective method that can be used to give the force contact force information to the surgeon through visual feedback. This method has been designed to be used with the trocar force sensor presented in Sec. 3.2 to improve the surgeon perception, also in the absence of the measure of the axial force component. To this purpose, the main approaches proposed in the literature are: (i) kinesthetic feedback, in which the force estimated on the slave side is applied on the master robot e.g. [108]; (ii) cutaneous force feedback, that

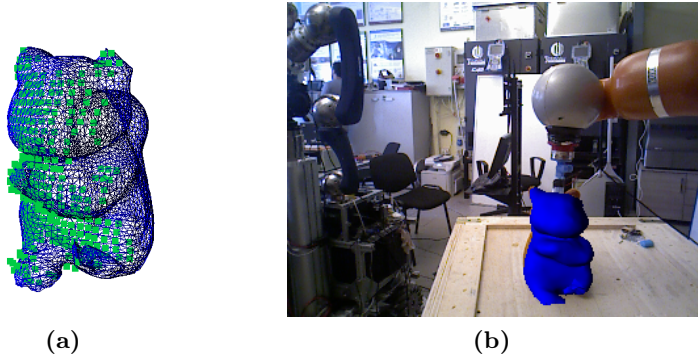


Figure 3.23. Registration process, with in Fig. 3.23a the fitting result between the mesh and the segmented point cloud.

allows perceiving the force via sensory substitution using wearables devices e.g. [124]; (iii) visual force feedback, retrieving the force information via sensory substitution in augmented reality [149]. The third approach is used here to test our sensing device on a dVRK performing typical surgical tasks. The results have been submitted to TRMECH 2018.

3.5.1 An Intuitive Vision-Based Force Feedback Method for the Trocar Sensor

The estimation of the two components of the external force provided by the trocar sensor is used here to develop an intuitive force feedback method based on augmented reality. In our surgical system, frame grabbers capture real-time stereoscopic images from the dVRK InSite stereo endoscope. The force is visualized on the two rectified stereo images with a graphic overlay following the instrument motion. To guarantee the intuitiveness of the proposed approach, the overlay is defined in the end effector frame $O_E - x_E y_E z_E$ and follows the tool during the motion as reported in the screenshots of Fig. 3.26.

The intuitiveness with respect to the lack of the measure of the force

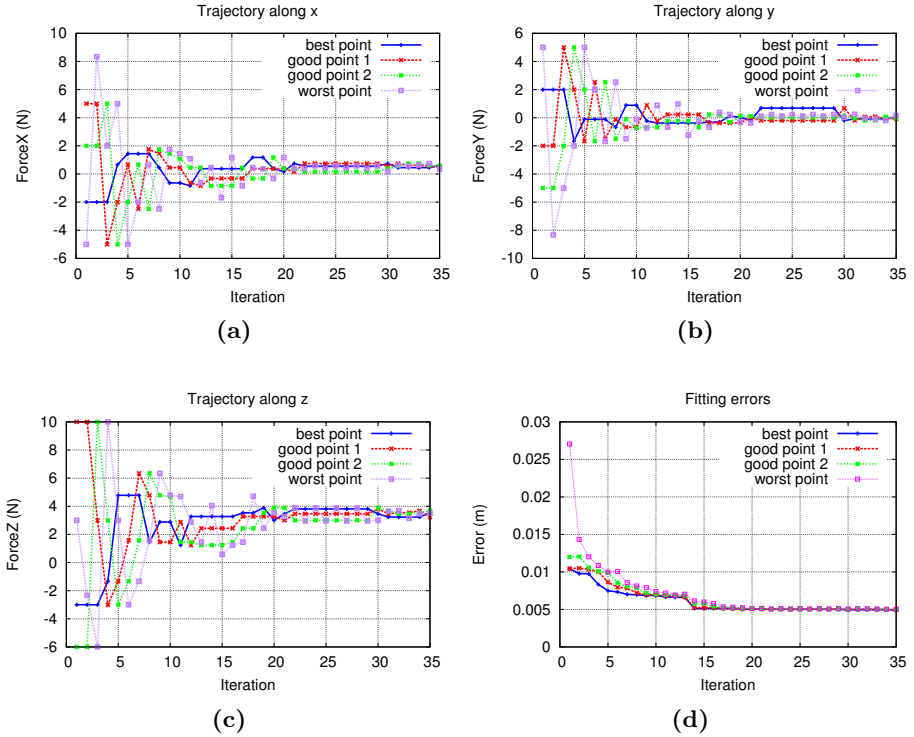


Figure 3.24. Results of the Nelder-Mead process for force estimation, for the first initial configuration.

along the axis z_E is preserved by representing the vector composed by the first two force components (f_{xE} and f_{yE}) directly in the plane orthogonal to the instrument axis. Moreover, the force vector is visualized with a directed line segment (i.e., a geometric vector) with the initial point on the tool's tip, then it is always inside the field of view. The graphical overlay is updated on the surgeon's stereoscopic display console with a frequency of 30 frames per second. The geometric vector can change length, direction and color to visualize three different information:

- force amplitude in a range $[0, f_{max}]$ proportional to the vector length;

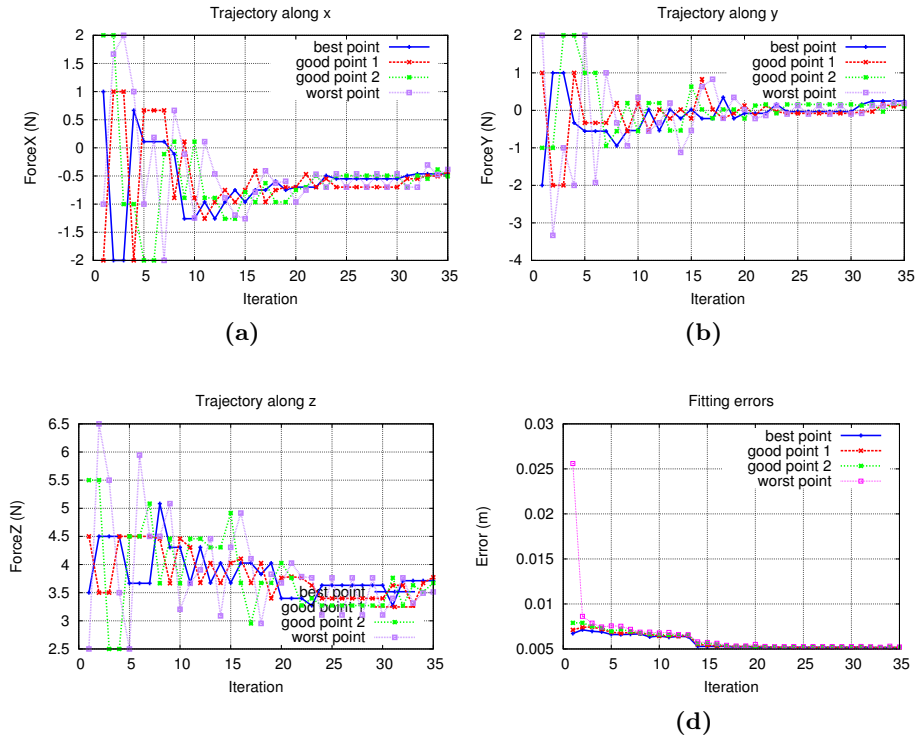


Figure 3.25. Results of the Nelder-Mead process for force estimation, for the first initial configuration.

- force direction on the plane orthogonal to the instrument axis through the vector direction;
- force thresholds set for particular surgical phases codified through the vector color.

To be more precise, the geometric vector connects the origin O_E of the end effector frame to point P_T , whose position vector \mathbf{p}_T , expressed in the base frame, is computed as:

$$\mathbf{p}_T = \mathbf{o}_E + \mathbf{R}_E \mathbf{l},$$

being \mathbf{o}_E the position vector of O_E and \mathbf{R}_E the rotation matrix of the end effector frame with respect to the robot base frame. These quantities are computed from the joint vector \mathbf{q} using the PSM direct kinematics. Moreover, vector \mathbf{l} is defined as $\mathbf{l} = l_{max}/f_{max}\mathbf{f}_E$ being l_{max} the length of the geometric vector when $\|\mathbf{f}_E\| = f_{max}$. Points P_T and O_E are projected on the rectified stereo image plane considering the known pinhole camera model transformation and the hand-eye calibration matrices between the camera left/right frames and the robot base frame, obtained using the method proposed in [168]. Finally, the vector color is set according to a continuous gradient scale between the green and the red color defined by the following RGB code:

$$\mathbf{c} = [\alpha|\mathbf{f}_E|/f_{max}, \quad \alpha(1 - |\mathbf{f}_E|/f_{max}), \quad 0]$$

with $\alpha = 255$.

In our framework, the task-related force thresholds are set empirically based on the average force the surgeon exerts while performing the specific task. In the experiment presented in this paper, the following parameters are used:

- $f_{max} = 5$ N
- $l_{max} = 0.02$ m
- green color for force less than 2 N
- yellow color for force in the range [2 – 4] N
- red color for force up to 5 N.

Three typical surgical subtasks have been considered: tissue palpating, needle passing, knot tying. The results are shown in Fig. 3.26, reporting the variation in direction, length and color of the overlapped geometric vectors. A video showing the sensing device and the proposed experiment can be downloaded from the link <https://youtu.be/YxIBzTMlKFo>.

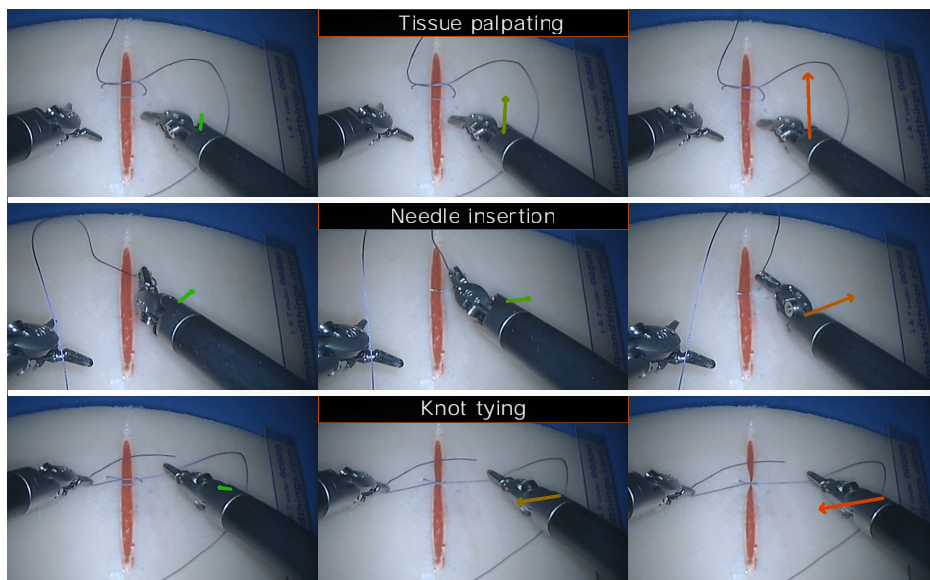


Figure 3.26. Vision-based force feedback. The tissue reaction force is shown in augmented reality. Top: Tissue pushing, Middle: Needle insertion, Bottom: Knot tying.

3.6 Conclusions

In this chapter, some new approaches enabling the force estimation and force feedback in minimally invasive surgical procedures have been presented. Our method consists in evaluating methods whose the word "non-invasiveness" can be considered a keyword. With this, we mean that the proposed approaches must be non-invasive for the robot, for the patient and also for the surgeon. Therefore we propose three different force sensing methods and a force feedback solution:

- A sensor-less, model-based force estimation method relying on the identified dVRK dynamic model that can be used without any modification to the robot structure.
- A new sensor that as it can be integrated into the PSM trocar not

require any modification to the surgical instrument, is fully adaptable to different instruments and also allows the surgeon to switch between different instruments intraoperatively without putting any mental effort on this procedure.

- A miniaturized sensorized hand fingertip with integrated fiber-optic force sensor that is able to estimate three component of the force.
- A vision-based method allowing both the estimation of the physical properties of a deformable object and the external force. This allows obtaining this information by using sensors that are usually included in the surgical robotic platforms, e.g. the stereo endoscope.
- A vision-based force feedback solution that used in combination with the trocar force sensor and/or the other approaches allows giving the surgeon a non-invasive, stable force information without distracting him from the surgical procedure.

On the other hand, some limitations of the proposed approaches can be discussed also focusing on the guidelines for future improvements.

In detail, using the current measurement and the robot dynamic model for robots like the dVRK could be a good approach only to estimate force with high intensity, such as $> 2\text{N}$ in our case study. This is because the unmodelled dynamics due to the tendon driven actuation, configuration and time-dependent friction and also a bad motor current estimation. On the other hand, using the proposed force sensor integrated into the trocar we are able to improve notably the resolution in the estimation of the two component of force lying on the plane orthogonal to the instrument axis with a resolution of 0.1N . This allows giving to the surgeon information about thread traction and instrument-tissue force. However, in order to estimate the complete force vector we need to use a combination of the two proposed methods. In future our purpose will be evaluating the possibility to fuse the two proposed method with a filtering solution,

e.g. Kalman filter, to improve the resolution and also to extend the range of measure using the better force measure (model-based/trocar) for each range. Furthermore, it is worthy of notice that the instrument physical properties (length, mass, inertia) should be taken into account when our trocar force sensor is used in the static and dynamic model; however, for standard lightweight instruments, the dynamic effects are usually small compared to the range of the measured forces and can also be neglected.

On the other hand, our finger-tip force sensor shows promising results in terms of resolution demonstrating also the possibility of miniaturization given by the use of fibre-optic Bragg based sensors. However, this technology has some drawbacks such as (i) high costs, (ii) high fragility, (iii) big and costly measure device.

Moreover, in this chapter, we discuss also the use of vision to estimate the external force. Despite the proposed method was only at a first stage and no surgical experiments have been conducted we are confident that the results presented can be applied in the surgical scenario, in particular, considering that the vision systems technology, miniaturisation and resolution are constantly improved over years. Our work shows also some guidelines for future works we'll report the following:

Considering the deformation capture set-up, it is based on a single Asus Xtion RGB-D sensor, providing in quite low resolution, partial and noisy point cloud data around the object. It results in a non-convex shape for the fitting error function in the elasticity estimation process, especially with respect to ν , or in registration errors within the vision system.

A more sophisticated set-up to capture deformations, such as the one proposed in [157], with a set of RGB-D sensors at different viewpoints, would give more accurate results for the estimation of both the mechanical parameters and the contact force.

Moreover, we assume the contact point between the object and the operator to be known, as well as the contact between the object and the

underlying flat surface. A further development of our approach would be the design of a vision system able to capture the interaction between the object and its interacting environment.

In the estimation of the force exerted by the operator, we use a gradient-free Nelder-Mead optimization method. It has the advantage of being quite easy to implement and robust to a coarse initialization, it is however quite slow to run. Indeed for force estimation, each evaluation of the error function requires at least 5 successive simulations to obtain a reliable error with respect to deformations of the registration process. An iteration in the Nelder-Mead algorithm requires in this case 7 evaluations, so around $350ms$, given that one simulation takes around $10ms$, making the process quite far from being real-time if considering a stream of successive RGB-D data. A possible improvement would be to investigate an efficient inversion of the full interaction model and some local optimization techniques such as quadratic programming, as proposed by [77].

Furthermore, we want to point up that our system is designed for the static case, for which deformations have reached a static equilibrium. It could be adapted to a dynamic case by benefiting from a measure, through vision, of the kinematics of the object or of interacting entities. Hence, based on Lagrangian dynamics, the system could track on-line both the deformations and the force.

In conclusion, we think that both the devices and the strategies presented in this chapter can open the possibility to create non-invasive haptic feedback methods improving the surgeon perception of the environment. Our novel trocar force sensor, combined with sensorless approaches and the vision-based haptic feedback can enable a precise contact force estimation and a simple force feedback. Moreover, the presented vision-based method can help the surgeon to estimate the physical properties of organs and tissues online enabling new diagnostic methods in MIRS.

Chapter 4

Motor Enhancement Through Advanced Instruments

Laparoscopic robotic surgery, and in general minimally invasive surgery (MIS), has obvious advantages compared to the classical open and laparoscopic surgery (see Sec. 1.2). The use of robots tried to overcome some limitation of the laparoscopic surgery by enhancing the surgeon dexterity, speeding up the recovery time, increasing comfort for the surgeon and surgery's performance, reducing the hemorrhaging and reduced risk of infections. The idea behind MIRS is improving the laparoscopic tools by enhancing precision, dexterity e.g. the EndoWrist technology¹ and making human friendly the user interface. Therefore, the surgical tools used in MIRS are designed to mimic and enhance the working principle of the standard laparoscopic tools. However, with the new design technology and miniaturisation is possible doing more. We imagine the next surgical robot generation giving the ability to the surgeon to reacquire some hands ma-

¹<http://www.davincisurgery.com/da-vinci-gynecology/da-vinci-surgery/da-vinci-surgical-system/system-safety.php>

nipulation/sensation capabilities also in laparoscopic surgery. With this goal, the aim of this Chapter is to show the development of a new generation of laparoscopic robotic instruments bio-inspired to the human hand. The need of a hand-like tool for laparoscopic surgery is demonstrated by the existence of a Hand-assisted laparoscopic surgery (HALS) technique [69] where the operator's hand is inserted through a small incision into the abdomen. This technique has the advantages of providing the surgeons with the capabilities of exposure, traction, palpation, tactile sensation and digital dissection of the operative specimen while the operative field is visualized as in standard laparoscopic surgery, namely with a video monitor. Besides the advantages, the application of HALS has been limited to a few major centers. This is due to the fact that instruments suitable for HALS are limited to few standard surgical procedures. Indeed, open issues are related to the operator fatigue, potential risk for injury to other organs, the need of suitable setup for HALS that requires appropriate operating table height and table orientation, and finally optimized positioning of the operating ports to avoid that the assisting hand is too close or too far from the target organ. Indeed, in the first case, the hand could obscure vision while in the latter could cause hand fatigue. The aim of the work presented in this Chapter and of the MUSHA project is to find a suitable trade-off between the use of classical laparoscopic forceps and the HALS technique by introducing the advantages of anthropomorphic manipulation capabilities in the daVinci setup by transferring the most recent results in robotic manipulation to the robotic surgical scenario. In detail, in Sec. 4.1 we will show a new concept for a robotic needle driver capable of in-hand rolling the suturing needle while in Sec. 4.2 a new three-fingered, underactuated, sensorized and miniaturized hand for MIRS is proposed.

4.1 A New Laparoscopic Tool with In-Hand Rolling Capabilities for Needle Reorientation

During suturing, the surgeon needs to constantly change the orientation of the needle in order to find the appropriate pose. To this end, the reorientation phase is conducted through successive grasp and release operations, according to a *grasping - release - positioning - re-grasping* sequence, using both arms of the robot. This sequence of operations is shown in the flow chart on the left of Fig. 4.2. This problem may be overcome by modifying the needle driver with a slot specifically designed to keep the needle perpendicular to the gripper [94, 136]. However, even in this case, the needle position and orientation inside the gripper would not be under the surgeon's control. In some cases, also the reaching of instrument's

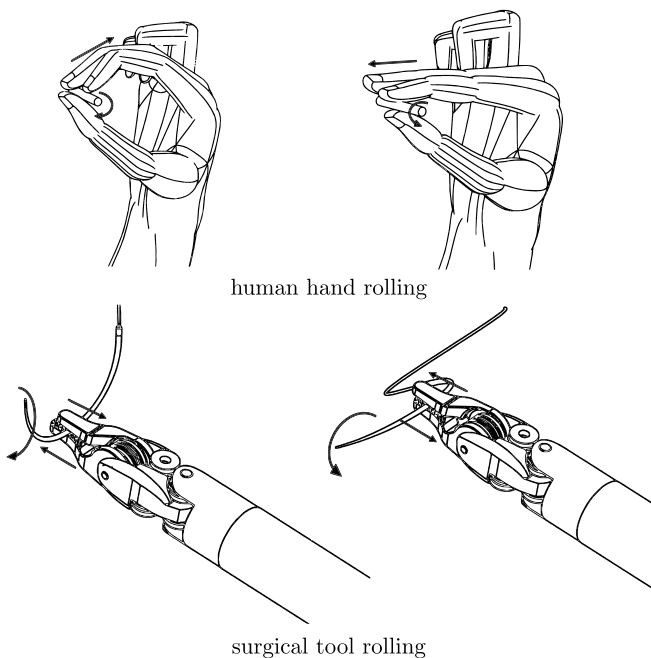


Figure 4.1. Object rolling capability of the novel suturing tool inspired by that of the human hand.

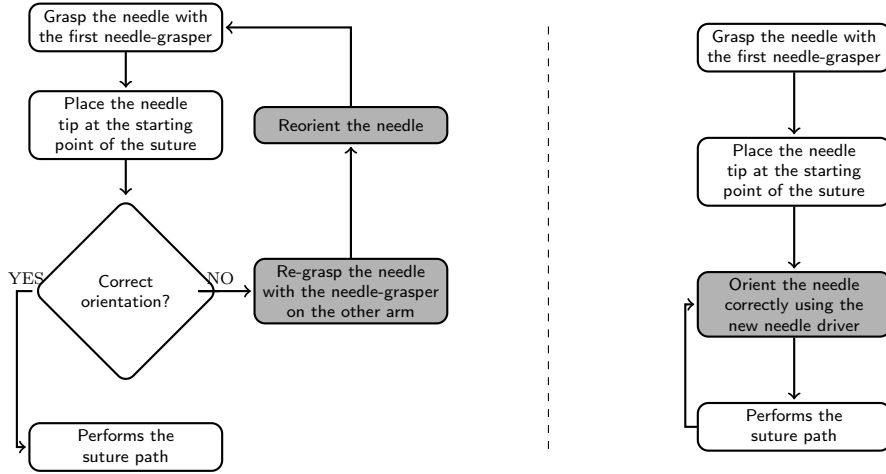


Figure 4.2. Suturing sequence flow charts. Left: standard tool (ST); right: modified tool (MT). The steps involving needle reorientation are highlighted in gray.

joint limits might require releasing and re-grasping the needle in a different configuration with the second arm intervention. Starting from these premises, we believe that an additional Degree of Freedom (DoF) can be extremely useful to manipulate rigid objects with a circular cross section, such as, needles for suturing. In this section, a new needle driver tool that allows a more natural and intuitive manipulation of the surgical needle is presented. Inspired by the human hand motion (see Fig. 4.1), our design enables the possibility to reorient the suturing needle without interruptions, controlling the additional DoF of the tool in telemanipulation or in autonomous mode. Hence, some surgical tasks, such as suturing, might be executed using only one arm. The presented tool together with the experimental results have been published in [43].

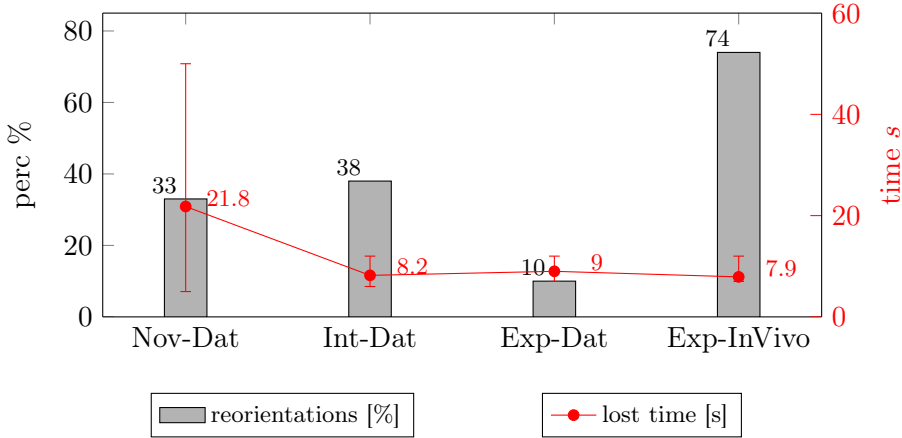


Figure 4.3. Percentage of stitches requiring needle reorientation and average/variance of the time lost for reorienting the needle. Data provided by the JIGSAWS dataset (-Dat) and real procedures (-InVivo) performed by novice (Nov-), intermediate (Int-) and expert (Exp-) surgeons.

4.1.1 Clinical Motivations

Suturing is one of the most challenging tasks in minimally invasive surgery and micro surgery [53, 35]; an error in suturing can produce significant tissue damage and is more likely to happen when the needle orientation is not completely under the surgeons control [136], especially in absence of force feedback information [149, 40, 116]. Due to the structure of standard needle drivers, the orientation of the needle during the suturing procedure is not completely controllable and multiple pairs of hand-off movements are required, before the execution of each stitch [136].

An evaluation of the occurrence of this behavior can be found by inspecting replicated suturing procedures. To this end, we have considered the suturing video data in the JHU-ISI Gesture and Skill Assessment Working Set (JIGSAWS) [7], captured using the da Vinci Research Kit [71]. The database comprises 39 suturing tasks each composed of four stitches on a bench-top model, performed by eight surgeons with different levels of skills. In addition to this, we have also inspected a number of videos acquired

during in vivo surgical procedures performed by expert surgeons. In the considered videos, we counted the number of stitches that require needle reorientation and measured the average and the variance of time lost in this operation, for the three levels of surgical skills. The results in Fig. 4.3 show that the percentage of stitches requiring needle reorientation is rather high, although it decreases when the surgeons' skills increase. The same trend can be observed for the average time lost. It is worth noting that in the real scenarios, in which the needle needs to be dropped and re-grasped to make knots or move organs, the number of stitches requiring reorientation is considerably higher than for the sutures performed on the phantom model.

4.1.2 Preliminaries: Dexterity Evaluation with Joint Limits

In order to quantitatively evaluate the benefits introduced by our tool, a dexterity analysis has been performed along suturing trajectories. A suitable dexterity measure has been used to quantify the overall motion capability of the robot with the new tool in comparison with the same robot using a standard da Vinci tool. This measure can be computed directly starting from the robot Jacobian matrix.

The influence of the joint limits on the robot's dexterity can be taken into account by weighting the entries of the Jacobian matrix according to a joint limits performance criterion as in [155]. More in detail, a penalization matrix $L(\mathbf{q}) \in \mathbb{R}^{r \times n}$ is introduced, where r and n are the task and the joint space dimensions, respectively. This matrix is used to compute the elements of the augmented Jacobian $\tilde{J}(\mathbf{q}) \in \mathbb{R}^{r \times n}$ as

$$\tilde{J}_{i,j}(\mathbf{q}) = L_{i,j}(\mathbf{q})J_{i,j}(\mathbf{q}), \quad i = 1, \dots, r, \quad j = 1, \dots, n, \quad (4.1)$$

where $J_{i,j}(\mathbf{q})$ is the (i, j) element of the robot Jacobian and $L_{i,j}(\mathbf{q})$ is

defined as

$$L_{i,j}(\mathbf{q}) = \frac{1}{\sqrt{1 + |\nabla h_j(\mathbf{q})|}}. \quad (4.2)$$

The scalar function $h(\mathbf{q}) : \mathbb{R}^n \rightarrow \mathbb{R}$ in (4.2) is a differentiable function of the joint vector \mathbf{q} which tends to infinity as the joint variables approach the corresponding joint limits. Taking inspiration from [19], we use the following function

$$h(\mathbf{q}) = \sum_{i=1}^n \frac{1}{4} \frac{(q_{i,max} - q_{i,min})^2}{(q_{i,max} - q_i)(q_i - q_{i,min})}. \quad (4.3)$$

The gradient $\nabla h(\mathbf{q})$ represents the direction of fastest increase of $h(\mathbf{q})$ and is useful to build the corresponding penalization index (4.2). The i -th component of the gradient $\nabla h_i(\mathbf{q}) = \partial h(\mathbf{q})/\partial q_i$ can be computed as

$$\nabla h_i(\mathbf{q}) = \frac{1}{4} \frac{(q_{i,max} - q_{i,min})^2 (2q_i - q_{i,max} - q_{i,min})}{(q_{i,max} - q_i)^2 (q_i - q_{i,min})^2}. \quad (4.4)$$

At this point, according to [148], a weighted dexterity measure d can be computed from the augmented Jacobian as:

$$d = \frac{\sqrt{rn}}{\sqrt{\text{tr}[(\tilde{J}\tilde{J}^T)^{-1}]}} \quad (4.5)$$

where $\text{tr}(\cdot)$ denote the trace operator. This index provides similar information of the standard manipulability index, but allows comparing manipulators with the same task space dimension independently from the joint space dimension. Moreover, it takes into account the distance from both joint limits and singularities.

4.1.3 Tool Working principle

In this section, the working principle of the new suturing tool is described.

Mechanics

A gripping mechanism capable of impressing tangential motions to a circular cross section object is described following. The tendon driven actuation mechanism of a standard da Vinci laparoscopic tool has been modified by adding an additional pulley used to actuate the extra DoF responsible for the rolling motion. This solution is fully compatible with the instruments of the ultimate da Vinci robots, such as the da Vinci Xi, which is equipped with an extra actuated DoF that can be used for advanced tools.

The design of the tool has been carried out considering the following constraints:

- the external radius of the tool must be smaller than the internal radius of the trocar (8.5 mm) used by the da Vinci robotic system;
- the dimensions of the two fingers must be equal to those of the fingers of the da Vinci standard needle driver tool whose efficiency has been largely demonstrated in their long time of use.
- the rolling mechanism must be designed to be general to be used also with fingers of different shape and dimensions.

Moreover, the maximization of the rolling motion that can be impressed to the most used needles in laparoscopic procedures [6] has been taken in to account.

In Figure 4.4 the four tool versions are reported to show the design process. In detail, versions V1 and V2 represent two first working solutions but not general in the sense that no different shape fingers can be used. On

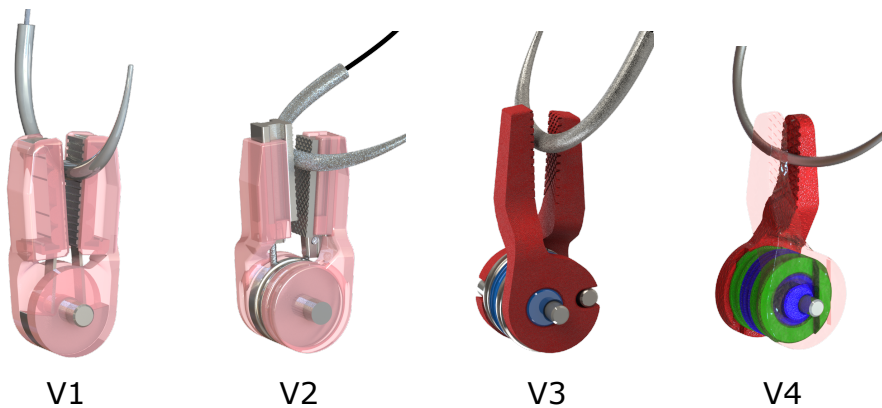


Figure 4.4. Tool versions.

the other hand versions V3 and V4 are in line with the requirements but the guide mechanism in V4 has been chosen due to the effectiveness and reliability compared with the solution in V3. Figure 4.5 shows an exploded view of the chosen tool (V4). The fingers 6A and 6B are actuated indirectly by the pulleys 7A and 7B to allow the fingers rotation. The pulley 8 creates the desired linear displacement along the fingers major direction. To this end, the pulley 8 has been designed with two eccentric cylinders disposed specularly with a phase displacement of 180° (8-1 in Fig. 4.5). These cylinders rotate within two slots made on the fingers to produce a linear motion. Two linear guides, represented by the parts 7A-1 and 6A-1 in Fig. 4.5, are used to constrain the linear motion between the fingers and the pulleys 7A and 7B. Therefore, a rotation of the eccentric cam causes a shift of the finger with respect to its rest position. Conversely, leaving the cam in the rest position (see Fig. 4.6 on the center) the fingers remain aligned. The actuation of the pulleys 7A, 7B and 8 is obtained by means of three pairs of tendons (direct and antagonist) fixed to the respective pulleys.

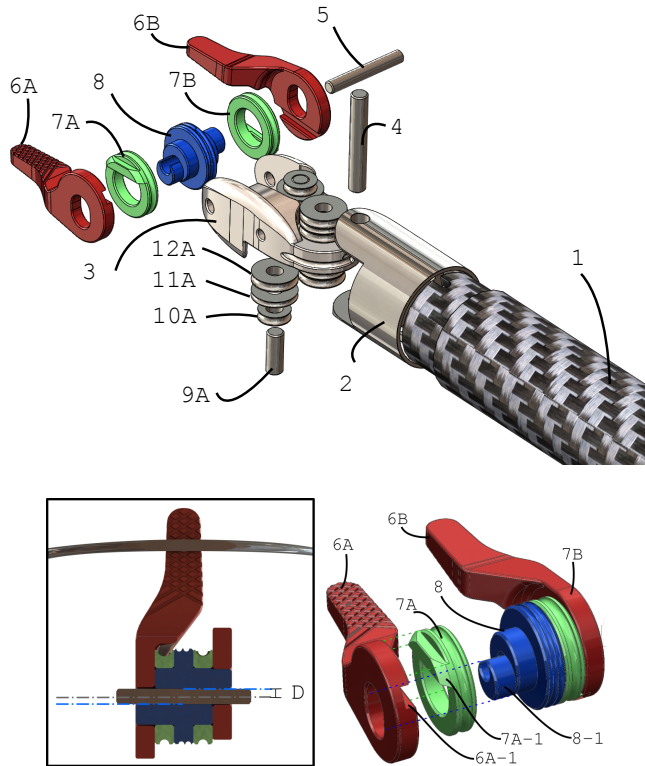


Figure 4.5. The new suturing tool: exploded view and cross section (in the frame).

Tool Modelling

The displacement Δx of the two fingers is mechanically related to the central pulley rotation angle $\Delta\vartheta$ (see Fig. 4.6). This displacement causes a certain rotation $\Delta\alpha$ of the cylindrical object depending on the object radius and on its position between the fingers. Assuming no slippage between the object and the fingers, the following equations hold

$$\begin{cases} \Delta x = D \sin(\Delta\vartheta) \\ \Delta x = R \Delta\alpha \end{cases} \iff \Delta\alpha = \frac{D \sin(\Delta\vartheta)}{R} \quad (4.6)$$

where R is the object radius and D is the misalignment between the center of the central pulley and the center of the eccentric (refer to Fig. 4.5).

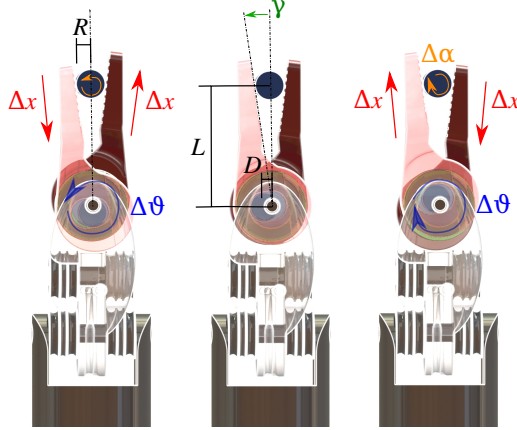


Figure 4.6. New suturing tool working principle. A rotation of the internal pulley of an angle $\Delta\theta$ causes the opposite translation of the two fingers (Δx) and hence the rotation of the grasped object of an angle $\Delta\alpha$.

To maximize the rolling capability of the tool, the needle needs to be grasped with its tangent parallel to the tool joint axis (the axis of the pulley 8 in Fig. 4.5). If there is a misalignment the velocity impressed by the instrument is not converted only into a rolling velocity but another component is determined.

In Fig. 4.7 this behavior is shown more in detail: consider two planes that translate in two opposite directions with velocities V_T and V_B and a cylinder in contact with the two planes oriented with an angle β with respect to the direction of motion. The velocity V_B can be decomposed into two components V_B^t, V_B^n , where

$$V_B^t = V_B \cos(\beta) \quad V_B^n = V_B \sin(\beta) \quad (4.7)$$

and the same equations can be written for the V_T velocity. Then, (4.6)

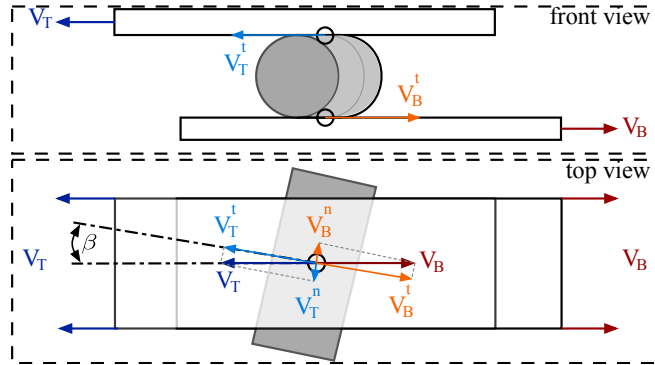


Figure 4.7. Rolling model representation.

must be rewritten taking into account that the rolling motion when $\beta \neq 0$ is reduced by $\cos(\beta)$

$$\Delta\alpha = \frac{D \sin(\Delta\vartheta)}{R} \cos(\beta). \quad (4.8)$$

Therefore, if the angle β is not equal to zero, both the normal and tangential components of the velocities V_B and V_T are different from zero. Notice that the normal velocities V_B^n and V_T^n are realizable only considering slippage in the direction of the object axis. Hence, if $\beta \neq 0$, during the rolling motion a higher velocity is required to rotate the needle by the same quantity, resulting in a more expensive operation. This means that, if the needle is not gripped with its tangent orthogonal to the direction of motion of the two fingers, the needle can be still rotated but a lower angular displacement can be accomplished.

To comply with specifications of Sec. 4.1.3, a constraint on the misalignment D has been imposed. In particular, we choose $D = 0.5 \text{ mm}$ while $\Delta\vartheta$ is in the range $[-\pi/2, \pi/2]$. The rolling angle ranges for four classes of needle, most used in laparoscopic surgery, with three different β values can be computed using (4.8) are given in Table 4.1.

Table 4.1. Maximum rolling angles for different needles

	R [mm]	$\beta = 0$	$\beta = \pi/12$	$\beta = \pi/4$
<i>RB-1</i>	0.25	$\pm 114^\circ$	$\pm 110.1^\circ$	$\pm 80.3^\circ$
<i>SH-Plus</i>	0.352	$\pm 88^\circ$	$\pm 85^\circ$	$\pm 62^\circ$
<i>GL-222</i>	0.38	$\pm 81^\circ$	$\pm 78.2^\circ$	$\pm 57^\circ$
<i>UR-6</i>	0.5	$\pm 57.5^\circ$	$\pm 55.3^\circ$	$\pm 40.5^\circ$

Finally, the aperture angle of the gripper γ is related to the object radius and to the distance of the object from the gripper center of rotation (R and L in Fig. 4.6) by the equation

$$R = L \sin(\gamma) \iff \gamma = \arcsin\left(\frac{R}{L}\right). \quad (4.9)$$

4.1.4 Evaluation Trough 3D Printed Prototype

Due to the difficulty of having a complete and fully functional metal tool attached to a surgical robot, the evaluation of the mechanism has been carried out through a plastic 2:1 scale prototype. The prototype was

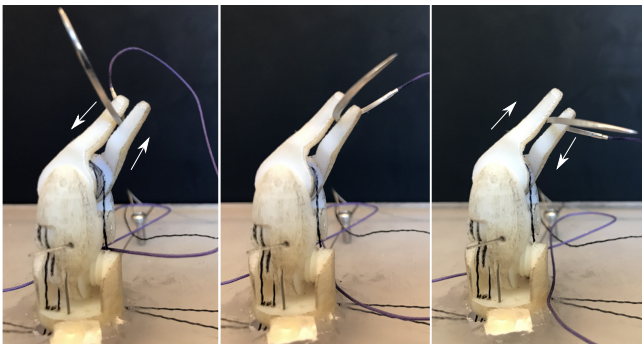


Figure 4.8. 3D printed prototype of the new tool (scale 2:1): evaluation of the working principle with a circular shape needle.

realized using a 3D printed technology based on the polyjet process². This technology allows achieving sufficiently high precision and accuracy.

Fig. 4.8 shows a sequence of the motion. The mechanism was manually actuated by tendons and the executed rotation angle was measured using a protractor. The experiments were performed on a needle with a circular cross-section with diameter doubled with respect to the SH-Plus needle. When the tendons were actuated to move the mechanism in the entire range of motion, we measured an angle of about 80°. This value is close to the predicted value of 88° for a SH-plus needle actuated using a non-scaled tool. Hence, despite the high friction of the employed material and the errors introduced by a non perfect needle alignment, the experiments showed a working behaviour of the prototype close to the expected one.

4.1.5 Evaluation Trough Simulated Case Studies

To measure the performance of the new needle driver we considered a set of real suturing procedures executed on da Vinci Research Kit (DVRK) with a standard tool (ST) and replicated them in a simulated environment with our modified tool (MT). Two case studies have been considered: the first is focusing on a *single stitch* trajectory execution; in the second, *complete sutures* procedures are considered, all with 5 stitches performed on different phantoms.

The goal of the analysis is to prove that our MT can both improve the surgeon precision and reduce the execution time by allowing in-hand needle reorientation during real suturing procedures. Moreover, we show that our tool is able to overcome the problem of reaching joint limits, within the range of movement.

Given these good results obtained on the scale prototype, in our simulation we have assumed that the MT is able to rotate the needle as expected,

²<http://www.stratasys.com/3d-printers/design-series/objet24>

Table 4.2. DH parameters of the modified tool (MT)

link	joint	prev	succ	a_i [m]	α_i [rad]	d_i [m]	θ_i [rad]
1	R	–	2	0	$\pi/2$	–	θ_4
2	R	1	3	0.009	$-\pi/2$	–	$\theta_5 + \pi/2$
3	R	2	4	L	0	–	θ_6
4	R	3	–	0	$-\pi/2$	–	$\theta_7 - \pi/2$

without slipping.

Simulation Environment

The simulation environment is composed by a simulated Patient Side Manipulator (PSM) of the da Vinci Research Kit that can be equipped with ST and MT. The simulator has been developed in V-REP and interfaced with the Master Tool Manipulator (MTM) of the da Vinci robot. Simulated trajectories have been planned with MATLAB.

Two different tools moved by the first 3 PSM DoFs are used in the case studies: the first is the ST whose kinematic model is that described in [41]; the second is our MT whose kinematic is described by the DH parameters in Table 4.2. In detail, the MT is a 4-DoFs kinematic chain in which the first 3-DoFs are the three joints of the ST wrist. The fourth DoF corresponds to a joint placed in the center of the circular section of the needle at the grasping point and is used to model the rotation induced by our mechanism. Notice that, in the experiments, we will assume that the object is already grasped and then the opening/closing DoF is not explicitly taken into account.

First Case Study: Single Stitch

Due to its kinematic structure, the PSM arm of the DVRK can easily reach configurations that are near to joint limits. When this happens,

the real trajectory of the robot PSM may deviate from the trajectory commanded by the surgeon through the master robot, because of the occurrence of joint saturations. The goal of this case study is that of showing how our instrument could help to overcome this problem. To this end, an experiment was carried out using the ST mounted on the PSM arm: a needle trajectory along a circular path was commanded through the master robot, starting from a configuration close to a joint limit, so that joint saturations occur. Then, the desired circular trajectory was extrapolated using the part of the real trajectory not influenced by joint saturations. This desired trajectory was used in simulation as reference for the model of the PSM arm with the MT.

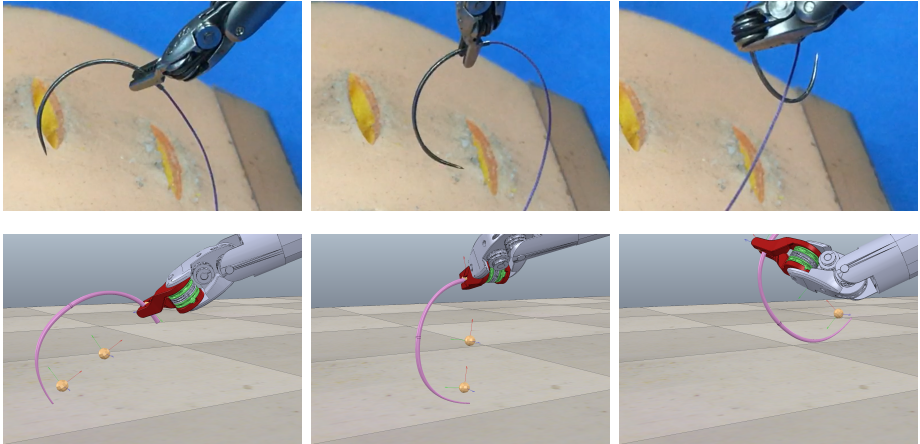


Figure 4.9. Snapshots sequence of a single stitch trajectory. Top: standard tool (ST); Bottom: modified tool (MT).

Table 4.3. Robot joint limits (in meters or radians)

	q_1 [rad]	q_2 [rad]	q_3 [m]	q_4 [rad]	q_5 [rad]	q_6 [rad]	q_7 [rad]
<i>Std.</i>	$\pm\pi/2$	$\pm\pi/3$	$[0, 1]$	$\pm 3/2\pi$	± 1.39	± 1.39	—
<i>Mod.</i>	$\pm\pi/2$	$\pm\pi/3$	$[0, 1]$	$\pm 3/2\pi$	± 1.39	± 1.39	± 1.4

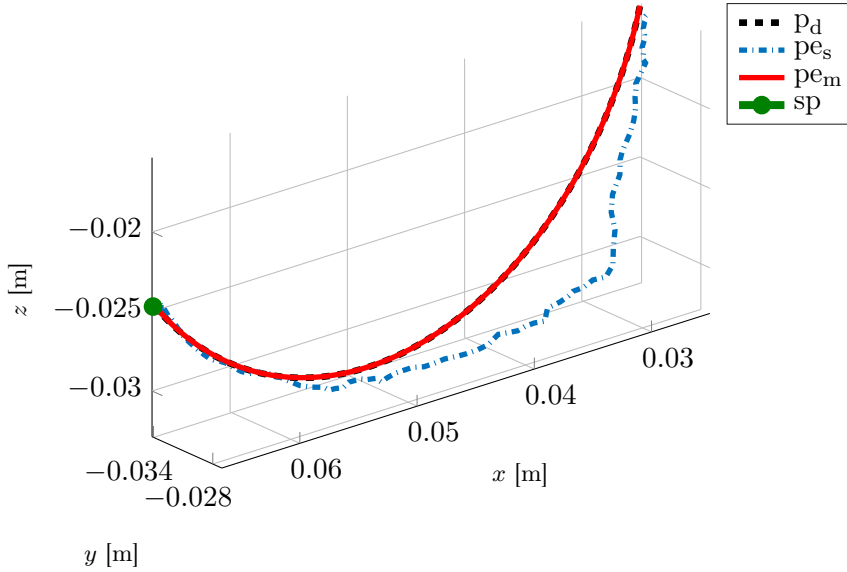


Figure 4.10. Needle tip paths. p_{e_s} is the path performed using the ST, p_d is the desired circular path and p_{e_m} is the path simulated using the MT. The point sp is the trajectory starting point.

The joint limits considered in the experiments are given in Table 4.3. A standard inverse kinematics algorithm has been implemented to solve for the da Vinci PSM joint values given the desired position and orientation of the needle frame [141]. Fig. 4.9 contains some snapshots from the real performed trajectory and the V-REP simulated environment.

The different behaviour of the two instruments can be better understood in Fig. 5.2 showing the needle tip path executed using the ST (p_{e_s}) and our MT (p_{e_m}), respectively. When the ST is used, due to the presence of the joint limits, the desired path cannot be successfully executed, as shown in Fig. 5.2 (dot dashed blue line). It can be observed that only in the first part of the commanded trajectory, before the joint limits occurrence, the path of the needle’s tip has a circular shape; when the joint limits occur, the corresponding joint variables saturate and the actual path

significantly deviates from the desired circular path. The desired circular trajectory, extrapolated using the part of the real trajectory not influenced by joint saturations, is depicted using dotted black line. This trajectory was commanded in simulation to the PSM arm with our MT. Since now the system is redundant, infinite solutions exist for the inverse kinematics problem and the redundancy could be used to efficiently avoid joint limits. In our problem, we do not explicitly exploit the redundancy; instead, we just want to show that a feasible solution could be easily found by a surgeon teleoperating the instrument. Therefore a simple solution corresponding to the minimum norm velocity is computed by using the Jacobian pseudo-inverse; despite this, the joint limits are not violated and the desired path for the needle is respected as shown in Fig. 5.2 (red continuous line). Quantitative results of the experiment are shown in Fig. 4.11. In particular, the figure shows the time histories of the joint variables \mathbf{q} using both the ST and the MT where the dashed lines represent the time history of the seventh joint, active only in the MT, and the dot-and-dash lines represent the time history of the sixth joint, which reaches its upper limit in the ST. It is clear that, with our MT, the redundancy allows to avoid the joint limits. This is quantitatively explained by considering the weighted dexterity index, better described in Appendix, which allows evaluating the manipulator's overall ability to move, by tacking into account the distance from both joint limits and singularities. This index has been chosen because it allows comparing the dexterity of manipulators with the same task space dimension independently from the joint space dimension, thus it constitutes a suitable measure of the introduced enhancements. As it can be seen from Fig. 4.11, this measure remains greater than zero for the whole trajectory execution only when the MT is used.

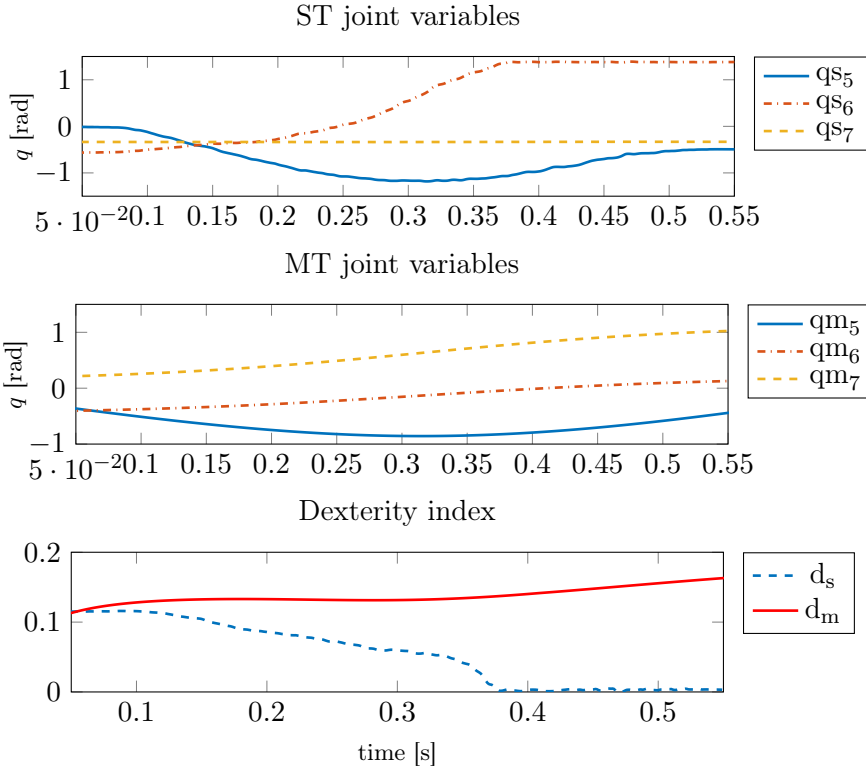


Figure 4.11. Numerical results for the single stitch trajectory. Top: time history of the joint variables for ST; Middle: time history of the joint variables for MT. Bottom: time history of the dexterity index with ST (d_s) and MT (d_m).

Second Case Study: Complete Suturing Procedures

In the second case study, the set of suturing procedures reported in Tab. 4.4 was recorded. The sutures have been executed by novice (N), intermediate (I) and expert (E) surgeons, using three types of needles. The procedures consist in 10 planar sutures with different wound angles, executed on two different types of phantoms, and 3 circular anastomosis on a vessel phantom. Each suture consists of 5 stitches. In the table, for

each suture, it is also indicated if a joint limit was reached at least once. The 13 suturing procedures have been monitored and, for each sequence of

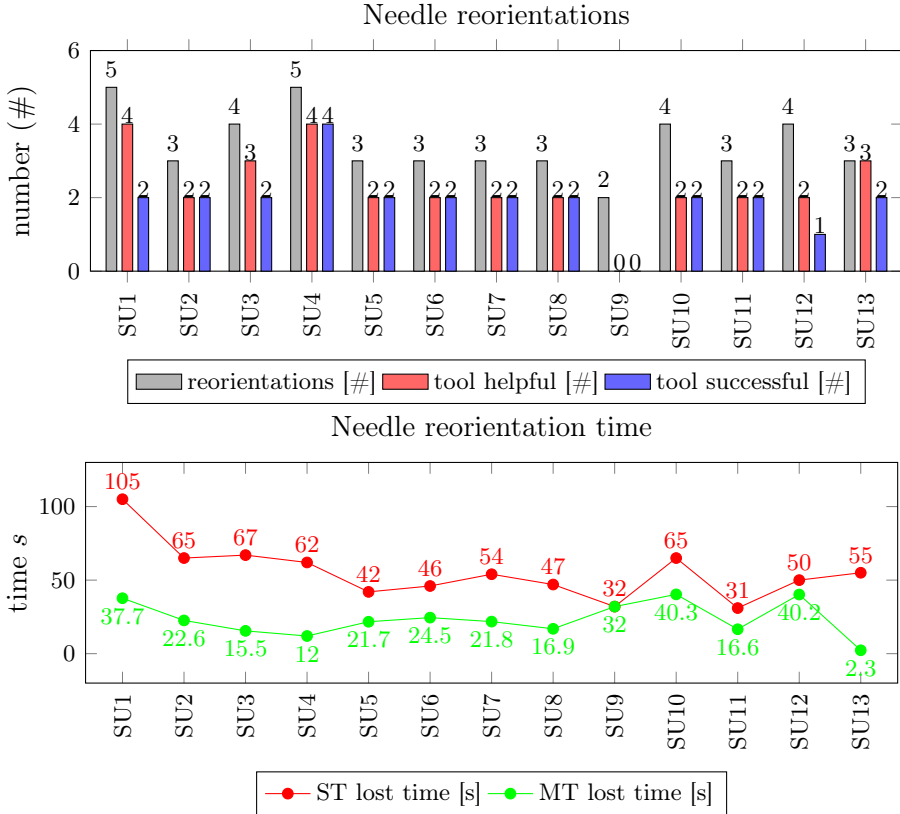


Figure 4.12. Collected data in 13 sutures (SU1, . . . , SU13) of 5 stitches. Top: Number of stitches requiring needle reorientation for each suture (gray bar), number of reorientations for which the MT would have been helpful (red bar), number of reorientations for which the MT would have been successful (blue bar). Bottom: Total time lost for reorienting the needle with the ST (red line) and with the MT (green line).

5 stitches, the following data have been evaluated and reported in Fig. 4.12 (Top):

- the number of stitches that required needle reorientation (gray bars);

- the number of reorientations performed along the needle tangent, for which the MT would have been helpful (red bars);
- the number of reorientations with rotation angles that were lower than the maximum rolling angles for the used needle (considering the values reported in Tab. 4.1), for which the MT would have been successful (blue bars).

The overall performance is summarized in Table 4.5. It can be seen that 69% of the stitches required reorientation and that the MT would be helpful in the 66% of the situations, allowing to complete the reorientation in the 55% of the cases.

To get a better understanding of the problems encountered during the suture performance we asked the surgeons to explain the reasons of each reorientation. In the 37.1% of the cases we found that the needle was dropped to move organs or to make knots and wasn't in the optimal orientation; in the 48.6% of the cases the needle was gripped in a bad orientation; finally, in the 14.3% of the cases, the needle lost the correct orientation during the stitch execution and needed to be reoriented.

Furthermore, for each suturing procedure, the total time lost in reorienting the needle was recorded. The results are reported in Fig. 4.12 (Bottom, red line). This time can be compared to the predicted reorientation time using the MT, reported in the same plot (green line). This latter has been computed as follows:

- for the reorientations that can be performed with the MT (i.e., those classified as successful and represented by the blue bars in Fig. 4.12), the execution time have been estimated considering a velocity of about 45deg/sec for the rolling degree of freedom of the tool;
- for all the other reorientations the same time measured during the execution of the real stitch with a standard tool has been considered.

Table 4.4. Suture procedures

	expertise	type	needle	joint limit
SU1	novice	planar vertical	GL-222	NO
SU2	novice	planar 15°	GL-222	YES
SU3	novice	planar 20°	RB-1	YES
SU4	novice	planar 110°	RB-1	NO
SU5	novice	planar 20°	RB-1	YES
SU6	intermediate	planar vertical	UR-6	NO
SU7	intermediate	planar vertical	UR-6	NO
SU8	intermediate	planar vertical	UR-6	NO
SU9	intermediate	planar vertical	UR-6	NO
SU10	intermediate	planar vertical	UR-6	NO
SU11	expert	circular vessel	UR-6	NO
SU12	expert	circular vessel	UR-6	NO
SU13	expert	circular vessel	UR-6	YES

Table 4.5. Overall performance of the MT

	stitches	reorient	help	success
#	65	45	30	25
		reorient/stitches	help/reorient	success/reorient
%		69%	66%	55%

The results show that the MT allows a significant reduction of the time spent for needle reorientation.

4.2 The MUSHA Underactuated Hand for MIRS

In this section, we show our last results in developing a new human-like laparoscopic robotic instrument aims to mimic the human hand. We call this new instrument MUSHA hand (MH). Besides humanoid robots and prosthetics applications, other areas such as the minimally invasive laparoscopic surgery could benefit by the use of suitably designed hands able to enter the patient's body through the trocar and to replace the hands of the surgeon by equaling dexterity and sensory ability at the same time. Due to the presence of multiple degrees of freedom (DoFs), a synergistic approach inspired by the human hand functioning can be adopted for design purposes. This kind of hand device will have a high number of degrees of freedom in order to allow complex and human-like motions but, at the same time, will be controlled with a lower number of signals, hence by means of few motors. This feature could be very useful to enhance the traction and counter-traction relationship during the dissection manoeuvre. Moreover, the grasp can be more efficient and less traumatic on the bowel during a colorectal procedure. In the same way, according to a multitasking concept, MH could be used as retractor of different organs (bowel, solid organ muscles, glands like the adrenal gland). For example, in a Hiatal Hernia Repair, MH could be useful as Hepatic Retractor, as well as can serve as an instrument passing under the esophagus during the peri-oesophageal fundoplication [97]. Moreover, the surgical hand could more than the actual forceps in the manoeuvre of rectal dissection from the prostate during robotic anterior resection [151]. Furthermore, due to the knowledge of the kinematic information, the hand can be used as a caliper, obtaining precisely the dimensions of wall defect during an abdominal wall reconstruction rather than to calculate the appropriate distance of bowel section from a tumour. In addition, thanks to the proposed fingertip force sensor, MH could be used for organ/tissues palpation to retrieve information about the organ consistency to discern, for example, between stools

and polyps in the bowel. Finally, it is conceivable the association of MH to bipolar energy or radiofrequency in order to gain an additional instrument for haemostasis, that could be very useful during bloody procedures like hepatic or partial kidney resections. Several works available in literature are dedicated at improving the dexterity of surgical tools and to provide forceps with force measurements. Most of them are devoted to surgical manipulators design. In [61] a new robotic system named "Hyper Finger" for minimally invasive surgery has been developed. The complete system provides multiple fingers as separated manipulators that enter in the abdomen through different ports. Each finger has 9 DoFs and has a diameter of 10 mm. In [18] a telesurgical system with millimeter-scale robotic manipulators is introduced. In [88] Seven different minimally invasive surgical tasks from 30 surgeons are acquired to design a kinematic optimization of a 7-DoFs cable-actuated spherical surgical robotic manipulator. In [153] Starting from a survey conducted among surgeons regarding their opinions on surgical training and surgical systems, a three-fingered surgical hand with shape memory alloy (SMA) helix actuators has been realized with a diameter of 18 mm and controlled using an exoskeleton as a master manipulator. In this way, the motion mapping from the surgeon's hand is simple and intuitive. In [89] a 10-DOF robotic metamorphic instrumental hand has been developed for MIS and controlled with a master glove. The hand can be inserted into the patient abdomen cavity through a port with a diameter of 24 mm. With respect to the cited surgical hands, the MUSHA hand has an innovative design that allows a diameter of 15 mm. The kinematics has 11 DoFs with an underactuated solution that maximize dexterity and grasp stability and at the same time reduce the complexity of the actuation system.

4.2.1 The MUSHA Prototype

In this section the design choices and the first prototype are shown.

Requirements and Design Choice

The design requirements have been identified in collaboration with the surgeons and taking into account the constraints due to the da Vinci configuration for the tools.

- To comply with the task requirements the tools should have a high number of degrees of freedom in order to allow complex and human-like motions.
- The need of a unified instrument that would allow simultaneous tissue traction and manipulation and could act as a retractor to gently manipulate organs, such as the bowel, has been considered.
- The instrument should provide the ability to perform both fine (needle and thread grasp) and power grasp (even for considerably large anatomical parts).
- The capability to perform dexterous movements while in contact with the tissue (e.g. torsion or rolling) would contribute to the diagnosis phase.
- The presented hand has been designed to be an instrument of the da Vinci robotic platform, hence, the robotic hand requires to pass through the trocar and has a restriction on the maximum number of actuators.

According to the requirements we choose the hand dimension reported in Fig. 4.15. In Fig. 4.14 are also reported the three versions of the MUSHA hand to find in the version V3 the optimal solution. In this first prototype the instrument diameter is of 15mm that is still not adequate for the daVinci robot where the trocar is of 13mm. The phalanges length has been chosen according to existing tools like the Storz retractor. In order to switch among different hand configuration: power grasp, fine grasp,

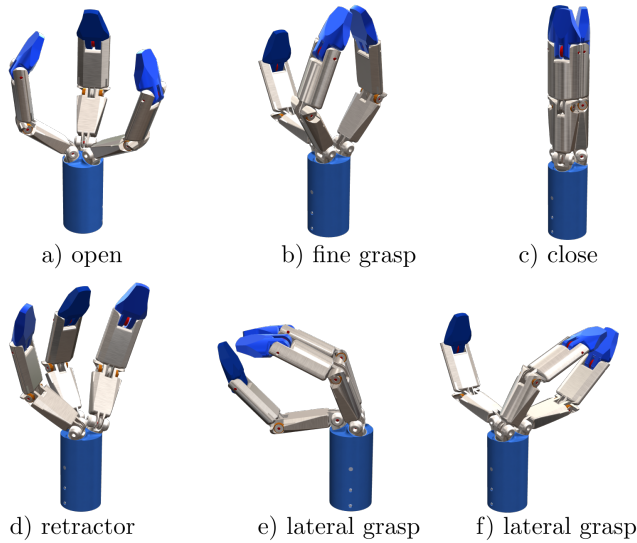


Figure 4.13. The hand configurations.

retractor (see Fig. 4.13), the mechanism is composed by two shafts, linked at the base of the index and medial phalanges, free to rotate due to the presence of a couple of bearings. The two joints axes are designed to form 20deg with respect to the central axis of the instrument. Two conical gears are linked to each shaft to guarantees an opposite and coupled motion. Moreover, another conical gears was linked to the instrument shaft with its axis orthogonal to the instrument axis and was designed to perfectly engage with the other two conical bearings. Finally, this last conical bearing was actuated by a couple of tendon in antagonistic configuration. This solution allows to rotate and at the same time turn away the medial and index fingers tip in order to obtain the retractor configuration as reported in Fig. 4.13(d).

Based on the requirements we develop a conceptual CAD design solution for the MUSHA hand. The tendon configuration reported in Fig. 4.15left was considered. More in detail, in each finger, the proximal fin-

ger is actuated by a couple of tendons in an antagonistic configuration; the medial finger rotation is obtained by a single tendon resorting to two springs to obtain the antagonistic motion. Moreover, the medial and the distal fingers are coupled using a couple of tendon linked to the distal finger pulley in an antagonistic way and crossed. The described mechanism permits the rotation of the distal finger coupled with the rotation of the medial finger and scaled of a value equal to the pulleys ratio, about 70% to implementing the human inspired ratio between the medial and distal phalanges.

Hence for each finger we have one actuation in antagonistic configuration composed by two tendons (green in fig. 4.15left) and a single tendon to move the coupled medial and distal fingers (purple in Fig. 4.15left). Additionally, two other tendons, in antagonistic configuration are used to actuate the reconfiguration mechanism.

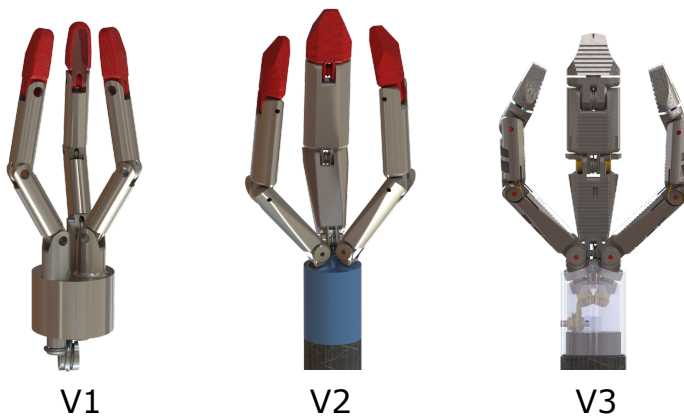


Figure 4.14. MUSHA versions.

3D Printed in Scale Prototype

In Figs. 4.15 and 4.16 the prototype in scale used for the first experiment is shown. More in detail, it is composed by a box containing the

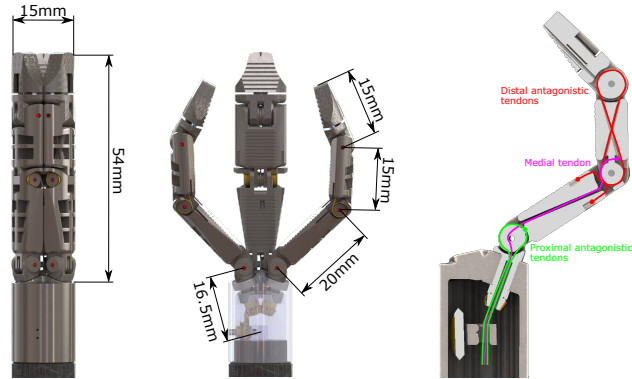


Figure 4.15. The hand prototype and the tendon configuration.

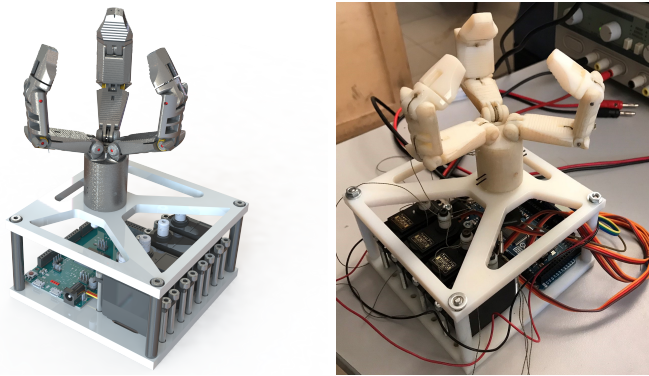


Figure 4.16. The hand with the motors box

motors, control and actuation electronic boards. The 2 : 1 scaled hand has been printed in plastic using the polyjet process³. For the actuation 4 servomotor Tower Pro MG995 are chosen considering the torque (1.1)Nm that they are able to produce. We found that a torque of 1Nm on all joints is enough to move the hand and to guarantees a maximum force on each distal phalanges of about 5N in the worst case. The motors are controlled using Arduino DUE micro-controller. A Matlab software has

³<http://www.stratasys.com/3d-printers/design-series/objet24>

been developed to implement all the algorithms described in Sect. 4.2.2.

4.2.2 Analysis of Different Kinematic Solutions

For guaranteeing human-inspired manipulation capabilities the robotic hand should have a number of DoFs comparable to that of the human hand. However, neuroscientific studies have demonstrated that, in the human hand, joint angles do not vary independently: for a given task, the hand posture is regulated by few postural synergies [129]. Principal components analysis showed that the first two components account for $> 80\%$ of the variance for grasping tasks. This permits to substantially reduce the complexity of the grasp synthesis and control. In our work, taking inspiration from this paradigm, we choose to develop a three fingered 11-DoFs mechanism actuated by four motors. This choice allows to keep human like dexterity in the mechanism while complying with the restrictions introduced by underactuation, like in the da Vinci Research Kit instrument interface. In this section we analyze three possible solutions involving different joint couplings (in the following we refer to this as mechanical synergies).

Underactuation can be mathematically described by the mechanical synergies matrix S that relates motor velocities vector $\dot{\mathbf{z}} = [\dot{z}_1, \dot{z}_2, \dots, \dot{z}_{n_z}]$ and joint velocities vector $\dot{\mathbf{q}} = [\dot{q}_1, \dot{q}_2, \dots, \dot{q}_{n_q}]$ usually in a linear fashion: $\dot{\mathbf{q}} = S\dot{\mathbf{z}}$, with n_z and n_q being the number of actuators and the number of joints, respectively. In the following we consider the vector \mathbf{q} composed of joint variables of the thumb, index and middle ordered from metacarpal to distal joints. That being said, in order to establish which mechanical constraints in motion transmission system gives the overall best performance for all the given task requirements we analysed and compared different solutions. Three S matrices are shown below that realize different joint

couplings:

$$S_1 = \begin{bmatrix} \mathbf{a} & \mathbf{0} & \mathbf{0} & \mathbf{b} \\ 0 & 0 & 0 & 0 \\ \mathbf{0} & \mathbf{a} & \mathbf{0} & \mathbf{b} \\ 0 & 0 & 0 & 0 \\ \mathbf{0} & \mathbf{0} & \mathbf{a} & \mathbf{b} \end{bmatrix} \quad S_2 = \begin{bmatrix} \mathbf{a} & \mathbf{0} & \mathbf{b} & \mathbf{0} \\ 0 & 0 & 0 & 0 \\ \mathbf{0} & \mathbf{a} & \mathbf{0} & \mathbf{b} \\ 0 & 0 & 0 & 0 \\ \mathbf{0} & \mathbf{a} & \mathbf{0} & \mathbf{b} \end{bmatrix} \quad S_3 = \begin{bmatrix} 1.0 & 0 & 0 & 0 \\ \mathbf{0} & \mathbf{a} & \mathbf{0} & \mathbf{b} \\ 0 & 0 & 0 & 0 \\ \mathbf{0} & \mathbf{0} & \mathbf{a} & \mathbf{b} \\ 0 & 0 & 0 & 0 \\ \mathbf{0} & \mathbf{0} & \mathbf{a} & \mathbf{b} \end{bmatrix} \quad (4.10)$$

where, $\mathbf{a} = [1.00, -0.30, -0.21]^T$, $\mathbf{b} = [0, 1.00, 0.70]^T$ and $\mathbf{0} = [0, 0, 0]^T$.

As it can be noticed S_1 matrix implements a solution in which all the metacarpal joints are uncoupled while all the other DoFs are coupled with human-like joint proportions [111]. Conversely, the S_2 matrix represents a solution in which the thumb joints are completely uncoupled from other fingers. The S_3 matrix is similar to S_1 but with the metacarpal joints of index and middle fingers coupled. Thus, there is one unused motor, therefore the matrix presents an additional row corresponding to a q_0 DoF that accounts for the presence of a wrist mechanism located at the base of the hand.

The mathematical model of the hand-object system constrained in a grasp configuration helps analysing the capabilities embodied in the mechanism. Following the approach in [122], we seek to analyse the controllable internal forces, rigid-body object motion and potential hand redundant motions. It is possible to show that the following relations between object displacements Δu , contact forces $\Delta \lambda$ and synergies actuation Δz hold

$$\Delta u = (GKG^T)^{-1} GKJS\Delta z = V\Delta z \quad (4.11)$$

and

$$\Delta \lambda = \left(I - G_K^\dagger G \right) KJS\Delta z = P\Delta z \quad (4.12)$$

where G is the grasp matrix, G_K^\dagger is the weighted right pseudoinverse of G , K is the symmetric and positive definite matrix of the equivalent stiffness at the contact, J is the block diagonal Jacobian matrix, S the mechanical

synergies matrix. For more details on the derivation of grasp and Jacobian matrices the reader can refer to [123]. For simplicity, the expressions of matrices P , V , and K summarized here are those obtained by neglecting the so-called geometric effects, arising from the linearization, and depending on J matrix variability with respect to hand and object configuration. The set of controllable active internal forces $\Delta\lambda$ can be, thus, expressed as

$$\Delta\lambda = E_s\alpha \quad (4.13)$$

where

$$\mathcal{R}(E_s) = \mathcal{R}\left(\left(I - G_K^\dagger G\right) KJSY\right) \quad (4.14)$$

and $\alpha \in \mathbb{R}^e$ is a vector parameterizing the solution. An optimal choice $\hat{\alpha}$ can be derived by means of suitable cost functions and optimization routines.

Complementary, the set of rigid-body motions that do not involve deformations in the contact points and that are controllable activating synergies can be derived imposing $\Delta\lambda = 0$ in the object equilibrium equation [122], $w + G\lambda = 0$, where w is the load on the object. The rigid-body motion can be thus obtained computing $\mathcal{N}([JS - G^T])$.

We can then define a matrix Γ , whose columns form a basis of such subspace. Under the hypothesis that the object motion is not indeterminate neither redundant, Γ can be expressed as

$$\Gamma = \mathcal{N}[JS - G^T] = \begin{bmatrix} \Gamma_{zcs} \\ \Gamma_{ucs} \end{bmatrix} \quad (4.15)$$

where the image space of Γ_{zcs} and Γ_{ucs} consist of coordinated rigid-body motions of the hand and the object position and orientation, respectively. It is easy to show that

$$\mathcal{R}(\Gamma_{ucs}) \subseteq \mathcal{R}\left(\left(GKG^T\right)^{-1} GKJSY\right), \quad (4.16)$$

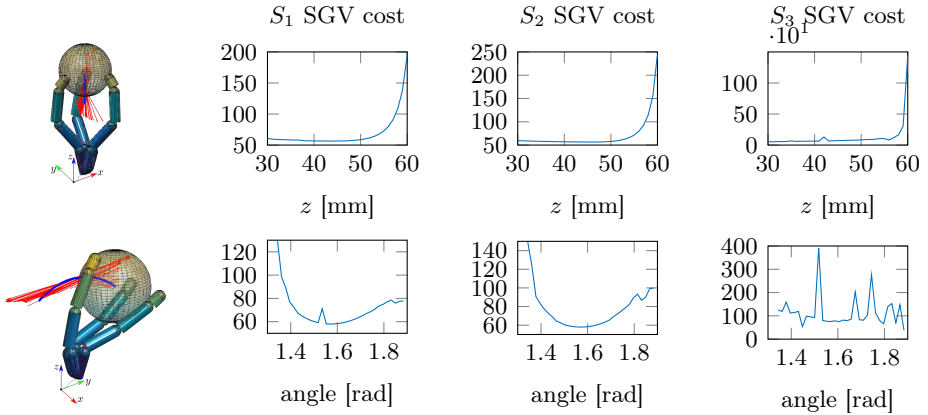


Figure 4.17. Principal direction of motion are represented on the left images along the two grasp paths, on the top the path along z and on the bottom the path in the $y - z$ plain. SGV cost variations along the paths are represented.

i.e. rigid body motions of the objects are a subset of all synergy-controlled object motion that also contains also motions due to elastic deformation.

Kinematic Evaluation

In this section, we present a comparison that aims at evaluating the hand grasping and manipulation capabilities, in terms of optimized forces and allowed movements of the three different solutions. First we evaluate the force-closure cost function [47]), computed using Syngrasp toolbox [92], for a given set of object poses along trajectories planned in the reachable workspace of the three kinematics solutions. It is worth to recall that the minimum of the cost represent the best grasp feasible with the given set of synergies. Two trajectories of object poses have been considered: one along z direction, and one along a circumference arc in the $y - z$ plane (see Fig.4.17, where in the left image the reference frame is represented). The path along z starts at $z_i = 30$ mm and ends at $z_f = 40$ mm measured

in the palm reference frame, while the path in the $y - z$ plain is an arc of radius $r = 45$ mm and $\theta_i = 77^\circ$, $\theta_f = 108^\circ$. The results are shown in Fig. 4.17. The force closure cost function has been computed assuming a friction coefficient $\mu = 0.5$, a minimum value of the normal force $\lambda_{min} = 0.1$ N and a maximum value $\lambda_{max} = 5$ N, and an external load on the object $w = [0, 0, 1, 0, 0, 0]$. The S_1 kinematic solution has smaller costs with respect to the other solutions in both the planned paths. Figure 4.17 also contains an example of the principal direction of motion of the object in Cartesian space calculated according to Eq. (4.16) for the S_1 (top) and S_2 (bottom) hands. We have found that the column space of Γ in Eq. (4.16) has $\dim=1$ for the hand having S_1 couplings and $\dim=2$ for the hand having S_2 and S_3 couplings. This means that the hand S_1 can realize one object movement along z axis, S_2 can move the object in the plane $y - z$, while S_3 in the plane $x - z$ due to the presence of the wrist. This means that S_2 and S_3 presents better manipulability with respect to the solution S_1 .

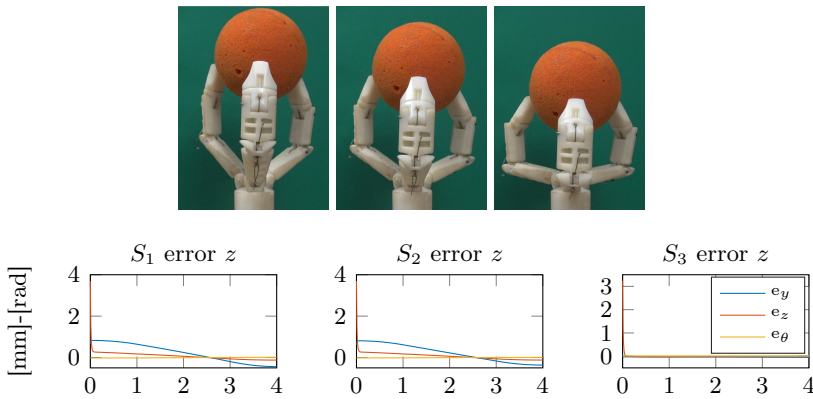


Figure 4.18. Object errors in the Cartesian space for S_1 and S_2 and S_3 in a vertical motion (along z) is represented. The top pictures are taken from real experiments performed on the prototype implementing S_1 coupling matrix.

Anyway, these presented here are theoretical results that are valid when

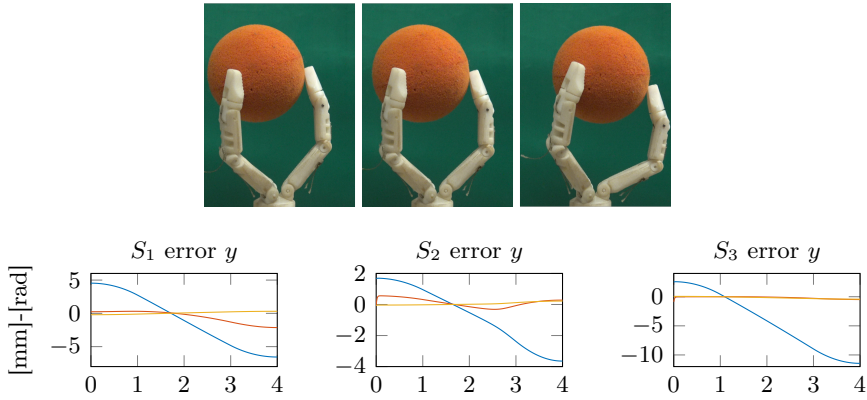


Figure 4.19. Object errors in the Cartesian space for S_1 and S_2 and S_3 in a horizontal motion (along y) is represented. The top pictures are taken from real experiments performed on the prototype implementing S_1 coupling matrix.

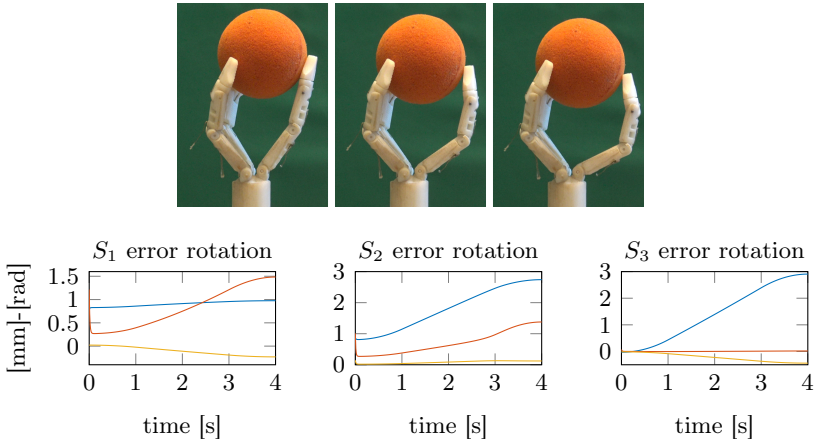


Figure 4.20. Object errors in the Cartesian space for S_1 and S_2 and S_3 in a rotational motion (in the $y - z$ plane) is represented. The top pictures are taken from real experiments performed on the prototype implementing S_1 coupling matrix.

the contact force do not vary. However, some trajectories of the object in Cartesian space can still be accomplished if we remove this hypothe-

sis. Thus, we performed a second set of experiments for evaluating the Cartesian space error introduced by the kinematic couplings along a given desired trajectory of the object. Three trajectories have been considered: pure translation along z axis, pure translation along y axis and pure rotation around x axis centered in the object. This have been chosen by looking at the potential tasks to be performed by the hand. Figure 5.2 contains the error with respect to the desired trajectory. The error given by the approximation in the inverse kinematic due to the underactuation. In these experiments we suppose that the motion implying rolling is small enough so as the contact points do not change over time in the object reference frame. The rotation error has been calculated as the angle, around x axis, between the plane containing the fingertips and a fixed horizontal plane. The z trajectory starts at $z_i = 40$ mm and ends at $z_f = 20$ mm, The y trajectory starts at $y_i = -5$ mm and ends at $y_f = 20$ mm measured in the palm reference frame, while the rotation os of $\theta = -25^\circ$ evaluated in the object reference frame. The graphs show that only the z trajectory is performed with a small tracking error since the desired path is planned in the hand workspace, therefore the inverse kinematics, obtained using the transpose Jacobian, provide a solution with a small error. Overall we can say that the rotational trajectory is better tracked by S_1 at the cost of higher errors on the other two axis. S_2 has the overall minimum error norm. The y trajectory is better performed by S_2 , while the z trajectory is better tracked by S_3 . As a final report we can say that S_1 solution is better to stably grasp objects while S_2 presents better performance in moving the objects, but still presents SGV costs comparable with the S_1 solution. According to these preliminary results the solution S_2 is preferable.

4.2.3 Comparison with a standard laparoscopic instrument in a simulated environment

In this section, we present a comparison that aims at evaluating MH potential with respect to classical tools in selected tasks performed during adrenalectomy and colectomy procedures. The simulated tasks are organs mobilization, grasping, and measurements of critical dimensions of affected organs. Since the MH is still a prototype, not ready to be used in surgical environments, the evaluation of the concept is obtained by moving our tool in a simulated environment qualitatively replicating the standard laparoscopic tool task execution in a real environment. Figure 4.21 presents the simulation environment. The dVRK and MH simulator is realized using V-REP [42]. The choice is motivated by the versatility and simplicity of this software for multi-robot applications. In our experimental setup, we

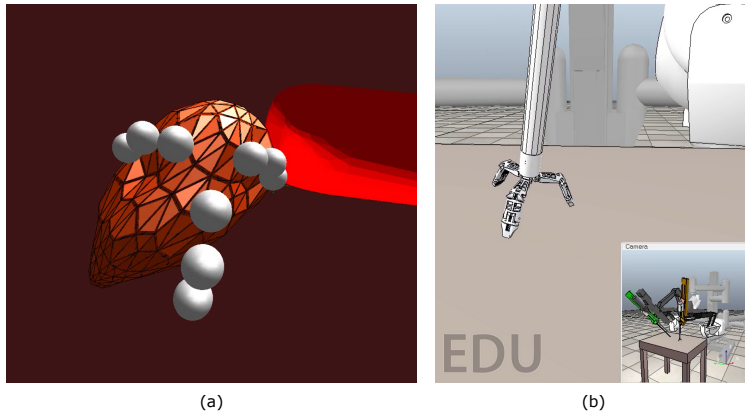


Figure 4.21. Simulation environment of the MH mounted on the daVinci robot.

use bullet physics engine to simulate the interaction between the MUSHA hand and a soft organ. The soft organ is simulated using a soft triangular mesh shape with elastic properties [35]. The organ has been anchored to the rigid scene in different points to simulate the interaction between the

organ and the abdominal surfaces. The MUSHA hand has been realized using three spheres for each finger in order to simulate the hand phalanges. We have linked the bullet simulated scene to our VREP simulator through remote API functions to have at each time step the position of each hand phalanges w.r.t. the robot Remote Center of Motion (RCM).

In Fig. 4.22, MH is used in retractor configuration to lift and mobilize organs to facilitate surgical intervention. This can be the case of the adrenal gland during adrenalectomy procedure. The advantage of MH is to provide an extended contact area, force distribution and thus more gentle and effective manoeuvres.

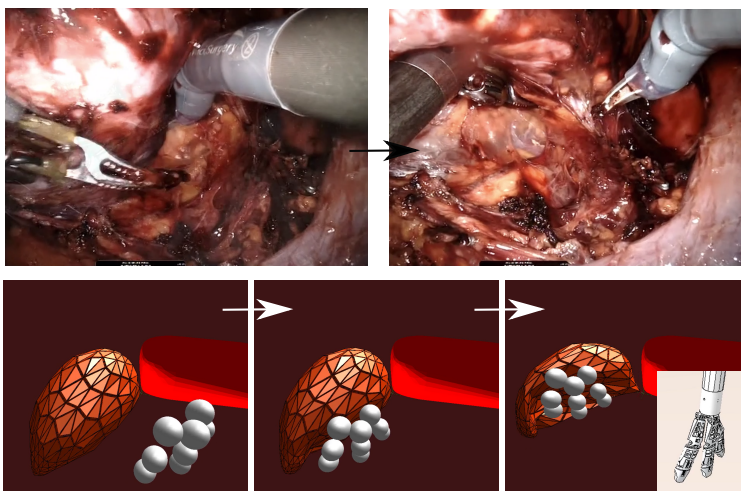


Figure 4.22. Retractor simulation. Top: real surgical procedure, Bottom: simulated environment.

In Fig. 4.23, MH is used as grasper to grab organs or tissues. The presence of articulations and of three fingers endowed with force sensors allows grasping with increased flexibility with respect to different organ/tissues dimensions and locations, and with increased stability while reducing the stress and damages of the affected organs.

Figure 4.24 shows the potential of MH has caliper by exploiting its

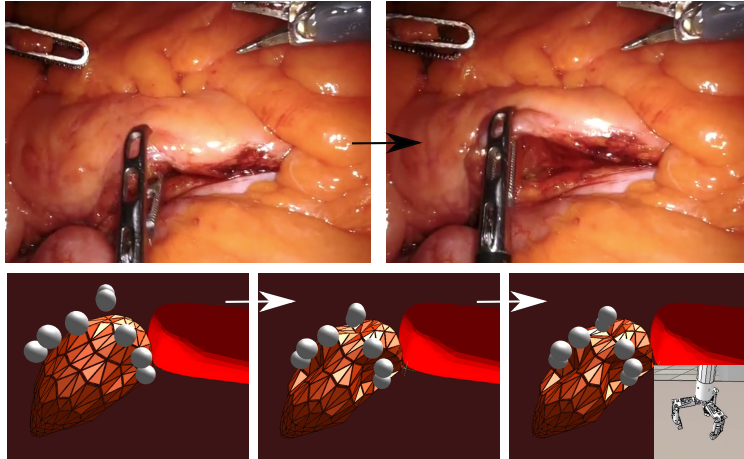


Figure 4.23. Grasp simulation. Top: real surgical procedure, Bottom: simulated environment.

kinematics. What represents an added value is that all these skills can be incorporated into one instrument: the MUSHA Hand. Changes of instruments during the intervention leads to time loss, distraction and stress for the surgeon and greater risk of infection for the patient.



Figure 4.24. Caliper simulation. The hand direct kinematics can be used to estimate organs or tissues critical dimensions.

4.3 Conclusions

In this chapter, two new surgical instruments enabling advanced in-hand capabilities have been proposed. In detail, we show:

- A new design concept for a laparoscopic needle driver with in-hand rolling capabilities. The new patent-pending mechanism allows rotating the surgical needle in-hand to find its optimal orientation. This approach promise to reduce the tedious hand-off movements required during surgical suturing procedures.
- A new miniaturised and under-actuated 3 fingered hand for laparoscopy. Our design aims to radically change the standard laparoscopic surgery philosophy by finding a perfect trade-off between the standard instruments and hand-assisted surgical techniques.

In both the cases we propose experiments with real 3D printed prototypes, in simulation and user studies to evaluate the effectiveness of the proposed design. The goal of this research activity was the development of high dexterous instruments with the aim to improve the surgical procedure

already possible in MIRS and also to enable the execution of other procedures which can not be performed yet. Therefore, we prove that our smart suturing instrument can improve the suturing procedure by reducing time spent and risks due to the occurrence of joints limits. On the other hand, the MUSHHA hand represent a new device enabling new possibilities and also a better control of the surgical environment. Moreover, with respect to existing devices, the provided underactuation and the mechanism miniaturization allows a better and simpler integration in the surgical robotic systems. Finally, the new presented reconfiguration mechanism enables the use of the MUSHHA hand in different modalities and scenarios and represent the first step for the development of multi-purpose instruments for MIRS.

Chapter 5

Physical-Mental Workload Reduction Through Shared Control Strategies

As discussed in Chapter 1.4, a better comfort for the surgeon can be also translated in a reduction of the physical and mental workload. This can be obtained by using new devices or sensor to give better environment's awareness and better control (See. Sec 3 and 4) but can be also obtained by reducing the number of DoFs directly under the surgeon control. This means providing the robot with more autonomy to reduce de surgeon fatigue and stress in some surgical tasks. For instance, repetitive and tiring task that usually increases the operation time, costs and complications risks, e.g. suturing or dissection, can benefit in the introduction of more degree of robot autonomy.

In [162] the future trends in assistive and autonomous robotic surgery are discussed, identifying six level of autonomy for medical robotics:

- *level 0*: no autonomy

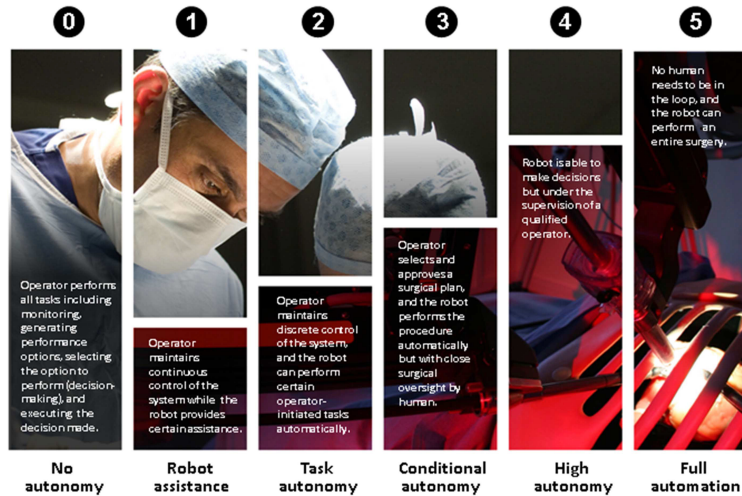


Figure 5.1. Six levels of autonomy in surgical robotics. Curtsey of [162].

- *level 1*: robot assistance
- *level 2*: task autonomy
- *level 3*: conditional autonomy
- *level 4*: high autonomy
- *level 5*: full automation

The current paradigm of robot-assisted surgeries (RASs) depends entirely on an individual surgeon’s manual capability. In this sense, we can suppose the standard telemanipulated systems can be identified between *level 0* and *level 1* because of some small assistance such as scaling and tremor filtering. On the other hand, autonomous/assisted robotic surgery promises enhanced efficacy, safety, and improved access to optimized surgical techniques. In [98] a review of the state of the art regarding the autonomous systems and algorithm for MIRS is presented. Many works can be found that use surgical laparoscopic robotic systems, such as da Vinci research

kit or the Reven robot. Furthermore in [101] a Learning by observation approach was used to define a Finite State Machine (FSM) that model some surgical sub-task. In [81] a vision-guided robotic system based on a Kuka lightweight robot equipped with a laparoscopic actuated tool is used to implement autonomous suturing task. More in detail, in this case, some markers, and in particular Near-infrared Fluorescent (NIRF) markers are used to define the suturing points on the tissues. Recent works are based on the shared-supervised-assisted control in which the robot can perform some task autonomously with the supervision of the surgeon in using telemanipulation and vice-versa. In [139] a teleoperated architecture for MIRS is proposed. In detail, a supervised agent is developed in order to autonomously perform or assist the surgeon with surgical sub-tasks. Furthermore, in [65] an automated surgical assistant is presented in particular focusing on the problem of the tissue retraction (an outer covering of tissue that is pulled away to expose an area of interest) using a FEM model of the tissues. In [106] a framework for the multilateral shared control is presented focusing on five possible type of collaboration model.

Special attention is reserved in the literature on the introduction of some degree of autonomy in the suturing procedure. Suturing is one of the most challenging problems in MIRS because of the high dexterity and mental attention required by the surgeon. In addition to the reference mentioned above, some other works regarding the autonomous and semi-autonomous suturing in MIRS are reported. In [102] the problem of the stitching task in laparoscopic surgery using a circular needle and a conventional 4 DOFs needle-holder is addressed. In particular, the paper provides a good view on the suturing problem in the robotic point of view and focuses on the principal steps needed to perform this task. In the following works assisted suturing procedure were performed using Virtual fixtures in order to constrain the surgeon motion along a specific path. In [67, 23] virtual fixtures are used to perform a collaborative suturing

procedure. The surgeon is guided through a specific path using the haptic interface to follow a specific trajectory for the needle and for the knot tying. Some other works in literature are on the completely autonomous suturing task execution, e.g. in [62] a single camera is used in combination with an elliptical pose measurement algorithm to find the needle, while simple markers are used to find the suturing points. A framework to optimize the needle trajectory for a multilateral suturing procedure using convex programming is presented in [136] using Da Vinci research kit system. The problem of the force interaction modelling between the needle and the tissues during suturing are investigated in [63] in order to obtain an autonomous path planner [64] for suturing that attempts to minimize the interaction forces between the tissue and the needle. Finally, in [137] a demonstration of in vivo supervised autonomous soft tissue surgery in an open surgical setting is evaluated using near-infrared fluorescent (NIRF) imaging system. An autonomous suturing algorithm is developed inspired by the best human surgical practices: a computer program generates a plan to complete complex surgical tasks on deformable soft tissue, such as suturing and intestinal anastomosis are developed.

In this Chapter, we aim to discuss about some methods and control strategies to help the surgeon in reducing his/her mental and physical workload. The described strategies can be identified in the first three level of autonomy (*no autonomy, robot assistance, task autonomy*). Two different case studies will be evaluated: assisted dissection and assisted suturing. The problem will be analysed from different points of view. We'll start discussing some results to give a better contextual knowledge of the environment to the robot during the suturing procedure in Sec. 5.2. In Sec. 5.3 we'll evaluate a surgeon-in-the-loop approach for surgical suturing. Finally, in Sec. 5.4 we will investigate a virtual fixtures adaptation method for dissection which will also be an opportunity to talk about robot stability (see Sec. 5.1.2).

5.1 Preliminaries: Master Robot Compliance

A common practice in robotic teleoperation is to have an admittance/impedance controlled master robot and a position/velocity controlled slave robot. This allows a precise motion of the slave robot and a full control on the master to implement advanced control strategies for HRI. However, changing the dynamic parameters to adapt the robot behaviour to the user or environment change can cause instability problem. In this section we discuss about master robot impedance control and about problems may occur such as external force estimation and the passivization to preserve the system stability.

5.1.1 Master Impedance Control

Considering a n degree-of-freedom (DoF) manipulator and defining a task space vector $\mathbf{x} \in \mathbb{R}^r$, with $r \leq n$, the following impedance dynamics can be achieved through control

$$\mathbf{M}\ddot{\tilde{\mathbf{x}}} + \mathbf{D}\dot{\tilde{\mathbf{x}}} = \mathbf{f}_h + \mathbf{f}_{\text{vf}}(\cdot), \quad (5.1)$$

where $\tilde{\mathbf{x}} = \mathbf{x}_d - \mathbf{x}$, with \mathbf{x}_d being the desired value for the robot task space variable, $\mathbf{M} \in \mathbb{R}^{r \times r}$ and $\mathbf{D} \in \mathbb{R}^{r \times r}$ are inertia and damping matrices respectively, usually designed to be fixed, diagonal and positive definite, $\mathbf{f}_h \in \mathbb{R}^r$ is the vector of the external forces applied by an interacting user and $\mathbf{f}_{\text{vf}}(\cdot)$ is the additional force due to the possible presence of VFs. The above dynamics can be obtained by setting the torque control input $\boldsymbol{\tau} \in \mathbb{R}^n$ of the master robot as (see [141] for more details)

$$\boldsymbol{\tau} = \mathbf{B}(\mathbf{q})\mathbf{v} + \mathbf{N}(\mathbf{q}, \dot{\mathbf{q}}) + \mathbf{J}^T(\mathbf{q})\mathbf{f}_h \quad (5.2)$$

$$\mathbf{v} = \mathbf{J}_A^{-1}(\mathbf{q})\mathbf{M}^{-1}(\mathbf{M}\ddot{\mathbf{x}}_d + \mathbf{D}\dot{\tilde{\mathbf{x}}} - \mathbf{M}\dot{\mathbf{J}}_A(\mathbf{q}, \dot{\mathbf{q}})\dot{\mathbf{q}} - \mathbf{f}_{h,A}), \quad (5.3)$$

where $\mathbf{B}(\mathbf{q}) \in \mathbb{R}^{n \times n}$ is the joint space inertia matrix, $\mathbf{J}(\mathbf{q})$, $\mathbf{J}_A(\mathbf{q}) \in \mathbb{R}^{r \times n}$ are the geometric and the analytical Jacobians, respectively, and

$$\mathbf{N}(\mathbf{q}, \dot{\mathbf{q}}) = \mathbf{C}(\mathbf{q}, \dot{\mathbf{q}})\dot{\mathbf{q}} + \mathbf{g}(\mathbf{q}) + \mathbf{h}(\mathbf{q}, \dot{\mathbf{q}}) \quad (5.4)$$

accounts for Coriolis and centrifugal contributions ($\mathbf{C}(\mathbf{q}, \dot{\mathbf{q}})\dot{\mathbf{q}}$), gravity ($\mathbf{g}(\mathbf{q})$), friction and other disturbance torques ($\mathbf{h}(\mathbf{q}, \dot{\mathbf{q}})$). Notice that the term $\mathbf{f}_{h,A}$ differs from \mathbf{f}_h by a mapping, depending on the orientation representation.

Master External force estimation

Equation (5.2) requires the measurement of the external forces \mathbf{f}_h . When they are not directly measurable, force estimation could be performed by resorting to a nonlinear dynamic observer presented in Sec. 3.1 (Eq. 3.1, 3.2, 3.4) using the MTM dynamic model discussed in Sec. 2.

5.1.2 Master Robot Passivity

We now proceed analysing the system passivity of a robot when subject to stiffness variations. This aspect is very important when assistive controllers are applied to the robot because the modulation of the assistance, e.g. virtual fixtures, is usually obtained by a modulation of the system stiffness (see Sec.5.4). The results presented in this section have been discussed in [135].

The following definition of passivity is used

Definition 1 *A system with state space model $\dot{\mathbf{x}} = f(\mathbf{x}, \mathbf{u}) \in \mathbb{R}^q$, with initial state $\mathbf{x}(0) = \mathbf{x}_0 \in \mathbb{R}^q$, input vector $\mathbf{u} \in \mathbb{R}^l$ and output $\mathbf{y} = h(\mathbf{x}, \mathbf{u})$ is said to be passive if there exists a positive semidefnite function $\mathcal{S} : \mathbb{R}^q \rightarrow$*

\mathbb{R}_+ , called storage function, such that

$$\mathcal{S}(\mathbf{x}(T)) - \mathcal{S}(\mathbf{x}_0) \leq \int_0^T \mathbf{y}^\top(t) \mathbf{u}(t) dt \quad (5.5)$$

for all input signals $\mathbf{u} : [0, T] \rightarrow \mathbb{R}^l$, initial states $\mathbf{x}_0 \in \mathbb{R}^q$ and $T > 0$. Thus, proving passivity is equivalent to finding an appropriate storage function $\mathcal{S}(\mathbf{x})$ such that

$$\dot{\mathcal{S}} \leq \mathbf{y}^\top \mathbf{u} \quad \forall(\mathbf{x}, \mathbf{u}). \quad (5.6)$$

It can be easily noted that the model in (5.39) is not guaranteed to be passive w.r.t. the input-output pair $(\mathbf{f}_h, \dot{\tilde{\mathbf{x}}})$ if we consider as storage function the system energy

$$H(\tilde{\mathbf{x}}, \dot{\tilde{\mathbf{x}}}) = \frac{1}{2} \dot{\tilde{\mathbf{x}}}^\top \mathbf{M} \dot{\tilde{\mathbf{x}}} + \frac{1}{2} \tilde{\mathbf{x}}^\top \mathbf{K}_{\text{vf}} \tilde{\mathbf{x}}, \quad (5.7)$$

where \mathbf{M} , and \mathbf{K}_{vf} have been defined in Sect. 5.3. Indeed, the time derivative of (5.7) (assuming that \mathbf{M} remains constant over time) can be written as follows (omitting arguments of $H(\tilde{\mathbf{x}}, \dot{\tilde{\mathbf{x}}})$)

$$\dot{H} = \dot{\tilde{\mathbf{x}}}^\top \mathbf{M} \ddot{\tilde{\mathbf{x}}} + \tilde{\mathbf{x}}^\top \mathbf{K}_{\text{vf}} \dot{\tilde{\mathbf{x}}} + \frac{1}{2} \tilde{\mathbf{x}}^\top \dot{\mathbf{K}}_{\text{vf}} \tilde{\mathbf{x}}, \quad (5.8)$$

which, evaluated along the system trajectories, becomes

$$\dot{H} = \dot{\tilde{\mathbf{x}}}^\top \mathbf{f}_h - \dot{\tilde{\mathbf{x}}}^\top \hat{\mathbf{D}} \dot{\tilde{\mathbf{x}}} + \frac{1}{2} \tilde{\mathbf{x}}^\top \dot{\mathbf{K}}_{\text{vf}} \tilde{\mathbf{x}}. \quad (5.9)$$

Since $\dot{\mathbf{K}}_{\text{vf}}$ can have both positive and negative eigenvalues, a sufficient, yet conservative, condition to satisfy (5.6) is to have a negative semidefinite $\dot{\mathbf{K}}_{\text{vf}}$ in (5.9).

A possible solution to this problem is to design a passivity preserving controller that tracks the desired stiffness profile while limiting its change

when condition (5.6) is violated. To this end, we exploit the concept of energy tanks, introduced in [132], which aims at recovering the dissipated energy of the system to a less conservative impedance variation without violating the overall passivity of the system. The master side manipulator is endowed with an energy storing element having the following storage function

$$T(z) = \frac{1}{2}z^2, \quad (5.10)$$

whose dynamics is described by the following equation

$$\dot{z} = \frac{\varphi}{z} \dot{\tilde{\mathbf{x}}}^T \hat{\mathbf{D}} \dot{\tilde{\mathbf{x}}} - \frac{\gamma}{z} \frac{1}{2} \tilde{\mathbf{x}}^T \dot{\mathbf{K}}_{\text{vf}} \tilde{\mathbf{x}}, \quad (5.11)$$

with $z \in \mathbb{R}$ being the state of the tank and $\varphi, \gamma \in \{0, 1\}$ are parameters used to guarantee the upper bound limitation \bar{T} for the energy stored in the tank [79]. We note that (5.11) is singular for $z = 0$, thus a lower threshold ε for the tank energy must be set.

Thus, the extended dynamics can be rewritten as follows

$$\begin{cases} M\ddot{\tilde{\mathbf{x}}} + \hat{\mathbf{D}}\dot{\tilde{\mathbf{x}}} + \mathbf{K}_{\text{vf}}\tilde{\mathbf{x}} = \mathbf{f}_h \\ \dot{\mathbf{K}}_{\text{vf}} = \alpha \left(\mathbf{\Lambda}_k (\mathbf{K}_{\text{vf,d}} - \mathbf{K}_{\text{vf}}) + \dot{\mathbf{K}}_{\text{vf,d}} \right) \\ \dot{z} = \frac{\varphi}{z} \dot{\tilde{\mathbf{x}}}^T \hat{\mathbf{D}} \dot{\tilde{\mathbf{x}}} - \frac{\gamma}{z} \frac{1}{2} \tilde{\mathbf{x}}^T \dot{\mathbf{K}}_{\text{vf}} \tilde{\mathbf{x}}, \end{cases} \quad (5.12)$$

where $\mathbf{\Lambda}_k \in \mathbb{R}^{r \times r}$ is a diagonal and positive definite matrix containing the stiffness tracking control parameter and $\alpha \in \{0, 1\}$ is a variable used to activate/deactivate the stiffness variation in case of passivity violation. The master system, endowed with the energy tank, has the following energy function

$$\mathcal{H} = H + T = \frac{1}{2} \dot{\tilde{\mathbf{x}}}^T \mathbf{M} \dot{\tilde{\mathbf{x}}} + \frac{1}{2} \tilde{\mathbf{x}}^T \mathbf{K}_{\text{vf}} \tilde{\mathbf{x}} + \frac{1}{2} z^2, \quad (5.13)$$

whose time derivative is given by

$$\dot{\mathcal{H}} = \dot{H} + \dot{T} = \dot{\tilde{\mathbf{x}}}^T \mathbf{M} \ddot{\tilde{\mathbf{x}}} + \tilde{\mathbf{x}}^T \mathbf{K}_{\text{vf}} \dot{\tilde{\mathbf{x}}} + \frac{1}{2} \tilde{\mathbf{x}}^T \dot{\mathbf{K}}_{\text{vf}} \tilde{\mathbf{x}} + z \dot{z} \quad (5.14)$$

which, evaluated along the system trajectories, becomes

$$\dot{\mathcal{H}} = \dot{\tilde{\mathbf{x}}}^T \mathbf{f}_h - (1 - \varphi) \dot{\tilde{\mathbf{x}}}^T \hat{\mathbf{D}} \dot{\tilde{\mathbf{x}}} + (1 - \gamma) \frac{1}{2} \tilde{\mathbf{x}}^T \dot{\mathbf{K}}_{\text{vf}} \tilde{\mathbf{x}}. \quad (5.15)$$

By defining the following control laws for α , φ and γ

$$\alpha = \begin{cases} 0 & \text{if } T \leq \varepsilon \text{ \& } \dot{\mathbf{K}}_{\text{vf}} > 0 \\ 1 & \text{otherwise} \end{cases} \quad \gamma = \begin{cases} \varphi & \text{if } \dot{\mathbf{K}}_{\text{vf}} < 0 \\ 1 & \text{otherwise} \end{cases} \quad (5.16)$$

$$\varphi = \begin{cases} 1 & \text{if } T \leq \bar{T} \\ 0 & \text{otherwise} \end{cases}$$

the system in (5.12) is passive with respect to the input-output pair $(\mathbf{f}_h, \dot{\tilde{\mathbf{x}}})$ with storage function (5.7). Indeed, it can be easily verified that (5.15) always satisfies condition (5.6).

5.2 Robot Contextual Knowledge of the Environment

Focusing on the suturing procedure in this section we discuss about some methods to provide the robot with a better contextual knowledge of the environment. This is of cumbersome importance to provide the robot with more autonomy.

5.2.1 Force-based task classification

The development of surgical tasks and skills level classification methods and its combination with adaptive assistance strategies is a very promising approach in robotic surgery. In order to employ adaptive and time-varying shared control methods, such as virtual fixtures (see Sec. 5.4), task classification constitutes an essential step. It allows to assess surgeon skills and intentions in both training and real interventions. In this section we discuss about the basis to develop a reliable method for the automatic classification of surgical tasks. This procedure is often challenging if it relies only on kinematic information. Vision sensors might be employed but they usually require fine parameters tuning and a huge programming effort. Hence, we propose to adopt the interaction force measurement in the learning process. In the past, similar approaches have been investigated: Zappella et al. have proposed several methods for automatic surgical gesture classification using video and kinematic data [166]; Pierre et al. have developed a human collaborative framework for bimanual surgical tasks based on learned model where they combine active constraints and learning from demonstration [12]; in the work of Despinoy et al. the operating gesture workflow has been taken into account, in order to provide more intuitive training as well as more accurate solutions for procedural knowledge assessment [29]; in the work of Perez-Del-Pulgar et al. the authors address the problem of learning from demonstration trajectories that depend on

contact forces instead of depending solely on time [114]. In detail, we use force and kinematic data to train a Gaussian Mixture Model (GMM) in order to cluster subtasks during a robotic surgical reconstructive procedure.

Our experimental setup is composed by the da Vinci Research Kit commanded in teleoperation mode via open controllers¹. The user teleoperates the Patient Side Manipulators (PSMs) using the Master Tool Manipulators (MTMs) by observing the scene through the endoscopic stereo camera. T

During our experiments the PSMs Cartesian state (positions and velocities) and the measured forces, obtained using the results presented in Sec. 3.2, are collected at a sampling rate of 200 Hz. In addition, an external Kinect2 RGB camera is used to collect videos of the training and test procedures which are lately exploited to verify the accuracy of our method. ROS is employed to collect all the data in a synchronized way. During the demonstration phase we obtain a sequence of n elements of sensory information $\hat{x}_n = (x_1, x_2, \dots, x_n)$. At each time step we encode a tuple $x_i = (p_i, v_i, f_i)$ with p_i being the Cartesian position of the manipulator, v_i its velocity and f_i the force exerted at the tool tip. These data are classified in an unsupervised way using GMM and Expectation-Maximization (EM) approach (see Fig. 5.2). A GMM is parametrized by two types of values: the mixture component weights and the component means and variances/covariances. For a multivariate GMM with K components, the k^{th} component has a mean μ_k and covariance matrix Σ_k . Given a tuple x the probability that this belongs to an encoded GMM is:

$$P(x) = \sum_{k=1}^K \phi_k \mathcal{N}(x | \mu_k, \Sigma_k) \quad (5.17)$$

where \mathcal{N} denotes the classical multivariate normal distribution and the

¹<https://github.com/jhu-dvrk>

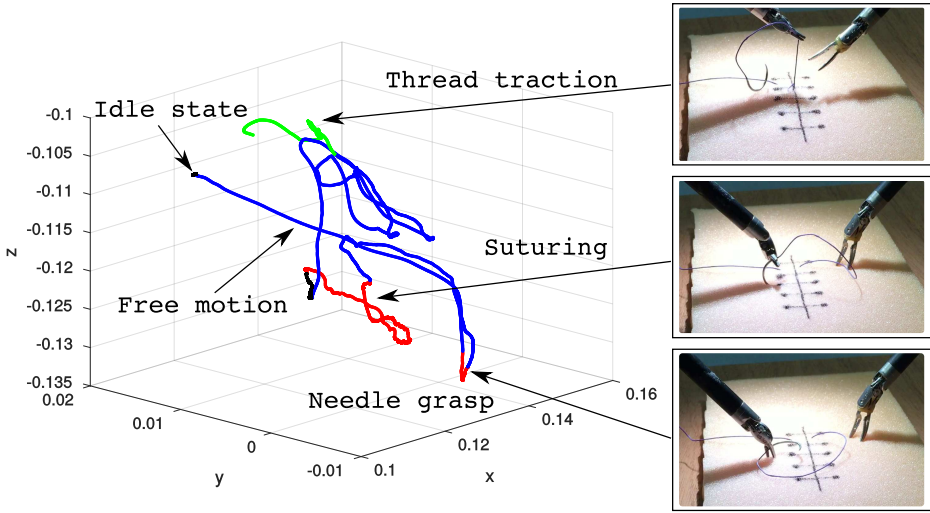


Figure 5.2. Example of task classification during a robotic surgical reconstructive procedure. The graph on the left depicts the Patient Side Manipulator tool tip Cartesian trajectory segmented using our approach. The pictures on the right represent some relevant suturing states.

sum of ϕ_k is unitary:

$$\mathcal{N}(x|\mu_k, \Sigma_k) = \frac{\exp\left(-\frac{1}{2}(x - \mu_k)^T \Sigma_k^{-1}(x - \mu_k)\right)}{\sqrt{(2\pi)^K |\Sigma_k|}} \quad (5.18)$$

$$\sum_{k=1}^K \phi_k = 1 \quad (5.19)$$

The log-likelihood function of a GMM can be written as follows:

$$L(\hat{x}_n) = \sum_{i=1}^n \log(P(x_i)) \quad (5.20)$$

The learning objective is to find a set of GMM parameters that maximizes Eq. (5.20). To this end, the EM algorithm iteratively maximizes the likeli-

hood of a statistical model given the training sequence \hat{x}_n and a predefined number of Gaussians. We have chosen this value to be $K=4$ in order to identify four states of a surgical reconstructive procedure. This value has been established in a heuristic way by observing several surgical reconstructive interventions performed by expert surgeons. We have used 30 suturing procedures as training set and evaluated the unsupervised classification procedure using 2 sequences. Both the training and the test data have been *offline* processed using the Statistical and Machine Learning Toolbox in MATLAB.

Finally, in order to validate our clustering procedure we trained the GMM and performed the evaluation using test set data. Demonstration and test phases consisted of suturing procedures conducted on a sponge phantom intended to act as dummy tissue. The result of a classification test is shown in Fig. 5.3. Here, only the time history of the measured force norm is reported, since it represents the most significant quantity for this evaluation. For the sake of clarity, only PSM1 data and states are shown but same results hold for PSM2. The four states we aimed at identifying were: *idle*, *interaction*, *free motion* and *thread traction*. To give an insightful explanation of the graph, the teleoperated robot is, at the beginning, in the *idle* configuration, then starts to move to perform its first action, *i.e.* needle grasping. The *interaction* state identified between 75 and 80 s is due to the contact occurred with the tissue while grasping the needle. Then, the operator moves and the next contact is detected while the needle is passing the phantom between 82 and 92 s. Successively, a new *idle* state is identified while the needle is regripped by the PSM2. A *free motion* state is identified during the process of thread scrolling performed in alternation with the PSM2. Finally, the *thread traction* state concludes the suturing procedure. Our method allows to classify the correct sequence of states with 88.32% of accuracy during the fully automated gesture recognition process. This result has been calculated by comparing the obtained

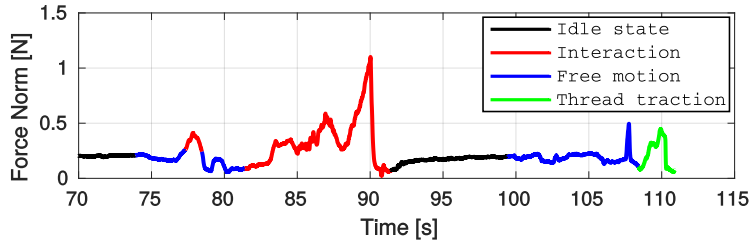


Figure 5.3. Force norm variation during a reconstructive procedure used as test set. Different states are classified and shown using different colors.

results to manually annotated data. The annotation phase have exploited the above mentioned recorded videos.

5.2.2 Needle Tracking

The circular shape of the suturing needle encouraged the development of a family of *model-based* approaches for detection and tracking. Authors in [20] present a RANSAC-based method for needle detection, where 3D needle pose reconstruction is achieved with the use of a stereo camera. However, the method does not run in real time and cannot be used for tracking. In [170], the 3D needle pose is adaptively reconstructed by relying on the observations of needle tip and junction, but tracking is not faced. Finally, [160] presents a method for a colored-needle tracking that involves a partial needle pose reconstruction and the use of markers. However, none of these works takes advantage of the kinematics information available from the robot, that are typically high-frequency and can ease the needle detection and tracking problem. In this section we focus on an approach to needle detection and tracking based on Kalman filtering to combine visual information from a monocular camera with the robot kinematics. Beside providing a fast and reliable needle pose estimation, the proposed method is robust with respect to scene variations as in case of partially needle occlusion or of needle re-grasping operation, as well as

external disturbances perturbing the needle pose. In addition, the covariance matrices can be adapted taking into account the particular task that is being performed.

Extended Kalman Filter

In our approach we propose the use of an Extended Kalman Filter (EKF) [150] for the estimation of the needle pose \mathcal{F}_n in Fig. 5.4a, expressed in the base frame \mathcal{F}_b with origin at the Remote Center of Motion (RCM) of the manipulator holding the needle.

In particular, the filter provides an estimate of the needle pose $\zeta = [\mathbf{p}_n, \mathbf{q}_n]^T$, being \mathbf{p}_n the true needle position, represented by the coordinates of the circle supporting the needle shape, and \mathbf{q}_n its quaternion-based true orientation in \mathcal{F}_b . The prediction step provides a preliminary estimation of the needle pose through the linear and angular velocities of the gripper provided by the manipulator kinematics. Then, a vision-based 3D pose reconstruction is used in the filter correction step.

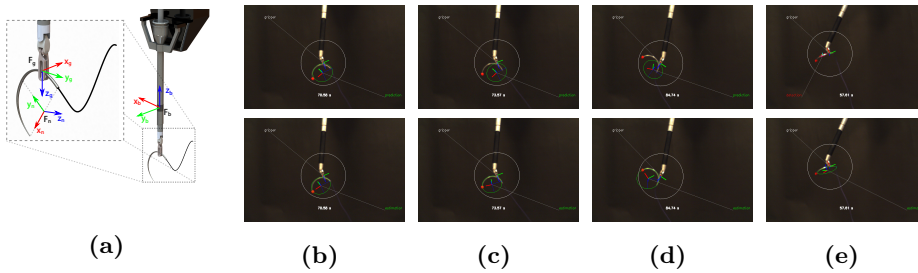


Figure 5.4. (5.4a): Frames of interest in our discussion. (5.4b)-(5.4c)-(5.4d): Prediction failure scenario compared with the vision-based corrected estimation. (5.4e): Detection failure scenario compared with the estimation. The white circle represents the image area in which the needle is assumed to be found, based on its radius and the depth of the gripper with respect to the camera.

Determined from robot kinematics the linear and angular velocities $[\mathbf{v}_g, \boldsymbol{\omega}_g]^T$

of the gripper in \mathcal{F}_b , we consider the following continuous-time process dynamics for the state vector ζ

$$\begin{aligned}\dot{\mathbf{p}}_n &= \mathbf{v}_g + [\boldsymbol{\omega}_{g\times}] \mathbf{r}_{gn} + \mathbf{w}_p \\ \dot{\mathbf{q}}_n &= \frac{1}{2} \boldsymbol{\Omega}({}^n\boldsymbol{\omega}_g) \mathbf{q}_n + \mathbf{w}_q\end{aligned}\tag{5.21}$$

where $[\ast_{\times}]$ denotes the skew-symmetric operator, $\mathbf{r}_{gn} = \mathbf{p}_n - \mathbf{p}_g$ is the relative position of the needle with respect to the gripper, expressed in \mathcal{F}_b , ${}^n\boldsymbol{\omega}_g$ is the angular gripper velocity expressed in \mathcal{F}_n , and $\mathbf{w} = [\mathbf{w}_p, \mathbf{w}_q]^T \sim \mathcal{N}(0, \mathbf{W})$ is the process noise. Details on the form of $\boldsymbol{\Omega}$ can be found in [152]. On the other hand, the measurement model of the filter employs the visual-based pose measurements extracted from the monocular camera: first, a detection algorithm computes the ellipse-shaped projection of the needle on the image plane. Then, the 3D pose is reconstructed from the size and projective reasonings ([27]). So, The measurement model is

$$\mathbf{y} = \boldsymbol{\zeta} + \mathbf{m}\tag{5.22}$$

where $\mathbf{m} \sim \mathcal{N}(0, \mathbf{M})$ is the measurement noise. The error-state vector is defined as

$$\tilde{\boldsymbol{\zeta}} = \begin{bmatrix} \tilde{\mathbf{p}} & \delta\tilde{\boldsymbol{\theta}} \end{bmatrix}^T\tag{5.23}$$

where $\tilde{\mathbf{p}} = \mathbf{p} - \hat{\mathbf{p}}$ is the position error and $\delta\tilde{\boldsymbol{\theta}}$ is the 3×1 small-angle approximation vector of the quaternion orientation error $\delta\tilde{\mathbf{q}} = \mathbf{q} \otimes \hat{\mathbf{q}}^{-1}$, defined to avoid numerical instability issues related to the unit norm constraint on the quaternion vector. Expressing the process dynamics (5.21) and the measurement model (5.22) with \mathbf{f} and \mathbf{h} , respectively, the corresponding jacobian matrices, \mathbf{F} and \mathbf{H} , are constant with respect to (5.23)

$$\mathbf{F} = \begin{bmatrix} [\boldsymbol{\omega}_{g\times}] & \mathbf{0}_3 \\ \mathbf{0}_3 & [{}^n\boldsymbol{\omega}_{g\times}] \end{bmatrix}, \quad \mathbf{H} = \mathbf{I}_6.\tag{5.24}$$

Then, the EKF state estimate is readily computed.

To evaluate the robustness of needle pose estimation with respect to perturbations due to the needle-tissues interactions, we use the simplified experimental setup shown in Fig. 5.4. Typical vision-related challenges (e.g., shadows, sparkling metal surfaces, small-sized objects) are not considered to focus on the geometric part of the pose reconstruction. So, an RGB segmentation procedure and a least-square fitting are sufficient to extract the projection of the needle on the image plane [39]. In addition, the needle tip has been colored to ease the detection of the projective point required for the 3D pose reconstruction.

The target experimental system is a da Vinci Research Kit robot (DVRK) [1]. Fig. 5.4 shows some preliminary results to prove the advantages in employing both robot kinematics and visual information for the needle pose estimation. During grasping, the needle is assumed as a rigid body attached to the gripper, and its pose can be predicted through robot kinematics, provided an initial estimate. However, since the needle-gripper transformation is not rigid, external disturbances (e.g., contact with tissues, slippages) can alter its pose, as shown in Fig (5.4b)-(5.4c)-(5.4d), where the needle pose has been explicitly changed. Robot kinematics can not cope with these disturbances, the prediction fails and propagates the error on the next iterations (top). The vision-based correction of our filter allows to detect the needle movements due to disturbances, and adjust the estimation accordingly (bottom). On the other hand, Fig (5.4e) shows a scenario where the vision-based detection fails, because the projected ellipse of the circular needle is degenerate on the image plane of the camera (top). However, kinematics information provided by the robot allows to maintain a stable estimation of the needle, even when this is not clearly visible. The figures are extracted from the videos that can be found at the [link](#)

5.2.3 Wound Tracking

Last but not least one of the biggest challenge in including some automation in surgical procedure regards the tissue tracking. In this section, we do not presume to treat the topic exhaustively but only to show a preliminary result regarding the tracking of a wound that is important also to find the guidelines for future works. In detail, we propose a simple and efficient GrubCut-based wound segmentation method and an automatic stitch planning that can be used to on-line obtain the optimal stitch poses.

Consider a suturing procedure composed of N stitches, the k -th stitch can be defined as a circular trajectory, for the needle tip, from the point a_k to b_k in the stitch frame $O_{s,k}$ ² (see Fig. 5.5). $O_{s,k}$ can be defined by choosing: (i) the axis \mathbf{x}_s along the direction from $\mathbf{x}_{e,k}$ to $\mathbf{x}_{i,k}$ (extraction and insertion points); (ii) the \mathbf{z}_s axis along the tissue normal unit vector \mathbf{n}_k , (iii) the axis \mathbf{y}_s to have an orthonormal frame; (iv) the frame origin in the center of the circle, with radius equal to the chosen needle radius r , passing through the points $\mathbf{x}_{i,k}$ and $\mathbf{x}_{e,k}$. Hence, each stitch k can be uniquely defined by the n-upla $s_k = [\mathbf{x}_{i,k}, \mathbf{x}_{e,k}, \mathbf{n}_k, r]$ extracted from the wound shape. Here we model the wound using: (i) a central spline ($\Sigma_c(\sigma)$) defining the wound shape, (ii) two lateral splines ($\Sigma_r(\sigma), \Sigma_l(\sigma)$) defining two guides for the stitch insertion and extraction points, (iii) a parametric unit vector $\mathbf{n}(\sigma)$ locally orthogonal to the tissue³.

Each stitch s_k have been calculated by equally spacing N points imposing a relative 25% of overlap between the stitches: $N = \lceil 1.25l/D \rceil$ where, both the wound length l and the wound depth D are obtained on-line respectively from the length of the central wound spline and the average distance between the wound borders.

²The stitch and PSM base frame has been calibrated w.r.t. the camera frame using a standard hand-eye approach

³ $\sigma \in [0, 1]$ is the curvilinear abscissa.

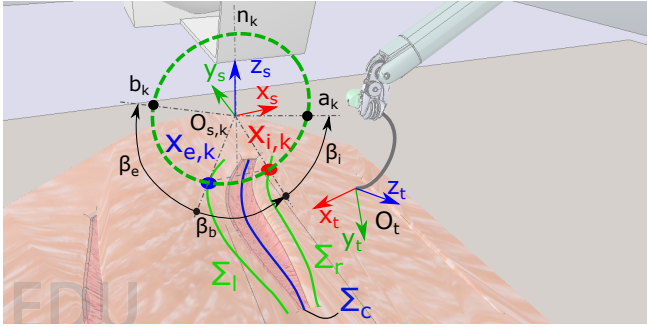


Figure 5.5. Stitch plan. β_i/β_e : insertion/extraction angles

Wound Segmentation and Registration

Using the force measure, obtained using our trocar force sensor [40] and the surgeon's visual perception in the loop, we design an effective method to interactively initialize the wound pose. In detail, the wound initialization is obtained by touching the tissue at the beginning and at the end of the wound, moving along the wound shape. All the collected points are smoothed using a spline and used to initialize the segmentation by defining a set of pixels belonging to the foreground.

To on-line segment the wound we rely on the efficient and widespread GrabCut method [127]. The GrabCut algorithm addresses the visual bi-layer segmentation task as an energy minimization problem, based on statistical models of the foreground (FGD) and the background (BGD). For an input image, we denote by $\alpha = [\alpha_i]_{i=1}^N$ the set of the unknown binary labels of the pixels ($\alpha_i = 0$ for the BGD pixels, $\alpha_i = 1$ for the FGD). Estimating the values $\hat{\alpha}$ of an unknown pixel can be formulated as the minimization of an energy-based Markov Random Field objective function

$$E(\alpha) = \sum_i (U_i(\alpha_i)) + \gamma E_s(\alpha)$$

with respect to α , where, E_s is a smoothness energy term, γ is a gain, and

$U_i(\alpha_i)$ is a term accounting for the observation probability $p(\mathbf{p}_i|\alpha_i)$ for a pixel \mathbf{p}_i to belong to the FGD or to the BGD. In our implementation this term is computed as Gaussian Mixture Models (GMM), based on image color distribution, learned, during the initialization process, for both the FGD and BGD layers.

Once the initial image is segmented through user interaction, the following frames are evaluated by considering a defined mask. In details, from the previous segmented foreground, we calculate the distance transform, providing a signed distance map. On this distance map, we define a narrow strip composed by three areas (trimap) with different probabilities of the pixels to be FGD or BGD. With reference to Fig. 5.6 (b) we have been defined. m1: $U_i(\alpha_i = 1) = inf$ (FGD); m2: $U_i(\alpha_i = 1) = -\log(p(\mathbf{p}_i|\alpha_i))$ (probably FGD/BGD); m3: $U_i(\alpha_i = 0) = inf$ (BGD). In this manner, temporal consistency is ensured, since energy minimization is only effective within the strip in the vicinity of the previous segmentation boundary, avoiding some outliers outside or inside, and reducing computations [118].

From the segmented image, the straight morphological skeleton of the polygon has been extracted⁴. The role of the skeleton is to account the topological structure of the incision. Moreover, the wound contours have been extracted relying to well known Open-Cv functions (*Canny* and *find contours*). Hence, we fitted: (i) the image central spline $\Sigma_{c,i}(\sigma)$ on the skeleton points; (ii) the two image lateral splines ($\Sigma_{r,i}(\sigma)$, $\Sigma_{l,i}(\sigma)$) by a defined offset w.r.t. the wound contours points belonging to the central spline normals unit vectors in the image plane. Finally, by resorting on the efficient stereo (ELAS) approach [51] the 3D point cloud of the tissue has been calculated. From the point cloud we obtained the wound normals $\mathbf{n}(\sigma)$, the 3D splines ($\Sigma_c(\sigma)$, $\Sigma_r(\sigma)$, $\Sigma_l(\sigma)$), by registering the image plane splines, and the 3D stitch points in order to have a 3D description of the wound.

⁴felix.abecassis.me/2011/09/opencv-morphological-skeleton/

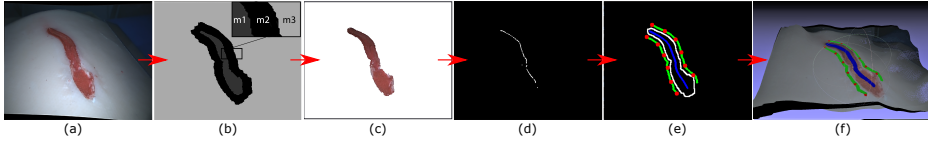


Figure 5.6. Snapshots: (a) initial image, (b) segmentation trimap mask, (c) segmented image, (d) wound skeleton, (e) wound model and stitching points overlapping, (f) registration onto the 3D point cloud. In (e,f) the central spline is indicated in blue, the lateral splines are indicated in green while the stitch points are indicated in red.

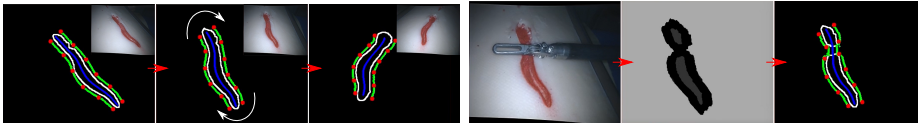


Figure 5.7. Left: robustness w.r.t. wound motion or deformation. Right: robustness w.r.t. partial occlusion occurrence.

Our experimental setup is composed of the full da Vinci Research Kit commanded in teleoperation mode. All the visual computations, including the 3D point cloud generation, have been obtained using the da Vinci endoscopic cameras acquired at 30 Hz. Figure 5.6 shows some snapshots resulting from the segmentation. From left to right all the segmentation phases and the stitch point selection and registration have been reported in a case study tested on a suturing phantom. Moreover, in Fig. 5.7right we report some snapshots showing the robustness of the proposed approach w.r.t. partially occluded images. Our preliminary experiments show also the capability of the method to maintain the segmentation during the wound motion or deformation allowing a wound tracking at 10Hz (Fig. 5.7left).

5.3 A Shared Control Method for Suturing

In this section, supervised and shared controllers have been developed in a vision-free, human-in-the-loop, control framework to help surgeon during a surgical suturing procedure. The presented results obtained in collaboration with the Hamlyn centre of the Imperial College of London have been published in [44]. Experiments conducted on the da Vinci Research Kit robot proves the effectiveness of the method indicating also the guidelines for improving results.

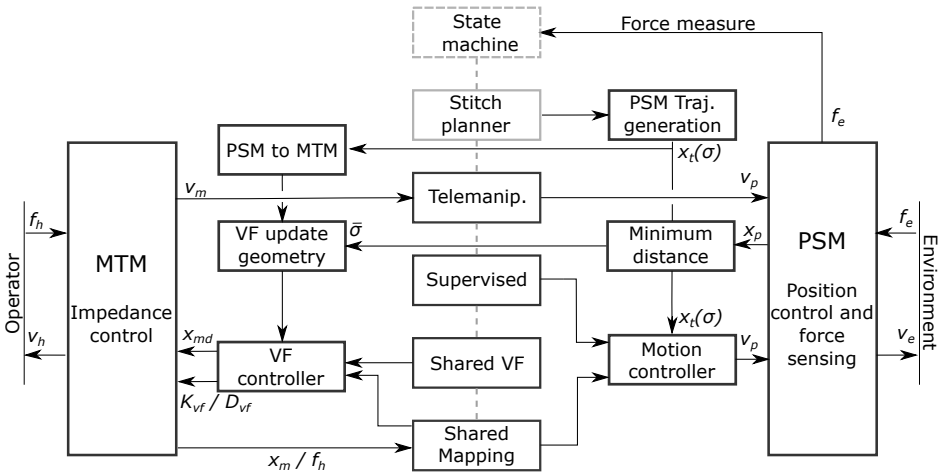


Figure 5.8. Proposed master-slave control structure. MTM: Master Tool Manipulator, PSM: Patient Side Manipulator.

5.3.1 Assisted Suturing Framework

In this section, the proposed framework is presented in details focusing on the adopted methodology for the stitch planning and presenting the three proposed assisted stitching control strategies (see Fig. 5.8 for a schematic visualization of the proposed controllers).

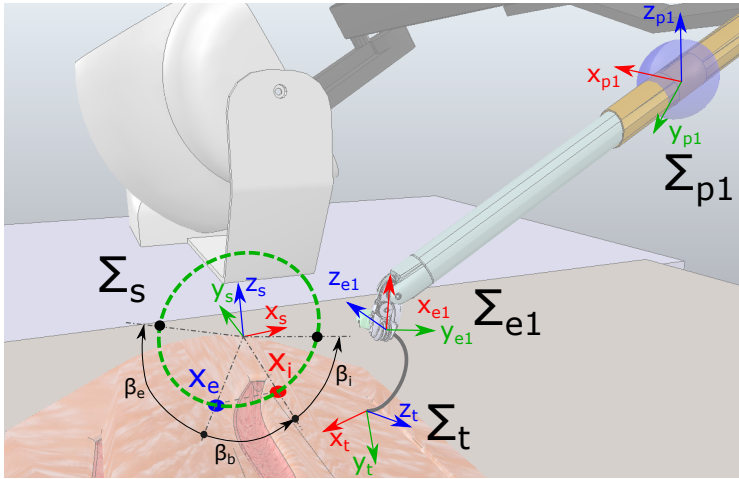


Figure 5.9. Slave side frames disposition. With Σ_s , Σ_t , Σ_{e1} , Σ_{p1} we indicate respectively the stitch frame, needle-tip frame, end-effector frame of the PSM1 and base frame. With x_e and x_i we indicate the insertion and extraction poses. β_b , β_i , β_e represent respectively the base, insertion and extraction angles described in Sub. Section 5.3.1.

Interactive stitch planning

In the proposed approach all the trajectories are planned in the relative stitch frame Σ_s (see Fig. 5.9). To this purpose, an interactive stitch selection strategy has been implemented. Using the slave side force measure and the surgeon's visual perception in the loop we design an effective method that can be locally used to interactively select the stitch frame without other visual input. In details, the norm of the force measured with our trocar force sensor has been used to classify the gripper-tissue interaction. Particularly, a threshold ρ_s has been defined experimentally considering both the tissue elasticity parameter, in order to minimize the tissue deformation during the selection, and the sensor resolution. Basically, the entrance and the exit point for each stitch have been selected touching the tissue sequentially at the desired insertion and extraction points x_i and x_e , with the PSM gripper fingers orthogonal to the tissue surface. At

each selection, the slave end-effector pose $\mathbf{x}_p \in \mathbb{R}^6$ has been recorded and, from that, the fingers normal unit vector $\mathbf{r}_{fi} \in \mathbb{R}^3$ and $\mathbf{r}_{fe} \in \mathbb{R}^3$ has been calculated respectively for the insertion and extraction points. Therefore, the Σ_s frame (see Fig. 5.9) has been obtained by choosing: (i) the \mathbf{x}_s axis along the direction from \mathbf{x}_e to \mathbf{x}_i ; (ii) the \mathbf{y}_s axis as cross product $\mathbf{y}_s = \mathbf{x}_s \times (\mathbf{r}_{fi} + \mathbf{r}_{fe})$, (iii) the axis $\mathbf{z}_s = \mathbf{x}_s \times \mathbf{y}_s$ to have an orthonormal frame; (iv) the frame origin in the center of the circle (with radius equal to the chosen needle radius) lying on the plane defined by \mathbf{x}_s and \mathbf{z}_s and passing through the points \mathbf{x}_i and \mathbf{x}_e .

After defining the stitch frame, the stitch planner deals with calculating the needle tip trajectory, in Σ_s , to approach and execute the needle insertion/extraction. The goal is to minimize the tissue stress during the stitch execution. To this purpose, based on the result presented in [64, 63], we define a circular tip trajectory tangent to the circular shape of the needle. More in details, defining an insertion and an extraction angle β_i and β_e , considering the angle β_b as shown in Fig. 5.9 and a needle with radius r , the tangential path to perform the stitch insertion/extraction is calculated as parametric pose, with respect to the scalar curvilinear abscissa $\sigma \in [0, 1]$,

$$\mathbf{x}_t^s(\sigma) = [\mathbf{p}_t^s(\sigma), \mathbf{\Phi}_t^s(\sigma)]^T \in \mathbb{R}^6 \quad (5.25)$$

where, in this implementation:

$$\mathbf{p}_t^s(\sigma) = [r \cos(-\beta\sigma + \theta_i), 0, r \sin(-\beta\sigma + \theta_i)]^T$$

and $\mathbf{\Phi}_t^s(\sigma) = [0, -\pi/2 + \theta_i + \beta\sigma, 0]^T$ with $\beta = \beta_b + \beta_i + \beta_e$, $\theta_i = \beta_b/2 + \beta_i - \pi/2$ (see Fig. 5.9).

This trajectory is used to plan the PSM motion or to plan the virtual fixture assistance as discussed in the next sections.

Following, we compare the standard fully telemanipulation paradigm

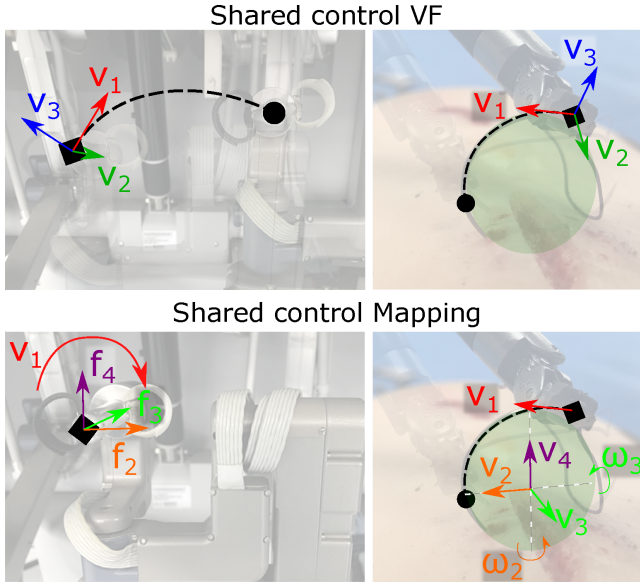


Figure 5.10. A visualization of the mapping between the master DoFs and the slave DoFs in the two implemented shared controllers.

with three different assistance strategies.

Fully telemanipulation

In this modality, the user is given the full control of the 6-DoFs of the slave robot. This can be achieved by implementing the classic velocity coupling between master and slave

$$\mathbf{v}_p = \begin{bmatrix} s\mathbf{R}_m^p & \mathbf{0} \\ \mathbf{0} & \mathbf{R}_m^p \end{bmatrix} \mathbf{v}_m \quad (5.26)$$

where, $\mathbf{v}_m = [\dot{\mathbf{p}}_m, \boldsymbol{\omega}_m]$ and $\mathbf{v}_p = [\dot{\mathbf{p}}_p, \boldsymbol{\omega}_p]$ ⁵ are respectively the master and the slave velocity, s is the scalar scale factor and $\mathbf{R}_m^p \in \mathbb{R}^{3 \times 3}$ is the rotation matrix between the MTM base frame “ m ” and the PSM base frame “ p ”.

⁵ $\dot{\mathbf{p}}$ and $\boldsymbol{\omega}$ represent respectively the linear and the angular velocity.

Supervised control

In our framework, the supervised control represents the higher level of autonomy given to the robot for the stitch execution. In this control paradigm, the slave robot motion is fully autonomous, when performing the stitch trajectory, while the user can supervise the robot by starting and stopping the controller as described in Sec. 5.3.2. The described behaviour has been obtained by considering a trapezoidal velocity profile temporal law [141] for the parameter $\sigma(t)$ in (5.25) and projecting, at each time interval, the desired tip velocity $\mathbf{v}_t^s(\sigma(t))$ to the slave robot end effector:

$$\mathbf{v}_p(\sigma(t)) = \begin{bmatrix} \mathbf{R}_s^p & -\mathbf{R}_s^p \mathbf{S} (\mathbf{R}_p^s \mathbf{p}_p - \mathbf{p}_t^s) \\ \mathbf{0} & \mathbf{R}_s^p \end{bmatrix} \mathbf{v}_t^s(\sigma(t)) \quad (5.27)$$

where, $\mathbf{R}_s^p \in \mathbb{R}^{3 \times 3}$ is the constant rotation matrix between the stitch frame Σ_s and the PSMs base frames Σ_{p1} or Σ_{p2} (see Fig. 5.9); \mathbf{p}_p , \mathbf{p}_t^s are the position vectors related to the PSMs direct kinematics and position vectors related to the needle tip in frame stitch respectively. Notice that, the two PSMs have been calibrated using the efficient hand-eye calibration approach proposed in [168] to find the relation between the two robots base frames. Finally, $\mathbf{S}(\cdot)$ represents the skew symmetric matrix operator.

Shared control using virtual fixtures (VF)

In this control strategy, we propose a guidance virtual fixture (GVFs) [14] method to constrain the user in position along the specified path while leaving his/her orientation free. On the other hand, on the slave side, the position is controlled in telemanipulation by the master while the orientation is automatically imposed. In Fig. 5.10 the defined mapping is visualized: the motion along the VF on the master side (v_1) is mapped into a tangential motion of the needle tip along the needle circular shape. Moreover, the slave motion in the two directions orthogonal to the path

(v_2, v_3) is even possible by applying a force $\mathbf{f}_h \neq \mathbf{0}$ on the master. The described behaviour has been obtained by considering a spatial variation law for the trajectory parameter σ based on the minimum distance \tilde{x}_t between the actual needle tip pose \mathbf{x}_{te}^s and the curve $\mathbf{x}_t^s(\sigma)$. In details, given the actual needle tip position, the curvilinear abscissa $\bar{\sigma}$, corresponding to the minimum distance, is calculated with respect to the trajectory $\mathbf{x}_t^s(\sigma)$ as:

$$\bar{\sigma} = \arg \min_{\sigma} \quad \|\mathbf{W}_p(\mathbf{x}_t^s(\sigma) - \mathbf{x}_{te}^s)\| \quad (5.28)$$

where, $\mathbf{W}_p = \text{diag}(1, 1, 1, 0, 0, 0)$ is a selection matrix used to consider only the position error. In the case of a circular path the minimum distance can be obtained in closed form. The mathematical derivation is not reported here for brevity. Finally, a low-pass filter has been used to smoothen the $\hat{\sigma}(t)$ behavior and avoid possible switching when the needle tip is near the circle center: $\bar{\sigma}_f(s) = \bar{\sigma}(s)/(1 + sk_fT)$ where T is the control sampling time and k_f is a positive scalar gain.

Therefore, to obtain the desired behaviour the virtual reference on the master side \mathbf{x}_{md} is calculated by opportunely projecting, at each time interval, $\mathbf{x}_t^s(\bar{\sigma}_f)$ on the master side by integrating the following velocity mapping between the slave and the master pose:

$$\mathbf{v}_{md}(\bar{\sigma}_f) = \begin{bmatrix} \frac{1}{s} \mathbf{R}_s^m & -\frac{1}{s} \mathbf{R}_s^m \mathbf{S} (\mathbf{R}_p^s \mathbf{p}_p - \mathbf{p}_t^s) \\ \mathbf{0} & \mathbf{R}_s^m \end{bmatrix} \mathbf{v}_t^s(\bar{\sigma}_f) \quad (5.29)$$

where, $\mathbf{R}_s^m = \mathbf{R}_p^m \mathbf{R}_s^p$.

Hence, the impedance controlled master manipulator described in (5.1), endowed with an attractive GVF constraint enforcement method given by a spring-damper force:

$$\mathbf{f}_c(\cdot) = \mathbf{f}_{vf}(\tilde{\mathbf{x}}_m, \dot{\tilde{\mathbf{x}}}_m) = -\mathbf{K}_{vf} \tilde{\mathbf{x}}_m - \mathbf{D}_{vf} \dot{\tilde{\mathbf{x}}}_m \quad (5.30)$$

is described by:

$$\mathbf{M}\ddot{\tilde{\mathbf{x}}}_m + \hat{\mathbf{D}}\dot{\tilde{\mathbf{x}}}_m + \mathbf{K}_{\text{vf}}\tilde{\mathbf{x}}_m = \mathbf{f}_h, \quad (5.31)$$

with $\hat{\mathbf{D}} = \mathbf{D} + \mathbf{D}_{\text{vf}}$ and

$$\mathbf{K}_{\text{vf}} = \text{diag}[k, k, k, 0, 0, 0] \quad (5.32)$$

chosen diagonal to constrain the user motion only in position.

On the other hand, at the slave side the desired velocity \mathbf{v}_p has been obtained considering the reference provided by the master, for the position, and by the programmed trajectory for the orientation:

$$\mathbf{v}_p(\bar{\sigma}_f) = \begin{bmatrix} {}^s\mathbf{R}_m^p & \mathbf{0} \\ \mathbf{0} & \mathbf{R}_m^p \end{bmatrix} \begin{bmatrix} \dot{\mathbf{p}}_m \\ \boldsymbol{\omega}_{md}(\bar{\sigma}_f) \end{bmatrix} \quad (5.33)$$

Shared control using an orientation mapping

The aim of this control strategy is to constrain the motion of the needle tip along the defined trajectory commanding the desired coordinate on the path, defined by $\bar{\sigma}$, using the master orientation. The described behaviour has been obtained by considering the parameter σ as a differential projection of the angular velocity around the axis of the master gripper and by using Eq. (5.27) to obtain the slave velocity.

$$\dot{\sigma} = \mathbf{W}_m(\mathbf{R}_e^m)^T \boldsymbol{\omega}_m \quad (5.34)$$

where \mathbf{R}_e^m is the rotation matrix related to the master direct kinematics used to evaluate the angular velocity in frame end effector and $\mathbf{W}_m = [0, 0, 1]$ is a selection matrix used to consider only the orientation around the master gripper axis. In this case, the master manipulator is controlled in impedance to have its position fixed in the space and the orientation free. To this purpose, the VF stiffness is imposed as described in Eq. 5.32. This choice is motivated by the fact that in this way the orientation of the user

is completely free and only the last joint needs to be rotated. This allows an intuitive control of the needle by minimizing the effort needed to reach the correct orientation. Moreover, in order to enable the user to correct possible errors in the stitch pose, due to imprecision in the stitch selection or due to the tissue motion, we design a stitch pose adaptation strategy. Basically, the pose transformation between the adapted stitch frame Σ_s and the current stitch frame Σ_s can be obtained by integrating the force at the master side to have a 3-dimensional motion. We choose to use only the force information without considering the torque information due to the noisy and less predictable master torque estimation. Hence, the camera pedal has been used to switch between the position and the orientation adaptation. In details, we consider the velocity \mathbf{v}_s^s of the adapted stitch frame w.r.t Σ_s as:

$$\mathbf{v}_s^s = \begin{bmatrix} -\gamma \mathbf{W}_p \mathbf{f}_h \\ (\gamma - 1) \mathbf{W}_o \mathbf{f}_h \end{bmatrix} \quad (5.35)$$

where, $\mathbf{W}_p = [\Delta \mathbf{p}, \mathbf{0}] \in \mathbb{R}^{3 \times 6}$ is a selection matrix used to extract only the position terms and $\mathbf{W}_o \in \mathbb{R}^{3 \times 6}$ is:

$$\mathbf{W}_o = \begin{bmatrix} \Delta \Phi_1 & 0 & 0 & & & \\ 0 & 0 & \Delta \Phi_3 & & \mathbf{0}_{3 \times 3} & \\ 0 & 0 & 0 & & & \end{bmatrix} \quad (5.36)$$

and γ a binary coefficient used to activate the position and the orientation adaptation; $\Delta \mathbf{p} = [\Delta p_1, \Delta p_2, \Delta p_3]$ and $\Delta \Phi = [\Delta \Phi_1, 0, \Delta \Phi_3]$ are respectively the position and orientation steps obtained experimentally. Finally, an element-wise force threshold of $\rho_m = 2\text{N}$ has been used to avoid undesired motion during the stitch execution.

5.3.2 Performance Evaluation

This section aims at proving with both performances metrics and user study whether and which type of assistance is useful to perform the stitch task minimizing the tissue damages and at the same time the surgeon's workload.

Experimental set-up

The experimental setup is composed by the full dVRK [71] robotic platform provided with a console composed by two master side manipulators (MTMs) and a stereo-visor; two patient side manipulators (PSMs) and an endoscopic arm (ECM) provided with a stereo camera. The provided ROS-based functions included in the "*dvrk-ros*" API have been used to read the robots state and to control (at 5ms) the slave and the master robots respectively in position and in torque. The stiffness value k in (5.32) has been opportunely filtered with a first order filter $\dot{\tilde{k}} + K_p \tilde{k} = 0$ with $\tilde{k} = k_d - k$ and $K_p > 0$ to smoothly adapt the stiffness variation, where, we chose $k_d = 300\text{N/m}$ for needle insertion and $k_d = 150\text{N/m}$ for needle extraction.⁶ A surgical suturing phantom has been used to simulate a human wound on which two red dots have been marked as a guide for the stitch selection. A large needle driver instrument from Intuitive Surgical Inc. has been used to move a GL-222 needle with an external diameter of 17.5 mm. In order to have the full control of the needle position a metal printed needle holder (see Fig. 5.11) has been used whose design was inspired by [136]. Finally, a VREP simulator of the slave set-up has been

⁶Is a worth noticing that since the stiffness matrix is not constant the passivity of the system is not proved [135] and hence instability problems can occur. Following the results presented in [74] by injecting a constant damping into the system $\mathbf{D}_{vf} > \alpha \mathbf{M}$, where \mathbf{M} is the master robot inertia matrix and α is such that $\dot{\mathbf{K}}_{vf}(t) - 2\alpha \mathbf{K}_{vf}(t)$ is negative semi-definite, the passivity is guaranteed. Hence, by choosing opportunely the K_p filter parameter we can bound the stiffness variation $\dot{\mathbf{K}}_{vf}(t)$ and avoid to inject undesirable high damping.

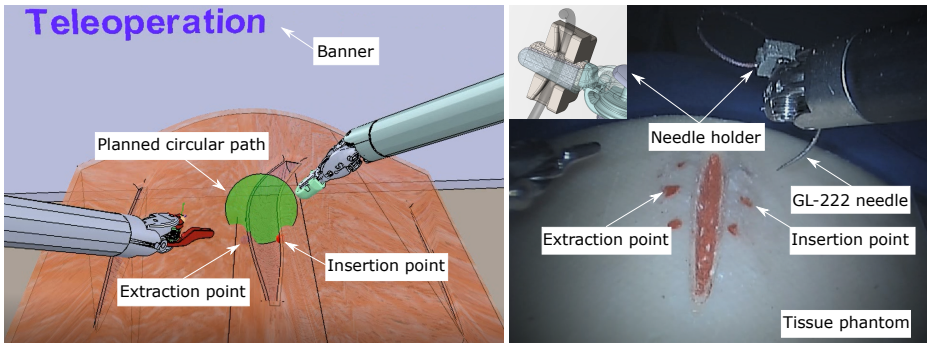


Figure 5.11. Description of the experimental setup. Left: Augmented Reality (AR) feedback. Right: setup used in the proposed experiments.

used for the preliminary tests and for augmented reality (see Fig. 5.11).

Moreover, as described in Fig. 5.12, we choose to use “gripper passwords” to give the user control of the high-level state machine. More in details, three different passwords have been used to switch between: (i) *telemanipulation*; (ii) *stitch selection*; (iii) *needle insertion*; (iv) *needle extraction*. Each password can be commanded when the robot is not in telemanipulation, e.g. $CP = 0$ (CP : coag pedal flag), by simply pressing a combination of the master right gripper (R) or master left gripper (L). Each control, including the standard *telemanipulation*, is activated by the pressure of the coag pedal ($CP = 1$) and is stopped when it is released returning at the state *telemanipulation*.

Test Setup

The user study has been performed by volunteer users recruited from a population of both engineers and surgeons in the Hamlyn Center of Imperial College of London. A total of ten right-handed subjects (average age 26) completed the experiment. All participants had at least one previous experience with the da Vinci platform. Each participant spent about 20 minutes, performing different suture in telemanipulation, for training both

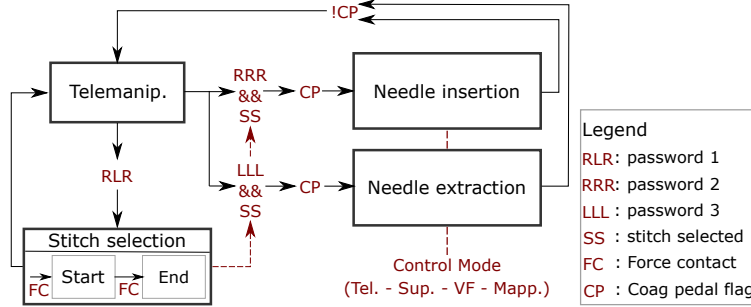


Figure 5.12. Description of the password-based state machine.

the robotic platform and the stitch framework, before to start the experiment. None of the participants has neurological or vision disorder that may negatively affect the results. The conducted experiment is composed of the following phases: (i) the surgeon selects the stitch using the provided force-enabled method; (ii) the surgeon executes the stitch performing both insertion and extraction of the needle by using, in a random sequence, the four described control paradigms. In each experiment the user is fully autonomous, receiving all the information regarding the stitch frame, the actual control active and instruction about the action to undertake directly in augmented reality by messages and visual information in the VREP simulated environment. In Fig. 5.13 the timeline of the experiment is shown. In details, we report the needle tip position and orientation in stitch frame in Figs. 5.13(a,b)⁷, the master robots (MTMR, MTML) position and orientation in Figs. 5.13(c,d,e,f), the PSM1 out-of-tangent needle tip force in Fig. 5.13(g) and the time evolution of the stiffness in Fig. 5.13(h). The behaviour of the four control paradigms, described in the previous sections, is clearly visible showing the different mapping between the master and the slave. In details it is possible to notice that: (i) the master needs to be moved in both position and orientation when the telemanipulation

⁷To have a clearer visualization, the trajectories are plotted only when the needle is gripped and the insertion or extraction trajectory is performed.

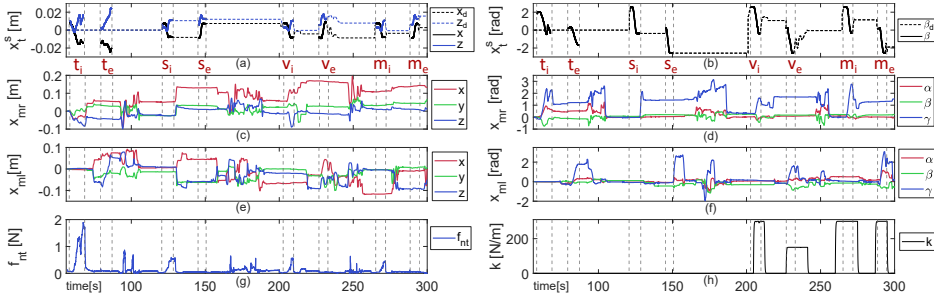


Figure 5.13. Experiment timeline. (t, s, v, m): telemanipulation, supervised, virtual fixtures, mapping controllers; (i, e): insertion, extraction phase. (a,b) needle tip position and orientation displacement, (c,d) MTMR position and orientation, (e,f) MTML position and orientation, (g) PSM1 out-of-tangent needle tip force, (h) master stiffness. We indicate with α , β and γ the orientation expressed in Euler angles.

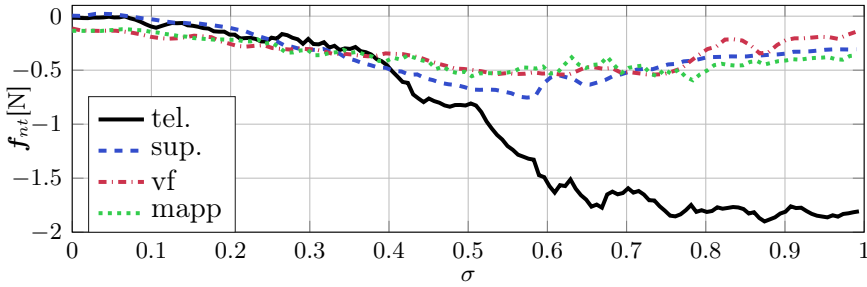


Figure 5.14. Out of tangent needle tissue interaction force in the four control cases. σ represents the curvilinear abscissa.

controller is active, (ii) it is fixed when the supervised controller is used, (iii) it needs to be moved only in position, leaving the orientation free, using the supervised VF control paradigm while only the orientation needs to be controlled considering the shared mapping control paradigm. This translates into different levels of workload as will be discussed in the next section.

Controllers Performance Evaluation

As evaluation metric, for each stitch (insertion and extraction), we calculate the execution time and the applied forces on the tissue. More in details, we measure the out-of-tangent forces acting on the needle tip during the needle insertion as $\mathbf{f}_{nt} = \|\mathbf{W}_f \mathbf{R}_p^t \mathbf{f}_s\|$, where, \mathbf{f}_s is the slave force obtained using our trocar force sensor described in Chapter 3.2, $\mathbf{R}_p^t \in \mathbb{R}^{3 \times 3}$ is a projection matrix and $\mathbf{W}_f \in \mathbb{R}^{2 \times 3}$ is an opportune matrix used to select only the y_t and z_t components. In Figs. 5.14, 5.15 are shown the results of one of the experiments performed in the user study by a trainee surgeon. In details, the out-of-tangent force for the needle insertion is reported in Fig. 5.14 and the executed needle tip trajectory respectively during the needle insertion and the needle extraction sub-task are shown in Fig. 5.15. It is clearly possible to notice that the executed trajectory in both tasks performed in telemanipulation is not following the correct circular path. Indeed, during the insertion usually the surgeons firstly moves following a linear path and after the needle is rotated (as was also reported in [23]). Furthermore, during needle extraction, the behaviour is still worst showing that in the 60% of the cases a linear trajectory in the opposite direction of the needle shape is performed. Moreover, the average measured time and the out-of-the-tangent needle force is double when the task is performed in telemanipulation compared to the use of one of the proposed assisted controllers(see Fig.5.16).

Comparing the three proposed control strategies, we can see an improved precision using the supervised and the shared mapping controllers while the time consumption and the out of tangent forces show similar results. This is because, with respect to the supervised and the shared mapping strategies, in the shared VF controller only the position is constrained and hence bigger errors in the needle trajectory are possible while, on the other hand, the automatic orientation control allows having bounded forces in all the cases. Finally, although the supervised controller shows the bet-

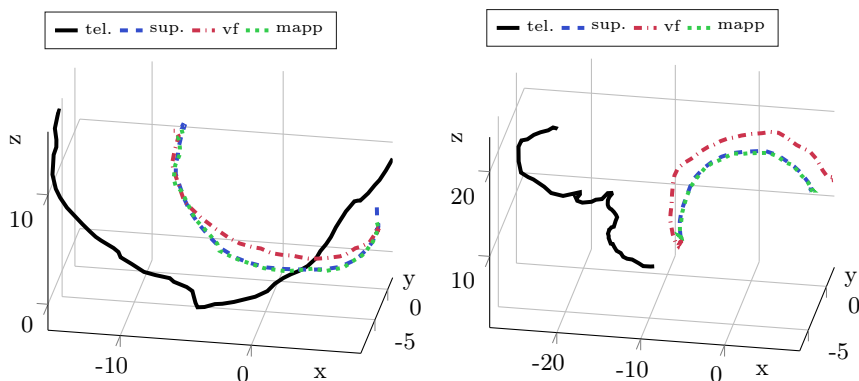


Figure 5.15. Needle tip trajectory during the needle insertion (top) and the needle extraction (bottom). The insertion is from the right to the left, the extraction is from the left to the right.

ter results in precision and exerted forces, we measured a success rate less than 75% considering our implementation. The failure cases are due to an incorrect needle position inside the gripper, a bad stitch selection or because the needle has not gone out on the other tissue side preventing a correct supervised needle extraction. On the other hand, the two shared strategies show a better success rate enabled by the possibility to correct, on-line, the performed trajectory.

Subjective User Evaluation

We have asked the users to complete a NASA TLX workload survey [57] to evaluate the level of workload required. In the analysis four parameters have been chosen by the user (Effort, Frustration, Mental, Physical) while the Temporal and Performance parameter has been calculated as discussed in the previous section. The result of the experiment is shown in Fig. 5.17. We can notice that for the three proposed control strategies the resulted workload is significantly lower with respect to the standard telemanipulation paradigm. Better results are shown considering the supervised controller, with less workload for the surgeon and also better

performances. However, as discussed before, this control is less robust and more prone to failure. Moreover, the two shared control solutions show similar results with a slightly better performances and less effort for the *Mapping* controller respect to the solution based on virtual guidance. At the question: "This type of assistance can be useful for both the needle insertion and extraction?" the answer has been positive in 70% of the cases for the needle insertion and 90% for the needle extraction. Moreover, we have asked whether with the proposed strategies the user felt to have less control of the robot and the answer has been: 55%, 21% and 23% positive respectively for the supervised, shared VF and shared mapping controls but never in a negative sense. Also for the supervised strategy, the possibility of the user to switch easily between autonomous and telemanipulation state give the sensation to not loose completely the system control. Finally, at the question: "Which is the preferred controller?" the result have been 20%, 20% and 60% respectively for the supervised, shared VF and shared mapping. Hence, instead of the slightly improved precision and the

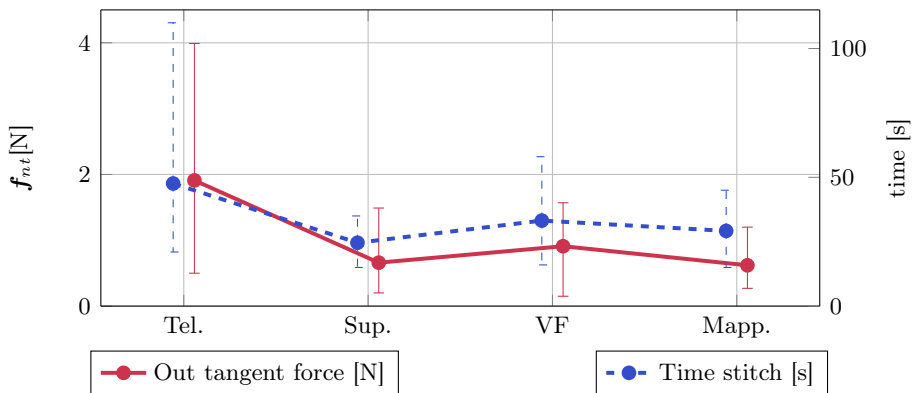


Figure 5.16. Performance evaluation of the four proposed controllers considering time spent for each stitch and out-of-tangent force exerted on the tissue.

reduced workload provided by the supervised controller, the users feel to

have better performance, control, and less workload when at least one degree of freedom, for the needle motion, is under his/her control. Moreover, the possibility to correct the stitch frame pose on-line has been appreciated giving the sensation of a better control of the task.

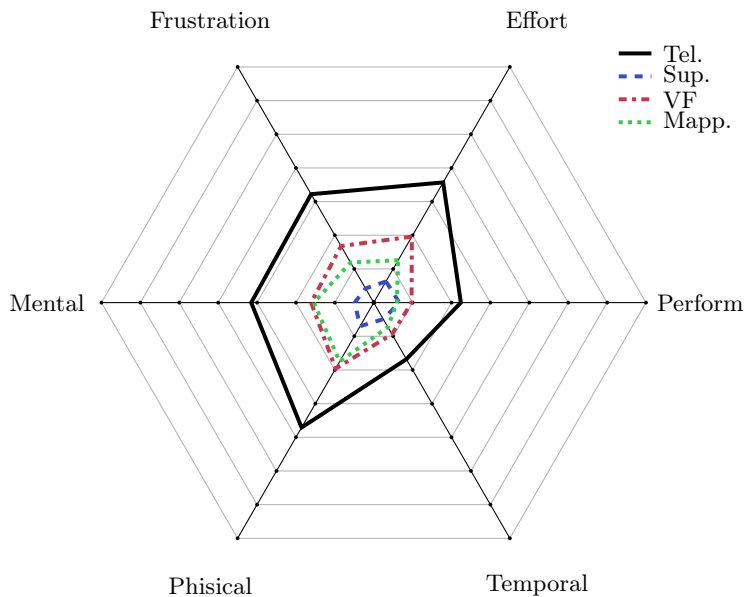


Figure 5.17. Nasa TLX workload survey using the four control strategies. Values near the center indicate better results.

5.4 A Shared Control Method for Dissection

Automatic VF generation/adaptation can be performed by exploiting vision-based techniques [134, 133]. Vision systems allows tracking of organs as they move or deform. However, this can be a demanding task, particularly in cases where surgical targets have few structural features for tracking. Alternatively, force controlled exploration of patient-specific anatomy can be a time consuming procedure and thus not practicable in some surgical interventions [158]. Whatever method is used to generate them, to be effective in the surgical scenario, VFs must be adapted on-line as the environment moves or deforms, i.e. they must be repositioned and/or opportunely refined in order to reflect the different environmental configuration. Very few papers make a significant consideration of *adaptive* VF, where the constraint geometry (semi-) autonomously moves as a result of environmental changes.

Historically, robotic teleoperation systems have made use of VF as a perceptual overlay to enhance the human experience in performing remote manipulation tasks. Rosenberg pioneered VF in his work [126]. Since then, renewed interest has been shown in their use for robotic surgical procedures. In [112] the first attempt to transfer VF to the operating room is shown. The authors used VF generated from preoperative computed tomography images and constrained the motions of a surgical robot to a predefined path during the dissection of the internal mammary artery. Interactive generation of VF in surgical applications has been addressed in [83] where constrained optimization is used to enforce the VF constraint with objective function derived by user inputs. More recently, it has been shown that VF can be opportunely generated using scans of the area of interest [13, 82]. A dynamic VF technique to enhance the surgical operation accuracy of admittance-type medical robots in the deforming environment is presented in [167]: the target deformation is tracked actively and the proxy motion is constrained on a deforming sphere to simulate the beating

heart surgery environment. One of the major obstacles in implementing vision generated VF in surgical applications is the organs displacement and deformation: whether the constraint geometry is defined preoperatively or intraoperatively, it must be mapped correctly to the organs as they move or deform. Alternatively, VF may be opportunely adapted according to the currently being executed task or on the estimation of surgeon's skills. Learning from demonstration has been used for task dependent VFs application in [4], whereas adaptive VFs, based on the surgeon's level of expertise, are shown in [138]. An algorithm to select an appropriate admittance ratio based on the nature of the task was developed in [93]: automatic admittance ratio tuning is recommended for an efficient use of VFs. A method for online task tracking and on the use of adaptive VFs that can cope with their inherent inflexibility is presented in [31]. On the other hand, guaranteeing a stable behavior of the robot endowed with adaptive VF control is of a paramount importance in robotic surgery. Interactive VF application results in variable impedance controllers that could threaten the stability of the robotic system are shown in [36, 76]. The analysis of the system behavior is complicated by the interaction with the user which further contributes to the overall system impedance parameters variation. Thus, passivity-based control techniques need to be exploited in order to ensure the safe use of the system for every change in the impedance parameters. When the impedance variation profile is known in advance, a state-independent stability constraint could be imposed [74]. However, this would imply the application of a fixed damping parameter on the system (opportunely defined on the basis of the maximum stiffness variation, *i.e.* worst case design) which degrades the system transparency when the bilateral teleoperation is enabled. The same applies to other passivity-based control techniques, such as the time domain passivity-based control approach [56]: here, the control action in the form of a dissipative element that absorbs the energy generated by the system causes, in general, the

presence of higher damping on the system. These considerations motivated us to use the energy tanks passivity-based control approach discussed in Sec. 5.1.2.

In this section we will discuss the results published in [135] focusing on virtual fixtures adaptation in the surgical dissection task.

Virtual Fixtures

VFs can be classified into two main classes: forbidden-region virtual fixtures (FRVF) and guidance virtual fixtures (GVF) [14]. Generally speaking, FRVF are suitable for simulating barriers, constraining surfaces or delicate regions that the user should be forbidden to enter. In contrast, a GVF has an attractive behavior that pulls the robot towards a desired path (see Fig. 5.18).

Here, we focus on the latter type (we will hereafter refer to GVF simply as VF). Two quantities are essential to describe a VF: its *geometry* and the *constraint enforcement* method.

VF geometry model

a simple, yet general, way of geometrically formulating a smooth continuous VF is through parametric curves. Without loss of generality, we adopt cubic splines. In its 1-dimensional form, a cubic spline is defined by

$$\Gamma_i(s) = C_0 + C_1(s - x_i) + C_2(s - x_i)^2 + C_3(s - x_i)^3 \quad (5.37)$$

where $\Gamma_i(s)$ denotes the curve in its i -th interval $[x_i, x_{i+1}]$, $s \in [0, 1]$ is the curve parameter, C_0, C_1, C_2, C_3 are constants determined by imposing four conditions (usually being boundary constraints $\Gamma_i(0), \Gamma_i(1), \Gamma'_i(0), \Gamma'_i(1)$, where $\Gamma'_i(\cdot)$ denotes the curve derivative w.r.t. the parameter s). As explained later (Sect. 5.4.1), we build the spline geometry by fitting a set of recorded interaction points. For this purpose, we use parabolically terminated splines.

VF constraint enforcement

a GVF exhibits attractive behavior towards the desired path. The simplest constraint enforcement method consists in applying a spring-damper like force. In the linear case this can be defined as

$$\mathbf{f}_{\text{vf}}(\tilde{\mathbf{x}}, \dot{\tilde{\mathbf{x}}}) = -\mathbf{K}_{\text{vf}}\tilde{\mathbf{x}} - \mathbf{D}_{\text{vf}}\dot{\tilde{\mathbf{x}}}, \quad (5.38)$$

where $\mathbf{K}_{\text{vf}} \in \mathbb{R}^{r \times r}$ and $\mathbf{D}_{\text{vf}} \in \mathbb{R}^{r \times r}$ are properly designed diagonal and positive definite matrices and \mathbf{x}_d is the set point belonging to the constraint geometry having minimum distance from \mathbf{x} (see Fig. 5.18). An impedance controlled manipulator (5.1), endowed with VF control forces defined in (5.38), exhibits a closed-loop behavior that can be described by

$$\mathbf{M}\ddot{\tilde{\mathbf{x}}} + \hat{\mathbf{D}}\dot{\tilde{\mathbf{x}}} + \mathbf{K}_{\text{vf}}\tilde{\mathbf{x}} = \mathbf{f}_h, \quad (5.39)$$

where $\hat{\mathbf{D}} = \mathbf{D} + \mathbf{D}_{\text{vf}}$ contains the damping assigned both by the impedance control and the VF constraint enforcement method. The desired dynamics (5.39) can be easily obtained by adding the elastic and damping contributions shown in the right-hand side of (5.38) to the control input defined in (5.3).

Minimum distance

For cubic splines, described by (5.37), there does not exist analytical solutions to the problem of minimum Euclidean distance computation. However, this problem can be tackled by resorting to iterative methods, such as Newton-Raphson (NR). This represents a general method of finding the extrema (minima or maxima) of a given function in an iterative manner. Our goal is to find the spline parameter \bar{s} corresponding to the minimum distance point $\mathbf{x}_d = \Gamma(\bar{s})$. For this purpose, starting from a

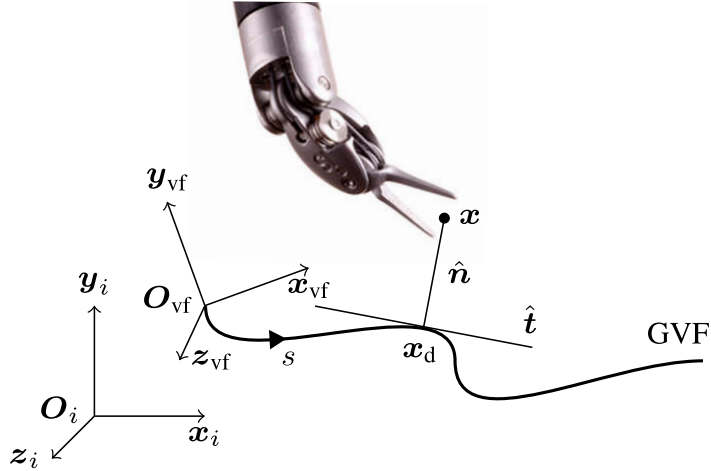


Figure 5.18. Example of Guidance Virtual Fixture (GVF) spline geometry and minimum distance from the robot tool central point \mathbf{x} . $\hat{\mathbf{t}}$ and $\hat{\mathbf{n}}$ denote the tangent and the normal directions, respectively, with origin in \mathbf{x}_d , i.e., the \mathbf{x} nearest point on the curve. $\mathcal{F}_i : \{\mathbf{O}_i; \mathbf{x}_i, \mathbf{y}_i, \mathbf{z}_i\}$ = inertial frame, $\mathcal{F}_{vf} : \{\mathbf{O}_{vf}; \mathbf{x}_{vf}, \mathbf{y}_{vf}, \mathbf{z}_{vf}\}$ = virtual fixture frame.

generic initial condition $s_0 \in [0, 1]$, we use the customary NR update law

$$s_{k+1} = s_k + \frac{\delta(\mathbf{x}, s_k)}{\delta'(\mathbf{x}, s_k)}. \quad (5.40)$$

where $\delta(\mathbf{x}, s) : \mathbb{R}^r \times \mathbb{R} \rightarrow \mathbb{R}$ is the distance function between a point \mathbf{x} and the spline $\Gamma(s)$, that is

$$\delta(\mathbf{x}, s) = \sqrt{(\mathbf{x} - \Gamma(s))^T (\mathbf{x} - \Gamma(s))} \quad (5.41)$$

and $\delta'(\mathbf{x}, s_k)$ denotes the derivative at s_k of (5.41) with respect to the curve parameter s .⁸

⁸Although computationally very efficient, NR method can converge to local maxima/minima. To tackle this problem, we use the previously determined \bar{s} as initial guess for the next minimum distance query. We empirically found this method to be effective for our scope.

5.4.1 Virtual Fixture Generation and Adaptation

We now proceed to describe the VF *generation* technique and the *adaptation* strategies.

VF generation

Our aim is to let the user interactively program VFs for interaction tasks (*e.g.* surgical dissections). Among many other choices, we adopt the policy of recording a set of interaction points that are then used to build the VF geometry. In this way, the surgeon is given the ability to program the VF geometric path by simply interacting with the environment. Interaction detection is possible by measuring forces at the slave side. Recorded points are then fitted through a penalized regression spline fitting algorithm in which coefficients of (5.37) are obtained minimizing the sum of least squares plus a penalty function which suppresses nonlinearity and controls the curve smoothing. Mathematically, the problem is described by

$$\Gamma(s) = \arg \min_{\Gamma(s)} \left(\sum_i (y_i - \Gamma(s_i))^2 + \lambda \int (\Gamma''(s))^2 ds \right) \quad (5.42)$$

where λ is the regularization parameter that penalizes nonlinearities in the path, y_i is the i -th recorded interaction point and $\Gamma''(s)$ is the curve second derivative of $\Gamma(s)$ with respect to its parameter s .

VF adaptation

To adapt a VF preserving the proposed human-in-the-loop approach, a non linear and time varying stiffness profile is adopted for \mathbf{K}_{vf} in (5.39). This is used to both limit the spatial and the temporal influence of a VF. More specifically, we design each non-zero entry of the stiffness matrix to be

$$k_{\text{vf},ii}(\tilde{x}, t) = \beta(\tilde{x}, t) K_{\text{max}} \quad \forall i = 1, \dots, r \quad (5.43)$$

where $k_{\text{vf,ii}}$ is the (i,i) entry of the \mathbf{K}_{vf} matrix, $\beta(\tilde{x}, t)$ is an impedance shaping function, t denotes time and K_{max} is the maximum stiffness value adopted. The definition of $\beta(\tilde{x}, t)$ allows to realize different adaptation strategies as detailed in the following two sections.

Pose adaptation

The pose adaptation strategy consists in positioning a predefined VF geometry into a desired location. With reference to Fig. 5.18 the problem is to define a desired reference frame $\mathcal{F}_{\text{vf,d}} : \{\mathbf{O}_{\text{vf,d}}; \mathbf{x}_{\text{vf,d}}, \mathbf{y}_{\text{vf,d}}, \mathbf{z}_{\text{vf,d}}\}$ to which the current VF reference frame $\mathcal{F}_{\text{vf}} : \{\mathbf{O}_{\text{vf}}; \mathbf{x}_{\text{vf}}, \mathbf{y}_{\text{vf}}, \mathbf{z}_{\text{vf}}\}$ must converge to. As explained, to make this procedure interactive for the user, we adopt the policy of recording a set of slave robot interaction points with the environment that are then used to fit the predefined geometry. To allow the user to freely record new interaction points, we found convenient to limit the spatial influence of the current VF adopting the $\beta(\tilde{x})$ function, qualitatively depicted in Fig. 5.19: this function allows the operator to easily exit the VF constraining zone and freely record new interaction points as sought. For each task space variable $\beta(\tilde{x})$ is mathematically described by

$$\beta(\tilde{x}) = \begin{cases} 0 & \text{if } |\tilde{x}| \geq l \\ \frac{1}{2} \left(1 + \cos \left(\frac{\pi (|\tilde{x}| - d)}{l - d} \right) \right) & \text{otherwise} \\ 1 & \text{if } |\tilde{x}| \leq d \end{cases} \quad (5.44)$$

where l is the distance at which the VF attractive action vanishes completely and d is the threshold distance value inside which the stiffness perceived is K_{max} . Once a set of recorded interaction points is available, the classical least-squares minimization method is used to fit the predefined geometry onto it. This gives the VF pose that minimizes the sum of squared residuals between the VF from the point set, *i.e.* $\mathcal{F}_{\text{vf,d}}$. This pose is then tracked online by suitably defining the pose error between $\mathcal{F}_{\text{vf,d}}$

and \mathcal{F}_{vf} frames. Indicating with $\mathbf{R} = [\mathbf{n}, \mathbf{s}, \mathbf{a}]$ and $\mathbf{R}_d = [\mathbf{n}_d, \mathbf{s}_d, \mathbf{a}_d]$ the rotation matrices associated with \mathcal{F}_{vf} and $\mathcal{F}_{\text{vf,d}}$, respectively, the error can be written as [141]

$$\mathbf{e} = \begin{bmatrix} \mathbf{e}_P \\ \mathbf{e}_O \end{bmatrix} = \begin{bmatrix} \mathbf{O}_{\text{vf,d}} - \mathbf{O}_{\text{vf}} \\ \frac{1}{2}(\mathbf{n} \times \mathbf{n}_d + \mathbf{s} \times \mathbf{s}_d + \mathbf{a} \times \mathbf{a}_d) \end{bmatrix}, \quad (5.45)$$

where $\mathbf{O}_{\text{vf,d}}$ and $\mathbf{O}_{\text{vf}} \in \mathbb{R}^3$ denote the desired and current frame origins, respectively. A simple proportional control law on the error defined in (5.45) allows the error to asymptotically converge to zero guaranteeing a smooth regulation behavior. The resulting error dynamics is indeed

$$\dot{\mathbf{e}} + \mathbf{\Lambda}_p \mathbf{e} = 0 \quad \mathbf{\Lambda}_p > 0, \quad (5.46)$$

where $\mathbf{\Lambda}_p$ is a positive definite diagonal matrix containing control gains that are numerically different to account the non-homogeneous dimensions of the error blocks.

Geometry adaptation

The geometry adaptation strategy consists in transforming the current VF geometry into a desired one.

We suppose that the user is performing a task aided by the currently active VF and necessarily needs to deviate, *e.g.* to comply with the environment deformation. The same interaction points fitting strategy used for the VF generation (see Sect. 5.4.1) can be used to define a new desired geometry. In this case, the user may want to completely deactivate the current VF to freely record new interaction points. To let the impedance parameters of the former VF to gradually vanish, we use the following temporal variation of the stiffness

$$\beta(t) = \frac{1}{2} \left(1 + \cos \left(\frac{\pi (t - t_s)}{t_i - t_s} \right) \right) \quad t_s < t < t_i \quad (5.47)$$

where t_s, t_i are the starting and final instant of the stiffness variation time interval. Once a new desired geometry has been defined, the problem is to redirect the robot tool central point \mathbf{x} towards the new VF.

To achieve a smooth behavior of the system, we let the impedance parameters gradually materialize. This is realized by the following temporal stiffness variation

$$\beta(t) = \frac{1}{2} \left(1 - \cos \left(\frac{\pi (t - t_i)}{t_f - t_i} \right) \right) \quad t_i < t < t_f \quad (5.48)$$

where t_i, t_f are initial and final instants of the positive impedance variation, respectively. To activate/deactivate the VF according to the stiffness variation laws (5.47) and (5.48) different strategies can be adopted. We decided to associate this functionality to the pressing of a dVRK console foot pedal.

It is worth noting that the proposed impedance variation strategy can be also employed to smoothly apply a VF or switch between two of them: switching the attraction point \mathbf{x}_d from one VF to another, when the stiffness reaches zero, guarantees a smooth transition of the system. From a passivity point of view this translates in not generating additional energy into the system.

5.4.2 Performance Evaluation

We now describe the experimental setup and present the VF pose and geometry adaptation experiments.

Experimental setup

The experiments have been performed on the dVRK platform. The robot has been used in teleoperation mode, with one Patient Side Manipulator (PSM) commanded by one Master Tool Manipulator (MTM). The MTM has been controlled using control inputs described in Sect. 5.1.1 with $m_{ii} = 1.5$, $d_{ii} = 0$ being the (i, i) entries of the matrices \mathbf{M} and \mathbf{D} ,

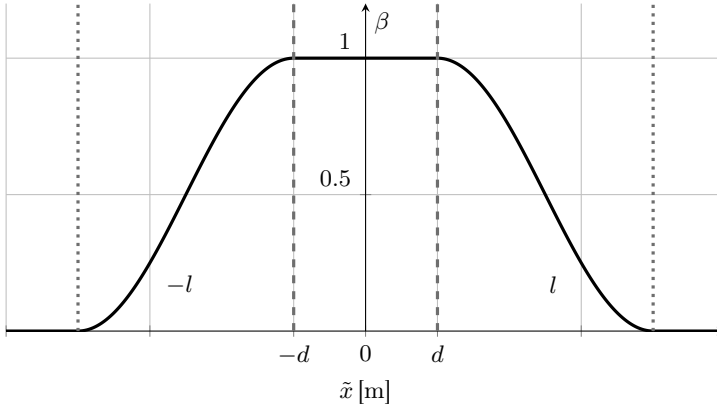


Figure 5.19. VF impedance shaping function $\beta(\tilde{x})$ used to limit the VF spatial influence. \tilde{x} denotes the difference between the desired and current value or the master task space variable.

respectively. The dVRK dynamic parameters used in (5.2) had been previously identified in [41]. The application of torque inputs has been possible thanks to the open-source hardware and software architecture developed by [72]. Given the discrete-time implementation and in order to have a critically damped system behavior, the \mathbf{D}_{vf} has been adapted based on the stiffness such that $d_{\text{vf},ii} = 2\sqrt{m_{ii}k_{\text{vf},ii}}$ where $d_{\text{vf},ii}$ and $k_{\text{vf},ii}$ are the (i, i) entries of the matrices \mathbf{D}_{vf} and \mathbf{K}_{vf} , respectively. Forces at the slave side have been measured making use of the dVRK trocar force sensor developed in [40]. The object used for experiments is a silicon rubber phantom commonly used by surgeons for training. It has been placed on a plastic 3D printed support. The fitting algorithm described by (5.42) has been implemented using the ALGLIB library⁹. The values of the β function limits in (5.44) have been fixed to $d = 0.005$ m and $l = 0.02$ m, while $t_i = t_f = 2.5$ s in (5.47) and (5.48). The maximum stiffness has been fixed to $K_{\text{vf,max}} = 600$ N/m. The energy tank upper threshold has been chosen as $\bar{T} = 0.01$ J while the lower threshold, has been set to $\varepsilon = 0.002$ J. The gap between these two quantities has been designed to be equal to

⁹www.alglib.net

the maximum potential energy that is possible to store using the proposed $\beta(\tilde{x})$ function (see Fig. 5.19), *i.e.* $E_{p,\max} = 1/2K_{\text{vf},\max}d^2$. The VF control loop runs at 5 ms while the teleoperation loop at 1 ms.

Pose adaptation experiment

The pose adaptation strategy (introduced in Sect. 5.4.1) is evaluated in multiple dissection tasks executed in spatially separated regions. Without loss of generality, we fix the geometry of the VF to be a spline representing a straight line. This particular choice is made to present clearer and more intuitive results of the pose adaptation. In this case, the fitting strategy for the VF geometry reduces to a linear regression problem where the desired $\mathbf{y}_{\text{vf},d}$ axis of the $\mathcal{F}_{\text{vf},d}$ reference frame is fitted using the last $n_p = 50$ recorded interaction poses of the slave robot with the environment. In addition, we leave the human operator free to move in the direction orthogonal to the phantom. Every dissection task requires multiple interaction phases with the environment in which points are recorded. The VF pose is continuously updated by fitting these recorded points. With reference to Fig. 5.20 the experiment starts with the VF approximatively placed on the first dissection line. As soon as the robot starts interacting with the environment, the desired stiffness reaches the K_{\max} value and the user is aided in accomplishing the first task by complying with the VF geometry. Around 20s the user switch to another task by exiting the current VF influence area ($|\tilde{x}| > l$). This can be seen in Fig. 5.20(e) in which we register a peak in the estimated force at the master side (≈ 5 N) when the stiffness starts to decrease. Notice that this exiting is made possible by the $\beta(\tilde{x})$ function chosen in (5.44). During the subsequent time period, the user moves in free motion, *i.e.* $f_h \approx 0$ as it can be seen in Fig. 5.20(e) (time interval [20,25]s). A new interaction phase takes place in a spatially separated region at 25s. The new desired VF pose is calculated and the VF is updated following the method described in Sect. 5.4.1. Figure 5.20(d)

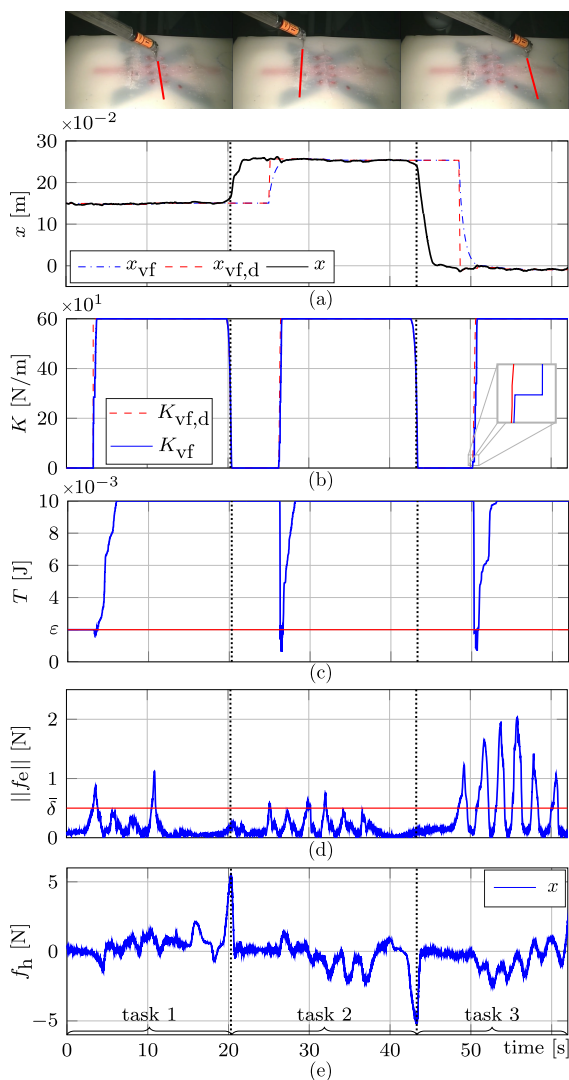


Figure 5.20. VF pose adaptation experiment. Time histories of: (a) VF and tool central point pose along the x direction; (b) stiffness; (c) energy tank level; (d) slave interaction force; (e) human operator force on the master side.

shows the interaction force norm recorded at the slave side together with the chosen threshold $\bar{\delta} = 0.5$ N. This has been used to discriminate between interaction and free motion during the acquisition of points for the VF generation. Also note that, upon the starting of a new task, $x_{\text{vf,d}}$ changes significantly. However, the user does not experience guidance forces until the VF reaches the proximity of the master robot position. Indeed, only when $|\tilde{x}| < l$ the stiffness is increased. This effect is again produced by the chosen $\beta(\tilde{x})$ function (5.44). As mentioned in Sect. 5.1.2, the change in stiffness threatens the system passivity. The energy tank passivity-based control ensures a passive behavior by implementing the change in stiffness only when sufficient tank energy is at disposal. This is evident looking at Figs. 5.20(b) and 5.20(c). In particular, we can notice that the stiffness is kept constant (*i.e.* $\dot{K}_{\text{vf}} = 0$) when the tank is at its lower threshold until it gets replenished, thus not introducing discontinuities. This is made possible through the use of control laws given in (5.12) and (5.16). Fig. 5.20(b) contains a focus around 50 s that emphasizes this behavior.

Finally, looking at the estimated forces in Fig. 5.20(e), it can be noticed that relatively high forces (≈ 5 N) are only applied at the task switching.

Geometry adaptation experiment

The geometry adaptation experiment consists in the refinement of a VF geometry to comply with a possible environmental change. We sought for a simple yet effective method to perform the VF geometry adaptation respecting the human-in-the-loop paradigm. This resulted in a procedure composed by the following steps: (*i*) the user can generate the desired VF geometry using the proposed interactive generation method presented in Sect. 5.4.1; (*ii*) the user can activate the VF by pressing a foot pedal and start performing the task; (*iii*) the user may want to deviate from the previously defined path to comply with the environment/plan change; thus she/he can deactivate the current VF and freely record new interaction

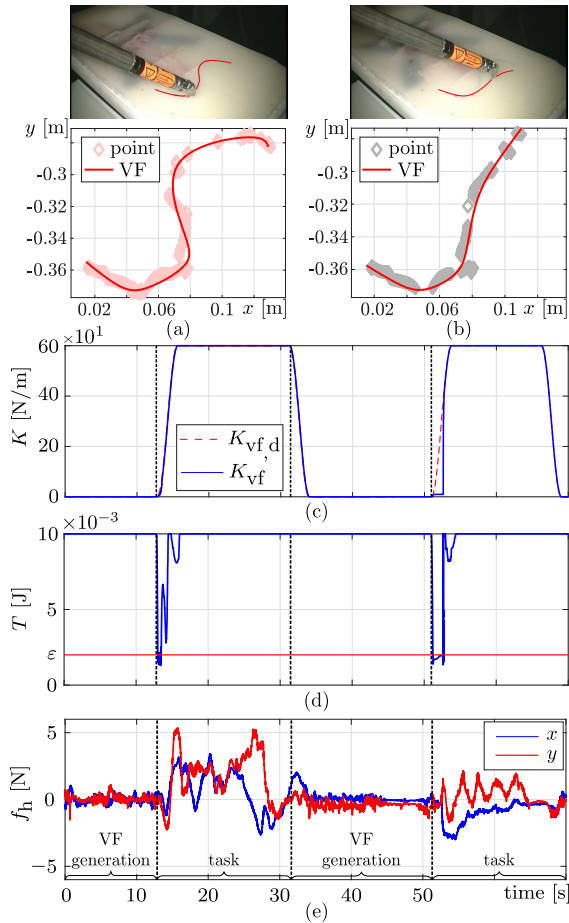


Figure 5.21. Geometry adaptation experiment. (a) First VF geometry generated by the recorded interaction points. (b) Second VF geometry. (c-e) Time histories of: (c) stiffness; (d) tank energy level; (e) human operator estimated force on the master side.

points for generating a new VF path; (iv) the user can activate the latest generated VF by releasing the foot pedal and be aided during the task completion. We have performed an experiment involving the above defined steps. Referring to Fig. 5.21, the experiment starts with the first VF

generation (time interval $[0, 13]$ s) in which interaction points are recorded and the path is generated by the fitting algorithm¹⁰. The resulting VF geometry is shown in Fig. 5.21(a) as a solid red line, together with the corresponding interaction points (in pink). Subsequently, the VF is activated and the dissection task is started (time interval $[13, 32]$ s). During the task the surgeon decides to change the previously defined VF geometry to comply with a possible plan/environmental change. First, the current VF is deactivated and a new VF generation phase is undertaken (time interval $[32, 51]$ s). To deactivate the current VF the impedance is brought to zero following the variation law presented in (5.47) by pressing a foot pedal. Newly recorded points are fitted as explained in Sect. 5.4.1 to generate a new VF. The resulting VF geometry is represented in Fig. 5.21(b) as a solid red line together with interaction points in gray. The VF is then activated to complete the task (time interval $[51, 70]$ s). Figure. 5.21(c) contains the time history of the desired stiffness variation according to the laws (5.47) and (5.48). Even in this case, the passivity of the system is preserved by means of the energy tanks passivity-based control described in Sect. 5.1.2. Figure 5.21(d) contains the time evolution of the tank energy used to implement the stiffness variation. The effect of the passivity-based control action is evident in 5.21(c) (around time 51 s) where the tank is discharged and the stiffness is kept constant until it gets replenished. Finally, figure 5.21(e) shows human operator's estimated forces on the master side during the task execution: it can be seen that when the VF is activated the user is aided by guidance forces in performing the task.

¹⁰We note that the VF generation time is negligible with respect to recording phase, thus we can assume it is an instantaneous process.

5.5 Conclusions

In this chapter, we discussed the use of advanced control strategies to reduce the surgeon mental and physical workload during repetitive and tedious surgical tasks. Focusing on the suturing and dissection procedure, we showed different approaches aimed to increase the level of the robot autonomy reducing the surgeon stress. In Sec. 5.2 we described preliminary results promising to improve the robot contextual knowledge of the surgical environment. In Sec. 5.3 we propose a comparison of different control modalities, with different level of robot autonomy, aimed at reducing the number of DoFs directly under the surgeon control. We prove with a complete user study that an human-in-the-loop approach can be used to improve the surgeon precision, reducing his/her workload and at the same time leaving to the surgeon the total control of the procedure. More in detail, we prove that, in the suturing procedure, solutions in which at least one degree of freedom, for the needle motion, is under the surgeon control are preferred by the surgeons.

Finally in Sec. 5.4 we showed simple and effective methods for VF adaptation during a surgical dissection task. This work gives us also the possibility to investigate the stability of the system when variable stiffness controllers are adopted. We also note that the VF path generation proposed in Sec. 5.4 constitutes a simple yet effective method of programming a VF path in real-time. This can be used whenever the desired path is not definable pre-operatively. For instance, tumour resections are some of the most critical and precision-demanding procedures that might benefit from the proposed approach.

Chapter 6

Conclusions

In this thesis, we discussed about surgeon sensory-motor enhancement in minimally invasive robotic surgery through novel innovative devices and control strategies. We had the opportunity to work closely with surgeons of the Policlinico of Naples on both the da Vinci research kit and the da Vinci Xi robotic platform. We worked to find advantages and issues of the current surgical platforms and identify the best strategies to improve both the surgeon capabilities and comfort. As discussed in Chapter 1, enhance the surgeon's comfort, capabilities and ergonomics allows improve the surgery results, increase safety, increase patient's outcomes and also enable new surgical procedures. In this thesis, we worked in three different direction: (i) improve the robot sensing capability to enhance the surgeon contextual knowledge of the surgical environment; (ii) design new innovative devices aimed at improving the robot, and hence the surgeon, manipulation capabilities and dexterity; (iii) design new shared control strategies to reduce the surgeon physical-cognitive workload by increasing the robot intelligence in surgical tasks in which the robot results to be more precise and reliable. The provided results have been validated with real prototypes, simulated environments and also in real surgical scenarios

as discussed in previous Chapters. We found that both the innovative devices presented and the control strategies developed give to the surgeon a better understanding and control of the surgical procedure. We presented different strategies aimed at improving the surgeon ergonomics at different levels such as sensing, actuation and comfort with the goal of presenting some innovative solutions but at the same time give to the reader an idea of issues and potentiality of the covered topics. We think also that our work on the dVRK dynamic model identification and simulation can be an useful tool for the research community helping to speed up the search with the dVRK. Most importantly, during this three years, we had the opportunity to listen to surgeons opinion and understanding better the impact of our solutions. Obviously, surgeons want have constantly the control of the environment and the robot not have to be a hindrance. Whatever assistance strategy or devices must leave the surgeon the ability to perform the surgical procedure how they are used to but at the same time increasing his/her capabilities. Hence, more than in other scenarios the researcher in this field must focus on the user interface and user experience, safety and reliability of every new improvement included in the surgical systems. We tried to do that founding our research on specific keywords, such as, human-in-the-loop, non-invasiveness, in order to enhance the surgeon capabilities, to open the way for new possibilities, but at the same time giving the surgeon the sensation to have full control of the situation.

Bibliography

- [1] *DVRK wiki web page.*
- [2] *Johns Hopkins University DVRK controller git repositories.*
- [3] *Software package, Fiber Bragg Gratings (Second Edition)* (Raman Kashyap, ed.), Academic Press, Boston, second edition ed., 2010.
- [4] D. Aarno, S. Ekvall, and D. Kragic, *Adaptive virtual fixtures for machine-assisted teleoperation tasks*, IEEE Int. Conf. on Robotics and Automation, 2005, pp. 1139–1144.
- [5] Niki Abolhassani, Rajni Patel, and Mehrdad Moallem, *Needle insertion into soft tissue: A survey*, Medical Engineering and Physics **29** (2007), no. 4, 413–431.
- [6] Thomas Ahlering, *da Vinci prostatectomy 3-arm and 4-arm approach*, Intuitive Surgical, Inc., 2013.
- [7] Narges Ahmidi, Lingling Tao, Shahin Sefati, Yixin Gao, Colin Lea, Benjamin Bejar, Luca Zappella, Sanjeev Khudanpur, Rene Vidal, and Gregory D Hager, *A dataset and benchmarks for segmentation and recognition of gestures in robotic surgery*, IEEE Transactions on Biomedical Engineering (2017), 2025–2041.

- [8] Stevenson AL, Solomon MJ, Lumley JW, and et al, *Effect of laparoscopic-assisted resection vs open resection on pathological outcomes in rectal cancer: The alacart randomized clinical trial*, JAMA **314** (2015), no. 13, 1356–1363.
- [9] K. Ayusawa and Y. Nakamura, *Identification of standard inertial parameters for large-dof robots considering physical consistency*, IEEE/RSJ Int. Conference on Intelligent Robots and Systems, 2010, pp. 6194–6201.
- [10] Luca Ballan, Aparna Taneja, Jürgen Gall, Luc Van Gool, and Marc Pollefeys, *Motion capture of hands in action using discriminative salient points*, European Conference on Computer Vision, Springer, 2012, pp. 640–653.
- [11] R. Berguer, *Surgery and ergonomics*, Archives of Surgery **134** (1999), no. 9, 1011–1016.
- [12] P. Berthet-Rayne, M. Power, H. King, and G. Z. Yang, *Hubot: A three state human-robot collaborative framework for bimanual surgical tasks based on learned models*, IEEE International Conference on Robotics and Automation, May 2016, pp. 715–722.
- [13] Alessandro Bettini, Samuel Lang, Allison M. Okamura, and Gregory D. Hager, *Vision assisted control for manipulation using virtual fixtures*, IEEE/RSJ Int. Conf. on Intelligent Robots and Systems, 2001, pp. 1171–1176.
- [14] Stuart A. Bowyer, Brian L. Davies, and Ferdinando Rodriguez Y Baena, *Active constraints/virtual fixtures: A survey*, IEEE Transactions on Robotics **30** (2014), no. 1, 138–157.
- [15] U Bracale, G Azioni, M Rosati, M Barone, and G Pignata, *Deep pelvic endometriosis (adamyian iv stage): multidisciplinary laparo-*

- scopic treatments.*, Acta Chirurgica Iugoslavica **56** (2009), no. 1, 41–46.
- [16] U Bracale, F Lazzara, G Merola, J Andreuccetti, M Barone, and G Pignata, *Single access laparoscopic left hemicolectomy with or without inferior mesenteric artery preservation: our preliminary experience*, Minerva chirurgica **68** (2013), no. 3, 315–320.
- [17] David B Camarillo, M S, Thomas M Krummel, M D, J Kenneth Salisbury, and D Ph, *Robotic technology in surgery : past , present , and future*, The American Journal of Surgery **188** (2004), no. October, 2–15.
- [18] M. C. Cavusoglu, W. Williams, F. Tendick, and S. S. Sastry, *Robotics for telesurgery: Second generation berkeley/ucsf laparoscopic telesurgical workstation and looking towards the future applications*, Industrial Robot: An International Journal **30** (2003), no. 1, 22–29.
- [19] Tan Fung Chan and R. V. Dubey, *A weighted least-norm solution based scheme for avoiding joint limits for redundant joint manipulators*, IEEE Transactions on Robotics and Automation **11** (1995), no. 2, 286–292.
- [20] Jaewon Chang, *Robust needle recognition using Artificial Neural Network (ANN) and Random Sample Consensus (RANSAC)*, Applied Imagery Pattern Recognition Workshop (AIPR), 2012 IEEE (2012), 1–3.
- [21] Yang Chen and Gérard Medioni, *Object modelling by registration of multiple range images*, Image and vision computing **10** (1992), no. 3, 145–155.
- [22] Zihan Chen, Anton Deguet, Russell H. Taylor, and Peter Kazanzides, *Software architecture of the da vinci research kit*, Proceedings - 2017

- 1st IEEE International Conference on Robotic Computing, IRC 2017, 2017, pp. 180–187.
- [23] Zihan Chen, Anand Malpani, Preetham Chalasani, Anton Deguet, S Swaroop Vedula Vedula, Russell H Taylor, and Peter Kazanzides, *Virtual Fixture Assistance for Needle Passing and Knot Tying*, IEEE/RSJ Int. Conference on Intelligent Robots and Systems (2016), 2343–2350.
- [24] A. Cirillo, F. Ficuciello, C. Natale, S. Pirozzi, L. Villani, and B. Siciliano, *A conformable force/tactile skin for physical human-robot interaction*, IEEE Robotics and Automation Letters **1** (2015), 41–48.
- [25] Robert D Cook, *Finite element modeling for stress analysis*, Wiley, 1994.
- [26] Martin O Culjat, Chih-Hung King, Miguel L Franco, Catherine E Lewis, James W Bisley, Erik P Dutson, and Warren S Grundfest, *A tactile feedback system for robotic surgery.*, International Conference of the IEEE Engineering in Medicine and Biology Society. (2008), 1930–1934.
- [27] Diego LÃşpez De Ipiña, Paulo R S Mendonça, Andy Hopper, D. L. Ipiña, P. R. S. Mendon\{c\}a, and Andy Hopper, *TRIP: A low-cost vision-based location system for ubiquitous computing*, Personal and Ubiquitous Computing **6** (2002), no. 3, 206–219.
- [28] Alessandro De Luca and Raffaella Mattone, *Sensorless robot collision detection and hybrid force/motion control*, IEEE Int. Conference on Robotics and Automation (2005), no. April, 999–1004.
- [29] Fabien Despinoy, David Bouget, Germain Forestier, Cédric Penet, Nabil Zemiti, Philippe Poignet, and Pierre Jannin, *Unsupervised*

- Trajectory Segmentation for Surgical Gesture Recognition in Robotic Training*, IEEE Transactions on Biomedical Engineering **63** (2016), no. 6, 1280–1291.
- [30] N. C. DuPont, R. Chandrasekhar, G Wilding, and K. A. Guru, *Current trends in robot assisted surgery: a survey of*, The international journal of medical robotics + computer assisted surgery : MRCAS **6** (2010), 468–472.
- [31] S. Ekvall, D. Aarno, and D. Kragic, *Online task recognition and real-time adaptive assistance for computer-aided machine control*, IEEE Trans. Robot. **22** (2006), no. 5, 1029–1033.
- [32] Oussama Elhage, Ben Challacombe, and Declan Murphy, *The Evolution and Ergonomics of Robotic-Assisted Surgical Systems*, Researchgate.Net (2007), no. August.
- [33] Olaf Eitzmuß, Michael Keckeisen, and Wolfgang Straßer, *A fast finite element solution for cloth modelling*, Computer Graphics and Applications, 2003. Proceedings. 11th Pacific Conference on, IEEE, 2003, pp. 244–251.
- [34] François Faure, Christian Duriez, Hervé Delingette, Jérémie Al-lard, Benjamin Gilles, Stéphanie Marchesseau, Hugo Talbot, Hadrien Courtecuisse, Guillaume Bousquet, Igor Peterlik, et al., *Sofa: A multi-model framework for interactive physical simulation*, Soft Tissue Biomechanical Modeling for Computer Assisted Surgery, Springer, 2012, pp. 283–321.
- [35] F Fazioli, F Ficuciello, G A Fontanelli, B Siciliano, and L Villani, *Implementation of a soft-rigid collision detection algorithm in an open-source engine for surgical realistic simulation*, IEEE International Conference on Robotics and Biomimetics, 2016, pp. 2204–2208.

- [36] F. Ferraguti, C. Secchi, and C. Fantuzzi, *A tank-based approach to impedance control with variable stiffness*, Proc. IEEE Int'l Conference on Robotics and Automation (2013), 4948–4953.
- [37] F. Ficuciello, L. Villani, and B. Siciliano, *Variable impedance control of redundant manipulators for intuitive human-robot physical interaction*, IEEE Transactions on Robotics **31** (2015), 850–863.
- [38] Fanny Ficuciello, Luigi Villani, and Bruno Siciliano, *Impedance control of redundant manipulators for safe human-robot collaboration*, Acta Polytechnica Hungarica, Journal of Applied Science, Special Issue on Recent Advances in Robotics **13** (2016), 223–238.
- [39] Andrew Fitzgibbon, Maurizio Pilu, and Robert B. Fisher, *Direct least square fitting of ellipses*, IEEE Transactions on Pattern Analysis and Machine Intelligence **21** (1999), no. 5, 476–480.
- [40] G A Fontanelli, L Buonocore, F Ficuciello, L Villani, and B Siciliano, *A novel force sensing integrated into the trocar for minimally invasive robotic surgery*, IEEE/RSJ Int. Conference on Intelligent Robots and Systems, 2017, pp. 131–136.
- [41] G .A. Fontanelli, F. Ficuciello, L. Villani, and B. Siciliano, *Modelling and identification of the da Vinci research kit robotic arms*, IEEE/RSJ Int. Conference on Intelligent Robots and Systems, 2017, pp. 1464–1469.
- [42] G A Fontanelli, M Selvaggio, M Ferro, F Ficuciello, M Vendittelli, and B Siciliano, *A V-REP Simulator for the da Vinci Research Kit Robotic Platform*.
- [43] Giuseppe Andrea Fontanelli, Mario Selvaggio, Luca Rosario Buonocore, Fanny Ficuciello, Luigi Villani, and Bruno Siciliano, *A New*

- Laparoscopic Tool with In-Hand Rolling Capabilities for Needle Re-orientation*, IEEE Robotics and Automation Letters **3** (2018), no. 3, 2354 – 2361.
- [44] Giuseppe Andrea Fontanelli, Guang-zhong Yang, and Bruno Siciliano, *A comparison of assistive methods for suturing in MIRS*, IEEE/RSJ Int. Conf. on Intelligent Robots and Systems, 2018.
- [45] Jason Franasiak, Renatta Craven, Prithima Mosaly, and Paola A. Gehrig, *Feasibility and Acceptance of a Robotic Surgery Ergonomic Training Program*, JSLs : Journal of the Society of Laparoendoscopic Surgeons **18** (2014), no. 4, e2014.00166.
- [46] Barbara Frank, Rüdiger Schmedding, Cyrill Stachniss, Matthias Teschner, and Wolfram Burgard, *Learning the elasticity parameters of deformable objects with a manipulation robot*, Intelligent Robots and Systems (IROS), 2010 IEEE/RSJ International Conference on, IEEE, 2010, pp. 1877–1883.
- [47] M. Gabbicini and Antonio Bicchi, *On the role of hand synergies in the optimal choice of grasping forces*, Robotics: Science and Systems (Zaragoza), 2010.
- [48] M. Gautier, *Numerical calculation of the base inertial parameters*, IEEE Int. Conference on Robotics and Automation, 1990, pp. 1020–1025.
- [49] M. Gautier and W. Khalil, *Exciting trajectories for the identification of base inertial parameters of robots*, Int. Journal of Robotics Research **11** (1992), 362–375.
- [50] M. Gautier and G. Venture, *Identification of standard dynamic parameters of robots with positive definite inertia matrix*, 2013

- IEEE/RSJ Int. Conference on Intelligent Robots and Systems, 2013, pp. 5815–5820.
- [51] Andreas Geiger, Martin Roser, and Raquel Urtasun, *Efficient large-scale stereo matching*, Asian conference on computer vision (2010), 25–38.
- [52] M.C. Grant and P. Boyd, *The cvx users' guide*, 2015.
- [53] Roger M. Greenhalgh, *Techniques of anastomosis*, Vascular Surgical Techniques, 1984, pp. 5 – 13.
- [54] Thomas R Grieve, John M Hollerbach, and Stephen A Mascaro, *Force prediction by fingernail imaging using active appearance models*, World Haptics Conference (WHC), 2013, IEEE, 2013, pp. 181–186.
- [55] G.S. Guthart and J.K. Salisbury, *The intuitiveTM telesurgery system: overview and application*, IEEE Int. Conference on Robotics and Automation, 2000, pp. 618–621.
- [56] B. Hannaford and Jee-Hwan Ryu, *Time-domain passivity control of haptic interfaces*, IEEE Trans. Robot. Autom. **18** (2002), no. 1, 1–10.
- [57] Sandra G. Hart, *Nasa-task load index (nasa-tlx); 20 years later*, The Human Factors and Ergonomics Society Annual Meeting **50** (2006), no. 9, 904–908.
- [58] Robert Haslinger, Patrick Leyendecker, and Ulrich Seibold, *A fiberoptic force-torque-sensor for minimally invasive robotic surgery*, IEEE International Conference on Robotics and Automation, 2013.
- [59] E. A M Heijnsdijk, J. Dankelman, and D. J. Gouma, *Effectiveness of grasping and duration of clamping using laparoscopic graspers*,

- Surgical Endoscopy and Other Interventional Techniques **16** (2002), no. 9, 1329–1331.
- [60] Dimitris Hristu, Nicola Ferrier, and Roger W Brockett, *The performance of a deformable-membrane tactile sensor: basic results on geometrically-defined tasks*, Robotics and Automation, 2000. Proceedings. ICRA'00. IEEE International Conference on, vol. 1, IEEE, 2000, pp. 508–513.
- [61] K. Ikuta, T. Hasegawa, and S. Daifu, *Hyper redundant miniature manipulator "hyper finger" for remote minimally invasive surgery in deep area*, IEEE International Conference on Robotics and Automation (Taipei, Taiwan), 2003, pp. 1098–1102.
- [62] Santosh Iyer, Thomas Looi, and James Drake, *A single arm, single camera system for automated suturing*, Proceedings - IEEE International Conference on Robotics and Automation (2013), 239–244.
- [63] R C Jackson, V Desai, J P Castillo, and M C Çavuşoğlu, *Needle-tissue interaction force state estimation for robotic surgical suturing*, 2016 IEEE/RSJ International Conference on Intelligent Robots and Systems (IROS) (2016), 3659–3664.
- [64] Russell C. Jackson and M. Cenk Cavusoglu, *Needle path planning for autonomous robotic surgical suturing*, IEEE Int.Conference on Robotics and Automation (2013), 1669–1675.
- [65] R. Jansen, K. Hauser, N. Chentanez, F. van der Stappen, and K. Goldberg, *Surgical retraction of non-uniform deformable layers of tissue: 2d robot grasping and path planning*, 2009 IEEE/RSJ International Conference on Intelligent Robots and Systems, 2009, pp. 4092–4097.

- [66] Paul J. Johnson, David E. Schmidt, and Umamaheswar Duvvuri, *Output control of da Vinci surgical system's surgical graspers*, Journal of Surgical Research **186** (2014), 56–62.
- [67] Ankur Kapoor and Russell H. Taylor, *A constrained optimization approach to virtual fixtures for multi-handed tasks*, Proceedings - IEEE International Conference on Robotics and Automation (2008), 3401–3406.
- [68] Raman Kashyap and J. M. Lopez Higuera, *Handbook of optical fiber sensing technology; fiber grating echnology: Theory, photosensitivity, fabrication and characterization*, John Wiley and Sons, 2002.
- [69] M. S. Kavic, *Hand-assisted laparoscopic surgery - hals*, Journal of the Society of Laparoendoscopic Surgeons **5** (2001), no. 2, 101–103.
- [70] B. S. Kawasaki, K. O. Hill, D. C. Johnson, and Y. Fujii, *Narrow-band bragg reflectors in optical fibers*, Opt. Lett. **3** (1978), no. 2, 66–68.
- [71] P. Kazanzides, Z. Chen, A. Deguet, G. S. Fischer, R. H. Taylor, and S. P. DiMaio, *An open-source research kit for the da Vinci surgical system*, IEEE International Conference on Robotics and Automation, May 2014, pp. 6434–6439.
- [72] Peter Kazanzidesf, Zihan Chen, Anton Deguet, Gregory S. Fischer, Russell H. Taylor, and Simon P. Dimaio, *An open-source research kit for the da Vinci Surgical System*, IEEE Int. Conference on Robotics and Automation (2014), 6434–6439.
- [73] Jelizaveta Konstantinova, Allen Jiang, Kaspar Althoefer, Prokar Dasgupta, and Thrishantha Nanayakkara, *Implementation of tactile sensing for palpation in robot-assisted minimally invasive surgery: A review*, IEEE Sensors Journal **14** (2014), no. 8.

- [74] K. Kronander and A. Billard, *Stability considerations for variable impedance control*, IEEE Trans. Robot. **32** (2016), no. 5, 1298–1305.
- [75] Nikolaos Kyriazis and Antonis Argyros, *Physically plausible 3d scene tracking: The single actor hypothesis*, Proceedings of the IEEE Conference on Computer Vision and Pattern Recognition, 2013, pp. 9–16.
- [76] Chiara Talignani Landi, Federica Ferraguti, Lorenzo Sabattini, Cristian Secchi, and Cesare Fantuzzi, *Admittance Control Parameter Adaptation for Physical Human-Robot Interaction*, (2017), 2911–2916.
- [77] Frederick Largilliere, Valerian Verona, Eulalie Coevoet, Mario Sanz-Lopez, Jeremie Dequidt, and Christian Duriez, *Real-time control of soft-robots using asynchronous finite element modeling*, 2015 IEEE International Conference on Robotics and Automation (ICRA), IEEE, 2015, pp. 2550–2555.
- [78] C.L. Lawson and R.J. Hanson, *Perturbation bounds for the solution of problem ls*, vol. 161, 1974.
- [79] D. Lee and K. Huang, *Passive-set-position-modulation framework for interactive robotic systems*, IEEE Trans. Robot. **26** (2010), no. 2, 354–369.
- [80] Dong Hyuk Lee, Uikyum Kim, Tauseef Gulrez, Woon Jong Yoon, Blake Hannaford, and Hyouk Ryeol Choi, *A Laparoscopic Grasping Tool with Force Sensing Capability*, IEEE/ASME Transactions on Mechatronics **21** (2016), no. 1, 130–141.
- [81] Simon Leonard, Azad Shademan, Yonjae Kim, Axel Krieger, and Peter C.W. Kim, *Smart Tissue Anastomosis Robot (STAR): Accuracy evaluation for supervisory suturing using near-infrared fluorescent*

- markers*, Proceedings - IEEE International Conference on Robotics and Automation (2014), 1889–1894.
- [82] M Li, M Ishii, and R H Taylor, *Spatial motion constraints using virtual fixtures generated by anatomy*, IEEE Transaction on Robotics **vol** (2007), no. April, 4–19.
- [83] Ming Li, Ankur Kapoor, and Russell H. Taylor, *Tele robotic control by virtual fixtures for surgical applications*, Springer Tracts in Advanced Robotics **31** (2007), 381–401.
- [84] Ziyun Li, Ling Jin, Jochen Lang, and Emil Petriu, *Dissection Simulation of Deformable Objects using the Extended Finite Element Method*, Haptic, Audio and Visual Environments and Games (HAVE), 2014 IEEE International Symposium on (2014).
- [85] Qiaokang Liang, Dan Zhang, Gianmarc Coppola, Yaonan Wang, Sun Wei, and Yunjian Ge, *Multi-dimensional MEMS/micro sensor for force and moment sensing: A review*, IEEE Sensors Journal **14** (2014), no. 8, 2643–2657.
- [86] Hongbin Liu, Jichun Li, Xiaojing Song, Lakmal D Seneviratne, and Kaspar Althoefer, *Rolling Indentation Probe for Tissue Abnormality Identification During Minimally Invasive Surgery Rolling Indentation Probe for Tissue Abnormality Identification during Minimally Invasive Surgery*, IEEE Transactions on Robotics, no. July, 2011.
- [87] Xuan Liu, Iulian I Iordachita, Xingchi He, Russell H Taylor, and Jin U Kang, *Miniature fiber-optic force sensor for vitreoretinal microsurgery based on low-coherence Fabry-Pérot interferometry.*, Proceedings of SPIE—the International Society for Optical Engineering **8218** (2013), no. 5, 82180O.

- [88] M. J. H. Lum, D. Trimble, J. Rosen, K. Dodero II, H. H. King, G. Sankaranarayanan, J. Doshier, B. Martin-Anderson R. Leuschke, M. N. Sinanan, and B. Hannaford, *Multidisciplinary approach for developing a new minimally invasive surgical robotic system*, IEEE/RAS-EMBS Int. Conf. Biomed. Robot. Biomechatoron. (Pisa, Italy), 2006, pp. 841–846.
- [89] Haifeng Luo and Shuxin Wang, *Multi-manipulation with a metamorphic instrumental hand for robot-assisted minimally invasive surgery*, The 2011 IEEE/ICME International Conference on Complex Medical Engineering (2011), 363–368.
- [90] Mohamed Mabrouk, Michael Frumovitz, Marilyn Greer, Kathleen M Schmeler, Pamela T Soliman, and T Pedro, *Trends in laparoscopic and robotic surgery among gynecologic oncologists : A survey update*, **112** (2009), no. 3, 501–505.
- [91] Emanuele Magrini, Fabrizio Flacco, and Alessandro De Luca, *Control of Generalized Contact Motion and Force in Physical Human-Robot Interaction*, International Conference on Robotics and Automation (2015), 2298–2304.
- [92] M. Malvezzi, G. Gioioso, G. Salvietti, and D. Prattichizzo, *Syngrasp: A matlab toolbox for underactuated and compliant hands*, Robotics Automation Magazine, IEEE **22** (2015), no. 4, 52–68.
- [93] Panadda Marayong and Allison M. Okamura, *Speed-accuracy characteristics of human-machine cooperative manipulation using virtual fixtures with variable admittance*, Human Factors **46** (2004), no. 3, 518–532.
- [94] D.T. Martin, J.A. Woodard, C.J. Shurtleff, and A.C. Yoo, *Articulating needle driver*, November 15 2012, US Patent App. 13/466,188.

- [95] Stephen A Mascaró and H Harry Asada, *Photoplethysmograph finger-nail sensors for measuring finger forces without haptic obstruction*, IEEE Transactions on robotics and automation **17** (2001), no. 5, 698–708.
- [96] V. F. Mohr, V. Falk, A. Diegeler, T. Walther, F.J. Gummert, J. Bucerius, S. Jacobs, and R. Autschbach, *Computer-enhanced "robotic" cardiac surgery: experience in 148 patients*, Journal of thoracic cardiovascular surgery (2001), 842–853.
- [97] Luca Morelli, Simone Guadagni, Maria Donatella Mariniello, Roberta Pisano, Cristiano D'Isidoro, Mario Antonio Belluomini, Giovanni Caprili, Giulio Di. Candio, and Franco Mosca, *Robotic giant hiatal hernia repair: 3-year prospective evaluation and review of the literature*, The International Journal of Medical Robotics and Computer Assisted Surgery **11** (2015), no. 1, 1–7, RCS-13-0162.R3.
- [98] G. P. Moustris, S. C. Hiridis, K. M. Deliparaschos, and K. M. Konstantinidis, *Evolution of autonomous and semi-autonomous robotic surgical systems: a review of the literature*, THE INTERNATIONAL JOURNAL OF MEDICAL ROBOTICS AND COMPUTER ASSISTED SURGERY, 2011.
- [99] Matthias Müller and Markus Gross, *Interactive virtual materials*, Proceedings of Graphics Interface 2004, Canadian Human-Computer Communications Society, 2004, pp. 239–246.
- [100] R. Muradore, D. Bresolin, L. Geretti, P. Fiorini, and T. Villa, *Robotic Surgery*, IEEE Robotics Automation Magazine **18** (2011), no. 3, 24–32.
- [101] Adithyavairavan Murali, Siddarth Sen, Ben Kehoe, Animesh Garg, Seth McFarland, Sachin Patil, W. Douglas Boyd, Susan Lim, Pieter

- Abbeel, and Ken Goldberg, *Learning by observation for surgical sub-tasks: Multilateral cutting of 3D viscoelastic and 2D Orthotropic Tissue Phantoms*, Proceedings - IEEE International Conference on Robotics and Automation **2015-June** (2015), no. June, 1202–1209.
- [102] F. Nageotte, P. Zanne, C. Doignon, and M. de Mathelin, *Stitching Planning in Laparoscopic Surgery: Towards Robot-assisted Suturing*, The International Journal of Robotics Research **28** (2009), no. 10, 1303–1321.
- [103] Matthieu Nesme, Yohan Payan, and François Faure, *Efficient, physically plausible finite elements*, Eurographics, 2005.
- [104] Richard A Newcombe, Andrew J Davison, Shahram Izadi, Pushmeet Kohli, Otmar Hilliges, Jamie Shotton, David Molyneaux, Steve Hodges, David Kim, and Andrew Fitzgibbon, *Kinectfusion: Real-time dense surface mapping and tracking*, Mixed and augmented reality (ISMAR), 2011 10th IEEE international symposium on, IEEE, 2011, pp. 127–136.
- [105] Camran Nezhat, Ofer Lavie, Madeleine Lemyre, Ofer Gemer, Lisa Bhagan, and Cean Nezhat, *Laparoscopic hysterectomy with and without a robot: Stanford experience.*, JSLs : Journal of the Society of Laparoendoscopic Surgeons / Society of Laparoendoscopic Surgeons **13** (2009), no. 2, 125–128.
- [106] K. A. Nichols and A. M. Okamura, *A framework for multilateral manipulation in surgical tasks*, IEEE Transactions on Automation Science and Engineering **13** (2016), no. 1, 68–77.
- [107] Iason Oikonomidis, Nikolaos Kyriazis, and Antonis A Argyros, *Full dof tracking of a hand interacting with an object by modeling occlusions and physical constraints*, 2011 International Conference on Computer Vision, IEEE, 2011, pp. 2088–2095.

- [108] Allison M Okamura, *Haptic Feedback in Robot-Assisted Minimally Invasive Surgery*, *Current opinion in urology* **19** (2009), no. 1, 102–107.
- [109] Allison M. Okamura, Christina Simone, and Mark D. O’Leary, *Force modeling for needle insertion into soft tissue*, *IEEE Transactions on Biomedical Engineering* (2004).
- [110] A.M. Okamura, *Methods for haptic feedback in teleoperated robot-assisted surgery*, *Industrial Robot: An International Journal* (2004).
- [111] G. Palli, C. Melchiorri, G. Vassura, U. Scarcia, L. Moriello, G. Berselli, A. Cavallo, G. De Maria, C. Natale, S. Pirozzi, C. May, F. Ficuciello, and B. Siciliano, *The dexmart hand: Mechatronic design and experimental evaluation of synergy-based control for human-like grasping*, *Int Journal of Robotics Research* **33** (2014), 799–824.
- [112] Shinsuk Park, Robert D. Howe, and David F. Torchiana, *Virtual fixtures for robotic cardiac surgery*, *Medical Image Computing and Computer-Assisted Intervention*, Springer Berlin Heidelberg, 2001, pp. 1419–1420.
- [113] Omeed H. Paydar, Christopher R. Wottawa, Richard E. Fan, Erik P. Dutton, Warren S. Grundfest, Martin O. Culjat, and Rob N. Candler, *Fabrication of a thin-film capacitive force sensor array for tactile feedback in robotic surgery*, *Proceedings of the Annual International Conference of the IEEE Engineering in Medicine and Biology Society*, EMBS (2012), 2355–2358.
- [114] C. J. Perez-Del-Pulgar, J. Smisek, V. F. Munoz, and A. Schiele, *Using learning from demonstration to generate real-time guidance for haptic shared control*, *IEEE International Conference on Systems, Man, and Cybernetics*, Oct 2016, pp. 3205–3210.

- [115] Brian S. Peters, Priscila R. Armijo, Crystal Krause, Songita A. Choudhury, and Dmitry Oleynikov, *Review of emerging surgical robotic technology*, *Surgical Endoscopy and Other Interventional Techniques* **32** (2018), no. 4, 1636–1655.
- [116] Antoine Petit, Fanny Ficuciello, Giuseppe Andrea Fontanelli, Luigi Villani, and Bruno Siciliano, *Using physical modeling and RGB-D registration for contact force sensing on deformable objects*, *IEEE Int. Conference on Informatics in Control, Automation and Robotics*, 2017, pp. 24–33.
- [117] Antoine Petit, Vincenzo Lippiello, Giuseppe Andrea Fontanelli, and Bruno Siciliano, *Tracking elastic deformable objects with an rgb-d sensor for a pizza chef robot*, *Robotics and Autonomous Systems* **88** (2017), 187 – 201.
- [118] Antoine Petit, Vincenzo Lippiello, Giuseppe Andrea Fontanelli, and Bruno Siciliano, *Tracking elastic deformable objects with an RGB-D sensor for a pizza chef robot*, *Robotics and Autonomous Systems* **88** (2017), no. September, 187–201.
- [119] Antoine Petit, Vincenzo Lippiello, and Bruno Siciliano, *Real-time tracking of 3d elastic objects with an rgb-d sensor*, *Intelligent Robots and Systems (IROS), 2015 IEEE/RSJ International Conference on* (2015).
- [120] ———, *Tracking fractures of deformable objects in real-time with an rgb-d sensor*, *3D Vision (3DV), 2015 International Conference on, IEEE, 2015*, pp. 632–639.
- [121] P. Polygerinos, L. D. Seneviratne, R. Razavi, T. Schaeffter, and K. Althoefer, *Triaxial catheter-tip force sensor for mri-guided cardiac procedures*, *IEEE/ASME Transactions on Mechatronics* **18** (2013), no. 1, 386–396.

- [122] D. Prattichizzo, M. Malvezzi, M. Gabiccini, and A. Bicchi, *On motion and force controllability of precision grasps with hands actuated by soft synergies*, IEEE Transactions on Robotics **29** (2013), no. 6, 1440–1456.
- [123] D. Prattichizzo and J. C Trinkle, *Chapter “grasping” in the springer handbook of robotics*, Springer, 2016.
- [124] Domenico Prattichizzo, Claudio Pacchierotti, and Giulio Rosati, *Cutaneous force feedback as a sensory subtraction technique in haptics*, IEEE Transactions on Haptics **5** (2012), no. 4, 289–300.
- [125] Pinyo Puangmali, Hongbin Liu, Lakmal D. Seneviratne, Prokar Dasgupta, and Kaspar Althoefer, *Miniature 3-axis distal force sensor for minimally invasive surgical palpation*, IEEE/ASME Transactions on Mechatronics **17** (2012), no. 4, 646–656.
- [126] L B Rosenberg, *Virtual Fixtures: Perceptual Tools for Telerobotic Manipulation*, Proceedings of IEEE Virtual Reality Annual International Symposium (1993), 76–82.
- [127] Carsten Rother, Vladimir Kolmogorov, and Andrew Blake, *Grabcut: Interactive foreground extraction using iterated graph cuts*, **23** (2004), 309–314.
- [128] A. Saccomanno, A. Laudati, Z. Szillasi, N. Beni, A. Cutolo, A. Irace, M. Giordano, S. Buontempo, A. Cusano, and G. Breglio, *Long-term temperature monitoring in cms using fiber optic sensors*, IEEE Sensors Journal **12** (2012), no. 12, 3392–3398.
- [129] Marco Santello, Martha Flanders, and JohnF. Soechting, *Postural hand synergies for tool use*, Journal of Neuroscience **18** (1998), no. 23, 10105–10115.

- [130] Katsunari Sato, Kazuto Kamiyama, Naoki Kawakami, and Susumu Tachi, *Finger-shaped gelforce: sensor for measuring surface traction fields for robotic hand*, IEEE Transactions on Haptics **3** (2010), no. 1, 37–47.
- [131] Leigh G. Seamon, David E. Cohn, Melissa S. Henretta, Kenneth H. Kim, Matthew J. Carlson, Gary S. Phillips, and Jeffrey M. Fowler, *Minimally invasive comprehensive surgical staging for endometrial cancer: Robotics or laparoscopy?*, Gynecologic Oncology **113** (2009), no. 1, 36–41.
- [132] C. Secchi, S. Stramigioli, and C. Fantuzzi, *Position drift compensation in port-hamiltonian based telemanipulation*, IEEE/RSJ Int. Conf. on Intelligent Robots and Systems, 2006, pp. 4211–4216.
- [133] M. Selvaggio, F. Chen, B. Gao, G. Notomista, F. Trapani, and D. Caldwell, *Vision based virtual fixture generation for teleoperated robotic manipulation*, Int. Conf. on Advanced Robotics and Mechatronics, 2016, pp. 190–195.
- [134] M. Selvaggio, G. Notomista, F. Chen, B. Gao, F. Trapani, and D. Caldwell, *Enhancing bilateral teleoperation using camera-based online virtual fixtures generation*, IEEE/RSJ International Conference on Intelligent Robots and Systems, Oct 2016, pp. 1483–1488.
- [135] Mario Selvaggio, Giuseppe Andrea Fontanelli, Fanny Ficuciello, Luigi Villani, and Bruno Siciliano, *Passive Virtual Fixtures Adaptation in Minimally Invasive Robotic Surgery*, IEEE Robotics and Automation Letters (2018).
- [136] Siddarth Sen, Animesh Garg, David V. Gealy, Stephen McKinley, Yiming Jen, and Ken Goldberg, *Automating multi-throw multilateral surgical suturing with a mechanical needle guide and sequential*

- convex optimization*, IEEE Int. Conf. on Robotics and Automation (2016), 4178–4185.
- [137] Azad Shademan, Ryan S. Decker, Justin D. Opfermann, Simon Leonard, Axel Krieger, and Peter C.W. W Kim, *Supervised autonomous robotic soft tissue surgery*, Science Translational Medicine **8** (2016), no. 337.
- [138] M. Shahbazi, S. F. Atashzar, and R. V. Patel, *A dual-user teleoperated system with virtual fixtures for robotic surgical training*, IEEE Int. Conf. on Robotics and Automation, 2013, pp. 3639–3644.
- [139] K. Shamaei, Y. Che, A. Murali, S. Sen, S. Patil, K. Goldberg, and A. M. Okamura, *A paced shared-control teleoperated architecture for supervised automation of multilateral surgical tasks*, 2015 IEEE/RSJ International Conference on Intelligent Robots and Systems (IROS), 2015, pp. 1434–1439.
- [140] Bruno Siciliano and Oussama. Khatib, *Springer handbook of robotics*, Springer Berlin Heidelberg, Berlin, Heidelberg, 2008.
- [141] Bruno Siciliano, Lorenzo Sciavicco, Luigi Villani, and Giuseppe Oriolo, *Robotics: Modelling, Planning and Control*, 2009.
- [142] C. D. Sousa and R. Cortesão, *Physically feasibility of robot base inertial parameters identification: A linear matrix inequality approach*, Int. Journal of Robotics Research **33** (2014), 931–944.
- [143] Nicholas Stylopoulos and David Rattner, *Robotics and ergonomics*, Surgical Clinics of North America **83** (2003), no. 6, 1321–1337.
- [144] Min Sun, Hao Su, Silvio Savarese, and Li Fei-Fei, *A multi-view probabilistic model for 3d object classes*, Computer Vision and Pattern Recognition, 2009. CVPR 2009. IEEE Conference on, IEEE, 2009, pp. 1247–1254.

- [145] Yu Sun, John M Hollerbach, and Stephen A Mascaró, *Predicting fingertip forces by imaging coloration changes in the fingernail and surrounding skin*, IEEE Transactions on Biomedical Engineering **55** (2008), no. 10, 2363–2371.
- [146] J. Swevers, C. Ganseman, J. De Schutter, and H. Van Brussel, *Experimental robot identification using optimized periodic trajectories*, Mechanical Systems and Signal Processing **10** (1996), 561–577.
- [147] J. Swevers, C. Ganseman, D. B. Tükel, and J. De Schutter, *Optimal robot excitation and identification*, IEEE Transactions on Robotics and Automation **13** (1997), 730–740.
- [148] S. Tadokoro, I. Kimura, and T. Takamori, *A dexterity measure for trajectory planning and kinematic design of redundant manipulators*, Annual Conference of IEEE Industrial Electronics Society, 1989, pp. 415–420.
- [149] Ali Talasaz, Ana Luisa Trejos, and Rajni V Patel, *The role of direct and visual force feedback in suturing using a 7-DOF dual-arm teleoperated system*, IEEE Transactions on Haptics **10** (2017), no. 2, 276–287.
- [150] Sebastian Thrun, Wolfram Burgard, and Dieter Fox, *Probabilistic Robotics (Intelligent Robotics and Autonomous Agents)*, The MIT Press, 2005.
- [151] J. W. T. Toh, A. Zakaria, I. Yang, and S. H. Kim, *Totally robotic single docking low anterior resection for rectal cancer: pearls and pitfalls*, Techniques in Coloproctology **21** (2017), no. 11, 893–895.
- [152] Nikolas Trawny and Stergios I Roumeliotis, *Indirect Kalman Filter for 3D Attitude Estimation A Tutorial for Quaternion Algebra Indirect Kalman Filter for 3D Attitude Estimation A Tutorial for*

Quaternion Algebra 1 Elements of Quaternion Algebra 1.1 Quaternion Definitions, (2005).

- [153] Antonia Tzemanaki, Peter Walters, Anthony Graham Pipe, Chris Melhuish, and Sanja Dogramadzi, *An anthropomorphic design for a minimally invasive surgical system based on a survey of surgical technologies, techniques and training*, *The International Journal of Medical Robotics and Computer Assisted Surgery* **10** (2014), no. 3, 368–378, RCS-13-0041.R2.
- [154] Sebastian Urban, Justin Bayer, Christian Osendorfer, Göran Westling, Benoni B Edin, and Patrick Van Der Smagt, *Computing grip force and torque from finger nail images using gaussian processes*, 2013 IEEE/RSJ International Conference on Intelligent Robots and Systems, IEEE, 2013, pp. 4034–4039.
- [155] Nikolaus Vahrenkamp, Tamim Asfour, Giorgio Metta, Giulio Sandini, and Rudiger Dillmann, *Manipulability analysis*, IEEE-RAS International Conference on Humanoid Robots (2012), no. 3, 568–573.
- [156] Lucie Viry, Alessandro Levi, Massimo Totaro, Alessio Mondini, Virgilio Mattoli, Barbara Mazzolai, and Lucia Beccai, *Flexible three-axial force sensor for soft and highly sensitive artificial touch*, *Advanced Materials* **26** (2014), no. 17, 2659–2664.
- [157] Bin Wang, Longhua Wu, KangKang Yin, Uri Ascher, Libin Liu, and Hui Huang, *Deformation capture and modeling of soft objects*, *ACM Transactions on Graphics (TOG)* **34** (2015), no. 4, 94.
- [158] Long Wang, Zihan Chen, Preetham Chalasani, Rashid M. Yasin, Peter Kazanzides, Russell H. Taylor, and Nabil Simaan, *Force-Controlled Exploration for Updating Virtual Fixture Geometry in Model-Mediated Telemanipulation*, *Journal of Mechanisms and Robotics* (2017).

- [159] Yangang Wang, Jianyuan Min, Jianjie Zhang, Yebin Liu, Feng Xu, Qionghai Dai, and Jinxiang Chai, *Video-based hand manipulation capture through composite motion control*, ACM Transactions on Graphics (TOG) **32** (2013), no. 4, 43.
- [160] Christian Wengert, Lukas Bossard, Charles Baur, GÁábor Székely, and Philippe C Cattin, *Endoscopic navigation for minimally invasive suturing.*, Computer aided surgery : official journal of the International Society for Computer Aided Surgery **13** (2008), no. 5, 299–310.
- [161] H. Xin, J. S. Zelek, and H. Carnahan, *Laparoscopic surgery, perceptual limitations and force: A review*, First Canadian Student Conference on Biomedical Computing (2006), no. January, 44–46.
- [162] Guang Zhong Yang, James Cambias, Kevin Cleary, Eric Daimler, James Drake, Pierre E. Dupont, Nobuhiko Hata, Peter Kazanzides, Sylvain Martel, Rajni V. Patel, Veronica J. Santos, and Russell H. Taylor, *Medical robotics - regulatory, ethical and legal considerations for increasing levels of autonomy*, Science Robotics **2** (2017), no. 4, 309–314.
- [163] Michael C. Yip, Shelten G. Yuen, and Robert D. Howe, *A robust uni-axial force sensor for minimally invasive surgery*, IEEE Transactions on Biomedical Engineering **57** (2010), no. 5, 1008–1011.
- [164] K. Yoshida and W. Khalil, *Verification of the positive definiteness of the inertial matrix of manipulators using base inertial parameters*, The Int. Journal of Robotics Research **19** (2000), 498–510.
- [165] Wenzhen Yuan, Rui Li, Mandayam A Srinivasan, and Edward H Adelson, *Measurement of shear and slip with a gelsight tactile sensor*, 2015 IEEE International Conference on Robotics and Automation (ICRA), IEEE, 2015, pp. 304–311.

-
- [166] Luca Zappella, Benjam̃n B jar, Gregory Hager, and Ren  Vidal, *Surgical gesture classification from video and kinematic data*, *Medical Image Analysis* **17** (2013), no. 7, 732 – 745.
- [167] G Y Zhang, A Wittek, G R Joldes, X Jin, and K Miller, *A three-dimensional nonlinear meshfree algorithm for simulating mechanical responses of soft tissue*, *Engineering Analysis with Boundary Elements* **42** (2014), 60–66.
- [168] Zhiqiang Zhang, Lin Zhang, and Guang Zhong Yang, *A computationally efficient method for hand eye calibration*, *International Journal of Computer Assisted Radiology and Surgery* **12** (2017), no. 10, 1775–1787.
- [169] Wenping Zhao, Jianjie Zhang, Jianyuan Min, and Jinxiang Chai, *Robust realtime physics-based motion control for human grasping*, *ACM Transactions on Graphics (TOG)* **32** (2013), no. 6, 207.
- [170] Fangxun Zhong, David Navarro-alarcon, Zerui Wang, Yun-hui Liu, Tianxue Zhang, Hiu Man Yip, and Hesheng Wang, *Adaptive 3D Pose Computation of Suturing Needle Using Constraints From Static Monocular Image Feedback*, (2016), 5521–5526.